TOPOLOGICAL SOFT MATTER

EDITED BY: Francesca Serra, Uroš Tkalec and Teresa Lopez-Leon
PUBLISHED IN: Frontiers in Physics

frontiers Research Topics

ISSN 1664-8714
ISBN 978-2-88966-145-9
DOI 10.3389/978-2-88966-145-9

About Frontiers

Frontiers is more than just an open-access publisher of scholarly articles: it is a pioneering approach to the world of academia, radically improving the way scholarly research is managed. The grand vision of Frontiers is a world where all people have an equal opportunity to seek, share and generate knowledge. Frontiers provides immediate and permanent online open access to all its publications, but this alone is not enough to realize our grand goals.

Frontiers Journal Series

The Frontiers Journal Series is a multi-tier and interdisciplinary set of open-access, online journals, promising a paradigm shift from the current review, selection and dissemination processes in academic publishing. All Frontiers journals are driven by researchers for researchers; therefore, they constitute a service to the scholarly community. At the same time, the Frontiers Journal Series operates on a revolutionary invention, the tiered publishing system, initially addressing specific communities of scholars, and gradually climbing up to broader public understanding, thus serving the interests of the lay society, too.

Dedication to Quality

Each Frontiers article is a landmark of the highest quality, thanks to genuinely collaborative interactions between authors and review editors, who include some of the world's best academicians. Research must be certified by peers before entering a stream of knowledge that may eventually reach the public - and shape society; therefore, Frontiers only applies the most rigorous and unbiased reviews.
Frontiers revolutionizes research publishing by freely delivering the most outstanding research, evaluated with no bias from both the academic and social point of view.
By applying the most advanced information technologies, Frontiers is catapulting scholarly publishing into a new generation.

What are Frontiers Research Topics?

Frontiers Research Topics are very popular trademarks of the Frontiers Journals Series: they are collections of at least ten articles, all centered on a particular subject. With their unique mix of varied contributions from Original Research to Review Articles, Frontiers Research Topics unify the most influential researchers, the latest key findings and historical advances in a hot research area! Find out more on how to host your own Frontiers Research Topic or contribute to one as an author by contacting the Frontiers Editorial Office: researchtopics@frontiersin.org

TOPOLOGICAL SOFT MATTER

Topic Editors:
Francesca Serra, Johns Hopkins University, United States
Uroš Tkalec, University of Ljubljana, Slovenia
Teresa Lopez-Leon, ESPCI ParisTech École Supérieure de Physique et de Chimie Industrielles de la Ville de Paris, France

Citation: Serra, F., Tkalec, U., Lopez-Leon, T., eds. (2020). Topological Soft Matter. Lausanne: Frontiers Media SA. doi: 10.3389/978-2-88966-145-9

Table of Contents

EDITORIAL
published: 11 September 2020
doi: 10.3389/fphy.2020.00373

Editorial: Topological Soft Matter

Francesca Serra[1]*, **Uroš Tkalec**[2,3,4] and **Teresa Lopez-Leon**[5]

[1] Department of Physics and Astronomy, Johns Hopkins University, Baltimore, MD, United States, [2] Faculty of Medicine, Institute of Biophysics, University of Ljubljana, Ljubljana, Slovenia, [3] Faculty of Natural Sciences and Mathematics, University of Maribor, Maribor, Slovenia, [4] Department of Condensed Matter Physics, Jožef Stefan Institute, Ljubljana, Slovenia, [5] Laboratoire Gulliver, UMR CNRS 7083, ESPCI Paris, Université PSL, Paris, France

Keywords: soft matter, mechanical metamaterials, liquid crystals, topology, active matter

Editorial on the Research Topic

Topological Soft Matter

In recent years, topology has acquired more and more importance in hard-condensed matter systems such as superconductors or photonic materials [1, 2]. Yet it also plays a central role in soft, non-crystalline materials. The behavior of many soft materials relies on vector fields, such as the nematic director in liquid crystals, velocity in fluids or in active particles, deformation in soft solids, or the orientation of fibers. All these fields can host singularities, or topological defects [3], which are crucial in determining the properties and behavior of soft systems [4]. The goal of this Special Topic is to bring together perspective from soft matter scientists on the role of topological defects in soft materials, focusing especially on metamaterials, liquid crystals, and active matter.

When thinking about topological materials, topological insulators immediately come to mind [5]. Soft analogs of such materials are provided by topological mechanical networks, or phononic metamaterials, where the propagation of mechanical deformations is suppressed in the bulk material but allowed at the boundaries, thus creating edge modes similar to those found in topological insulators. An example of such a material is described in the work by Ronellenfitsch and Dunkel, which shows the emergence of chiral edge modes in mechanical networks. These systems open new perspectives for the design of phononic metamaterials with exotic properties such as negative Poisson's ratio, negative effective mass, or gapped vibrational spectra.

Liquid crystals also offer fascinating perspectives in the design of photonic metamaterials, where matter and light can interact in unusual ways. Liquid crystal defects are characterized by strong elastic interactions and can therefore be used to direct the self-assembly of colloidal particles into complex 3D-architectures, with an optical index that is modulated at the scale of the light wavelength. Do et al. study defects in smectic-A liquid crystals, called oily streaks, to understand how nanoparticles are trapped and assembled within the defect.

Topological defects exist in all vectorial fields, but can defects from different fields crosstalk and interact? This crucial question has recently been addressed in different ways. Piccirillo et al. present an example of crosstalk between singularities in liquid crystals and phase singularities in optics, showing that the manipulation of liquid crystal defects can be a powerful tool to control optical beams.

Beyond applications, liquid crystals also constitute real laboratories to test predictions on topological defects and understand their behavior and interactions, since liquid crystal defects are observable and controllable [6]. This collection shows two important examples of this fine control. On the one hand, Pieranski and Godinho show a "defect collider" to study the annihilation between "dowsons," special topological defects in nematic liquid crystals whose dynamics resemble that of vortices in superconductors. On the other hand, the work by Harth and Stannarius presents a detailed study of the dynamics of defect interaction in smectic-C liquid crystal films, thus focusing on a nearly 2-dimensional system.

Edited and reviewed by:
Jasper Van Der Gucht,
Wageningen University and
Research, Netherlands

***Correspondence:**
Francesca Serra
francesca.serra@jhu.edu

Specialty section:
This article was submitted to
Soft Matter Physics,
a section of the journal
Frontiers in Physics

Received: 27 July 2020
Accepted: 31 July 2020
Published: 11 September 2020

Citation:
Serra F, Tkalec U and Lopez-Leon T
(2020) Editorial: Topological Soft
Matter. Front. Phys. 8:373.
doi: 10.3389/fphy.2020.00373

The ability to control liquid crystal defects comes from the existence of experimental tools to manipulate defects and from the development of predictive tools resulting from the understanding of the liquid crystal free energy. The work by Sussmann and Beller provides a detailed characterization of a new simulation tool to minimize the Landau-deGennes free energy, especially suited for capturing defects in confined nematic liquid crystals and in liquid crystals with imposed surface alignment.

A new open question in soft matter is to understand the role that topological defects have in the organization of active systems and living matter [7]. Defects in living systems appear at several length-scales, from lipid domains to cells, and at all length-scales there is evidence that they drive self-organization. Sengupta offers a perspective focusing on the micro-scale, highlighting the role that defects have in the interaction between microbes and their microenvironment.

Liquid crystal organization of biological material is also the subject of the work by Khadem and Rey, which focuses on the liquid crystalline behavior of tropocollagen, a polymer present in cells' extracellular matrix. This polymer forms rigid structures that create liquid crystal assemblies and drive the orientation of collagen fibers. The role of condensed liquid crystalline phases both in the cell cytoskeleton and in the extracellular matrix is still debated, and this paper sheds light on the energy of condensation of tropocollagen in various micro-environments.

Although the organization of biofibers in the cell cytoskeleton is responsible for the cell mechanical properties, complex cell functions, such as motility or replication, require the presence of force-generators, which bring the system out-of-equilibrium. A bioinspired "active nematic" has recently been developed by mixing microtubules with kinesin motors [8]. Here topological defects behave as self-propelled particles that control the flows in the material. In this out-of-equilibrium system, questions such as defect-mediated self-assembly of colloidal particles need to be reformulated. The work by Hardoüin et al. focuses on the formation and the dynamics of a line defect around a colloidal particle, paving the way for future research in the field.

Through examples of the behavior of topological defects in mechanical metamaterials, liquid crystals, and active matter, we hope to raise more questions and interest in the role that soft matter systems can play in understanding both the mechanism of formation of topological defects and their practical importance for materials technology and biology.

AUTHOR CONTRIBUTIONS

All authors listed have made a substantial, direct and intellectual contribution to the work, and approved it for publication.

FUNDING

We acknowledge the following funding by the Americal Chemical Society Petroleum Research Fund ACS-PRF 59931DNI10 (to FS), the Slovenian Research Agency (ARRS) under contract P1-0099 (to UT), and the French National Research Agency (ANR) under contract ANR- 18-CE09-0028-02 (to TL-L).

REFERENCES

1. Sato M, Ando Y. Topological superconductors: a review. *Rep Prog Phys*. (2017) **80**:076501. doi: 10.1088/1361-6633/aa6ac7
2. Lu L, Joannopoulos JD, Soljačić M. Topological photonics. *Nat Photon*. (2014) **8**:821–9. doi: 10.1038/nphoton.2014.248
3. Mermin ND. The topological theory of defects in ordered media. *Rev Mod Phys*. (1979) **51**:591. doi: 10.1103/RevModPhys.51.591
4. Nagel SR. Experimental soft-matter science. *Rev Mod Phys*. (2017) **89**:025002. doi: 10.1103/RevModPhys.89.025002
5. Moore J. The birth of topological insulators. *Nature*. (2010) **464:**194–8. doi: 10.1038/nature08916
6. Bowick MJ, Chandar L, Schiff EA, Srivastava AM. The cosmological Kibble mechanism in the laboratory: string formation in liquid crystals. *Science*. (1994) **263**:943–5. doi: 10.1126/science.263.5149.943
7. Hirst LS, Charras G. Liquid crystals in living tissue. *Nature*. (2017) **544**:164–5. doi: 10.1038/544164a
8. Sanchez T, Chen DTN, DeCamp SJ, Heymann M, Dogic Z. Spontaneous motion in hierarchically assembled active matter. *Nature*. (2012) **491**:431–4. doi: 10.1038/nature11591

Conflict of Interest: The authors declare that the research was conducted in the absence of any commercial or financial relationships that could be construed as a potential conflict of interest.

frontiers in Physics

ORIGINAL RESEARCH
published: 13 June 2019
doi: 10.3389/fphy.2019.00088

Theoretical Platform for Liquid-Crystalline Self-Assembly of Collagen-Based Biomaterials

Sayyed Ahmad Khadem and Alejandro D. Rey*

Department of Chemical Engineering, McGill University, Montréal, QC, Canada

The collagen triple helix is a ubiquitous biomacromolecule used in acidic aqueous solutions as precursor in the fabrication of artificial compact bone and cornea and in tissue engineering. The primary architecture of these highly structured solid tissues is formed during the cholesteric liquid-crystalline stage of their morphogenesis. The theoretical platform that describes the coupled dynamics of phase-ordering and mass transfer developed, implemented and validated here can be used for optimal material design and plays a significant complementary role to future experimental studies. Based on uniaxiality assumption, we have recently developed and validated a theory for the free energy tailored for acidic collagenous dispersions. Here we significantly expand and generalize our previous study, by including biaxiality since cholesteric phases must have a degree of biaxiality. In this work, we first modify the proposed interchain interaction and excluded-volume contribution by use of the addition theorem for spherical harmonics. Then, the Euler-Lagrange minimization followed by expansion around I/N* transition allows us to construct the free energy of ordering in terms of the phenomenological Landau–de Gennes formulation. Finally, we use the time-dependent Ginzburg-Landau equations to study the non-Fickian evolution of a single two dimensional cholesteric tactoid through a shallow quench from the isotropic to biphasic region of the phase diagram. Although equilibrium biaxiality is considerably low for these long-pitch cholesterics, we found that during self-assembly the biaxial order parameter achieves significant larger values than the equilibrium value. Additionally, the relaxed director field becomes both onion-like and defect-less, which is consistent with the twisted bipolar structure observed experimentally. The self-assembly simulations demonstrate that the formulated theoretical platform is not only consistent with previous theoretical and experimental studies but also able to be used to explore new routes for non-equilibrium collagen self-assembly. Taken together, this study deepens our understanding of cholesteric (chiral nematic N*) mesophase in acidic solutions of tropocollagen, and suggests a systematic spatio-temporal model that is capable of being used to extract the engineering principles for processing of these sought-after biomaterials.

Keywords: biaxiality, liquid-crystalline self-assembly, collagen-based bioinspired materials, cholesteric tactoids, Landau–de Gennes model, time-dependent Ginzburg-Landau model, chiral nematic nucleation and growth, uphill diffusion

Edited by:
Teresa Lopez-Leon,
ESPCI ParisTech École Supérieure de Physique et de Chimie Industrielles de la Ville de Paris, France

Reviewed by:
Xuejin Li,
Zhejiang University, China
Martin Kröger,
ETH Zürich, Switzerland

***Correspondence:**
Alejandro D. Rey
alejandro.rey@mcgill.ca

Specialty section:
This article was submitted to Soft Matter Physics, a section of the journal Frontiers in Physics

Received: *30 March 2019*
Accepted: *27 May 2019*
Published: *13 June 2019*

Citation:
Khadem SA and Rey AD (2019) Theoretical Platform for Liquid-Crystalline Self-Assembly of Collagen-Based Biomaterials. Front. Phys. 7:88. doi: 10.3389/fphy.2019.00088

INTRODUCTION

Type I Collagen is composed of three left-handed polypeptide helices (denoted by $[\alpha 1\,(\mathrm{I})]_2\,[\alpha 2\,(\mathrm{I})]$) twisted together to yield a right-handed triple helix. This rod-shaped biomacromolecule, also known as tropocollagen, commonly has a 1.5 nm bare diameter and 300 nm height. The tropocollagen falls into the class of fibrous proteins and is abundantly found in both soft and hard human's tissues, namely cornea, tendon, cortical bone, and more [1]. Over the past two decades, biomimetic fabrication of collagen-based biomaterials has received considerable attention in view of the abundant critical applications such as artificial bone [2–5] and cornea [6, 7] reconstruction. Moreover, for *in-vitro* replication of these collagenous biological tissues, there is fortunately no concern about supply because tropocollagen can be readily accessible through mammalian and non-mammalian resources [8]. Consequently, numerous promising applications of biomimetic fabrication of collagenous biomaterials [9–11] in conjunction with the availability of precursor play a central role in the drive to create the bioinspired collagen-based materials.

The structural pattern of tropocollagen rods bestows great structural-relation properties on collagenous biological materials and biomaterials. Furthermore, their structures are analogous with architecture of tropocollagen in liquid-crystalline states [12], hence these materials are called "solid analogs." This correspondence establishes the role and impact of liquid-crystalline morphogenesis [13–15] and singles out liquid-crystal-based biomimetic material process engineering as a promising route to enhance the quality of collagen-based biomaterials or even to explore new ones [3, 16–19].

Normally, tropocollagen is immiscible in aqueous solutions due to its hydrophobicity. To attain a stable aqueous isotropic phase, which is the starting point of biomimetic fabrication, hydrophobicity of tropocollagen must be reduced by being dispersed in acidic solutions. Basically, numerous amine function groups that are good proton receptors are found along the tropocollagen backbone. Once these functional groups are protonated, the intrachain repulsion causes that, the semi-flexible (worm-like) backbones become uncoiled and essentially rigid rods. The existing interchain repulsion also impedes aggregation, in other words the rods have an effective diameter between two or three times the bare one [20–22]. Finally, due to being charge-carrier rigid rod-like molecules, tropocollagen is capable of exhibiting lyotropic cholesteric phase organization. For example, for an acetic acid concentration of $[\mathrm{AC}] \approx 2,900$ mM, a phase transition from isotropic to chiral nematic (N*) takes places at tropocollagen concentrations of $[C] \approx 88$ mg/ml [21].

Although the primary architecture of these versatile biomaterials are formed at the molecular level (i.e., mesophasic stage), the focus has been at the tissue level [23] and studies on molecular level are few [21, 22]. Furthermore, to the best of authors' knowledge, theoretic studies of cholesteric self-assembly of aqueous acidic tropocollagen solutions have not been carried out, which also reflects the case of chiral nematic phase ordering in general [24–26]. To address this gap, we have recently developed, implemented, and validated a theoretical model tailored for self-assembly of tropocollagen dispersed in acidic aqueous solutions [20]. This thermodynamic theory [20], which is based on the uniaxiality assumption, has integrated microscopic mechanisms of mixing entropy and enthalpy, attraction, repulsion, twisting, excluded-volume, and chirality. In the present study, we lift the uniaxiality assumption by generalizing the free energy that includes biaxial effects. This is crucial for cholesteric materials because chiral nematic phase is described by two vectors: the director (**n**) and the chiral axis (**h**), additionally cholesterogens are intrinsically biaxial as discussed by Wulf [27] and Wright and Mermin [28]. Incorporation of the biaxial order parameter into the cholesteric self-assembly deserves consideration because biaxiality influences pattern-formation even in nematic mesophase, such as interfacial biaxiality under tangential director orientation [29–32], the biaxial core of singular disclinations [31, 33], and sometimes more pronounced biaxiality under time-dependent conditions than under static equilibrium [34]. For the above reasons we first include biaxiality in the model formulation stage and then focus on its emergence in bulk, defect core, and interfacial regions; which are of significant importance in all structured materials [30, 33, 35–37].

In our previous validated work [20], we showed that our thermodynamic model of acidic collagen solutions captures two key features: (i) the expected chimney diagram predicted by Flory and found experimentally for many lyotropic rod-like liquid-crystalline polymers [38], and (ii) the parabolic bi-phasic funnel in aqueous acidic collagenous solutions under increasing pH, where cholesteric tactoids (drops) emerge from isotropic phases. Study of cholesteric tactoids is important because of three main reasons: (i) tactoid formation process must occur in to chimney and funnel phase diagrams, which are the fingerprint of rod-like macromolecules. Thus, these cholesteric drops are a crucial element in the validation of thermodynamics of rod-shaped rigid macromolecules; (ii) these stable but deformable drops serve a sources of material properties information such as bulk Frank-Oseen-Mermin elasticity [27], novel coupled gradient contributions between nematic order parameter and collagen concentration, and the cholesteric pitch; (iii) characterizing and understanding the emergence, growth, annihilation, and coalescence of tactoids are essential to future developments of collagen-based material processing. To focus on collagen tactoids, as shown in **Figure 1**, we then target the dynamic of self-assembly through a shallow quench from isotropic phase into the bi-phasic funnel of the previously obtained phase diagram [20]. In contrast to the better known single component monomeric thermotropic tactoids, in the present case concentration is a conserved transport variable that need to be included. For this purpose, we formulate the coupled phase ordering/mass transfer Model C [39, 40] in order to derive the governing equations of collagen self-assembly. Afterward, we impose proper auxiliary conditions (e.g., initial and boundary conditions for the computational domain) on the obtained governing equations to capture a thorough spatio-temporal evolution of a single cholesteric tactoid—see **Figure 2**. This evolution has two steps: (i) emergence of a cholesteric nucleus in a continuous isotropic phase, (ii) followed by the formation of a stable chiral nematic tactoid coexisting with the isotropic phase.

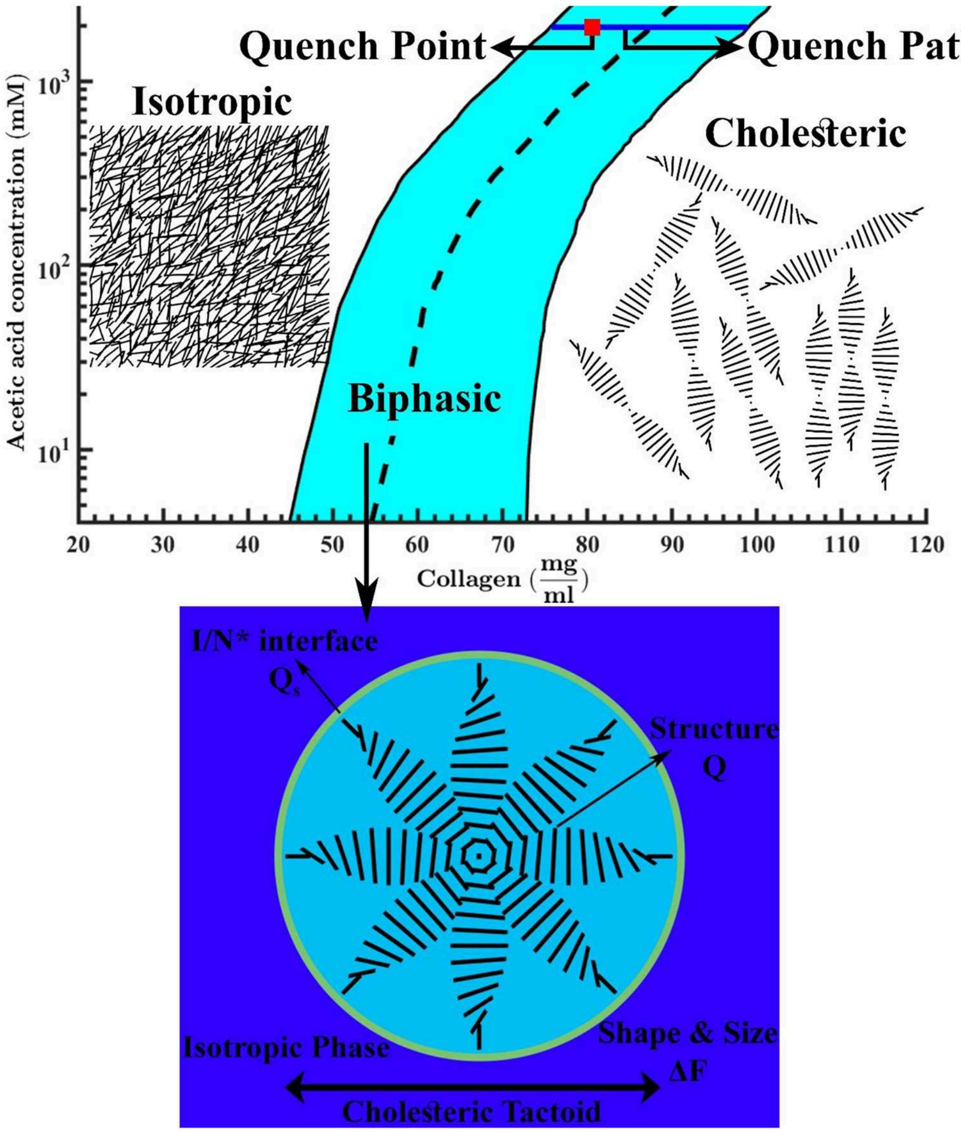

FIGURE 1 | Phase diagram of tropocollagen in acidic aqueous solutions. The black solid lines are binodal curves and the black dashed line is phase transition boundary. The quench point and the evolution path are shown by a red square and a blue solid line, respectively. This figure is adapted from Khadem and Rey [20]. The schematics denote the isotropic phase at low collagen concentrations, a typical micron-sized cholesteric drop in an isotropic bulk at intermediate concentrations, and the chiral nematic (N*) or cholesteric phase at higher concentrations.

In this work we restrict simulations to a single collagen tactoid with the aim of contributing to the evolving understanding of chiral phase ordering [24, 25, 41]. The simulations are also restricted to 2D. In principle, 3D spatio-temporal simulations can give a full picture of tactoid formation stages. Yet, from practical viewpoint, the present phase ordering/mass transfer coupled non-linear model with nano-to-micron scales becomes essentially intractable [42]. Furthermore, we have previously shown [43–45] that 2D simulations can provide invaluable predictions, and as discussed later on, in this study the important metrics of size, shape, and structure are not lost when using our 2D simulation box. In particular, we capture bulk disclinations, interfacial anchoring, interfacial biaxiality, growth modes, and self-selected shapes. Hence, this 2D study gives a necessary foundation for future 3D simulations.

The paper is organized as follows. Section Continuum Methodology for Simulation of Liquid-Crystalline Self-assembly of Tropocollagen Dispersed in Acidic Aqueous Solutions presents the methodology used in the formulation of self-assembly, including: (1) Formulation of the free energy for a system consisting of charged cholesterogen dispersed in a mixture of water solvent and mobile ions—see subsections Long-Range Description of Molecular Alignment to Total Free Energy Tailored for Tropocollagen Self-assembly in Acidic Aqueous

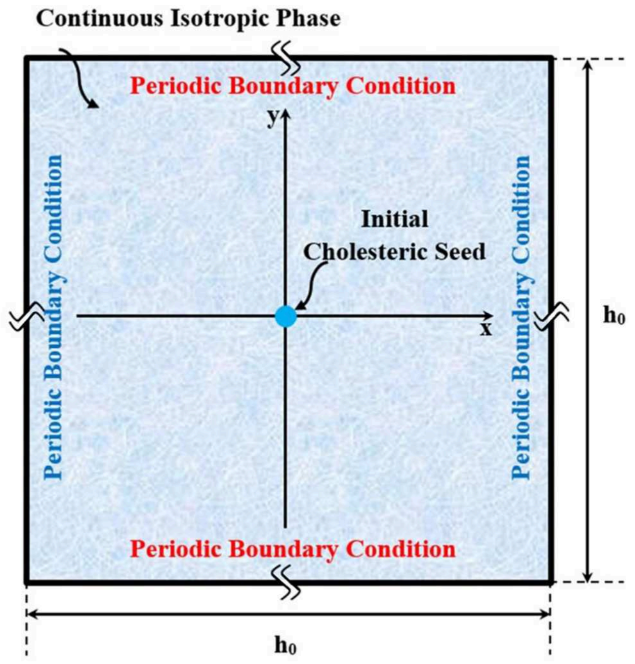

FIGURE 2 | Schematic of the computational domain, in which a small chiral nematic drop is initially seeded, and allowed to naturally grow in coexistence with an isotropic phase.

Solutions. Subsection Long-Range Description of Molecular Alignment defines the **Q**-tensor. In Free Energy Contributions for Pure Charged Cholesterogens; Incorporation of Biaxial Order Parameter, the free energy of pure charged cholesterogen is developed taking into account the biaxial order parameter. In Mixing Free Energy of Binary Dispersions Consisting a Charged Cholesterogen and Small-Sized Solvent, the obtained free energy is generalized for a mixture of charged cholesterogen and small-sized solvent. In Total Free Energy Tailored for Tropocollagen Self-assembly in Acidic Aqueous Solutions, we discuss and incorporate other free energy contributions involved in the evolution of mesophasic state, such as the elasticity of Frank-Oseen-Mermin [28] and gradient contributions, and formation of the I/N* interface. Thus, in Total Free Energy Tailored for Tropocollagen Self-assembly in Acidic Aqueous Solutions, the total free energy of system is formulated [2]. Formulation of governing equations along with the appropriate auxiliary conditions for simulation of liquid-crystalline self-assembly in which a cholesteric nucleus of tropocollagen is initially seeded and allowed to spontaneously growth in coexistence with isotropic phase—see subsections Governing Equations for Kinetics of Self-assembly; Orientational Relaxation, and Uphill Diffusion to Computational Details. In Governing Equations for Kinetics of Self-assembly; Orientational Relaxation, and Uphill Diffusion, the governing transport equations (Model C) are formulated. Finally, subsection Computational Details presents the implementation of self-assembly simulation for nucleation and growth of a single cholesteric tactoid coexisting with an isotropic phase. Section Results and Discussions, presents results of emergence and growth of a cholesteric tactoid. Lastly, the conclusions and nomenclature are summarized in sections Conclusions and Nomenclature, respectively.

CONTINUUM METHODOLOGY FOR SIMULATION OF LIQUID-CRYSTALLINE SELF-ASSEMBLY OF TROPOCOLLAGEN DISPERSED IN ACIDIC AQUEOUS SOLUTIONS

Long-Range Description of Molecular Alignment

The long-range orientational order in a liquid-crystalline phase is parameterized by a second-order symmetric traceless tensor called **Q**-tensor [14, 15, 46].

$$\mathbf{Q} = S\,(\mathbf{nn} - \boldsymbol{\delta}/3) + \frac{1}{3}\mathrm{P}\,(\mathbf{mm} - \mathbf{ll}) \tag{1}$$

where δ is the Kronecker delta. The orientation of a mesogen is characterized by the orthogonal director triad of $(\mathbf{n}, \mathbf{m}, \mathbf{l})$. The degree of alignment along the uniaxial director, **n**, and biaxial director, **m**, are S and P, respectively. Due to the quadrupolar symmetry of **Q**-tensor, it possesses the salient feature of head-tail invariance of molecular alignment (i.e., $\mathbf{n} \equiv -\mathbf{n}$, $\mathbf{m} \equiv -\mathbf{m}$, and $\mathbf{l} \equiv -\mathbf{l}$). The largest absolute eigenvalue of **Q**-tensor equals to 2S/3 and the corresponding eigenvector is equivalent of uniaxial director, **n**. The difference between the absolute medium and smallest eigenvalues is 2P/3 and the eigenvector corresponds to the second largest absolute eigenvalue is biaxial director, **m**. Thus, in the isotropic and ordered phases, the **Q**-tensor becomes the 3 × 3 zero matrix, $\mathbf{Q} = \mathbf{0}$, and non-zero matrix, $\mathbf{Q} \neq 0$, respectively.

The uniaxial and biaxial order parameters are also defined in terms of directors/**Q**-tensor or the normalized orientational distribution function on the unit sphere, $\psi(\mathbf{u})$, for any given molecular orientation, **u**:

$$\mathrm{S} = \int \mathrm{P}_2\,(\cos(\theta))\,\psi(\mathbf{u})\,d\Omega = 3\mathbf{n}\cdot\mathbf{Q}\cdot\mathbf{n}/2 \tag{2}$$

$$\mathrm{P} = \int \Delta(\theta,\phi)\psi(\mathbf{u})\,d\Omega = 3\,(\mathbf{m}\cdot\mathbf{Q}\cdot\mathbf{m} - \mathbf{l}\cdot\mathbf{Q}\cdot\mathbf{l})/2 \tag{3}$$

$d\Omega = \sin(\theta)\,d\theta d\varphi$ represents a solid angle, and θ and φ are the polar and azimuthal angles. $\Delta(\theta,\varphi)$ is defined as $3\sin^2(\theta)\cos(2\varphi)/2$. As explained below, $\mathrm{P}_2(\cos(\theta))$ and $\Delta(\theta,\varphi)$ are representative of uniaxiality and biaxiality, respectively. In addition, the normalized distribution function, employed in Equations (2, 3), implies following constraint [47]:

$$\int \psi(\mathbf{u})\,d\Omega = 1 \tag{4}$$

Free Energy Contributions for Pure Charged Cholesterogens; Incorporation of Biaxial Order Parameter

The total dimensionless Helmholtz free energy per particle, $\tilde{\mathrm{F}}$, for a dispersion comprising N_A charged cholesterogens is

[20, 48, 49]:

$$\begin{aligned}\tilde{F} \;=\; \frac{\beta F}{N_A} &= \beta\mu^{o}(T) - 1 + \ln c_A + \sigma(\psi(\mathbf{u})) + B_2(\psi(\mathbf{u})) \\ &+ M(\psi(\mathbf{u})) \end{aligned} \tag{5}$$

where β, $\mu^{o}(T)$, and c_A stand for thermal energy, standard chemical potential and number density, respectively. The last three terms in Equation (5) account for the contribution of molecular orientation (i.e., uniaxiality and biaxiality) in the mesophasic state. $\sigma(\psi(\mathbf{u}))$ describes the decrease of orientational entropy upon alignment of the mesogenic molecules.

$$\sigma(\psi(\mathbf{u})) = \int \psi(\mathbf{u}) \ln(4\pi\psi(\mathbf{u}))d\Omega \tag{6}$$

Since we focus on rod-like rigid mesogen, the second virial approximation is capable of accurately describing the excluded volume effect, given by Odijk [49] and Drwenski et al. [50]:

$$B_2(\psi(\mathbf{u})) = c_A\overline{\upsilon}_{AA}\rho(\psi(\mathbf{u})) \tag{7a}$$

$$\rho(\psi(\mathbf{u})) = \frac{4}{\pi}\iint \Gamma(\gamma)\,\psi(\mathbf{u})\,\psi(\mathbf{u}')d\Omega d\Omega' \tag{7b}$$

$$\begin{aligned}\Gamma(\gamma) &= |\sin(\gamma)| \\ &\times \left\{1 + h\left[-\ln|\sin(\gamma)| - \ln(2) + \frac{1}{2}\right]\right\}\end{aligned} \tag{7c}$$

$\overline{\upsilon}_{AA}$ is the average excluded volume defined as $\pi D_{eff}L^2/4$ in which L and D_{eff} denote contour length and effective diameter of tropocollagen. D_{eff} has a dependence on the bare diameter, $D = 1.5$ nm, and concentration [20]. To take biaxiality into consideration, in accordance with Drwenski [51, 52] and Matsuyama and Crystals [53], we make use of the addition theorem for spherical harmonics to express the angle between two rods, γ, in terms of the polar, θ, and azimuthal, φ, angles in spherical coordinate:

$$P_2(\cos(\gamma)) = P_2(\cos(\theta))\,P_2(\cos(\theta')) + \Delta(\theta,\varphi)\Delta(\theta',\varphi')/3 \tag{8}$$

First term in Equation (8) is independent from azimuthal angle and represents uniaxiality. Second term is related to biaxial contribution and has the dependence on both polar and azimuthal angles.

The intermolecular interaction and angle between rods interchangeably affect each other because the electrostatic repulsion and twisting favors perpendicular orientation while the van der Waals attraction prefers the parallel alignment (i.e., nematic phase) [49, 50, 54]. Hence, based on our previous work [20] and [51], we suggest the net interchain potential expressed by

$$\beta U_i = \beta\left(U'^{elc} - U'^{MS}\right)\upsilon_A P_2(\cos(\gamma)) \tag{9}$$

where υ_A is the volume of an individual rigid rod, $\upsilon_A = \pi D_{eff}^2 L/4$. U'^{elc} and U'^{MS} are parameters of electrostatic repulsion and a positive constant, respectively. The contribution of intermolecular interaction, $M(\psi(\mathbf{u}))$, is then obtained by taking average over all possible rod configurations [20]:

$$M(\psi(\mathbf{u})) = \frac{3}{2}\beta U c_A \upsilon_A^2 \mathbf{Q}{:}\mathbf{Q} \tag{10}$$

$U = U^{elc} - U^{MS}$ is called the potential of the orientation-dependent intermolecular interactions where U^{elc} and U^{MS} are the strength of electrostatic repulsion and Maier-Saupe constant that is a positive constant independent of temperature. Note that $\mathbf{Q}:\mathbf{Q}$ is related to uniaxial and biaxial order parameters by $2\left(S^2 + P^2/3\right)/3$.

We note that the effective diameter reflects the intermolecular repulsion, or to put it another way, the effective thickness of the attached ions on the backbone of tropocollagen. This effective thickness is called double-layer thickness, $\alpha\kappa^{-1}$ [49, 50]:

$$D_{eff} = D + \alpha\kappa^{-1} \tag{11}$$

α and κ^{-1}, which are defined as follows, are parameter of double-layer thickness and Debye screening length, respectively:

$$\begin{aligned}\alpha &= \ln A' + \gamma_E + \ln(2) - \frac{1}{2} \\ &- \frac{4}{\pi}\left[|\sin(\gamma)|\,\mathrm{Ei}\left(-\frac{A'}{|\sin(\gamma)|}\right)\right]_i\end{aligned} \tag{12a}$$

$$A' = A\frac{e^{\kappa D}}{\kappa D},\; A = 2\pi\Lambda^2\lambda_B D \tag{12b}$$

$$\left[f(\mathbf{u},\mathbf{u}')\right]_i = \frac{1}{16\pi^2}\iint f(\mathbf{u},\mathbf{u}')\,d\Omega d\Omega' \tag{12c}$$

$$\kappa^{-1} = (8\pi\lambda_B N_{avo}\epsilon)^{-1/2} \tag{12d}$$

$$\epsilon = \frac{1}{2}\sum_i m_i Z_i^2 \tag{12e}$$

where λ_B, N_{avo}, ϵ, m, Z, Ei$(\bullet)$, γ_E, and Λ are the Bjerrum length, Avogadro's number, ionic strength, molar concentration, charge number, the exponential integral defined as $\mathrm{Ei}(x) = -\int_{-x}^{\infty}\exp(-t)/t\,dt$, Euler constant equals to 0.5772, and linear charge density. A detailed account of parameters' values, their selection and physical significance and physical properties for aqueous acidic collagen I solutions is given in Khadem and Rey [20].

Mixing Free Energy of Binary Dispersions Consisting a Charged Cholesterogen and Small-Sized Solvent

The mixing free energy of the binary solution is given by Matsuyama and Kato [48]

$$F = \Delta F_{mixing}(N_A,N_I) = F^s(N_A,N_I) - F^s(N_A,0) - F^s(0,N_I) \tag{13}$$

where $F^s(N_A,N_I)$, $F^s(N_A,0)$ and $F^s(0,N_I)$ are free energies of solution, pure anisotropic component dispersed in isotropic state and isotropic component, respectively. Thus, in this subsection, we shall first derive the free energy of solution, and then formulate the mixing free energy of a binary dispersion by use of Equation (13).

Substituting Equations (7, 10) into Equation (5) leads to the free energy of pure charged chiral nematic rods. The free energy for binary mixture of charged chiral mesogen and small-sized solvent (water in our case)—denoted by subscript A and I, respectively—is then formulated as

$$\begin{aligned}\beta F^{s} = {} & N_A\beta\mu_A^{o} + N_I\beta\mu_I^{o} - N_A - N_I + N_A \ln c_A + N_I \ln c_I + N_A\sigma \\ & (\psi(\mathbf{u})) + \overline{\upsilon}_{AA} N_A c_A \rho(\psi(\mathbf{u})) + 2\overline{\upsilon}_{AI} N_I c_A + \overline{\upsilon}_{II} N_I c_I \\ & + N_A \beta U c_A \upsilon_A^2 \left(S(\psi(\mathbf{u}))^2 + \frac{1}{3} P(\psi(\mathbf{u}))^2 \right) \qquad (14)\end{aligned}$$

Equation (14) is not usable unless the unknown normalized distribution function, $\psi(\mathbf{u})$, is known. To formulate the normalized distribution function, the total free energy of system subjected to the normalizing constraint, given by Equation (4), is minimized using Euler-Lagrange method. This minimization yields an irreducible algebraic integral equation expressed by

$$\begin{aligned}\ln(4\pi\psi(\theta,\varphi)) = {} & \eta' - 2\beta U c_A \upsilon_A^2 \left\{ SP_2(\cos(\theta)) + \frac{1}{3} P\Delta(\theta,\varphi) \right\} \\ & - \frac{8}{\pi}\overline{\upsilon}_{AA} c_A \int \Gamma(\gamma)\,\psi\left(\theta',\varphi\right) d\Omega' \qquad (15)\end{aligned}$$

Simplicity of free energy expression is essential since our ultimate objective is the self-assembly simulation which in itself is computationally complex. A heavy computational load is expected because the self-assembly process covers a wide range of length scale (i.e., ranging from nano- to macro-scale) and it may go through a variety of complex microscopic mechanisms [41, 55–59]. Thus, to improve tractability, we expand the functional part of Equation (15), $\Gamma(\gamma)$, in terms of the second Legendre polynomial by use of Equation (8):

$$\begin{aligned}\Gamma(\gamma) \approx {} & \frac{\pi}{4} - \frac{5\pi}{32}\left(1 - \frac{11}{8}h\right) \\ & \left\{ P_2(\cos(\theta))\, P_2\left(\cos\left(\theta'\right)\right) + \frac{1}{3}\Delta(\theta,\varphi)\Delta(\theta',\varphi') \right\} \qquad (16)\end{aligned}$$

Having substituted Equation (16) into Equation (15), the normalized distribution function is obtained:

$$\psi(\theta,\varphi) = \frac{\exp\left(W\left\{SP_2(\cos(\theta)) + P\Delta(\theta,\varphi)/3\right\}\right)}{I_{00}} \qquad (17)$$

where the I_{00} is a definite integral defined as

$$I_{00}(S,P,W) = \int_0^1 \int_0^1 \exp\left(W\left\{SP_2(x) + P\Delta(x,y)/3\right\}\right) dx\,dy \qquad (18)$$

W is known as the net cholesteric potential, which is similar to Khadem and Rey [20] and can be parameterized as

$$W = \alpha_w \phi_A \qquad (19a)$$

$$\alpha_w = \frac{5}{4}\left(1 - \frac{11}{8}h\right)\frac{L}{D_{eff}} - \frac{\pi}{2} D_{eff}^2 \beta U L \qquad (19b)$$

ϕ_A is the effective volume fraction and $h = (\kappa D_{eff})^{-1}$. α_W is assumed to only be dependent on concentration of acid throughout the evolution—a reasonable assumption because α_W is mainly affected by concentration of acid [20].

Next the mixing free energy, Equations (20a–c), is obtained by use of Equations (13, 14, 17). Detailed account of such algebraic derivation are given in Khadem and Rey [20] and Odijk [48]. Note that hereafter, for convenience, we use ϕ to represent the effective volume fraction of tropocollagen—it can be related to the concentration of tropocollagen in units of mg of tropocollagen pre ml of solution by $C = \phi/\alpha_c$ where α_c is a unit conversion factor. The dimensionless mixing free energy density is:

$$\tilde{f}_{mxing} = \tilde{f}_{iso} + \tilde{f}_h \qquad (20a)$$

$$\tilde{f}_{iso} = \frac{\phi \ln(\phi)}{n} + (1-\phi)\ln(1-\phi) + \chi\phi(1-\phi) \qquad (20b)$$

$$\tilde{f}_h = \frac{\phi}{n}\left[\frac{3}{4} W\mathbf{Q}:\mathbf{Q} - \ln\left(I_{00}(W,S,P)\right)\right] \qquad (20c)$$

where n stands for number of segments on tropocollagen backbone. $\tilde{f}_{iso}$ and $\tilde{f}_h$ describe different physics; the former explains the phase separation which is the well-known Flory-Huggins equation and the latter controls the phase transition (i.e., homogenous contribution). In the absence of biaxiality, $P = 0$, the obtained mixing free energy, Equations (20a–c), is reduced to the validated free energy functional given in Khadem and Rey [20] which was validated with experimental data of tropocollagen and with previous theoretical studies. It is worth mentioning that with further assumptions the obtained free energy density leads to the formulation given in Matsuyama and Kato [48] as well as the well-established theory of Onsager—see ESI of Khadem and Rey [20] for further discussion. For numerical tractability, similar to Matsuyama [51] and Matsuyama and Kato [48], we make use of a Taylor expansion in vicinity of I/N* to expand Equation (20c) in a power series of order parameters, $S^i P^j$–the resulting polynomial is the phenomenological Landau-de Gennes (LdG) theory [60]:

$$\tilde{f}_h = \frac{a}{2}\mathrm{Tr}\left(Q^2\right) - \frac{b}{3}\mathrm{Tr}\left(Q^3\right) + \frac{c}{4}\left(\mathrm{Tr}\left(Q^2\right)\right)^2 \qquad (21a)$$

$$a(\phi) = \frac{3}{2}\frac{\alpha_w}{n}\left(1 - \frac{\alpha_w\phi}{5}\right)\phi^2 \qquad (21b)$$

$$b(\phi) = \frac{9}{70}\frac{\alpha_w^3}{n}\phi^4 \qquad (21c)$$

$$c(\phi) = \frac{\alpha_w}{10} b\phi \qquad (21d)$$

Although self-assembly simulations by use of the Equations (21a–d) is appreciably more tractable than with Equation (20c), it should be noted that the used expansion may affect the accuracy of simulations in the cases of deep quenches. However, this study only focuses on the self-assembly of shallow quenches into biphasic region which is a narrow region around I/N* boundary, see **Figure 1**.

An order-disorder phase transition takes place if and only if $W = \alpha_W\phi = \alpha_W\alpha_c C > 5$ to make the coefficient of second invariant of **Q**-tensor, a, negative. The derived LdG coefficients satisfy two general theoretical expectations; (1) the first-order phase transition (i.e., $B \neq 0$), and (2) two minima correspond to isotropic and ordered phases (i.e., $A<0$ and $C>0$) [46]. Furthermore, in the cholesteric phase, W can be about 10, and under such conditions the proposed LdG coefficients becomes similar to the well-established lyotropic LCP Doi's model, were $b \approx c$ [14, 15, 61].

Total Free Energy Tailored for Tropocollagen Self-Assembly in Acidic Aqueous Solutions

In addition to $\tilde{f}_{mxing}$ which is capable of describing phase separation and an order–disorder phase transition, for constructing the total free energy of mesogenic solutions, the contributions of gradients should be taken to account [62–64]:

$$\tilde{F}_{net} = \int_{\tilde{V}} \left(\tilde{f}_{iso} + \tilde{f}_h + \tilde{f}_e + \tilde{f}_{cg} + \tilde{f}_c\right) d\tilde{V} \tag{22a}$$

$$\tilde{f}_e = \frac{1}{2}\left(\frac{\xi}{h_0}\right)^2 \left[\left[\tilde{\nabla} \times \mathbf{Q} + 4\pi\left(\frac{h_0}{p_\infty}\right)\mathbf{Q}\right]^2 + \left(\frac{L_2}{L_1}\right)\left[\tilde{\nabla} \cdot \mathbf{Q}\right]^2\right] \tag{22b}$$

$$\tilde{f}_{cg} = \frac{1}{2}\tilde{L}_\phi\left(\tilde{\nabla}\phi\right)^2 \tag{22c}$$

$$\tilde{f}_c = \tilde{L}_{\phi-\mathbf{Q}}\left(\tilde{\nabla}\phi\right) \cdot \left(\tilde{\nabla} \cdot \mathbf{Q}\right) \tag{22d}$$

$\xi = \sqrt{a^3 L_1 \beta}$ is the coherence length in which a^3 stands for the volume of each lattice unit and L_i are elastic constants. $\tilde{\nabla} = h_0 \nabla$ is dimensionless gradient in which h_0 denotes a macroscopic length scale and the spatial domain is scaled by h_0, $\tilde{L}_\phi = L_\phi a^3 \beta / h_0^2$ and $\tilde{L}_{\phi-Q} = L_{\phi-Q} a^3 \beta / h_0^2$ where L_ϕ is cost of interfacial formation and $L_{\phi-Q}$ represents coupling constant. The total free energy as well as the evolution of chiral nematic phase for tropocollagen are mesoscopic because it retains both microscopic length scale, ξ, in a nanometer range and macroscopic length scale, h_0, in the range of micrometers.

Governing Equations for Kinetics of Self-Assembly; Orientational Relaxation, and Uphill Diffusion

Simulations of pattern-formation in fibrous composites, including collagen-based tissues, were first carried out by De Luca and Rey [61, 64, 65]. Their approaches were based on diffusionless evolution of mesophase, and capable of predicting macroscopic architecture of these materials to a great extent. However, recent studies have revealed the imperative role of diffusion in accurately capturing the growth of order-disorder interface [43, 45]. Hence, for the purpose of realistic self-assembly modeling, in this subsection, we formulate the spatio-temporal evolution of tropocollagen in which the **Q**-tensor augmented with a mass transfer equation.

The cholesteric micro-structures in collagenous biomaterials are formed through the liquid-crystalline self-assembly stage. Two simultaneous mesoscopic mechanisms govern this thermodynamically driven assembly. First, mass transfer mechanism allows tropocollagen macromolecules to diffuse into cholesteric phase (i.e., tropocollagen-rich phase) from isotopic phase (i.e., tropocollagen-lean phase). The mentioned demixing is known as uphill or non-Fickian diffusion and reduces the total free energy of system. Second, orientational relaxation mechanism induces cholesteric architecture inside the formed high-concentration domain. To describe these two phenomena; two coupled fields are required. First, the conserved scalar field of concentration, C, or equivalently volume fraction, ϕ , governing the phase separation. Secondly, the non-conserved tensorial field of **Q**-tensor by which the orientation of tropocollagen biomacromolecules is primarily specified. The spatio-temporal evolution of $\{\mathbf{Q}, \phi\}$ is found using the time-dependent Ginzburg–Landau (TDGL) formalism, also known as model C in Hohenberg and Halperin classification [39, 40]. The dimensionless form of model C adjusted for self-assembly simulation reads [17, 61, 64, 66, 67]:

$$\frac{\partial \mathbf{Q}}{\partial \tilde{t}} = -\frac{1}{\left(1 - 3\mathrm{Tr}\left(\mathbf{Q}^2\right)/2\right)^2}\left(\frac{\delta \tilde{F}_{net}}{\delta \mathbf{Q}}\right)^{[s]} \tag{23a}$$

$$\frac{\partial \phi}{\partial \tilde{t}} = \tilde{M}_\phi \tilde{\nabla} \cdot \left([\mathbf{I} + \mathbf{Q}] \cdot \tilde{\nabla}\frac{\delta \tilde{F}_{net}}{\delta \phi}\right) \tag{23b}$$

$\delta\tilde{F}_{net}/\delta Q$ represents functional derivative. $\tilde{t}$ is dimensionless time defined as $\tilde{t} = t M_Q / \left(a^3 \beta\right)$ where t is time, $\tilde{M}_\phi = M_\phi / \left(M_Q h_0^2\right)$ in which the mobilities of **Q** and ϕ are $M_\mathbf{Q}$ and M_ϕ, respectively. Additionally, the superscript [*s*] indicates that the functional derivative must be symmetric traceless in order to be consistent with the nature of **Q**-tensor—for any given second rank tensor $\mathbf{T}^{[s]} = \left(\mathbf{T} + \mathbf{T}^t\right)/2 - \mathrm{Tr}\left(\mathbf{T}\right)\boldsymbol{\delta}/3$ where superscript t denotes transpose.

The system given in Equations (23a,b) is a set of six coupled non-linear PDEs. Equation (23a) accounts for the spatio-temporal evolutions of the orientational tensor order parameter. This equation is the compact tensorial form of five independent second-order PDEs. Furthermore, Equation (23b) is a fourth-order PDE, known as the Cahn-Hilliard equation, to describe the concentration field by which the chiral nematic and isotropic phases gradually evolve through the uphill diffusion mechanism.

Computational Details

Here we elaborate on the simulation of nucleation and growth of an isolated cholesteric tactoid in a continuous isotropic phase. This simulation consists of a diffusional phenomenon coupled with structural relaxation. The general schematic representation of this implementation is illustrated in **Figure 2**.

As above mentioned, the biomimetic formation of collagen-based tissues starts with dissolving tropocollagen in acidic aqueous solutions to obtain the isotropic phase. In such condition, a nucleus is thermodynamically allowed to grow, providing its radius is greater than a critical value. In that case, as a single tactoid grows, the tropocollagen rods diffuse from collagen-lean phase to collagen-rich phase, in turn, the isotopic and cholesteric phases become depleted from and enriched in tropocollagen, respectively. The diffusion of tropocollagen from lean phase (isotropic phase) to rich phase (cholesteric phase) continues till a point where the chemical potentials of two phases become identical.

As illustrated in the **Figure 2**, we consider the bulk of system as a square with $[-0.5\ 0.5] \times [-0.5\ 0.5]$ normalized by h_0. Each pair of sides are subjected to the periodic boundary condition. Initially $\mathbf{Q} = 0$ and the phase is isotropic. Afterwards, an initial cholesteric tactoid is seeded by a circular Gaussian distribution with FWHM (full width at half maximum of Gaussian function) greater than the critical drop diameter. The seeding is expressed:

$$\mathbf{Q}|_{t=0} = \left[S_e\left(\mathbf{n}_e\mathbf{n}_e - \boldsymbol{\delta}/3\right) + \frac{1}{3}P_e\left(\mathbf{m}_e\mathbf{m}_e - \mathbf{l}_e\mathbf{l}_e\right)\right] \times e^{-\frac{1}{2}\left(\left(\frac{x-x_0}{\sigma_x}\right)^2 + \left(\frac{y-y_0}{\sigma_y}\right)^2\right)} + \boldsymbol{\Xi} \tag{24a}$$

$$\phi|_{t=0} = (\phi_{ch} - \phi_{iso}) \times e^{-\frac{1}{2}\left(\left(\frac{x-x_0}{\sigma_x}\right)^2 + \left(\frac{y-y_0}{\sigma_y}\right)^2\right)} + \phi_{iso} + \Xi \tag{24b}$$

$\boldsymbol{\Xi}$ and Ξ, that are, respectively, a second rank symmetric traceless random tensor and scalar random number, are included in the modeling to represent the fluctuations existing in a real system. The subscript e indicates the equilibrium condition given by:

$$\mathbf{n}_e = \left[0\ \cos\left(\frac{2\pi}{p_\infty}x\right)\ \sin\left(\frac{2\pi}{p_\infty}x\right)\right] \tag{25a}$$

$$\mathbf{m}_e = \left[0\ -\sin\left(\frac{2\pi}{p_\infty}x\right)\ \cos\left(\frac{2\pi}{p_\infty}x\right)\right] \tag{25b}$$

In accordance with $\mathbf{l} = \mathbf{n} \times \mathbf{m}$, $\mathbf{l}_e$ is computed as $\left[0\ 0\ 1\right]$. Equations (24a,b, 25a,b) describe a nucleus whose center placed at position (x_0, y_0) at a concentration equivalent to the effective volume fraction of ϕ_{ch}. For convenience, we choose the center at $(x = 0,\ y = 0)$. The concentration of tropocollagen from the center, which is a cholesteric phase, gradually decreases along the radius to the concentration of continuous isotropic phase, ϕ_{iso}. This approach for simulating the initial nucleus was adapted from Wincure and Rey [30, 31, 33]. In order to make sure that the initial drop is sufficiently large, we choose the $\sigma_x = \sigma_y = \sigma$ and obtain σ in way that FWHM equals two times the critical diameter: $\mathrm{FWHM} = 2\sqrt{2\ln 2}\,\sigma = 2D_c = 4R_c$. Classical Nucleation theory [68] provides a rough estimation of the critical radius of a drop as expressed by $R_c = \left|2\gamma_i/\left(c_A\Delta\mu^{iso-Cho}\right)\right|$ in which $\gamma_i$and $\Delta\mu^{iso-Cho}$are the interfacial tension and the chemical potential difference between isotropic and cholesteric phase [68, 69]. Additionally, Equation (24b) yields the quenched concentration as $\phi_q = \iint_{CD}\phi|_{t=0}dxdy/\iint_{CD}dxdy$ in which CD denotes the entire system (computational domain). Consequently, ϕ_{iso} plays an appreciable role in the size of tactoid because its value affects the initial amount of tropocollagen existing in the system.

Furthermore, the total conservation of mass is imposed by:

$$\frac{d}{dt}\int_{CD}\phi\,dxdy = 0 \tag{26}$$

Simulation parameters used in this study are summarized in **Table 1**—also readers are referred to the Khadem and Rey [20] for detailed account of parameters selection in order to accurately capture the available experimental data.

Although the $\tilde{L}_{\phi-\mathbf{Q}}$, $\tilde{L}_{\phi}$, and L_2/L_1 have not been documented for tropocollagen, we choose common values which satisfy the energy transformation constraint [70–72]:

$$\frac{\left(\tilde{L}_{\phi-Q}\right)^2}{\tilde{L}_{\phi} \times (L_2/L_1)} < 1 \tag{27}$$

Equations (24a,b) in conjunction with the above-explained conditions are solved with an adaptive finite elements technique with biquadratic basis functions (General PDE solver of COMSOL Multi-physics 5.3a). Furthermore, to acquire the acceptable spatial resolution, we considered at least 50 elements per pitch which resulted in nearly 10^4 triangular elements, and temporal resolution was carried out by the Backward Euler method. Convergence, accuracy, and stability were checked using standard techniques—for further information on the method and solution approach, please see the accompanying **Supplementary Material**.

RESULTS AND DISCUSSIONS

In this section, the dynamics of mesophasic evolution and the resulting equilibrium configuration for a shallow quench from the isotropic phase into the cholesteric phase in the presence of one small cholesteric seed are given and discussed (see **Figures 1**, **2**).

Figures 3a–d show snapshots of a growing tactoid corresponding to dimensionless times 0, 900, 960, and 1,100, respectively. **Figure 3a** shows the initial condition of a small chiral nematic drop seeded in a large isotropic phase area. Note that only a small section of the computational domain, in which the self-assembly is supposed to take place, is shown in **Figure 3**. The computational domain is actually chosen as a fairly large square with length of $h_0 = 100\,\mu m$ in order to make sure that the existing amount of tropocollagen in the system is sufficient for formation of a single cholesteric tactoid with diameter of the order of 30 μm—as experimentally observed [21]. The size of initial seed must be greater than a critical value in order for the drop to grow based on the mechanism of uphill diffusion, otherwise downhill diffusion takes place and the initial drop is dissolved in isotropic phase.

Although the initial configuration of rods is chosen as twisting around x-axis, see **Figure 3a1**, the rods prefer to be aligned in a concentric configuration, as shown in **Figure 3b1**. During the early growth of the tactoid, rods attempt to radially twist—the helicoidal axes are along the radii of the circular tactoid. Yet, rods placed at the center of drop exhibit orientational frustration. This frustration emerges in $\tilde{t} = 900$, **Figure 3b1**, and yields a τ^{+1} cholesteric defect. As the tactoid grows, the central rods resolve the orientational frustration with an escaped configuration (see **Figure 3d1**) known as a non-singular λ^{+1} cholesteric disclination. These important predictions may be

TABLE 1 | The material properties and parameter values used in the present paper.

Parameters	Values	Parameters	Values	Parameters	Values
n	10 [–]	χ	1.4 [–]	L_2/L_1	1[-]
$\tilde{L}_{\phi-\mathbf{Q}}$	-4.4×10^{-7}[–]	$\tilde{L}_{\phi}$	2.8×10^{-4} [-]	$\tilde{M}_{\phi}$	1.1×10^{-5} [-]
S_e	1[–]	P_e	10^{-3}[-]	h_0	100 [µm]
C_{ch}	98 [mg/ml]	C_{iso}	79 [mg/ml]	p_{∞}	10 [µm]

The square-brackets next to the values indicate the corresponding unit, and [–] shows dimensionless. For those parameters which have not been documented for solutions of tropocollagen, the common values are used instead. Readers are referred to Khadem and Rey [20], Gobeaux et al. [21], De Luca and Rey [61], Gurevich et al. [62], Das and Rey [63], and De Luca and Rey [64] for details of parameter selection.

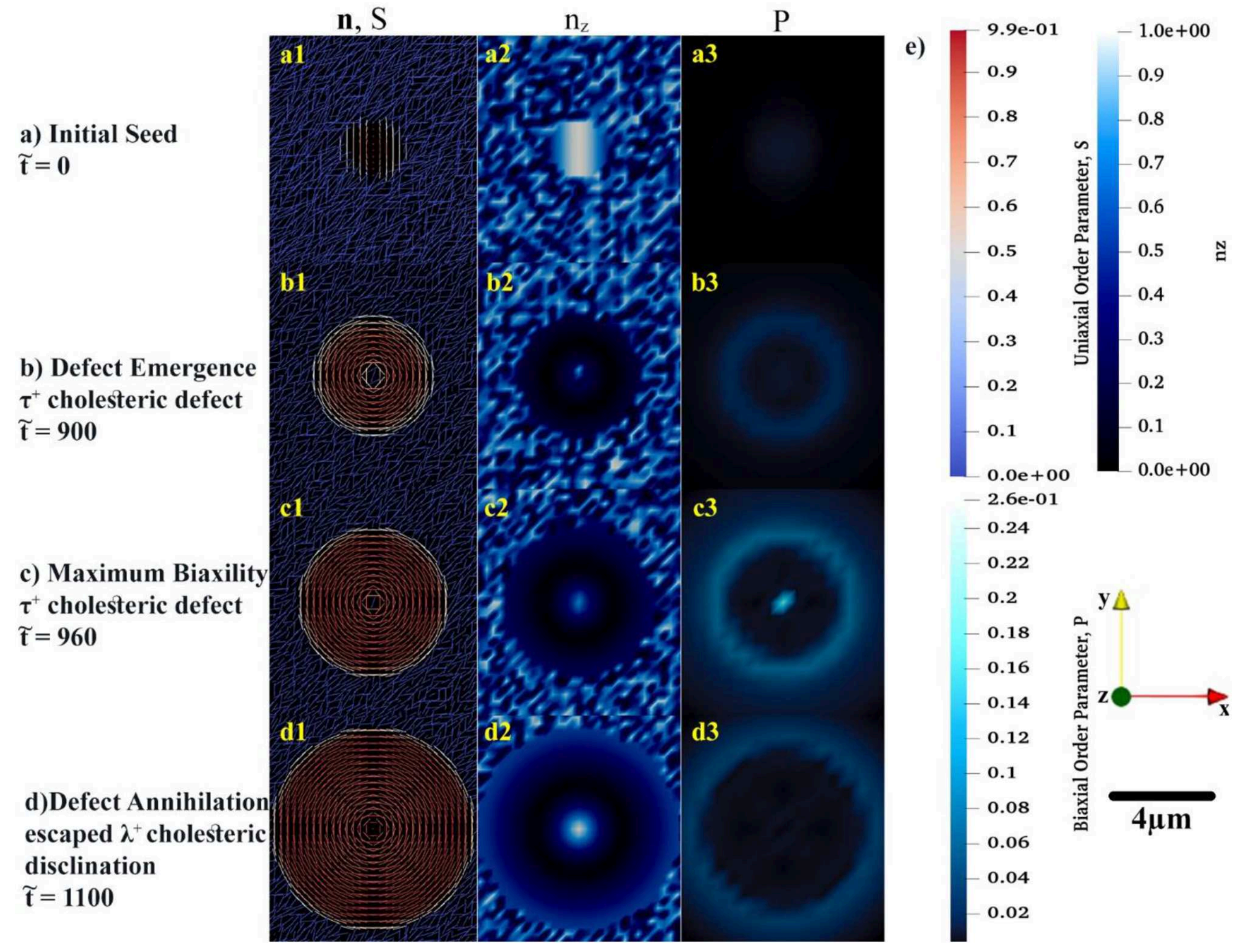

FIGURE 3 | The spatial distributions of order parameters, S and P, in conjunction with the director configuration at the early growth of cholesteric tactoid shown in **(a–d)**. In the first column, the uniaxial configuration, **n**, of tropocollagen macromolecules are represented by rods whose color (blue to red) shows the uniaxial order parameter, S. To complete the understanding about the configuration of rods in xy-plane, in the second column, the z component of **n** is shown by use of a monochromatic blue spectrum. In last column, the monochromatic cyan denotes the variation of biaxial order parameter during the time evolution. **(e)** Illustrating the color bars for S, n_z, and P, the used coordination of system and length-scale bar.

difficult to be captured experimentally due to intrinsic size length scale resolutions when using optical methods [73–75].

Figures 3a2–d2 show the z component of uniaxial director, **n**. The figures show that the central director regions evolves slower and lags the radial helix formation that results in tangential interfacial orientation experimentally observed for tropocollagen tactoids [37]. The tangential orientation minimizes the interfacial free energy at $\mathbf{n}.\mathbf{k}=0$ where $\mathbf{k}$ is the interfacial normal vector. This tangential configuration, $\mathbf{n}.\mathbf{k}=\mathbf{0}$, emerges when the coupling coefficient, $\tilde{L}_{\phi-\mathbf{Q}}<0$ [21, 71, 72, 76]. The structure of the

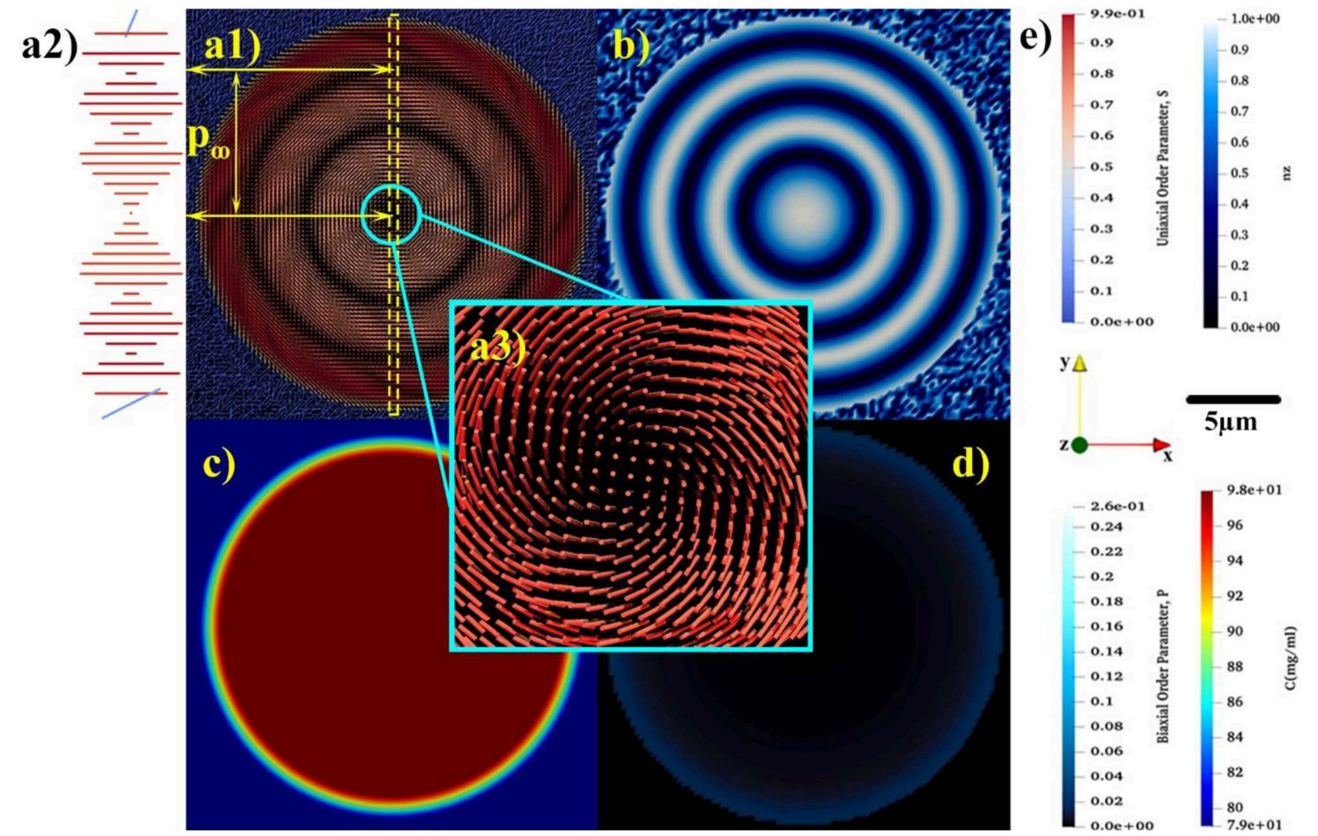

FIGURE 4 | The equilibrium spatial distributions of **(a1)** uniaxial order parameter, S, and the relaxed uniaxial director, **n**, **(b)** z component of uniaxial director, **(c)** concentration, and **(d)** biaxial order parameter, P. **(a2)** showing the magnified rotation of tropocollagen placed in the yellow dash-line box. **(a3)** indicating the non-singular escaped λ^{+1} disclination emerges at the center of tactoid. **(e)** Representing the color bars for S, n_z, P, and C, the used coordination of system and length-scale bar.

2D tactoid is a radial helix, with tangential interface orientation at the edge and non-singular escape orientation at its center.

Of particular interest to this study is incorporation and analysis of biaxial order parameter during the evolution of the cholesteric tactoid. In the third column of **Figures 3a3–d3**, the spatial variation of biaxial order parameter, P, is shown in the early stages of growth. The biaxial order parameter becomes particularly noticeable at the interface and at the defect core. Thus, we found that although the equilibrium biaxiality for rod-like macromolecules is small [27, 51], during the phase ordering it takes a larger value than its equilibrium; the difference between dynamical and equilibrium values for biaxiality may be up to three orders of magnitude.

In the course of time, the **Q**-tensor is relaxed, mass transfer ceases and the structure equilibrates, as shown in **Figure 4**. As depicted in **Figures 4a1,b**, the equilibrium configuration of tropocollagen rods becomes concentric, also known as onion-like. This defectless configuration, which has a non-singular λ^{+1} cholesteric disclination at its center, thoroughly matches with the xy-cross-section of Twisted Bipolar Structure (TBS) given in Sec et al. [77]. Moreover, the experimental POM image reported in Gobeaux et al. [21] confirms TBS for the 3D tropocollagen tactoids. Consequently, the resulting 2D configuration, shown in **Figures 3**, **4**, is consistent with experimental observation. **Figure 4a1** shows that the size of tactoid is also consistent with experimental results given in Gobeaux et al. [21]. As can be seen, the diameter of tactoid contains three pitches that each of which has a length of 10 μm. Therefore, the tactoid shape becomes a nearly 30 μm spherulite. **Figure 4c** represents the equilibrium concentration field. Although a gradient of concentration exists in the interface, the drop remains intact and stable in the isotropic phase. This feature verifies that the growth of cholesteric tactoid is according to the mechanism of uphill diffusion. **Figure 4d** demonstrates that the equilibrium biaxial order parameter P in the interface is nearly 0.04, however its value sharply decreases to 10^{-4} confirmed by previous theoretical studies [27, 51].

Through the entire evolution we find: (1) the interfacial uniaxial order parameter is approximately $S_c = 0.39$ that is quite close to the critical uniaxial order parameter reported in Khadem and Rey [20] and Gobeaux et al. [21]; (2) The biaxial order parameter at the tactoid's interface is at all times greater than in the interior. The

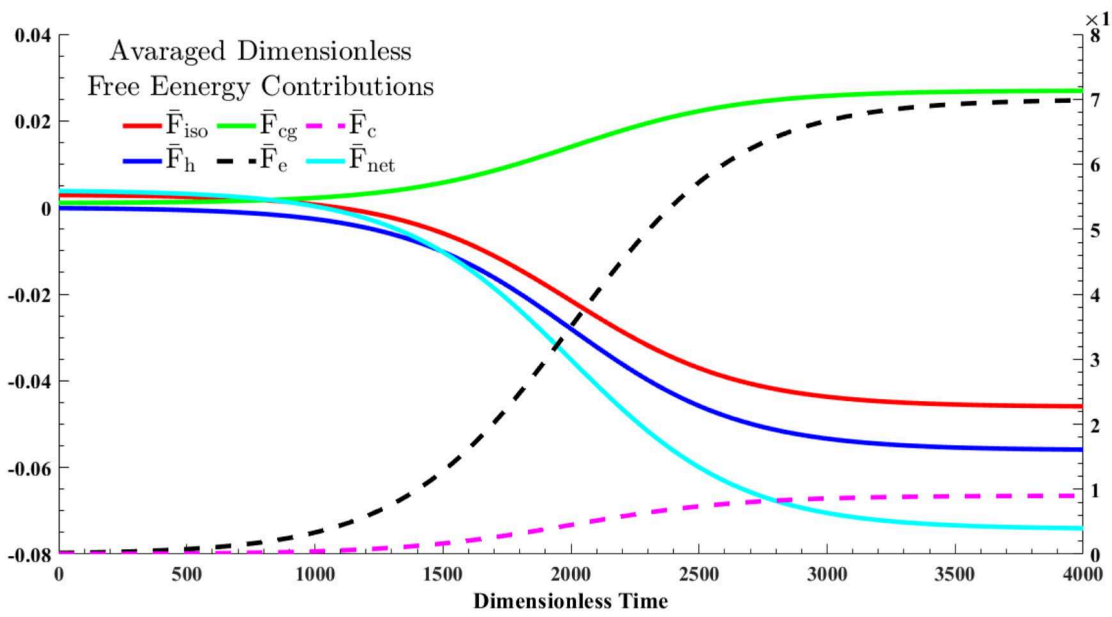

FIGURE 5 | The dynamics of the averaged free energy contributions, given in Equation (28), through a shallow quench from an isotropic state into cholesteric phase—the quench point and evolution path are shown in **Figure 1**. The solid lines correspond to the left y-axis and dash lines should be referred to the right y-axis.

only exception is during initial defect nucleation where biaxiality pronouncedly appears at the core and edge of the 2D drop.

According to the principle of minimum free energy, the kinetic of a spontaneous process follows a path over which the free energy progressively decreases and ends up in a minimum at equilibrium. **Figure 5** illustrates the averaged free energy contributions through the phase ordering process of tropocollagen dispersed in the constant concentration of 2.9 M acetic acid. These spatial averages are defined as

$$\bar{F}_i\left(\tilde{t}\right) = \iint\limits_{CD} \tilde{f}_i \cdot dxdy \Big/ \iint\limits_{CD} dxdy;\ i \in \left\{iso,\ h,\ e,\ cg,\ c\right\} \qquad (28)$$

The formation of the single cholesteric drop is the interplay of five free energy contributions. The entropic and enthalpic contributing factors in isotropic phase separation are described by Flory-Huggins theory, $\tilde{f}_{iso}$. The LdG theory, $\tilde{f}_h$, also accounts for the homogeneous effect of phase transition. The spatial averages of these contributions are shown by $\bar{F}_{iso}$ and $\bar{F}_h$, respectively. The monotonic decrease in $\bar{F}_{iso}$ and $\bar{F}_h$ shows that the phase separation and phase ordering are energetically favorable. In addition, it emphasizes on the lyotropic nature of phase ordering in acidic collagenous dispersions; rods are spontaneously accumulated in cholesteric phase, in turn, removed from the isotropic phase. Hence, $\bar{F}_{net}$ which is the summation of all contributions, is considerably affected by contributions of phase separation and phase ordering.

In spite of these energetically favorable contributions, formation of I/N* interface and cholesteric configuration inside the tactoid require energy costs which are reflected as penalty terms in the net free energy; see Equations (22a–d). The green solid line in **Figure 5**, $\bar{F}_{cg}$, depicts the cost of interface formation (i.e., mass gradient zone shown in the **Figure 4c**). This cost is nearly 40 percent of the energy reduction in either phase separation, $\bar{F}_{iso}$, or phase ordering, $\bar{F}_h$, thus the interfacial formation cost can be compensated. Furthermore, the black dash line, $\bar{F}_e$, and the purple dash line, $\bar{F}_c$, stand for the average costs for the onion-like configuration of rods inside the chiral nematic tactoid and the tangential configuration in interface, respectively. As seen, the formation cost of the interfacial parallel anchoring, $\bar{F}_c$, is ∼2% of the interior cholesteric energy, $\bar{F}_e$.

CONCLUSIONS

Building on our prior work [20], in this study, we have developed and validated a theoretical framework to study the spatio-temporal phase ordering of tropocollagen dispersed in acidic aqueous solutions into 2D drops. By use of the addition theorem for spherical harmonics (Equation 8), we first incorporated the biaxial order parameter P (Equation 3) into the orientational entropy (Equation 6), the second virial approximation Equations 7a–c), and the intermolecular interaction (Equation 10). We then obtained the LdG coefficients (Equations 21a–d), and formulated the net free energy of system, (Equations 21a–d). To capture the kinetic of the emerging 2D tactoids size, shape, and structure, we relied on the proposed net free energy and phase ordering/mass transfer process (Model C) to establish the governing equations, Equations (23a,b), which were numerically solved under the mentioned auxiliary conditions elaborated in subsection Computational Details.

Figures 3a–d reveal two findings. First, the physical origin for the non-singular escaped λ^{+1} disclination. Basically, in the early evolution a τ^{+1} defect emerges at center of nucleus. As time progresses, the central directors go through a defect shedding stage and the τ^{+1} cholesteric defect evolves into the escaped λ^{+1} disclination. Second, at the interface and defect core region, the biaxial order parameter takes appreciably large value in the early evolution. Furthermore, **Figures 4a1–a3,b** demonstrate that the resulting equilibrium state of collagen tactoid is an $\sim$30 μm spherulite in which the rod-shaped macromolecules are aligned in concentric configuration, consistent with experimental observations [21]. Taken together, these results contribute to the development of optimized processing protocols for collagen-based materials and their material property characterization.

DATA AVAILABILITY

All datasets generated for this study are included in the manuscript and the **Supplementary Files.**

AUTHOR CONTRIBUTIONS

SK developed the theoretical framework, carried out the simulations, and analyzed the results. AR supervised the study, analyzed and interpreted the results. All authors discussed the results, contributed to writing, and agree about the content.

ACKNOWLEDGMENTS

SK acknowledges financial support from the McGill Engineering Doctoral Awards (MEDA) program. This work is supported by a grant from Natural Sciences and Engineering Research Council of Canada (NSERC). AR is thankful to McGill University for financial support through the James McGill Professorship appointment.

SUPPLEMENTARY MATERIAL

The Supplementary Material for this article can be found online at: https://www.frontiersin.org/articles/10.3389/fphy.2019.00088/full#supplementary-material

REFERENCES

1. Voet D, Voet JG. *Biochemistry*. Hoboken, NJ: John Wiley & Sons (2011).
2. Ashammakhi N, Hasan A, Kaarela O, Byambaa B, Sheikhi A, Gaharwar AK, et al. Advancing frontiers in bone bioprinting. *Adv Healthc Mater*. (2019) **8**:1801048. doi: 10.1002/adhm.201801048
3. Giraud Guille MM, Mosser G, Helary C, Eglin D. Bone matrix like assemblies of collagen: from liquid crystals to gels and biomimetic materials. *Micron*. (2005) **36**:602–8. doi: 10.1016/j.micron.2005.07.005
4. Kurfurst A, Henits P, Morin C, Abdalrahman T, Hellmich C. Bone ultrastructure as composite of aligned mineralized collagen fibrils embedded into a porous polycrystalline matrix: confirmation by computational electrodynamics. *Front Phys*. (2018) **6**:18. doi: 10.3389/fphy.2018.00125
5. Schwarcz HP, Abueidda D, Jasiuk I. The ultrastructure of bone and its relevance to mechanical properties. *Front Phys*. (2017) **5**:13. doi: 10.3389/fphy.2017.00039
6. Levis HJ, Kureshi AK, Massie I, Morgan L, Vernon AJ, Daniels JT. Tissue engineering the cornea: the evolution of RAFT. *J Func Biomater*. (2015) **6**:50–65. doi: 10.3390/jfb6010050
7. Torbet J, Malbouyres M, Builles N, Justin V, Roulet M, Damour O, et al. Orthogonal scaffold of magnetically aligned collagen lamellae for corneal stroma reconstruction. *Biomaterials*. (2007) **28**:4268–76. doi: 10.1016/j.biomaterials.2007.05.024
8. Rastian Z, Putz S, Wang YJ, Kumar S, Fleissner F, Weidner T, et al. Type I collagen from Jellyfish *Catostylus mosaicus* for biomaterial applications. *ACS Biomater Sci Eng*. (2018) **4**:2115–25. doi: 10.1021/acsbiomaterials.7b00979
9. Boraschi-Diaz I, Wang J, Mort JS, Komarova SV. Collagen type I as a ligand for receptor-mediated signaling. *Front Phys*. (2017) **5**:11. doi: 10.3389/fphy.2017.00012
10. Perez AG, Nieminen HJ, Finnila M, Salmi A, Pritzker KPH, Lampsijarvi E, et al. Delivery of agents into articular cartilage with electric spark-induced sound waves. *Front Phys*. (2018) **6**:7. doi: 10.3389/fphy.2018.00116
11. Poulon F, Chalumeau A, Jamme F, Pallud J, Varlet P, Mehidine H, et al. Multimodal analysis of central nervous system tumor tissue endogenous fluorescence with multiscale excitation. *Front Phys*. (2018) **6**:10. doi: 10.3389/fphy.2018.00109
12. Neville AC. *Biology of Fibrous Composites: Development Beyond the Cell Membrane*. New York, NY: Cambridge University Press (1993).
13. Mitov M. Cholesteric liquid crystals in living matter. *Soft Matter*. (2017) **13**:4176–209. doi: 10.1039/C7SM00384F
14. Rey AD. Liquid crystal models of biological materials and processes. *Soft Matter*. (2010) **6**:3402–29. doi: 10.1039/b921576j
15. Rey AD, Herrera-Valencia EE. Liquid crystal models of biological materials and silk spinning. *Biopolym Banner*. (2012) **97**:374–96. doi: 10.1002/bip.21723
16. Gutierrez OFA, Rey AD. Theory and simulation of cholesteric film formation flows of dilute collagen solutions. *Langmuir*. (2016) **32**:11799–812. doi: 10.1021/acs.langmuir.6b03443
17. Aguilar Gutierrez OF, Rey AD. Biological plywood film formation from para-nematic liquid crystalline organization. *Soft Matter*. (2017) **13**:8076–88. doi: 10.1039/C7SM01865G
18. De Sa Peixoto P, Deniset-Besseau A, Schmutz M, Anglo A, Illoul C, Schanne-Klein M-C, et al. Achievement of cornea-like organizations in dense collagen I solutions: clues to the physico-chemistry of cornea morphogenesis. *Soft Matter*. (2013) **9**:11241–8. doi: 10.1039/c3sm52097h
19. Dehsorkhi A, Castelletto V, Hamley IW, Adamcik J, Mezzenga R. The effect of pH on the self-assembly of a collagen derived peptide amphiphile. *Soft Matter*. (2013) **9**:6033–6. doi: 10.1039/c3sm51029h
20. Khadem SA, Rey AD. Thermodynamic modelling of acidic collagenous solutions: from free energy contributions to phase diagrams. *Soft Matter*. (2019) **15**:1833–46. doi: 10.1039/C8SM02140F
21. Gobeaux F, Belamie E, Mosser G, Davidson P, Panine P, Giraud-Guille MM. Cooperative ordering of collagen triple helices in the dense state. *Langmuir*. (2007) **23**:6411–7. doi: 10.1021/la070093z
22. Lovelady HH, Shashidhara S, Matthews WG. Solvent specific persistence length of molecular type I collagen. *Biopolymers*. (2014) **101**:329–35. doi: 10.1002/bip.22365
23. Echalier C, Jebors S, Laconde G, Brunel L, Verdie P, Causse L, et al. Sol-gel synthesis of collagen-inspired peptide hydrogel. *Mater Today*. (2017) **20**:59–66. doi: 10.1016/j.mattod.2017.02.001
24. Bernardino NR, Pereira MCF, Silvestre NM, da Gama MMT. Structure of the cholesteric-isotropic interface. *Soft Matter*. (2014) **10**:9399–402. doi: 10.1039/C4SM01857E
25. Zhou Y, Bukusoglu E, Martinez-Gonzalez JA, Rahimi M, Roberts TF, Zhang R, et al. Structural transitions in cholesteric liquid crystal droplets. *ACS Nano*. (2016) **10**:6484–90. doi: 10.1021/acsnano.6b01088

26. Almeida AP, Canejo JP, Fernandes SN, Echeverria C, Almeida PL, Godinho MH. Cellulose-based biomimetics and their applications. *Adv Mater Banner.* (2018) **30**:1703655. doi: 10.1002/adma.201703655
27. Wulf A. Biaxial order in cholesteric liquid crystals: phenomenological argument. *J Chem Phys*. (1973) **59**:6596–8. doi: 10.1063/1.1680039
28. Wright DC, Mermin ND. Crystalline liquids: the blue phases. *Rev Mod Phys Rev Modern Phys*. (1989) **61**:385–432. doi: 10.1103/RevModPhys.61.385
29. Kamil SM, Bhattacharjee AK, Adhikari R, Menon GI. The isotropic-nematic interface with an oblique anchoring condition. *J Chem Phys*. (2009) **131**:9. doi: 10.1063/1.3253702
30. Wincure B, Rey AD. Interfacial nematodynamics of heterogeneous curved isotropic-nematic moving fronts. *J Chem Phys*. (2006) **124**:13. doi: 10.1063/1.2206768
31. Wincure B, Rey AD. Growth and structure of nematic spherulites under shallow thermal quenches. *Continuum Mech Thermodyn.* (2007) **19**:37–58. doi: 10.1007/s00161-007-0043-z
32. Wincure B, Rey AD. Computational modelling of nematic phase ordering by film and droplet growth over heterogeneous substrates. *Liquid Cryst.* (2007) **34**:1397–413. doi: 10.1080/02678290701614657
33. Wincure BM, Rey AD. Nanoscale analysis of defect shedding from liquid crystal interfaces. Nano Lett. (2007) **7**:1474–9. doi: 10.1021/nl0701408
34. PopaNita V, Sluckin TJ, Wheeler AA. Statics and kinetics at the nematic-isotropic interface: effects of biaxiality. *J Phys II*. (1997) **7**:1225–43. doi: 10.1051/jp2:1997183
35. Mirzaeifard S, Servio P, Rey AD. Molecular dynamics characterization of the water-methane, ethane, and propane gas mixture interfaces. *Chem Eng Sci*. (2019). doi: 10.1016/j.ces.2019.01.051. [Epub ahead of print].
36. Mirzaeifard S, Servio P, Rey AD, Molecular dynamics characterization of temperature and pressure effects on the water-methane interface. *Colloid Interface Sci Commun*. (2018) **24**:75–81. doi: 10.1016/j.colcom.2018.04.004
37. Rey AD. Pitch contributions to the cholesteric– isotropic interfacial tension. *Macromolecules*. (2000) **33**:9468–70. doi: 10.1021/ma0001685
38. Wang XJ, Zhou QF. *Liquid Crystalline Polymers*. Singapore; London: World Scientific Publishing Company: (2004).
39. Karttunen M, Vattulainen I, Lukkarinen A. *Novel Methods in Soft Matter Simulations*. Berlin: Heidelberg: Springer (2004).
40. Halperin BI. Theory of dynamic critical phenomena. *Phys Today*. (2019) **72**:42–3. doi: 10.1063/PT.3.4137
41. Nyström G, Arcari M, Mezzenga R. Confinement-induced liquid crystalline transitions in amyloid fibril cholesteric tactoids. *Nat Nanotechnol*. (2018) **13**:330–6. doi: 10.1038/s41565-018-0071-9
42. Nos RL, Roma AM, Garcia-Cervera CJ, Ceniceros HD. Three-dimensional coarsening dynamics of a conserved, nematic liquid crystal-isotropic fluid mixture. *J Non-Newton Fluid Mech*. (2017) **248**:62–73. doi: 10.1016/j.jnnfm.2017.08.009
43. Abukhdeir NM, Soulé ER, Rey AD. Non-isothermal model for nematic spherulite growth. *Langmuir*. (2008) **24**:13605–13. doi: 10.1021/la8022216
44. Abukhdeir NM, Rey AD. Shape-dynamic growth, structure, and elasticity of homogeneously oriented spherulites in an isotropic/smectic-a mesophase transition. *Liquid Cryst*. (2009) **36**:1125–37. doi: 10.1080/02678290902878754
45. Soule ER, Abukhdeir NM, Rey AD. Thermodynamics, transition dynamics, and texturing in polymer-dispersed liquid crystals with mesogens exhibiting a direct isotropic/smectic-a transition. *Macromolecules*. (2009) **42**:9486–97. doi: 10.1021/ma901569y
46. Gennes PGd, Prost J. *The Physics of Liquid Crystals*. Oxford: Clarendon Press (1995).
47. Doi M. *Soft Matter Physics*. Oxford: OUP (2013).
48. Matsuyama A, Kato T. Theory of binary mixtures of a flexible polymer and a liquid crystal. *J Chem Phys*. (1996) **105**:1654–60. doi: 10.1063/1.472024
49. Odijk T. Theory of lyotropic polymer liquid crystals. *Macromolecules*. (1986) **19**:2313–29. doi: 10.1021/ma00163a001
50. Drwenski T, Dussi S, Hermes M, Dijkstra M, Roij RV. Phase diagrams of charged colloidal rods: can a uniaxial charge distribution break chiral symmetry? *J Chem Phys*. (2016) **144**:094901. doi: 10.1063/1.4942772
51. Matsuyama A. Biaxiality of cholesteric phases in rod-like polymer solutions. *Liquid Cryst*. (2015) **42**:423–9. doi: 10.1080/02678292.2015.1006148
52. Matsuyama A. Biaxial nematic phases in rod/liquid crystal mixtures. *Liquid Cryst.* (2011) 38:729–36. doi: 10.1080/02678292.2011.570795
53. Matsuyama A, Crystals L. Biaxial nematic phase in mixtures of a liquid crystal and a rodlike polymer. *Liquid Cryst.* (2011) **540**:42–9. doi: 10.1080/15421406.2011.568325
54. Stroobants A, Lekkerkerker HNW, Odijk T. Effect of electrostatic interaction on the liquid crystal phase transition in solutions of rodlike polyelectrolytes. *Macromolecules*. (1986) **19**:2232–8. doi: 10.1021/ma00162a020
55. Mirzaeifard S, Abel SM. Confined semiflexible polymers suppress fluctuations of soft membrane tubes. *Soft Matter*. (2016) 12:1783–90. doi: 10.1039/C5SM02556G
56. Matus Rivas OM, Rey AD. Effects of sodium and magnesium cations on the aggregation of chromonic solutions using molecular dynamics. *J Phys Chem B*. (2019) **123**:1718–32. doi: 10.1021/acs.jpcb.8b12130
57. Rivas OMM, Rey AD. Molecular dynamics on the self-assembly of mesogenic graphene precursors. *Carbon*. (2016) **110**:189–99. doi: 10.1016/j.carbon.2016.09.014
58. Roohnikan M, Toader V, Rey A, Reven L. Hydrogen-bonded liquid crystal nanocomposites. *Langmuir*. (2016) 32:8442–50. doi: 10.1021/acs.langmuir.6b02256
59. Bagnani M, Nystrom G, De Michele C, Mezzenga R. Amyloid fibrils length controls shape and structure of nematic and cholesteric tactoids. *ACS Nano*. (2019) **13**:591–600. doi: 10.1021/acsnano.8b07557
60. Soule ER, Rey AD. A good and computationally efficient polynomial approximation to the Maier-Saupe nematic free energy. *Liquid Cryst*. (2011) **38**:201–5. doi: 10.1080/02678292.2010.539303
61. De Luca G, Rey AD. Chiral front propagation in liquid-crystalline materials: formation of the planar monodomain twisted plywood architecture of biological fibrous composites. *Phys Rev E Stat Nonlin Soft Matter Phys*. (2004) **69(Pt 1)**:011706. doi: 10.1103/PhysRevE.69.011706
62. Gurevich S, Soule E, Rey A, Reven L, Provatas N. Self-assembly via branching morphologies in nematic liquid-crystal nanocomposites. *Phys Rev E*. (2014) **90**:020501. doi: 10.1103/PhysRevE.90.020501
63. Das SK, Rey AD. Texture formation under phase ordering and phase separation in polymer-liquid crystal mixtures. *J Chem Phys*. (2004) **121**:9733–43. doi: 10.1063/1.1804494
64. De Luca G, Rey AD. Monodomain and polydomain helicoids in chiral liquid-crystalline phases and their biological analogues. *Eur Phys J E*. (2003) **12**:291–302. doi: 10.1140/epje/i2002-10164-3
65. De Luca G, Rey AD. Theory and simulation of texture transformations in chiral systems: applications to biological fibrous composites. In: Mather PT, Broer DJ, Bunning TJ, Walba DM, Zentel R, editors. *Advances in Liquid Crystalline Materials and Technologies. Materials Research Society Symposium Proceedings*. Phoenix, AZ. p. 141-6.
66. Khabibullaev PK, Gevorkyan EV, Lagunov AS. *Rheology of Liquid Crystals*. New York, NY: Allerton Press (1994).
67. Rey AD. Theory and simulation of gas diffusion in cholesteric liquid crystal films. *Mol Cryst Liquid Cryst Sci Technol Section A*. (1997) **293**:87–109. doi: 10.1080/10587259708042767
68. Fletcher NH. Size effect in heterogeneous nucleation. *J Chem Phys*. (1958) **29**:572–6. doi: 10.1063/1.1744540
69. Sear RP. Nucleation: theory and applications to protein solutions and colloidal suspensions. *J Phys-Condens Matter*. (2007) **19**:28. doi: 10.1088/0953-8984/19/3/033101
70. Rey AD, Servio P, Herrera-Valencia EE. Bioinspired model of mechanical energy harvesting based on flexoelectric membranes. *Phys Rev E*. (2013) **87**:12. doi: 10.1103/PhysRevE.87.022505
71. Das SK, Rey AD. Computational thermodynamics of multiphase polymer-liquid crystal materials. *Comput Mater Sci*. (2006) **38**:325–39. doi: 10.1016/j.commatsci.2005.10.009
72. Das SK, Rey AD. Magnetic field-induced shape transitions in multiphase polymer-liquid crystal blends. *Macromol Theory Simul*. (2006) **15**:469–86. doi: 10.1002/mats.200600024

73. Dierking I. *Textures of Liquid Crystals*. Weinheim: Wiley-VCH (2003).
74. Yang DK. *Fundamentals of Liquid Crystal Devices*. Wiley (2014).
75. Ondriscrawford R, Boyko EP, Wagner BG, Erdmann JH, Zumer S, Doane JW. Microscope textures of nematic droplets in polymer dispersed liquid-crystals. *J Appl Phys*. (1991) **69**:6380–6. doi: 10.1063/1.348840
76. Das SK, Rey AD. Colloidal crystal formation via polymer-liquid-crystal demixing. *Europhys Lett*. (2005) **70**:621–7. doi: 10.1209/epl/i2005-10034-2
77. Sec D, Porenta T, Ravnik M, Zumer S. Geometrical frustration of chiral ordering in cholesteric droplets. *Soft Matter*. (2012) **8**:11982–8. doi: 10.1039/c2sm27048j

Conflict of Interest Statement: The authors declare that the research was conducted in the absence of any commercial or financial relationships that could be construed as a potential conflict of interest.

NOMENCLATURE

Symbol	Units	Description
a^3	m^3	Volume of each lattice unit
$B_2(\psi(\mathbf{u}))$	[–]	Second virial approximation to represent the excluded-volume effect
c_A	m^{-3}	Number density
C	mg/ml	Concentration of tropocollagen
D_{eff}	m	Effective diameter
D	m	Bare diameter
$d\Omega$	Radian	Solid angle
Ei	[–]	Exponential integral
$\tilde{f}$	[–]	Dimensionless free energy density
F^S	j	Free energy of solution
$\bar{F}_i$	[–]	Average of total dimensionless free energy contribution i
h	[–]	Magnitude of the twisting effect
ε	Molar	Ionic strength
k_B	$m^2.kg.s^{-2}.K^{-1}$	Boltzmann constant, $1.38064852 \times 10^{-23}$
$\mathbf{l}$	[–]	$\mathbf{l} = \mathbf{n} \times \mathbf{m}$
L	m	Contour length
L_1 and L_2	j/m	Elastic constants
$\tilde{L}_{\phi-\mathbf{Q}}$	[–]	Dimensionless coupling parameter
$\tilde{L}_\phi$	[–]	Dimensionless cost of interfacial formation
m	[–]	Biaxial director
$M(\psi(\mathbf{u}))$	[–]	The orientation-dependent intermolecular interactions
$\tilde{M}_\phi$	[–]	Dimensionless mass-transfer mobility
m_i	Molar	Molar concentration of ith mobile ion
N_{avo}	mol^{-1}	Avogadro's number, $6.022140857 \times 10^{23}$
N_A and N_I	[–]	Number of chiral mesogens and isotropic component
N_T	[–]	Total number of lattice site
n	[–]	Number of segments in the backbone of mesogen
$\mathbf{n}$	[–]	Uniaxial director
P	[–]	Biaxial director
p_∞	m	Pitch
$P_2(\cos(\gamma))$	[–]	Second Legendre polynomial of angle between the macromolecules
$\mathbf{Q}$	[–]	Quadrupole moment tensor, well-known as **Q**-tensor
S	[–]	Macroscopic uniaxial order parameter
U	$j.m^{-3}$	Potential of orientation-dependent intermolecular interaction
U_i	j	The net one-body mean field potential of ith rod
U'^{MS}	$j.m^{-3}$	Positive constant independent of temperature related to Maier-Saupe parameter
U^{MS}	$j.m^{-3}$	Positive constant independent of temperature, Maier-Saupe parameter
U_i^{elc}	j	One-body mean field potential of ith rod for electrostatic interactions (i.e., repulsion and twisting) on the other existing rods in the system
U'^{elc}	$j.m^{-3}$	Strength of electrostatic potential (i.e., repulsion and twisting)
U^{elc}	$j.m^{-3}$	Strength of electrostatic interaction among the rods (i.e., repulsion and twisting)
$\mathbf{u}$ and u'	[–]	The orientations of two rod-like macromolecules
V	m^3	Volume of system
W	[–]	Net cholesteric potential
x	m	x-component of space
Z_i	[–]	Charge number of ith mobile ion
α	[–]	Double-layer thickness parameter
α_W	[–]	Dimensionless constant defined as $\alpha_W = 5/\phi^*$ where ϕ^* is the effective volume fraction of tropocollagen
α_C	ml/mg	Unit conversion used for converting the effective volume fraction to concentration in unit of mg/ml
β	j^{-1}	Thermal energy
γ	Radian	Angle between rods
γ_E	[–]	Euler constant, 0.5772
δ	[–]	Kronecker delta
η	[–]	Constants determined by normalization of distribution function
θ	Radian	Polar angle
κ^{-1}	m	Debye screening length
λ_B	m	Bjerrum length
Λ	Charge number per meter	Linear charge density
μ^O	j	Standard particle chemical potential
ξ	m	Coherence length or correlation length
$\sigma(\psi(\mathbf{u}))$	[–]	Effect of orientational entropy
$\overline{\upsilon}_{AA}$, $\overline{\upsilon}_{IA}$, and $\overline{\upsilon}_{II}$	m^3	Average excluded-volume between mesogen-mesogen, mesogen-isotropic component and isotropic component—isotropic component
υ_A and υ_I	m^3	Molecular volumes of mesogen and isotropic component
φ	radian	Azimuthal angle
ϕ	[–]	Effective volume fraction of mesogen
χ	[–]	Isotropic Flory-Huggins parameter
$\psi(\mathbf{u})$	[–]	Single-rod orientational distribution function

ORIGINAL RESEARCH
published: 31 October 2019
doi: 10.3389/fphy.2019.00165

Dynamics of Ring Disclinations Driven by Active Nematic Shells

*Jérôme Hardoüin [1,2], Pau Guillamat [1,2,3], Francesc Sagués [1,2] and Jordi Ignés-Mullol [1,2]**

[1] Department of Materials Science and Physical Chemistry, University of Barcelona, Barcelona, Spain, [2] Institute of Nanoscience and Nanotechnology, University de Barcelona, Barcelona, Spain, [3] Department of Biochemistry, University of Geneva, Geneva, Switzerland

When dispersed in thermotropic nematic liquid crystal oils, surfactant-ladden aqueous droplets often lead to the formation of a equatorial ring disclination in the nearby nematic matrix as a result of a balance between elasticity and interfacial energy. In this experimental work, the aqueous phase contains an extract of cytoskeletal proteins that self-assemble into an active quasi-two-dimensional shell featuring self-sustained periodic flows. The ensuing hydrodynamic coupling drives the surrounding liquid crystal and triggers oscillations in the disclinations. We describe the dynamic modes of the disclinations under different driving conditions, and explore their pathway to collapse under flow conditions.

Keywords: liquid crystals, nematic emulsions, active nematics, disclinations, nematic shells

Edited by:
Uroš Tkalec,
University of Ljubljana, Slovenia

Reviewed by:
Rui Zhang,
University of Chicago, United States
Guillaume Duclos,
Brandeis University, United States
Chenhui Peng,
University of Memphis, United States

****Correspondence:***
Jordi Ignés-Mullol
jignes@ub.edu

Specialty section:
This article was submitted to
Soft Matter Physics,
a section of the journal
Frontiers in Physics

Received: *17 August 2019*
Accepted: *11 October 2019*
Published: *31 October 2019*

Citation:
Hardoüin J, Guillamat P, Sagués F and Ignés-Mullol J (2019) Dynamics of Ring Disclinations Driven by Active Nematic Shells. Front. Phys. 7:165.
doi: 10.3389/fphy.2019.00165

1. INTRODUCTION

Nematic liquid crystals (NLCs) are liquids whose molecules organize with long-range orientational order, which is locally characterized by a director field, $\hat{\boldsymbol{n}}$ [1]. The latter is typically controlled by means of the boundary conditions on the confinement walls or through the action of electric or magnetic fields. The equilibrium distribution of $\hat{\boldsymbol{n}}$ is established through the minimization of bulk and interfacial energies compatible with topological constraints dictated by confinement, which may lead to frustrated configurations and the appearance of defects [2]. Although technological applications of these materials are based on their use in defect-free systems, significant current research efforts in Condensed Matter Physics are centered in the preparation and control of tunable defect assemblies, with potential use in the development of metamaterials [3].

A particular case of frustrated geometries in NLCs is obtained by preparing nematic colloidal suspensions [4, 5]. These are systems in which the ordered mesophase, which is typically oriented in a homogeneous fashion by means of the anchoring conditions on bounding plates (far field), is disrupted by the presence of sub-millimeter solid [6–13] or liquid [14–16] inclusions. Realizations include from spherical to more complex geometries such as fractal-like shapes, from sparse to dense colloidal ensembles, from spontaneous to tailored self-assembly [9, 17–20]. Except from the preparation of assemblies of driven colloidal particles [21] or defects [22], or the study of defects formed under flow conditions [23], most research on nematic colloids has focused on stable, equilibrium structures.

Recently, we brought a nematic emulsion out of equilibrium by dispersing aqueous droplets of an active gel in a nematic liquid crystal [24]. The active gel, which is prepared from an *in-vitro* reconstitution of cytoskeletal proteins develops, under suitable conditions, an active layer with nematic order at the water/oil interface, denoted active nematic (AN) [25, 26]. At the inner side of the spherical droplets, the resulting AN shell exhibits self-sustained flows that are transmitted hydrodynamically into the surrounding nematic matrix. As a result, the ring disclination (Saturn ring, SR) that, in our case, surrounds the dispersed droplets [27–29] is perturbed from its (equilibrium) equatorial position, into different oscillations modes. With the support of numerical simulations, our earlier study revealed a feedback mechanism between the orientation of the SR, determined by the nematic far field, and the spatial arrangement of the AN shell, which led to sustained periodic oscillations of the SR. However, such regimes were not the norm in the experiments, and often driven SR became unstable and collapsed into a dipolar configuration.

In this article, we provide a thorough revision of the different dynamic modes of SR driven by the underlying AN shell, the possible dynamic states, which involve both synchronous and asynchronous oscillations, and the different pathways that lead to the collapse of the SR into a dipolar point-like defect configuration.

The article is structured as follows. After a succinct description of the used materials and employed experimental methods, we describe the main features of the emulsified droplets, including the structure of the underlying AN shell. Then, we describe the observed dynamic modes of the SR, both stable and unstable, and their dependence on control parameters. Finally, we focus on the long term behavior of the dynamic SR.

2. MATERIALS AND METHODS

2.1. Active Material

The active system we used consisted of an active gel formed by an aqueous suspension of tubulin microtubules, dimeric kinesin molecular motors, and the non-adsorbing depleting agent polyethylene glycol (PEG), which concentrates the microtubules into bundles, hundreds of micrometers long [25]. Precise details of the experimental procedures leading to the preparation of all materials can be found elsewhere [24]. In brief, microtubules were polymerized from tubulin purified from bovine brain (a gift from Brandeis University Biological Materials Facility) in the presence of 0.6 mM of Guanosine-5-[(α, β)-methyleno]triphosphate (GMPCPP), which promotes the formation of short microtubules, $1-2\ \mu$m in length, required for the formation of the active material. About 3% of the tubulin is labeled with the fluorophore Alexa-647. Heavy chain kinesin-1 (K401-BCCP-6His) from *Drosophila Melanogaster* was in-house purified from *Escherichia coli* that contained the plasmid WC2 from the Gelles Laboratory (Brandeis University, MA, USA). The kinesin was biotinilated and incubated with streptatividin to obtain dimeric clusters, which would act as cross-linkers when mixed with the microtubule suspension. The active mixture was completed with 20 kDa PEG that acted as a depleting agent, Adenosine Triphosphate (ATP) that drove the activity of the gel, anti-bleaching agents, and an enzymatic ATP-regenerating system to maintain a constant activity in the mixture for hours. In order to emulsify the active aqueous suspension in the liquid crystal oil, suitable surfactants were added to the active mixture to ensure a biocompatible water/oil interface and to determine the anchoring conditions for the liquid crystal molecules in contact with the droplets. To promote the desired homeotropic (perpendicular) anchoring, PEGylated phospholipids were used at a concentration 0.2 %w/v.

2.2. Liquid Crystal-Based Emulsions

As dispersing oil phase, we used 4-Cyano-4'-pentylbiphenyl (5CB, Synthon chemicals), which features a nematic phase at room temperature. In order to enhance the homeotropic anchoring on the aqueous droplets surface, about 0.4 w/w% of stearic acid was dissolved in the mesogen. The emulsion was prepared by combining the active gel and the oil in a 1 mL centrifuge tube at a ratio 1:30, and mixed by the action of a vortex stirrer at room temperature.

2.3. Sample Preparation and Characterization

Liquid crystal cells were assembled by gluing two parallel glass plates together with a spacing of 140 μm set by double-sided adhesive tape. The inner side of the plates was treated to promote planar anchoring of the NLC by rubbing a previously spin-coated and baked layer of poly-vinyl alcohol. After the cell is filled by capillarity with the active emulsion, the openings are sealed using UV-curing adhesive. Microscopy observation was performed using a Nikon E400Pol multimode microscope. Fluorescence was used to visualize the AN layer while brightfield was employed to visualized the SR disclinations. The latter is typically preferred to polarized microscopy, which we have occasionally employed, since it results in a more homogeneous appearance of the disclination along all its length. Time-lapse acquisition is performed with an Andor Zyla 4.2 Plus camera controlled with the open-source software ImageJ Micro-Manager [30], which is also employed for further image processing and analysis.

3. RESULTS AND DISCUSSION

Dispersed in the mesogenic oil, spherical aqueous droplets promote homeotropic anchoring of the NLC director on their surface due to the employed surfactants (see section 2). This results in a topological mismatch with the homogeneous planar far-field imposed by the boundary conditions on the cell plates. As a result, a ring disclination forms around the droplet's equator, perpendicularly to the NLC far-field direction (**Figure 1A**). As discussed below, this configuration is metastable [28], and may relax to a less energetic dipolar configuration where the SR collapses as a point-like defect near the North or the South pole of the droplet. Inside the aqueous droplets, the filament bundles formed by fluorescent microtubules crosslinked with kinesin clusters are pushed toward the water/oil interface by the depleting action of PEG. This process is usually studied on a flat interface, leading to the formation of an AN layer a few microns thick, where the filaments are intrinsically prone to buckling instabilities due to internal extensile active stresses. This results in the unbinding of complementary pairs of semi-integer defects, with the $+1/2$ defects creating flow while the negative counterparts being simply advected [26]. In **Figure 1B**, some defects present in the observation window of a flat AN, in an independent experiment, are marked. In particular, the tip of

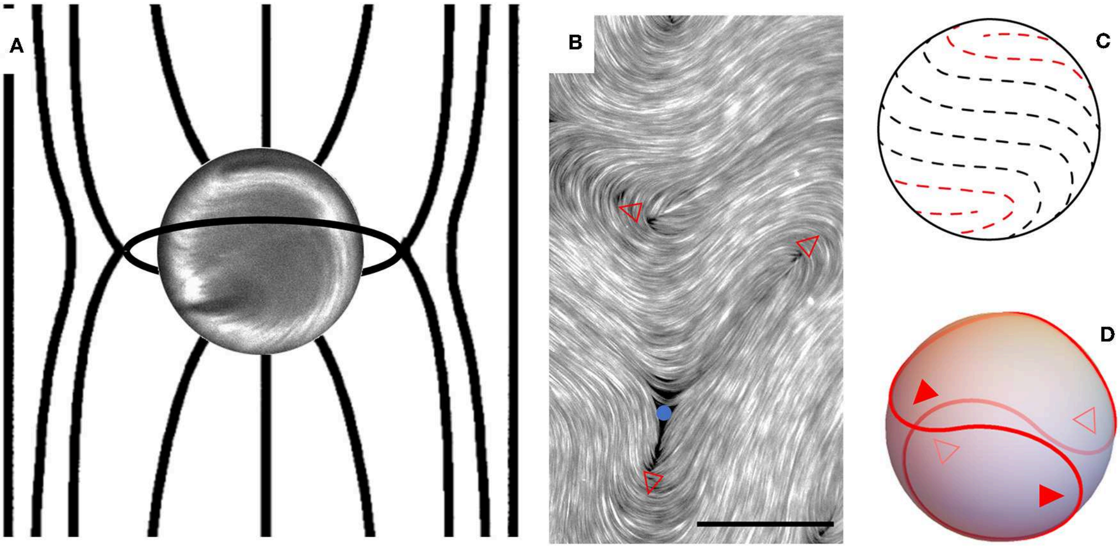

FIGURE 1 | (A) Sketch of the nematic director field lines around a dispersed droplet of aqueous based active material that imposes homeotropic anchoring conditions. The NLC has a homogeneous far field oriented in the vertical direction in this sketch. The confining plates are parallel to the plane of the sketch. The droplet, which is visualized with fluorescence microscopy, has a diameter of 80 μm. The homeotropic anchoring conditions on the droplet surface lead to the formation of a line disclination that wraps around the equator. **(B)** Structure of an Active Nematic layer forming at a flat water/oil interface, with the core of some positive (red empty triangles) and negative (blue full circles) semi-integer defects being marked. The ruler is 20 μm long. **(C)** Approximate director field lines of the Active Nematic shell observed in the droplet of **(A)**. In red, the core of the two visible +1/2 defects is sketched. **(D)** Theoretical rendering of the four +1/2 defects that organize the flows in active shells present in droplets of this size. Solid triangles correspond to visible defects while empty triangles correspond to hidden defects.

+1/2 defects is indicated with a red triangle that points in the direction of the local defect trajectory.

The average distance between defects in the AN is characterized by the so-called active length scale [31, 32], which balances the active stresses and the elastic modulus of the filaments [33, 34]. When topology demands the coexistence of a given number of defects, this length scale determines the smallest confinement compatible with the AN. This is important, for instance, in the case of the *soft confinement* of AN in contact with anisotropic interfaces patterned with disks [35], or in spherical shells [24, 36], which is the relevant case for our purpose.

Wrapping of a two-dimensional nematic on a closed spherical surface requires a net topological charge +2 of the defects present in the director field [37, 38]. In the case of an AN shell, where only semi-integer defects are possible, the simplest conformation compatible with this topological constraint involves four +1/2 defects that will be placed at the vertices of an imaginary rotating tetrahedron in the steady state [36, 39] (**Figures 1C,D**). Because of the above-mentioned intrinsic active length scale, droplets that are too small cannot accommodate the four defects required for a stable active nematic shell, and droplets that are too large, enable the unbinding of more than four defects, resulting in turbulent-like flow regimes [26, 40]. For the material parameters used in our active preparation, we have found optimal to restrict our studies to droplets with diameters in the range 60–120 μm.

On the other hand, the distance between the disclination and the droplet surface will be instrumental to the coupling between the SR and the underlying active flow, with stronger coupling presumably occurring for SRs that are closer to the droplet. For strong anchoring conditions, this distance is proportional to the droplet size [27, 28], and is determined by the balance between NLC elasticity, represented by an elastic constant K, the radius of curvature of the director field distortions around the droplet, R, and the anchoring strength on the droplet surface, W, through the dimensionless ratio WR/K [1, 2]. For weak anchoring, the homeotropic surface alignment condition will not be satisfied, which results in distortions with small curvature that lead to the disclination stabilizing closer to the surface. In our experiments, W is determined by the nature and concentration of the employed surfactants. In earlier experiments [24], we tested the use of surfactants that led to conical, rather than homeotropic, anchoring, resulting in SR that were closer to the droplet surface and did not exhibit the high energy oscillation modes we report here. In the current study we have restricted to the use phospholipid-based surfactants, which we have found to offer a richer collection of dynamic SR regimes.

Interestingly, we have found a disparity of behaviors in droplets of similar sizes within a single preparation. A possible source for this dispersion is an heterogeneous droplet composition during the emulsification process, which we have assessed by preparing ensembles of droplets of nearly identical size by means of a microfluidic droplet generation device (**Figure 2A**). We observe disparities in the fluorescence intensity from different droplets, which points to the heterogeneous composition of the encapsulated active aqueous phase. In the example shown in **Figure 2A**, the continuous phase is a

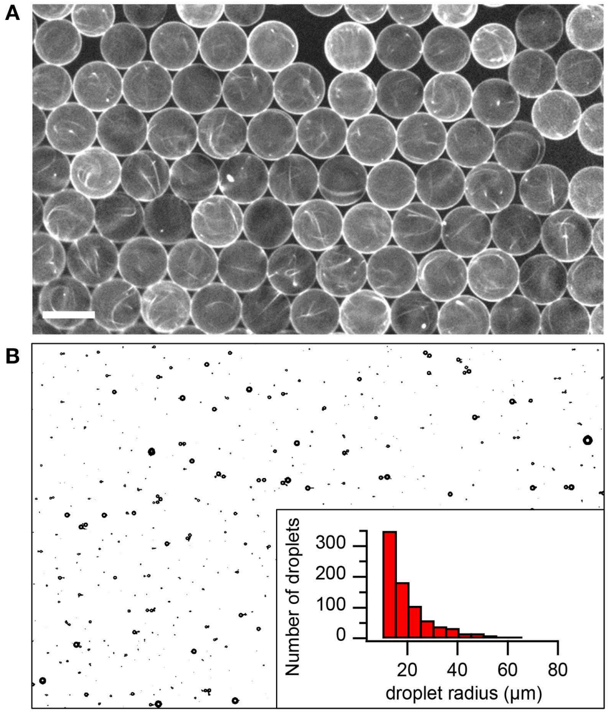

FIGURE 2 | Sources of heterogeneity of the active emulsions. **(A)** Heterogeneous composition of monodisperse active droplets prepared using microfluidic techniques and dispersed in an isotropic oil. The ruler is 100 μm long. **(B)** Size distribution of droplets in a typical active nematic emulsion prepared using traditional emulsification techniques. The field of view is 3 mm wide.

fluorinated oil, which offers better chemical compatibility than the NLC oil with the microfluidic device. For the purpose of the present work, in which we study the behavior of isolated droplets, we have resorted to more traditional emulsification methods, leaving the assembly of lattices of identical active droplets in NLC for future work in which coupling, synchronization, and frustration in driven SR will be explored. In the emulsions prepared by shaking the mixture, droplet sizes feature a broad distribution (**Figure 2B**), but enough droplets of the suitable size range are obtained for the qualitative study reported here.

In the presence of active stresses, the AN shell develops periodic cortical flows [24, 36]. The latter propagate, through hydrodynamic coupling, both into the aqueous and into the NLC bulk phases. As a result, the SR is set into motion and the steady influx of energy may lead to a wealth of dynamic modes. The presence of the plate walls is likely to affect the flow profile in the NLC. Because of the antagonistic NLC anchoring conditions on the droplets and on the plates, homeotropic and planar, respectively, elastic repulsion prevents the droplets from fully sedimenting on the bottom plate [41]. When the continuous phase is an isotropic oil [25], active droplets self-propel erratically on the supporting surface. Such motion is not observed in our case, presumably due to the elastic repulsion due to the NLC matrix, although the higher viscosity of the NLC will also contribute to hamper such self-propulsion. Moreover, the use of cell gaps much larger than the droplets considered in our study ensures that friction on the complementary plate can also be neglected.

In **Figure 3** we display the range of dynamical regimes observed for the activated SR. For each case, a panel with an experimental micrograph and one with a sketch highlighting the main features of the corresponding regime is illustrated. The experimental micrographs are obtained with brightfield and parallel illumination to enhance the ring disclination. The elastic energy in the NLC matrix increases with the length of the SR, and this has an increasing trend from panel A till panel E.

In **Figures 3A–C**, we report regimes in which the SR distortion can be considered 1D, in the sense that it can be described by a uni-valued function of the angular coordinate around the droplet's equator. Among these regimes, the first two correspond to synchronized dynamics between the SR and the underlying AN. This dynamics is better put into evidence in the least energetic regime (**Figure 3A**), where SR oscillations are characterized by a single distortion mode. These distorted SRs lack rotational symmetry, which allows to observe slow degenerate rotations of the dynamic SR about the North-South droplet axis, thus changing the point-of-view, and thus the perception of the oscillating SR and allowing to more clearly assess its oscillation mode (**Figure 4**). The synchronization between the oscillations of the AN and those of the driven SR are clearly evidenced in fluorescence images. In **Figure 5** we show three different fluorescence micrographs that span one half cycle of the SR oscillation. We observe that the SR transits past its equilibrium plane at the same time that the AN is aligned either parallel or perpendicular to this plane, and the SR is farthest from equilibrium when it is being driven by two +1/2 defects moving in antiparallel directions in the underlying AN (**Figure 5B**). With the help of numerical simulations, we recently demonstrated that this tight coupling between the AN and SR oscillatory dynamics is only possible if a feedback mechanism orients the AN shell with respect to the SR [24].

More energetic multi-mode oscillations can also be observed (**Figure 3B**). On average, such configurations are found by increasing the AN activity, which can be tuned by increasing the ATP concentration. In **Figure 6** we compare the dynamics of two droplets that feature synchronous oscillations, found in active nematic emulsions with [ATP] = 140 μM and 1,400 μM, respectively. In the analysis in **Figure 6B** we find that the oscillations observed in **Figure 6A** feature a single mode with frequency $f \simeq 14$ mHz. On the other hand, in **Figure 6D** we see that the oscillations observed in **Figure 6C** are multimode, with a leading frequency $f \simeq 60$ mHz and three of its harmonics present in the spectrum. This change in leading frequency with the corresponding change in ATP concentration is consistent with the results obtained in an earlier detailed analysis performed with flat AN layers, where the inverse of a intrinsic time scale of the system was found to scale linearly with the activity parameter, which is related in a non-linear way with the concentration of ATP [42].

As the deformations of the SR become more energetic, the synchronization with the underlying AN can be lost (**Figure 3C**),

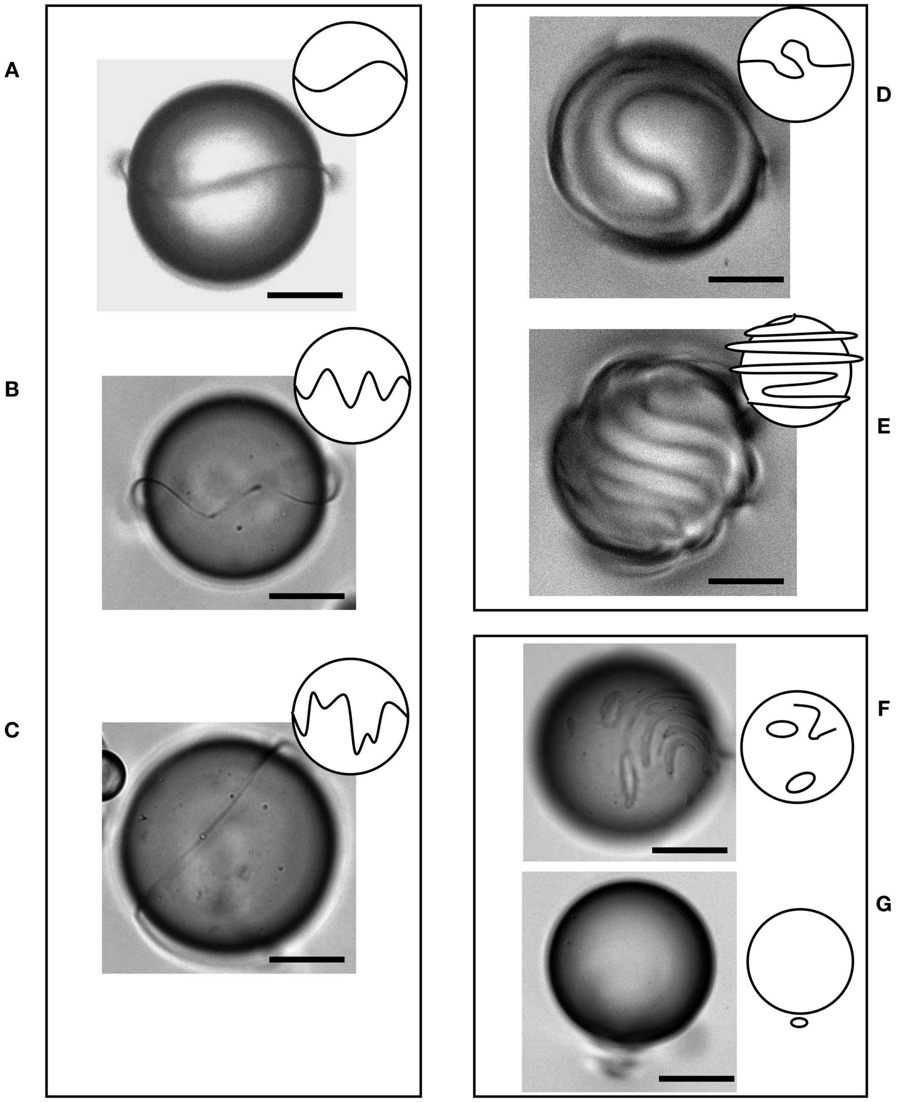

FIGURE 3 | Different dynamic structures of the perturbed Saturn Rings. Sketches on the left and micrographs on the right are included with each case. **(A)** Single mode ($m = 2$) synchronous oscillations. **(B)** Multi-mode synchronous oscillations. **(C)** Multi-mode asynchronous oscillations. **(D)** Multi-valued single wrapping of the SR. **(E)** Multi-valued multiple wrapping of the SR. **(F)** SR has fragmented into multiple disconnected disclinations and loops. **(G)** SR has collapsed into a point defect to the South of the droplet. Scale bars, 20 μm.

resulting in severely distorted SRs. This regime is often unstable, and it may either revert back to synchronous oscillations or, more likely, develop into more complex asynchronous modes, where the SR cannot be described by a single-valued function of the spherical azimuthal coordinate (**Figures 3D,E**), as it can be for the simpler geometries in (**Figures 3A–C**). In these more complex modes, highly distorted SR may develop large folds but still be wrapped just once around the droplet (**Figure 3D**), or even be wrapped multiple times around the droplet (**Figure 3E**). This latter configuration is reminiscent of the multi-wrapping of SR due the helical twist of the director field in cholesteric liquid crystal layers [43], where the equilibrium spacing between consecutive turns is set by the cholesteric pitch. However, these are two very different systems since, in the case of our active nematic emulsions, the spacing between consecutive SR turns is a non-equilibrium feature, and it never reaches a steady state. As seen in **Figure 7**, the SR progressively increases its length and wraps an increasing number of times around the droplet, until the *pitch* between neighboring turns of the disclination reaches a limit value. Such configuration is unstable, and the SR can snap and link neighboring turns of the disclination, forming a shrinking fold. Such process is dynamic, and can be repeated numerous times. A possible subsequent outcome is a fragmentation of the SR into disconnected disclination loops (**Figure 3F**). In equilibrium, these would normally shrink and annihilate but, because of the underlying AN flow, and because

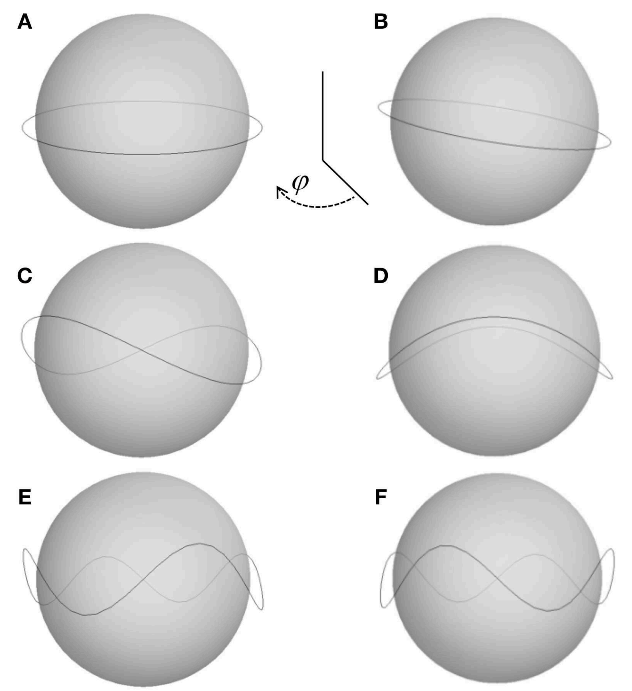

FIGURE 4 | Simulated perception of the Saturn Ring disclination. Different single-mode oscillations are reconstructed at the highest amplitude of deformation for two point-of-view observations, φ. Deformation modes are $m = 1$ **(A,B)**, $m = 2$ **(C,D)**, $m = 4$ **(E,F)**. **(B,D,F)** correspond to points of view rotated 45° clockwise with respect to **(A,C,E)**, respectively.

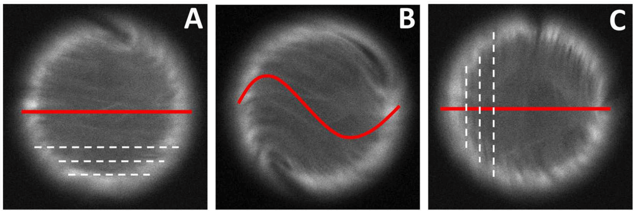

FIGURE 5 | Coordination between the SR and AN orientation during synchronized oscillations. Fluorescence micrographs with three snapshots of the AN oscillation. The SR is sketched as a red line. The dashed lines in **(A)** and **(C)** represent the two complementary states of the active shell where filaments are aligned, while panel **(B)** includes the distorted SR configuration. The droplet has a diameter of 80 μm.

of surface impurities, the loops can remain for extended periods of time.

A SR disclination is not the only distortion compatible with homeotropic anchoring conditions on the droplet surface. Indeed, another possibility is a hyperbolic point defect located near either pole of the droplet (**Figure 3G**), called hedgehog defect [5]. Upon preparation of the active nematic emulsions, we observe that a similar number of droplets with either type of defects coexist. As the emulsion ages, this distribution changes, and progressively most droplets feature a point-like defect. As a matter of fact, SRs appear less stable and some of them are observed to eventually transit to hedgehog-like defects [28]. The opposite transition, however, is never observed. We explain this phenomenon by the tendency of line disclinations to shrink in order to minimize the elastic energy per unit length associated to director field distortions.

Our experiments show that the kinetics of the collapse of a SR to a point-like defect strongly depends on the dynamic

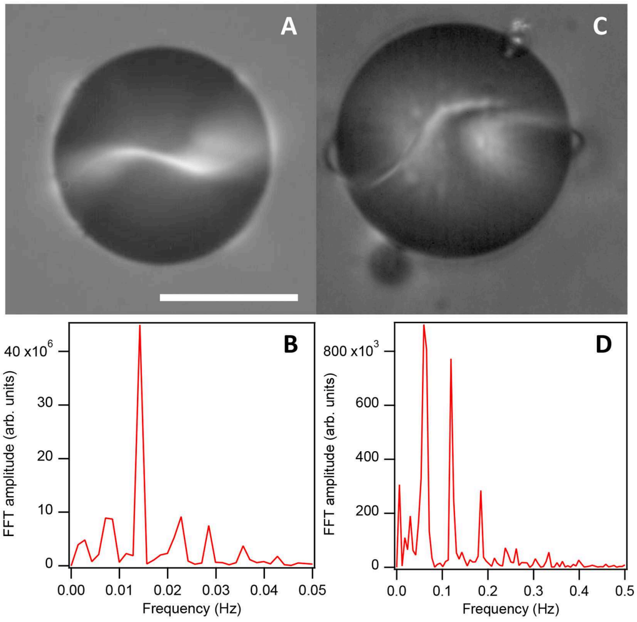

FIGURE 6 | Effect of activity on the SR dynamics. **(A)** Polarizing micrograph of a single mode oscillating SR driven by an AN shell with [ATP] = 140 μm, and the corresponding power spectrum of the oscillations **(B)**. **(C)** Polarizing micrograph of a multimode oscillating SR driven by an AN shell with [ATP] = 1,400 μm, and the corresponding power spectrum of the oscillations. **(D)** Scalebar, 50 μm. See also **Video S1**.

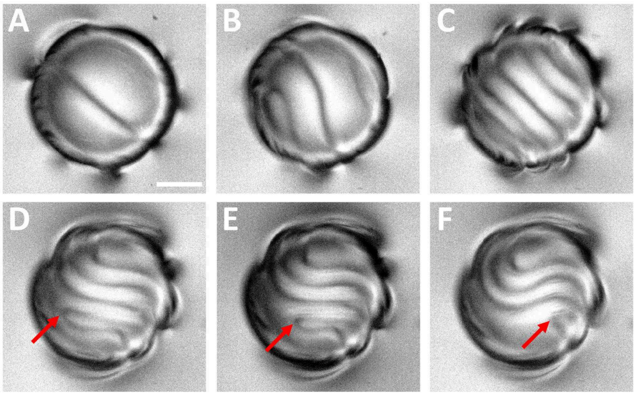

FIGURE 7 | Dynamics of the wrapped SR. **(A–C)** Progressive increase of the number of turns around the droplet of a SR of increasing length. **(D–F)** Two neighboring parts of the SR from ajdancent turns snap, and the resulting fold in the disclination shrinks. Red arrow points to the tip of the shrinking fold. Scalebar, 20 μm. See also **Video S2**.

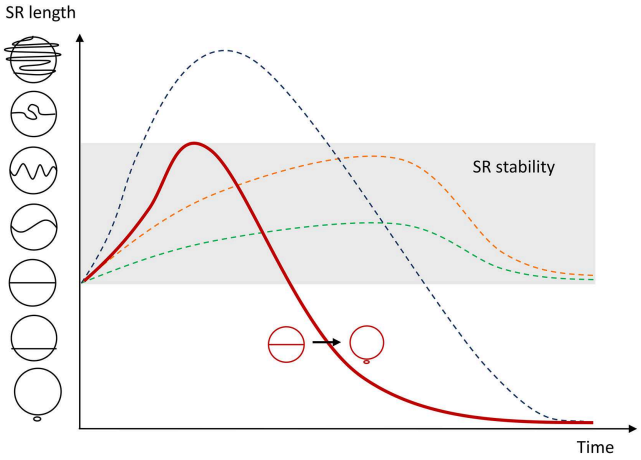

FIGURE 8 | The different dynamic configurations of the system are sketched and ordered in terms of the length of the SR, which determines the elastic energy landscape. The shaded region represents regimes with stable SR oscillations. Solid and dashed lines represent possible pathways in the evolution of the SR, as described in the text. At long times (ATP running out), the SR may either return to its equilibrium conformation or collapse into a dipole.

regime of the SR. Synchronous oscillation regimes may never develop into a point defect, while highly-wrapped, asynchronous regimes, which may involve SRs that wrap several times around the droplet, are invariably seen to collapse into a point-like defect. Schematically, we can rationalize this scenario by considering that an energy barrier must be overcome by the SR in order to collapse into a point-like defect. In **Figure 8**, we have organized the different observed SR configurations in increasing order of elastic energy. As discussed, the equilibrium SR is not the lowest energy level. Below it, we find a sequence of states in which the SR moves from the equatorial position toward a pole, progressively shrinking, i.e., decreasing the NLC elastic energy, until it collapses into a point-like defect. Activated SRs have an average energy above the equilibrium state. Since synchronous oscillation regimes seldom destabilize, their energy levels allow to qualitatively describe a band (shaded in **Figure 8**) that must be overcome for the SR to evolve into the dipolar defect. Certainly, during their oscillations, SR increase their average energy, which reaches a steady state. Eventually, the fuel of the underlying AN, ATP, encapsulated in the droplet, will run out, and the average energy falls back to the equilibrium value as the SR ceases to oscillate. Two trajectories with stable oscillations in this schematic energy landscape are qualitatively traced in **Figure 8**. For more energetic configurations, such as for the asynchronous oscillation regime, the energy level may cross the edge of the *protected region*, and the SR may irreversibly collapse to a point-like defect (red trajectory in **Figure 8**). Finally, the fact that highly distorted SR regimes are always unstable suggests that their energies invariably reach levels above the stable band, and SRs in these dynamic regimes will evolve into a point-like defect well before activity vanishes due to ATP consumption in the AN shell.

4. CONCLUSIONS

In this manuscript we have described experiments in which Saturn ring disclinations, often encountered in colloids dispersed in nematic liquid crystals, are brought far from equilibrium by the encapsulation of droplets containing an aqueous active suspension of cytoskeletal proteins. Under the used experimental conditions, well-characterized in previous studies, this material condenses as an active nematic shell with periodic self-sustained flows that propagate into the passive nematic phase. As a result, the Saturn ring is set into motion and the steady influx of energy leads to a rich array of dynamic modes. The latter span from simple synchronous oscillations in which the disclination remains close to its equilibrium length, to situations in which the length increases steadily, even wrapping several times around the spherical inclusion. In such cases, the metastable quadrupolar defect might eventually collapse into a dipolar configuration.

The dynamic state of the driven Saturn ring depends on the energy influx received from the underlying active nematic layer. This energy depends on the activity and on the efficiency of the coupling between the active and the passive fluids. While the former can be tuned with the concentration of ATP in the aqueous phase, the latter can be influenced by the nature and concentration of the surfactants that decorate the water/oil interface. We have found, however, that the emulsification process leads to a dispersion in the droplet composition, resulting in a disparity of behaviors.

In this manuscript, we have focused on the dynamics of driven disclinations around individual droplets. Our work should pave the way for the future study of collective effects that should arise when multiple disclinations are linked [44]. This would allow to explore the effects arising from synchronization and topological frustration of knotted driven Saturn ring disclinations.

DATA AVAILABILITY STATEMENT

The data that support the findings of this study are available from the corresponding author upon reasonable request.

AUTHOR CONTRIBUTIONS

PG, JI-M, and FS conceived the experiments. PG and JH performed the experiments and analysis of experimental data. JI-M wrote the manuscript with input from all the authors.

FUNDING

JH, PG, JI-M, and FS acknowledge funding from MINECO (project FIS2016-78507-C2-1-P, AEI/FEDER, EU). PG acknowledges funding from Generalitat de Catalunya through a FI-DGR PhD Fellowship. JH acknowledges funding from the European Union's Horizon 2020 research and innovation programme under grant agreement No 674979-NANOTRANS.

Brandeis University MRSEC Biosynthesis facility is supported by NSF MRSEC DMR-1420382.

ACKNOWLEDGMENTS

The authors are indebted to the Brandeis University MRSEC Biosynthesis facility for providing the tubulin. We thank M. Pons, A. LeRoux, G. Iruela, and B. Martínez-Prat (Universitat de Barcelona) for their assistance in the expression of motor proteins.

SUPPLEMENTARY MATERIAL

The Supplementary Material for this article can be found online at: https://www.frontiersin.org/articles/10.3389/fphy.2019.00165/full#supplementary-material

Video S1 | Oscillating Saturn rings observed between crossed polarizers. ATP concentrations in the encapsulated active material are 140 μM (**left**) and 1400 μM (**right**).

Video S2 | Dynamics of a wrapped Saturn ring observed without polarizers.

REFERENCES

1. Oswald P, Pieranski P. *Nematic and Cholesteric Liquid Crystals : Concepts and Physical Properties Illustrated by Experiments*. The liquid crystals book series. Boca Raton, FL: Taylor & Francis (2005).
2. Kléman M, Lavrentovich OD. *Soft Matter Physics : An Introduction*. Partially ordered systems. New York, NY: Springer (2003).
3. Zheludev NI, Kivshar YS. From metamaterials to metadevices. *Nat Mater*. (2012) **11**:917–24. doi: 10.1038/nmat3431
4. Stark H. Physics of colloidal dispersions in nematic liquid crystals. *Phys Rep*. (2001) **351**:387–474. doi: 10.1016/S0370-1573(00)00144-7
5. Muševič I. *Liquid Crystal Colloids. Soft and Biological Matter*. Cham: Springer Nature (2017).
6. Wood TA, Lintuvuori JS, Schofield AB, Marenduzzo D, Poon WC. A self-quenched defect glass in a colloid-nematic liquid crystal composite. *Science*. (2011) **334**:79–83. doi: 10.1126/science.1209997
7. Martinez A, Mireles HC, Smalyukh I. Large-area optoelastic manipulation of colloidal particles in liquid crystals using photoresponsive molecular surface monolayers. *Proc Natl Acad Sci USA*. (2011) **108**:20891–6. doi: 10.1073/pnas.1112849108
8. Trivedi RP, Klevets I, Senyuk B, Lee T, Smalyukh I. Reconfigurable interactions and three-dimensional patterning of colloidal particles and defects in lamellar soft media. *Proc Natl Acad Sci USA*. (2012) **109**:4744–9. doi: 10.1073/pnas.1119118109
9. Senyuk B, Liu Q, He S, Kamien RD, Kusner RB, Lubensky TC, et al. Topological colloids. *Nature*. (2013) **493**:200–5. doi: 10.1038/nature11710
10. Martinez A, Ravnik M, Lucero B, Visvanathan R, Zumer S, Smalyukh I. Mutually tangled colloidal knots and induced defect loops in nematic fields. *Nat Mater*. (2014) **13**:258–63. doi: 10.1038/nmat3840
11. Eremin A, Hirankittiwong P, Chattham N, Nadasi H, Stannarius R, Limtrakul J, et al. Optically driven translational and rotational motions of microrod particles in a nematic liquid crystal. *Proc Natl Acad Sci USA*. (2015) **112**:1716–20. doi: 10.1073/pnas.1419850112
12. Liu Q, Ackerman PJ, Lubensky TC, Smalyukh I. Biaxial ferromagnetic liquid crystal colloids. *Proc Natl Acad Sci USA*. (2016) **113**:10479–84. doi: 10.1073/pnas.1601235113
13. Peng C, Turiv T, Guo Y, Shiyanovskii SV, Wei QH, Lavrentovich OD. Control of colloidal placement by modulated molecular orientation in nematic cells. *Sci Adv*. (2016) **2**:e1600932. doi: 10.1126/sciadv.1600932
14. Poulin P, Stark H, Lubensky TC, Weitz DA. Novel colloidal interactions in anisotropic fluids. *Science*. (1997) **275**:1770–3. doi: 10.1126/science.275.5307.1770
15. Loudet JC, Barois P, Poulin P. Colloidal ordering from phase separation in a liquid-crystalline continuous phase. *Nature*. (2000) **407**:611–3. doi: 10.1038/35036539
16. Yamamoto J, Tanaka H. Transparent nematic phase in a liquid-crystal-based microemulsion. *Nature*. (2001) **409**:321–5. doi: 10.1038/35053035
17. Musevic I, Skarabot M, Tkalec U, Ravnik M, Zumer S. Two-dimensional nematic colloidal crystals self-assembled by topological defects. *Science*. (2006) **313**:954–8. doi: 10.1126/science.1129660
18. Smalyukh II. Liquid crystal colloids. *Annu Rev Condens Matter Phys*. (2017) **9**:207–26. doi: 10.1146/annurev-conmatphys-033117-054102
19. Hashemi SM, Jagodic U, Mozaffari MR, Ejtehadi MR, Musevic I, Ravnik M. Fractal nematic colloids. *Nat Commun*. (2017) **8**:14026. doi: 10.1038/ncomms14026
20. Solodkov NV, Shim JU, Jones JC. Self-assembly of fractal liquid crystal colloids. *Nat Commun*. (2019) **10**:198. doi: 10.1038/s41467-018-08210-w
21. Hernandez-Navarro S, Tierno P, Farrera JA, Ignes-Mullol J, Sagues F. Reconfigurable swarms of nematic colloids controlled by photoactivated surface patterns. *Angew Chem Int Ed Engl*. (2014) **53**:10696–700. doi: 10.1002/anie.201406136
22. Li BX, Borshch V, Xiao RL, Paladugu S, Turiv T, Shiyanovskii SV, et al. Electrically driven three-dimensional solitary waves as director bullets in nematic liquid crystals. *Nat Commun*. (2018) **9**:2912. doi: 10.1038/s41467-018-05101-y
23. Giomi L, Kos Z, Ravnik M, Sengupta A. Cross-talk between topological defects in different fields revealed by nematic microfluidics. *Proc Natl Acad Sci USA*. (2017) **114**:E5771–7. doi: 10.1073/pnas.1702777114
24. Guillamat P, Kos Z, Hardouin J, Ignes-Mullol J, Ravnik M, Sagues F. Active nematic emulsions. *Sci Adv*. (2018) **4**:eaao1470. doi: 10.1126/sciadv.aao1470
25. Sanchez T, Chen DT, DeCamp SJ, Heymann M, Dogic Z. Spontaneous motion in hierarchically assembled active matter. *Nature*. (2012) **491**:431–4. doi: 10.1038/nature11591
26. Doostmohammadi A, Ignes-Mullol J, Yeomans JM, Sagues F. Active nematics. *Nat Commun*. (2018) **9**:3246. doi: 10.1038/s41467-018-05666-8
27. Kuksenok OV, Ruhwandl RW, Shiyanovskii SV, Terentjev EM. Director structure around a colloid particle suspended in a nematic liquid crystal. *Phys Rev E*. (1996) **54**:5198–203. doi: 10.1103/PhysRevE.54.5198
28. Gu Y, Abbott N. Observation of saturn-ring defects around solid microspheres in nematic liquid crystals. *Phys Rev Lett*. (2000) **85**:4719–22. doi: 10.1103/PhysRevLett.85.4719
29. Stark H. Saturn-ring defects around microspheres suspended in nematic liquid crystals: an analogy between confined geometries and magnetic fields. *Phys Rev E*. (2002) **66**:032701. doi: 10.1103/PhysRevE.66.032701
30. Edelstein AD, Tsuchida MA, Amodaj N, Pinkard H, Vale RD, Stuurman N. Advanced methods of microscope control using μManager software. *J Biol Methods*. (2014) **1**:e10. doi: 10.14440/jbm.2014.36
31. Giomi L. Geometry and topology of turbulence in active nematics. *Phys Rev X*. (2015) **5**:031003. doi: 10.1103/PhysRevX.5.031003
32. Martínez-Prat B, Ignés-Mullol J, Casademunt J, Sagués F. Selection mechanism at the onset of active turbulence. *Nat Phys*. (2019) **15**:362–6. doi: 10.1038/s41567-018-0411-6
33. Aditi Simha R, Ramaswamy S. Hydrodynamic fluctuations and instabilities in ordered suspensions of self-propelled particles. *Phys Rev Lett*. (2002) **89**:058101. doi: 10.1103/PhysRevLett.89.058101
34. Voituriez R, Joanny JF, Prost J. Spontaneous flow transition in active polar gels. *Europhys Lett*. (2005) **70**:404–10. doi: 10.1209/epl/i2004-10501-2
35. Guillamat P, Ignes-Mullol J, Sagues F. Taming active turbulence with patterned soft interfaces. *Nat Commun*. (2017) **8**:564. doi: 10.1038/s41467-017-00617-1
36. Keber FC, Loiseau E, Sanchez T, DeCamp SJ, Giomi L, Bowick MJ, et al. Topology and dynamics of active nematic vesicles. *Science*. (2014) **345**:1135–9. doi: 10.1126/science.1254784

37. Lopez-Leon T, Koning V, Devaiah KBS, Vitelli V, Fernandez-Nieves A. Frustrated nematic order in spherical geometries. *Nat Phys*. (2011) **7**:391–4. doi: 10.1038/nphys1920
38. Shin H, Bowick M, Xing X. Topological defects in spherical nematics. *Phys Rev Lett*. (2008) **101**:037802. doi: 10.1103/PhysRevLett.101.037802
39. Zhang R, Zhou Y, Rahimi M, de Pablo JJ. Dynamic structure of active nematic shells. *Nat Commun*. (2016) **7**:13483. doi: 10.1038/ncomms13483
40. Tan AJ, Roberts E, Smith SA, Olvera UA, Arteaga J, Fortini S, et al. Topological chaos in active nematics. *Nat Phys*. (2019) **15**:1033–9. doi: 10.1038/s41567-019-0600-y
41. Pishnyak O, Tang S, Kelly J, Shiyanovskii S, Lavrentovich O. Levitation, lift, and bidirectional motion of colloidal particles in an electrically driven nematic liquid crystal. *Phys Rev Lett*. (2007) **99**:127802. doi: 10.1103/PhysRevLett.99.127802
42. Guillamat P, Ignes-Mullol J, Sagues F. Control of active liquid crystals with a magnetic field. *Proc Natl Acad Sci USA*. (2016) **113**:5498–502. doi: 10.1073/pnas.1600339113
43. Gvozdovskyy I, Jampani VS, Skarabot M, Musevic I. Light-induced rewiring and winding of Saturn ring defects in photosensitive chiral nematic colloids. *Eur Phys J E Soft Matter*. (2013) **36**:97. doi: 10.1140/epje/i2013-13097-8
44. Tkalec U, Ravnik M, Copar S, Zumer S, Musevic I. Reconfigurable knots and links in chiral nematic colloids. *Science*. (2011) **333**:62–5. doi: 10.1126/science.1205705

Conflict of Interest: The authors declare that this study received funding from MINECO. The funder was not involved in the study design, collection, analysis, interpretation of data, the writing of this article or the decision to submit it for publication.

frontiers in Physics

ORIGINAL RESEARCH
published: 08 November 2019
doi: 10.3389/fphy.2019.00178

Chiral Topological Phases in Designed Mechanical Networks

Henrik Ronellenfitsch and Jörn Dunkel*

Department of Mathematics, Massachusetts Institute of Technology, Cambridge, MA, United States

Mass-spring networks (MSNs) have long been used as approximate descriptions of biological and engineered systems, from actomyosin networks to mechanical trusses. In the last decade, MSNs have re-attracted theoretical interest as models for phononic metamaterials with exotic properties such as negative Poisson's ratio, negative effective mass, or gapped vibrational spectra. A numerical advantage of MSNs is their tuneability, which allows the inverse design of materials with pre-specified bandgaps. Building on this fact, we demonstrate here that designed MSNs, when subjected to Coriolis forces, can host topologically protected chiral edge modes at predetermined frequencies, thus enabling robust unidirectional transmission of mechanical waves. Similar to other recently discovered topological materials, the topological phases of MSNs can be classified by a Chern invariant related to time-reversal symmetry breaking.

Keywords: mechanical networks, topological matter, Chern insulator, classical mechanics and quantum mechanics, edge modes

Edited by:
Francesca Serra,
Johns Hopkins University,
United States

Reviewed by:
Massimo Pica Ciamarra,
Nanyang Technological University,
Singapore
Martin Kröger,
ETH Zürich, Switzerland

****Correspondence:***
Henrik Ronellenfitsch
henrikr@mit.edu

Specialty section:
This article was submitted to
Soft Matter Physics,
a section of the journal
Frontiers in Physics

Received: *04 July 2019*
Accepted: *21 October 2019*
Published: *08 November 2019*

Citation:
Ronellenfitsch H and Dunkel J (2019)
Chiral Topological Phases in Designed
Mechanical Networks.
Front. Phys. 7:178.
doi: 10.3389/fphy.2019.00178

1. INTRODUCTION

Topological mechanics [1] is a rapidly growing research field that studies classical analogs of topological effects in quantum many-body physics [2]. A prime example are spectrally gapped mechanical systems that can host topologically protected zero modes at their boundaries [3–5], similar to localized electronic excitations in the quantum spin Hall effect [6]. Another important class of examples are solid- or fluid-mechanical systems with broken time-reversal symmetry, which can exhibit chiral edge modes at finite frequency [7–10], analogous to the (anomalous) quantum Hall effect [11, 12]. Because these edge modes are topologically protected and robust against the introduction of defects, they may provide a powerful tool for the resilient localized transmission of sound signals in elastic materials [13].

Over the last 5 years, substantial progress has been made in the understanding of topological phenomena in a wide variety of classical systems, ranging from mechanical systems with lattice symmetry inspired by quantum analogs [14, 15] and amorphous networks [9, 16] to active systems [7, 17, 18], electrical circuits [19–21], and even ocean waves [22]. Many of the recently discovered mechanical topological insulators rely on a known underlying lattice structure [7, 14] or curvature [22] to induce the required gaps in their excitation spectra. From a practical perspective, it would be interesting to design and build more general structures with desired topological properties.

Complementing recent work aimed at engineering continuum topological insulators [23], we consider here the design of topological excitations in bandgap-optimized [24] mass-spring networks (MSNs). Specifically, we will demonstrate that MSNs with an inversely designed bandgap can host topologically protected finite-frequency edge modes, and convert non-robust non-topological edge modes into robust topological edge modes when time-reversal symmetry is broken. While many traditional topological materials, including those based on a hexagonal lattice like the Haldane model [25], do not possess the mode conversion property, this desirable feature is frequently encountered in our designed MSNs.

In the remainder, we focus on the dynamics of periodic crystals of 2D mechanical balls-and-springs networks. In all cases, the spring stiffnesses of these MSNs were numerically tuned such that the excitation spectrum exhibits a band gap (using the algorithm introduced in [24]). In formal analogy with quantum Hall systems [11, 12], we will then break time reversal symmetry by placing the MSN into a rotating frame, with the Coriolis forces acting equivalently to an external magnetic field. To study and characterize the topological phase transition and the emerging protected chiral edge modes in detail, we will (i) numerically calculate the non-zero Chern invariant associated to the topological phase, (ii) demonstrate the dynamics of the localized chiral edge excitations in numerical simulations, and (iii) explicitly identify those dynamical edge modes that are related to topological protection. The underlying inverse-design framework [24] uses a generic linear response optimization and is, therefore, broadly applicable. Promising candidates for experimental implementations are mechanically coupled phase oscillators under Coriolis acceleration, such as hydrodynamic spin lattices of walking droplets [26] or gyroscopic mechanical metamaterials [8, 10].

2. DYNAMICS OF MECHANICAL NETWORKS

MSNs provide a generic modeling framework for many physical systems. The potential energy of an MSN with E springs is given by

$$V = \frac{1}{2}\sum_{e=1}^{E} k_e \left(\ell_e - \ell_e^{(0)}\right)^2,$$

where k_e is the stiffness of spring e, ℓ_e is its current length and $\ell_e^{(0)}$ is its preferred rest length. Here, we are interested in the dynamics near the equilibrium configuration where all springs are at their rest lengths, $\ell_e = \ell_e^{(0)}$, corresponding to the masses being at positions $\mathbf{x}_i^{(0)}$. Expanding in small deviations $\mathbf{u}_i = \mathbf{x}_i - \mathbf{x}_i^{(0)}$ and neglecting frictional effects, we obtain the linearized equations of motion,

$$m\ddot{\mathbf{u}} + K\mathbf{u} = 0, \tag{1}$$

where K is the stiffness matrix of the network and m is the mass of the balls (we assume identical masses throughout). The vector $\mathbf{u}$ generally has dN components, where d is the dimension of space and N is the number of masses. From now on, we specialize to the case $d = 2$. The stiffness matrix can be further decomposed as $K = Q\hat{k}Q^\top$, where Q is the equilibrium matrix encoding the network geometry and $\hat{k} = \operatorname{diag}(k_1, k_2, \ldots, k_E)$ is the diagonal matrix of spring stiffnesses [27]. Neglecting thermal fluctuations throughout, the subsequent discussion focuses on macroscopic topological metamaterials, similar to those realized experimentally in Chen et al. [28]. In principle, it is possible to incorporate thermal or non-thermal noise [18] and/or more general nonlinear potentials, such as in the elastic Lennard-Jones model [29], provided these admit linearizations in the form of Equation (1).

The MSN dynamics, specifically its harmonic response and its phononic modes, are encoded in the eigenmodes

$$K\mathbf{u}_j = m\omega_j^2\mathbf{u}_j, \tag{2}$$

where ω_j are the eigenfrequencies. If the network is a crystal consisting of N_c periodically repeated unit cells with lattice vectors $\mathbf{R}_\ell$, the dynamical problem can be simplified by performing a lattice Fourier transform [27],

$$u_n(\mathbf{R}_\ell) = \frac{1}{N_c}\sum_{\mathbf{k}} e^{-i\mathbf{k}\cdot\mathbf{x}_i} u_n(\mathbf{k})$$
$$u_n(\mathbf{k}) = \sum_{\mathbf{R}_\ell} e^{i\mathbf{k}\cdot\mathbf{x}_i} u_n(\mathbf{R}_\ell),$$

where we decompose the rest positions $\mathbf{x}_i = \mathbf{R}_\ell + \mathbf{v}_n$. Here, ℓ indexes the unit cell and n indexes the degree of freedom within the unit cell. The wavevector $\mathbf{k} = \sum_{i=1}^{d} \frac{b_i}{N_i}\mathbf{K}_i$ with $b_i \in \mathbb{Z}$ lies in the first Brillouin zone, N_i is the number of unit cells in the ith dimension, and the reciprocal lattice vectors satisfy $\mathbf{K}_i \cdot \mathbf{R}_j = 2\pi\delta_{ij}$ for the primitive lattice vectors $\mathbf{R}_j$. The Fourier transform decouples the eigen-problem Equation (2) for different wavevectors $\mathbf{k}$ and leads to a phononic band structure $\omega_n(\mathbf{k})$.

The band structure $\omega_n(\mathbf{k})$ is of great interest both scientifically and for engineering applications because it efficiently encodes the elastic response of the infinite network. Specifically, band structure engineering allows for explicit tuning of wave propagation in acoustic materials and can be used to design, for instance, waveguides, acoustic cloaks, or selective sound suppression. Whereas in a generic band structure, the shape and frequency of the acoustic modes depends strongly on the details of the dynamics, topological modes are protected by an integer invariant, which cannot change through continuous changes of the interaction parameters.

Although the physical realizations of topological insulators are vast already in the quantum case [2, 12], the possible invariants and topological phases have been completely classified [30]. In linear topological mechanics, a similar scheme exists as long as the dynamical matrix is positive definite [1]. For our MSNs, this condition is always satisfied. In the following, we shall focus on one particular class of classical topological band structures for two-dimensional systems.

3. PLANAR CHERN INSULATORS

Topological band structure is intimately related to the theory of Berry phases, or geometrical phases [31]. While a full account of the underlying theory is beyond the scope of this paper, the fundamental result can be stated for a linear dynamical system

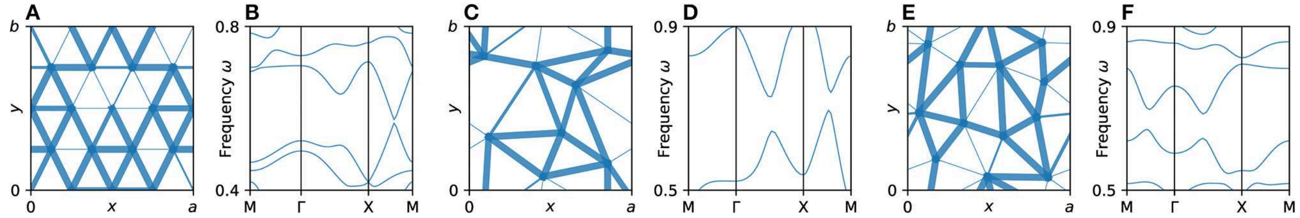

FIGURE 1 | Bandgap tuned networks and topological band structures. **(A)** Tuned spring stiffnesses (indicated by line thickness) on the basis of triangular grids with 4 × 4 unit cells were tuned to have band gaps. **(B)** The final band structures exhibit band shapes reminiscent of band inversion. **(C,E)** Tuned network on top of a topology based on the Delaunay triangulation of a randomized point set. **(D,F)** The band structure again appears to exhibit band inversion. All three networks undergo a topological phase transition as time-reversal symmetry is broken.

$i\dot{\boldsymbol{\psi}} = H(\mathbf{r})\boldsymbol{\psi}$ with Hermitian matrix $H(\mathbf{r})$ which depends on some parameter $\mathbf{r}$. The band structure topology is then encoded in the eigenstates of this effective 'Hamiltonian' H, and can be characterized by calculating an integer topological invariant, the *Chern number*. We now give a brief sketch of this calculation.

If the system is prepared in an instantaneous eigenstate $H(\mathbf{r})\mathbf{u}(\mathbf{r}) = \lambda(\mathbf{r})\mathbf{u}(\mathbf{r})$ and the parameter $\mathbf{r}$ is varied adiabatically along a closed curve $\mathcal{C}$ in parameter space, then the solution will always remain in the instantaneous eigenstate. After traversing the curve, the solution will pick up a phase factor $e^{i\gamma_{\mathcal{C}}}$ with

$$\gamma_{\mathcal{C}} = \int_{\mathcal{C}} d\mathbf{r} \cdot \mathbf{A}(\mathbf{r}), \quad \mathbf{A}(\mathbf{r}) = i\mathbf{u}(\mathbf{r})^{H}\nabla_{\mathbf{r}}\mathbf{u}(\mathbf{r}). \tag{3}$$

This is the celebrated Berry phase with $\mathbf{A}(\mathbf{r})$ the Berry connection (superscript H denotes the Hermitian transpose). While the Berry connection changes under reparametrizations of the curve (gauge transformations), the phase is invariant up to 2π, and therefore in principle a physical observable. One particular parameter space of interest is the Brillouin zone of a crystal. In two dimensions, the BZ has the topology of a torus, such that any curve connecting $\mathbf{k}$ and $\mathbf{k} + \mathbf{K}$ is closed (because wavevectors $\mathbf{k}$ and $\mathbf{k} + \mathbf{K}$ are equivalent if $\mathbf{K}$ is a reciprocal lattice vector). By Stokes' theorem, Equation (3) can then be expressed as a surface integral independent of the curve,

$$\gamma_{\mathcal{C}} = \int_{\mathrm{BZ}} d\mathbf{k}\, \Omega(\mathbf{k}) \equiv \chi, \tag{4}$$

where

$$\Omega(\mathbf{k}) = \partial_{k_1} A_2(\mathbf{k}) - \partial_{k_2} A_1(\mathbf{k})$$

is called the Berry curvature. Equation (4) defines the Chern number χ, which is an integer modulo 2π, and characterizes the eigenstates $\{\mathbf{u}(\mathbf{k})\}_{\mathbf{k}\in\mathrm{BZ}}$. Thus, because in a crystal each eigenstate parametrized by the wavevector $\mathbf{k}$ corresponds to a band, it is possible to assign a topological Chern number χ_n to each band n. This Chern number does not change under perturbations of the matrix $H(\mathbf{k})$, unless bands cross. Then, the eigenstates are no longer non-degenerate and the above analysis fails.

The Chern number defined by Equation (4) is nonzero only if the dynamics are not time-reversal invariant. If the system has time reversal invariance, $\Omega(\mathbf{k})$ is an odd function of $\mathbf{k}$, and the integral over the Brillouin zone vanishes.

For systems with many bands and a gap between bands n' and $n' + 1$, the key insight [32] is then that one can associate an invariant to the *gap* itself, namely

$$C(n') = \sum_{n\leq n'} \chi_n,$$

which can only change if the gap closes due to a perturbation of $H(\mathbf{k})$. The gap-Chern number C characterizes the bulk of a gapped crystal. Near a boundary to another gapped crystal with a different C or to the vacuum, the topology of the system must therefore change locally by closing the gap. This argument implies the existence of modes that are localized to the boundary between different topological phases and located in the bulk gap. Because these modes are tied to the bulk topological invariants, they are robust and must always exist, regardless of the specific shape of the boundary. We note that while for historical reasons the notion of adiabatic changes of parameters was invoked to define the Chern number, no actual adiabatic processes are necessary for it to exist, and it makes sense for any Fourier-transformed Hamiltonian.

For numerical purposes, the above integrals can be discretized while retaining their gauge-invariant characteristics [33]. This way, Chern numbers can be computed robustly and quickly with reasonably coarse discretizations of the Brillouin zone. In addition, any Chern number numerically computed in this way will automatically be an integer.

In the remainder, we demonstrate that such topologically protected edge modes can indeed exist in mechanical networks which have been tuned to exhibit bandgaps at specified frequencies, opening up an inverse-design pathway toward explicitly programmable topology.

4. INVERSE BANDGAP DESIGN

There are many mechanical systems that possess topological gaps by virtue of their lattice structure. Here, we consider a different approach by tuning a desired gap into the spectrum of a mechanical network through numerical Linear Response Optimization (LRO) [24]. Starting from a basic lattice topology such as a triangular grid or a randomized unit cell topology defining mass points and springs (**Figure 1**), the spring stiffnesses k_e are numerically optimized to produce a gapped material between two desired bands. Applying the numerical LRO approach introduced and described in detail in Ronellenfitsch et al. [24], we minimize the average response of the network at frequency ω,

$$R_\omega(\hat{k}) = \mathrm{Tr}\left(G_\omega(\hat{k})^H G_\omega(\hat{k})\right), \tag{5}$$

where $G_\omega(\hat{k}) = \left(m\omega^2\mathbb{1} - Q\hat{k}Q^\top\right)^{-1}$ is the linear response matrix to harmonic forcing with frequency ω and $\mathrm{Tr}(\cdot)$ is the matrix trace. Numerically minimizing Equation (5) over the individual spring stiffnesses $\hat{k}$ while fixing a certain $\omega_n < \omega < \omega_{n+1}$ for eigenmodes ω_n is then equivalent to maximizing a spectral gap between the nth and $(n+1)$th eigenvalue. Generalizing from spectral gaps to bandgaps, since the Fourier transform is a linear map that block-diagonalizes $G_\omega(\hat{k})$, the trace in Equation (5) is replaced by a sum over the traces over the responses at each individual wavevector $\mathbf{k}$, $G_\omega(\hat{k}, \mathbf{k})$. For practical purposes, this sum is truncated, and only traces over a small number of wavevectors are actually used in the numerical optimization. To avoid the spring stiffnesses converging to either zero or infinity, we additionally impose bound constraints $0.1 \le k_e \le 1.0$, and employ the Limited-memory Broyden–Fletcher–Goldfarb–Shanno algorithm [34] to perform the numerical optimization. Particle masses are set to unity ($m = 1$).

The above LRO approach generalizes to arbitrary network topologies and dimensions [24]. Throughout this paper, we will illustrate general ideas by focusing on three specific examples of bandgap-tuned networks: One with a regular triangular grid unit cell topology, and two different randomized unit cell topologies (**Figures 1A,C,E**). All three networks were optimized to exhibit a bandgap at some predetermined frequency. Despite some notable differences between them, their band structures all show features reminiscent of band inversion (**Figures 1B,D,F**), a characteristic that is often (but not always) present in topological band structures [35–37].

Adopting band inversion as an indicator for the potential existence of a topological transition, all that remains to do is to break time-reversal invariance of the system dynamics by introducing a suitable interaction. In the case of electronic systems, an externally applied magnetic field can provide such a symmetry-breaking interaction [12]. A classical formal counterpart considered in the remainder is the Coriolis force [38] which breaks the time reversal symmetry of the MSN dynamics when the mechanical network is placed in a rotating frame [14].

5. MECHANICAL NETWORKS IN ROTATING FRAMES

To sketch the general procedure for formulating the MSN dynamics in a rotating frame, we first consider a point mass in a harmonic potential with stiffness K confined to the x–y plane, and under the influence of a constant rotation perpendicular to the plane, $\Omega = (0, 0, \Omega)$. Let $\mathbf{x}$ be the position of the point mass as measured from the rotational axis. Then, Newton's equations of motion in the rotating frame take the form

$$\ddot{\mathbf{x}} = -K(\mathbf{x} - \mathbf{x}_0) - 2\Omega \wedge \dot{\mathbf{x}} - \Omega \wedge (\Omega \wedge \mathbf{x}). \tag{6}$$

The Coriolis force is

$$-2\Omega \wedge \dot{\mathbf{x}} = -2(0, 0, \Omega) \wedge (\dot{x}, \dot{y}, 0) = 2\Omega(\Gamma\dot{\mathbf{x}}', 0),$$

where

$$\Gamma = \begin{pmatrix} 0 & 1 \\ -1 & 0 \end{pmatrix}$$

encodes the cross product and we introduced the 2D vector $\mathbf{x}'$. Similarly, the centrifugal force is $-\Omega\wedge(\Omega\wedge\mathbf{x}') = \Omega\wedge(\Omega\Gamma\mathbf{x}', 0) = -\Omega^2(\Gamma^2\mathbf{x}', 0) = \Omega^2(\mathbf{x}', 0)$. Clearly, the fictitious forces lie in the plane of rotation, so that from now on we can analyze the system in 2D. Dropping the primes, Equation (6) then yields the in-plane equations of motion

$$\ddot{\mathbf{x}} = -K(\mathbf{x} - \mathbf{x}_0) + 2\Omega\Gamma\dot{\mathbf{x}} + \Omega^2\mathbf{x}. \tag{7}$$

We can now generalize from a single particle to the full MSN dynamics by collecting all the x coordinates of the point masses in the network into the first N components of the $2N$-component vector $\mathbf{x}$, and all the y coordinates into the second N components. Then the matrix Γ takes the form

$$\Gamma = \begin{pmatrix} 0 & \mathbb{1} \\ -\mathbb{1} & 0 \end{pmatrix},$$

where $\mathbb{1}$ is the $N \times N$ identity matrix, and K now denotes the stiffness matrix such that Equation (7) remains formally unchanged.

We would like to express these equations in terms of small displacements around an equilibrium configuration. In doing so, we need to take into account that the equilibrium configuration is changed by the rotation. To find the new equilibrium positions $\mathbf{x}^*$ in the rotating frame, we set $\ddot{\mathbf{x}} = \dot{\mathbf{x}} = 0$ and solve for $\mathbf{x}^*$,

$$(K - \Omega^2\mathbb{1})\mathbf{x}^* = -K\mathbf{x}_0.$$

Thus, a steady state exists unless the rotation frequency Ω^2 resonantly matches one of the eigenfrequencies of the stiffness matrix K. In the absence of resonance, we introduce displacements $\mathbf{u} = \mathbf{x} - \mathbf{x}^*$, and find their equations of motion,

$$\begin{aligned} \ddot{\mathbf{u}} &= -K(\mathbf{u} + \mathbf{x}^* - \mathbf{x}_0) + 2\Omega\Gamma\dot{\mathbf{u}} + \Omega^2\mathbf{u} + \Omega^2\mathbf{x}^* \\ &= -(K - \Omega^2\mathbb{1})\mathbf{u} + 2\Omega\Gamma\dot{\mathbf{u}}. \end{aligned}$$

Here, the stiffness matrix was shifted due to the centrifugal force, and a new Coriolis term has appeared.

In the following, we further assume slow rotations compared to the smallest eigenmode of interest, typically the frequency of the gap, and neglect the term proportional to $\Omega^2 \ll 1$. This leads to the final equations of motion,

$$\ddot{\mathbf{u}} = -K\mathbf{u} + 2\Omega\Gamma\dot{\mathbf{u}}. \tag{8}$$

The Coriolis term proportional to $\dot{\mathbf{u}}$ is responsible for breaking time-reversal symmetry in this classical system (the transformation $t \mapsto -t$ maps $\dot{\mathbf{u}}$ to $-\dot{\mathbf{u}}$ but leaves all other terms invariant), analogous to the Lorentz force in a quantum electron gas [12]. Because the eigenmodes of Equation (8) cannot be computed directly by inserting a harmonic ansatz, we must resort to the equivalent first order system

$$\dot{\mathbf{y}} = D\mathbf{y}, \qquad D = \begin{pmatrix} 0 & \mathbb{1} \\ -K & 2\Omega\Gamma \end{pmatrix}, \tag{9}$$

where $\mathbf{y} = (\mathbf{u}, \mathbf{w})^\top$, $\mathbf{w} = \dot{\mathbf{u}}$, and D is the dynamical matrix, the eigenmodes of which can be readily computed.

Equation (9) can be brought into a form manifestly equivalent to the Schrödinger equation by introducing the change of variables [1],

$$\boldsymbol{\psi} = \begin{pmatrix} \sqrt{K} & 0 \\ 0 & i\mathbb{1} \end{pmatrix} \mathbf{y},$$

where the matrix square root $\sqrt{K}$ is well-defined because K is positive-semidefinite. Under this change of variables, the dynamics becomes

$$i\dot{\boldsymbol{\psi}} = H\boldsymbol{\psi}, \qquad H = \begin{pmatrix} 0 & \sqrt{K} \\ \sqrt{K} & 2i\Omega\Gamma \end{pmatrix}, \tag{10}$$

where the "Hamiltonian" H is manifestly Hermitian. This form makes explicit the connection between classical mechanical and quantum systems, as now the machinery of quantum mechanics is applicable to Equation (10).

Below, we illustrate and analyze the generic consequences of time-reversal symmetry breaking via rotation for three distinct mechanical networks based on the inversely designed unit cells in **Figure 1**. We will see that the corresponding MSNs undergo a topological phase transition when the rotation frequency exceeds a critical value, resulting in topologically protected gapless modes that are exponentially localized at the boundary of samples.

6. TOPOLOGICAL EXCITATIONS IN ROTATED NETWORKS

The three mechanical networks from **Figure 1** exemplify typical phenomena encountered with mechanical Chern networks. For each of them, a topological phase transition occurs at some finite $0 < |\Omega_c| < 0.1$, independent of the sign of Ω. This is due to the fact reversing the sign of the rotation frequency Ω is equivalent to reversing time $t \mapsto -t$, and therefore mirrors the band structure, $\omega(\mathbf{k}, \Omega) = \omega(-\mathbf{k}, -\Omega)$. In particular, this means that one can use the sign of Ω to control the unidirectional propagation of excitations: A wave packet will reverse direction when the sign of Ω is flipped. In the topological phase $|\Omega| > \Omega_c$, all of the considered networks have a gap-Chern invariant $C = \pm 1$, which we calculated using the numerical procedure outlined in Fukui et al. [33].

Generally, edge bands can be visualized by taking an infinite periodic crystal in 2D and restricting to a ribbon-like slice that is finite in one direction with open boundary conditions (**Figure 2G**). The resulting 1D crystal now possesses a one-dimensional band structure in which localized edge modes are directly visible. Mode localization can be measured by the participation ratio $\lambda = (\sum_n |u_n|^4)/(\sum_n |u_n|^2)^2$ of the eigenvector $\mathbf{u}(k)$. The ratio λ is large if the mode is localized to few elements of the vector, and small if it is spread over many elements of the vector.

For all three example networks from **Figure 1**, the corresponding 1D crystals exhibit two bands of localized modes in the bulk gap in the topological phase $|\Omega| > \Omega_c$ (**Figures 2B,D,F**). The two bands host wave packets with opposite group velocity $v_g = d\omega/dk$, and are localized at opposite edges of the semi-infinite ribbon system. They thus correspond to one single *chiral* edge excitation. The match between the bulk gap-Chern number $C = \pm 1$ and the number of edge excitations (more precisely, the difference between clockwise and counter-clockwise edge modes) is a direct manifestation of the celebrated bulk-boundary correspondence [32, 39].

We further note that although the existence of $|C|$ protected edge bands is guaranteed in the topological regime $|\Omega| > \Omega_c$, this does not preclude unprotected edge states in the trivial phase $|\Omega| < \Omega_c$. To illustrate this fact explicitly, consider the example in **Figures 2E,F**. The band structure for $\Omega = 0$ in **Figure 2E** is topologically trivial ($C = 0$) but exhibits features two localized edge bands, which are converted into the topologically protected bands in **Figure 2F** as one crosses the phase transition at finite $|\Omega| = \Omega_c > 0$.

All three networks analyzed in **Figures 1**, **2** have in common that they support only a single chiral edge mode, the direction of which can be reversed by changing the sign of Ω. Additional simulation scans suggest that this is typical of mechanical networks designed with the LRO scheme: Among all bandgap-designed networks that exhibited a topological transition, we never observed a case with $|C| > 1$. This empirical finding is consistent with results from previous studies which reported that larger Chern numbers are typically associated with materials that possess long-range interactions or with systems that are periodically quenched or driven [40]. Mechanical networks with long-range interactions could, in principle, be designed by introducing additional bonds that connect beyond the nearest neighbor unit cells. While certainly intriguing, such "non-local" networks are beyond the scope of the present study.

The wave packets hosted by the topological edge bands of our short-range MSNs can be excited dynamically by forcing a semi-infinite or a finite network near the boundary at a frequency inside the bulk gap. As a specific example showcasing this generic effect, we consider the mechanical network from **Figure 1C** and construct a finite realization consisting of 12 × 12 unit cells. To demonstrate the robustness of the topological modes, we remove three unit

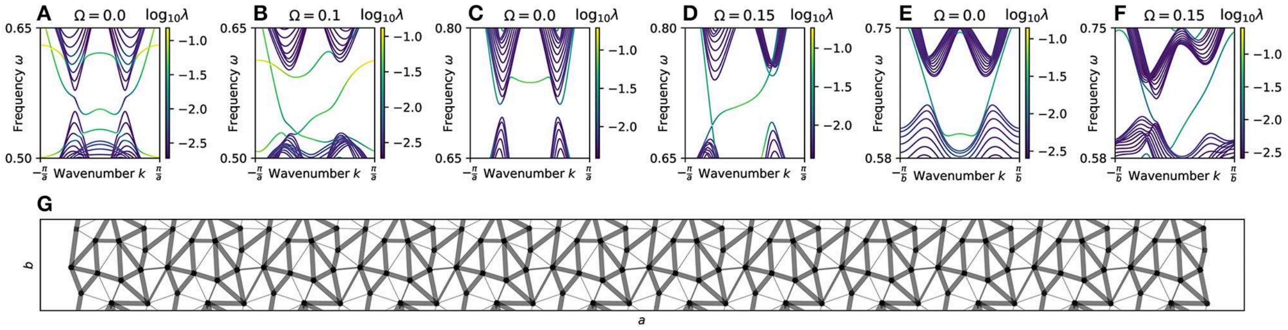

FIGURE 2 | Topologically protected edge bands. Considering the same networks as in **Figure 1**, we constructed ribbon-like 1D crystal realizations that are infinitely periodic in one lattice direction, and of finite extent (12 unit cells wide) with open boundary conditions in the other direction; see example in **(G)**, which corresponds to 12 horizontally concatenated units of the network in **Figure 1E** periodically continued along the vertical direction. **(A–F)** The resulting one-dimensional band structures consist of bulk bands that are delocalized (dark blue) and localized edge bands (green and yellow). All bands are colored according to the how localized the corresponding modes are, with the localization of a mode $\mathbf{u}(k)$ being measured by the participation ratio $\lambda = (\sum_n |u_n|^4)/(\sum_n |u_n|^2)^2$ where index n runs over all vertices in the unit cell of the ribbon. **(A,B)** Correspond to the optimized network topology in **Figure 1A**; **(C,D)** correspond to the network topology in **Figure 1C**; **(E,F)** correspond to the network topology in **Figure 1E**. Generically, networks designed via LRO can and will have localized edge modes even in the topologically trivial regime $|\Omega| < \Omega_c$, see **(A,C,E)**. However, when the topological phase transition is crossed at some nonzero rotation rate $|\Omega| = \Omega_c$, topologically protected localized bands appear as evident from **(B,D,F)**. We note that the frequency of rotation is always smaller than the gap frequency $\Omega^2 \ll \omega_{\text{gap}}^2$, justifying our approximation.

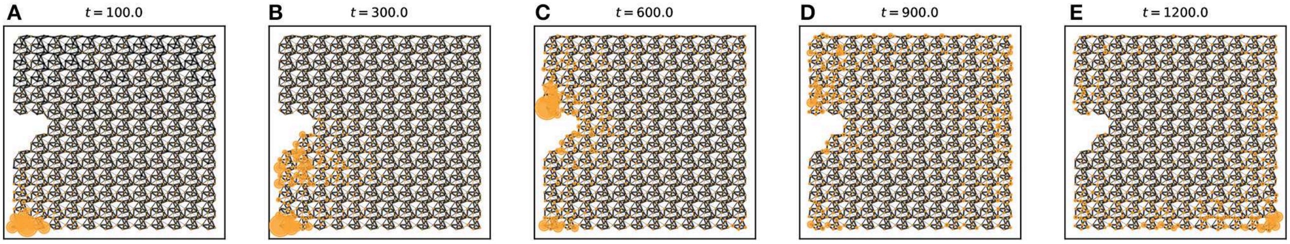

FIGURE 3 | Traveling excitation in a rotating mechanical Chern network. We simulated the dynamics of an MSN consisting of 12 × 12 unit cells as shown in **Figure 1C** and analyzed in **Figures 2C,D**. To create an edge defect, a number of unit cells was removed from the left boundary. Simulations of Equation (11) were performed in the topological regime with $\Omega = 0.15$; see also **Supplemental Video 1**. **(A)** Between $t = 0$ and $t = 150$, a single node in the bottom left corner is harmonically forced with a frequency $\omega = 0.71$ in the bulk gap; see **Figure 2D**. **(B–E)** Starting at $t = 150$, a localized excitation travels along the edge of the mechanical Chern insulator, moving over a local perturbation of the boundary.

cells from the left side boundary to introduce a boundary perturbation (**Figure 3A**). We then numerically simulate the forced dynamics

$$\ddot{\mathbf{u}} + K\mathbf{u} - 2\Omega\Gamma\dot{\mathbf{u}} = \mathbf{f}\sin(\omega t)\,h(t), \tag{11}$$

where the forcing vector $\mathbf{f} = (1, 0, \ldots, 0, 1, 0, \ldots, 0)^\top$ is zero except for the x and y components of one single node near the bottom left corner. We pick $\Omega = 0.15$ such that the network is in the topological phase, and $\omega = 0.71$ inside the bulk gap. The window function $h(t) = \sin(\pi t/150)\,\Theta(150 - t)$, where $\Theta(t)$ is the Heaviside Theta function, slowly turns on the forcing at $t = 0$, and turns it off entirely at $t = 150$. The forcing injects energy into the network at the frequency ω, which preferentially excites edge modes and creates a wave packet that travels unidirectionally along the edge of the network (**Figures 3B–E**, **Supplemental Video 1**). In particular, due to the topological protection of the edge modes, the precise shape of the boundary does not matter for the existence of these wave packets. Back-scattering modes are suppressed, and the wave packet is able to travel around the perturbation in the boundary (**Figures 3B,C**). As anticipated at the beginning of this section, the chirality of these wave packets is controlled by the sign of the rotation rate Ω (**Supplemental Video 2**). If the network is put in the topologically trivial regime, no edge modes exist and the energy injected by forcing does not create a chiral traveling wave packet (**Supplemental Video 3**).

The dynamical behavior described above is encoded in a set of eigenmodes $\mathbf{u}$ with $D\mathbf{u} = i\omega\mathbf{u}$ that are exponentially localized to the boundaries of the system, and where ω lies in the bulk gap. For the three networks shown in **Figure 1**, we again constructed finite realizations consisting of many unit cells in a square array, and computed the eigenmodes of the finite dynamical matrix D from Equation (9). For all three networks, we identified modes inside the bulk gap which were then found to be localized at the boundary (**Figures 4A–C**). To demonstrate exponential localization in each case, we analyzed a slice of the eigenmodes in y direction. Plotting

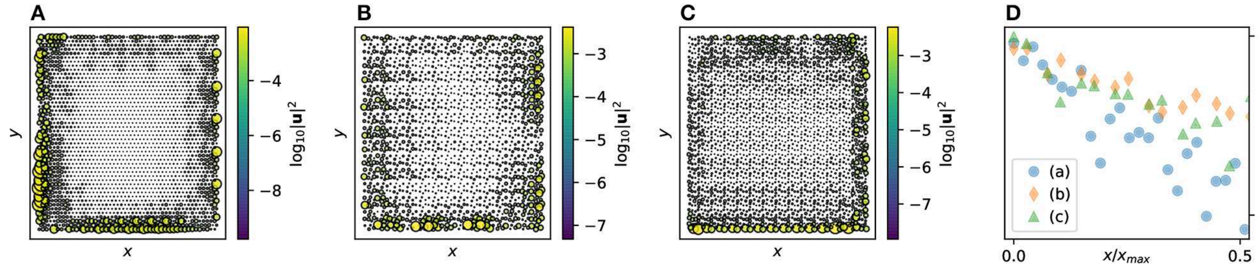

FIGURE 4 | Exponential localization of edge modes in rotating tuned mechanical Chern networks. We construct finite realizations consisting of **(A)** 12 × 12 and **(B,C)** 14 × 14 unit cells of the three networks from **Figure 1**, and plot a single eigenmode of the dynamical matrix D from Equation (9) with a frequency inside the bulk gap. The values of Ω are $\Omega = 0.1$ **(A)**, $\Omega = 0.15$ **(B,C)**, in the topological regime. The sizes and colors of the circles are proportional to the magnitude of the local node displacement $u_{i,x}^2 + u_{i,y}^2$, where $\mathbf{u} = (\mathbf{u}_x, \mathbf{u}_y)$ is the eigenmode. Each network hosts topological modes entirely localized at the boundary. **(D)** We consider a small slice in y direction of the networks from **(A–C)** and again plot the magnitude of the local node displacement. For all three networks, the magnitude decreases approximately exponentially in the bulk, demonstrating localization of the modes to the boundary.

the logarithm of the average node displacement $u_{i,x}^2 + u_{i,y}^2$ as a function of the x position of the node confirms an exponential decay of the node displacement with distance from the boundary (**Figure 4D**).

7. CONCLUSIONS

We have demonstrated the existence of topologically protected chiral edge modes in the gaps of *inversely designed* mechanical networks, and have characterized their dynamical properties. For the network realizations considered here, we found that band inversion near the gap was a robust predictor for a topological phase transition induced by sample rotation. The direction of rotation enables control over the chirality of the edge excitation, and topological protection of the edge excitations was confirmed in direct numerical simulations and through calculations of an appropriate Chern invariant.

We hope that the present work can serve as a stepping stone toward the precise inverse programming of topological features into discrete disordered metamaterials. Instead of constructing gapped materials on the basis of known lattices by using certain features of the band structure (e.g., band inversion) as indicators of potential topological transitions, we envision that Linear Response Optimization [24] may eventually allow the direct tuning of such properties by implementing the desired topological characteristics into the optimization objectives.

DATA AVAILABILITY STATEMENT

The datasets generated for this study are available on request to the corresponding author.

AUTHOR CONTRIBUTIONS

HR and JD conceived the study and wrote the paper. HR performed calculations, numerical simulations, and visualized results.

SUPPLEMENTARY MATERIAL

The Supplementary Material for this article can be found online at: https://www.frontiersin.org/articles/10.3389/fphy.2019.00178/full#supplementary-material

Supplemental Video 1 | Clockwise movement of edge excitation in a topological designed mechanical network.

Supplemental Video 2 | Counter-Clockwise movement of edge excitation in a topological designed mechanical network.

Supplemental Video 3 | No chiral edge excitation when the designed network is in the trivial phase.

REFERENCES

1. Süsstrunk R, Huber SD. Classification of topological phonons in linear mechanical metamaterials. *Proc Natl Acad Sci USA*. (2016) **113**:E4767–75. doi: 10.1073/pnas.1605462113
2. Asbóth JK, Oroszlány L, Pályi A. *A Short Course on Topological Insulators*, Lecture Notes in Physics, Vol. 919. Cham: Springer International Publishing (2016).
3. Kane CL, Lubensky TC. Topological boundary modes in isostatic lattices. *Nat Phys*. (2014) **10**:39–45. doi: 10.1038/nphys2835
4. Süssman DM, Stenull O, Lubensky TC. Topological boundary modes in jammed matter. *Soft Matt*. (2016) **12**:6079–87. doi: 10.1039/C6SM00875E
5. Susstrunk R, Huber SD. Observation of phononic helical edge states in a mechanical topological insulator. *Science*. (2015) **349**:47–50. doi: 10.1126/science.aab0239
6. Kane CL, Mele EJ. Z2 Topological order and the quantum spin hall effect. *Phys Rev Lett*. (2005) **95**:146802. doi: 10.1103/PhysRevLett.95.146802
7. Souslov A, van Zuiden BC, Bartolo D, Vitelli V. Topological sound in active-liquid metamaterials. *Nat Phys*. (2017) **13**:1091–4. doi: 10.1038/nphys4193
8. Nash LM, Kleckner D, Read A, Vitelli V, Turner AM, Irvine WTM. Topological mechanics of gyroscopic metamaterials. *Proc Natl Acad Sci USA*. (2015) **112**:14495–500. doi: 10.1073/pnas.1507413112

9. Mitchell NP, Nash LM, Irvine WTM. Realization of a topological phase transition in a gyroscopic lattice. *Phys Rev B*. (2018) **97**:100302. doi: 10.1103/PhysRevB.97.100302
10. Wang P, Lu L, Bertoldi K. Topological phononic crystals with one-way elastic edge waves. *Phys Rev Lett.* (2015) **115**:104302. doi: 10.1103/PhysRevLett.115.104302
11. Nagaosa N, Sinova J, Onoda S, MacDonald AH, Ong NP. Anomalous hall effect. *Rev Mod Phys*. (2010) **82**:1539–92. doi: 10.1103/RevModPhys.82.1539
12. Hasan MZ, Kane CL. Colloquium: topological insulators. *Rev Mod Phys*. (2010) **82**:3045–67. doi: 10.1103/RevModPhys.82.3045
13. Xia BZ, Jiao JR, Dai HQ, Yin SW, Zheng SJ, Liu TT, et al. Steerable sound transport in a 3D acoustic network. *Appl Phys Lett*. (2017) **111**:161903. doi: 10.1063/1.4985240
14. Wang YT, Luan PG, Zhang S. Coriolis force induced topological order for classical mechanical vibrations. *N J Phys*. (2015) **17**:073031. doi: 10.1088/1367-2630/17/7/073031
15. Kariyado T, Hatsugai Y. Manipulation of dirac cones in mechanical graphene. *Sci Rep.* (2016) **5**:18107. doi: 10.1038/srep18107
16. Agarwala A, Shenoy VB. Topological insulators in amorphous systems. *Phys Rev Lett.* (2017) **118**:236402. doi: 10.1103/PhysRevLett.118.236402
17. Shankar S, Bowick MJ, Marchetti MC. Topological sound and flocking on curved surfaces. *Phys Rev X*. (2017) **7**:031039. doi: 10.1103/PhysRevX.7.031039
18. Woodhouse FG, Ronellenfitsch H, Dunkel J. Autonomous actuation of zero modes in mechanical networks far from equilibrium. *Phys Rev Lett.* (2018) **121**:178001. doi: 10.1103/PhysRevLett.121.178001
19. Lee CH, Imhof S, Berger C, Bayer F, Brehm J, Molenkamp LW, et al. Topolectrical circuits. *Commun Phys*. (2018) **1**:39. doi: 10.1038/s42005-018-0035-2
20. Imhof S, Berger C, Bayer F, Brehm J, Molenkamp LW, Kiessling T, et al. Topolectricalcircuit realization of topological corner modes. *Nat Phys*. (2018) **14**:925–9. doi: 10.1038/s41567-018-0246-1
21. Kotwal T, Ronellenfitsch H, Moseley F, Stegmaier A, Thomale R, Dunkel J. Active topolectrical circuits. *arXiv:1903.10130 [Preprint]*.
22. Delplace P, Marston JB, Venaille A. Topological origin of equatorial waves. *Science*. (2017) **358**:1075–7. doi: 10.1126/science.aan8819
23. Christiansen RE, Wang F, Sigmund O. Topological insulators by topology optimization. *Phys Rev Lett.* (2019) **122**:234502. doi: 10.1103/PhysRevLett.122.234502
24. Ronellenfitsch H, Stoop N, Yu J, Forrow A, Dunkel J. Inverse design of discrete mechanical metamaterials. *Phys Rev Mater*. (2019) **3**:095201. doi: 10.1103/PhysRevMaterials.3.095201
25. Haldane FDM. Model for a quantum hall effect without Landau levels: condensed-matter realization of the parity anomaly. *Phys Rev Lett.* (1988) **61**:2015–8. doi: 10.1103/PhysRevLett.61.2015
26. Sáenz PJ, Pucci G, Goujon A, Cristea-Platon T, Dunkel J, Bush JWM. Spin lattices of walking droplets. *Phys Rev Fluids*. (2018) **3**:4–6. doi: 10.1103/PhysRevFluids.3.100508
27. Lubensky TC, Kane CL, Mao X, Souslov A, Sun K. Phonons and elasticity in critically coordinated lattices. *Rep Prog Phys.* (2015) **78**:073901. doi: 10.1088/0034-4885/78/7/073901
28. Chen BGG, Upadhyaya N, Vitelli V. Nonlinear conduction via solitons in a topological mechanical insulator. *Proc Natl Acad Sci USA*. (2014) **111**:13004–9. doi: 10.1073/pnas.1405969111
29. Tsamados M, Tanguy A, Goldenberg C, Barrat JL. Local elasticity map and plasticity in a model Lennard-Jones glass. *Phys Rev E*. (2009) **80**:026112. doi: 10.1103/PhysRevE.80.026112
30. Altland A, Zirnbauer MR. Nonstandard symmetry classes in mesoscopic normal-superconducting hybrid structures. *Phys Rev B*. (1997) **55**:1142–61. doi: 10.1103/PhysRevB.55.1142
31. Berry MV. Quantal phase factors accompanying adiabatic changes. *Proc R Soc A Math Phys Eng Sci*. (1984) **392**:45–57. doi: 10.1098/rspa.1984.0023
32. Hatsugai Y. Chern number and edge states in the integer quantum Hall effect. *Phys Rev Lett*. (1993) **71**:3697–700. doi: 10.1103/PhysRevLett.71.3697
33. Fukui T, Hatsugai Y, Suzuki H. Chern numbers in discretized brillouin zone: efficient method of computing (spin) hall conductances. *J Phys Soc Jpn*. (2005) **74**:1674–7. doi: 10.1143/JPSJ.74.1674
34. Byrd RH, Lu P, Nocedal J, Zhu C. A limited memory algorithm for bound constrained optimization. *SIAM J Sci Comput*. (1995) **16**:1190–208. doi: 10.1137/0916069
35. Xi W, Ku W. Non-necessity of band inversion process in two-dimensional topological insulators for bulk gapless states and topological phase transitions. *Phys Rev B*. (2017) **96**:201110. doi: 10.1103/PhysRevB.96.201110
36. Zhu Z, Cheng Y, Schwingenschlogl U. Band inversion mechanism in topological insulators: a guideline for materials design. *Phys Rev B*. (2012) **85**:235401. doi: 10.1103/PhysRevB.85.235401
37. Fu L, Kane CL. Topological insulators with inversion symmetry. *Phys Rev B*. (2007) **76**:045302. doi: 10.1103/PhysRevB.76.045302
38. Oza AU, Harris DM, Rosales RR, Bush JWM. Pilot-wave dynamics in a rotating frame: on the emergence of orbital quantization. *J Fluid Mech*. (2014) **744**:404–29. doi: 10.1017/jfm.2014.50
39. Mong RSK, Shivamoggi V. Edge states and the bulk-boundary correspondence in Dirac Hamiltonians. *Phys Rev B*. (2011) **83**:125109. doi: 10.1103/PhysRevB.83.125109
40. Xiong TS, Gong J, An JH. Towards large-Chern-number topological phases by periodic quenching. *Phys Rev B*. (2016) **93**:184306. doi: 10.1103/PhysRevB.93.184306

Conflict of Interest: The authors declare that the research was conducted in the absence of any commercial or financial relationships that could be construed as a potential conflict of interest.

frontiers in Physics

ORIGINAL RESEARCH
published: 03 December 2019
doi: 10.3389/fphy.2019.00204

Fast, Scalable, and Interactive Software for Landau-de Gennes Numerical Modeling of Nematic Topological Defects

Daniel M. Sussman[1,2]* *and Daniel A. Beller*[3]*

[1] Department of Physics, Syracuse University, Syracuse, NY, United States, [2] Department of Physics, Emory University, Atlanta, GA, United States, [3] Department of Physics, University of California, Merced, Merced, CA, United States

Numerical modeling of nematic liquid crystals using the tensorial Landau-de Gennes (LdG) theory provides detailed insights into the structure and energetics of the enormous variety of possible topological defect configurations that may arise when the liquid crystal is in contact with colloidal inclusions or structured boundaries. However, these methods can be computationally expensive, making it challenging to predict (meta)stable configurations involving several colloidal particles, and they are often restricted to system sizes well below the experimental scale. Here we present an open-source software package that exploits the embarrassingly parallel structure of the lattice discretization of the LdG approach. Our implementation, combining CUDA/C++ and OpenMPI, allows users to accelerate simulations using both CPU and GPU resources in either single- or multiple-core configurations. We make use of an efficient minimization algorithm, the Fast Inertial Relaxation Engine (FIRE) method, that is well-suited to large-scale parallelization, requiring little additional memory or computational cost while offering performance competitive with other commonly used methods. In multi-core operation we are able to scale simulations up to supra-micron length scales of experimental relevance, and in single-core operation the simulation package includes a user-friendly GUI environment for rapid prototyping of interfacial features and the multifarious defect states they can promote. To demonstrate this software package, we examine in detail the competition between curvilinear disclinations and point-like hedgehog defects as size scale, material properties, and geometric features are varied. We also study the effects of an interface patterned with an array of topological point-defects.

Keywords: Landau-de Gennes modeling, nematic, topological defect, numerical modeling, GPGPU

Edited by:
Uroš Tkalec,
University of Ljubljana, Slovenia

Reviewed by:
Douglas John Cleaver,
Sheffield Hallam University,
United Kingdom
Simon Čopar,
University of Ljubljana, Slovenia
Marco G. Mazza,
Max-Planck-Institute for Dynamics and Self-Organization, Max Planck Society (MPG), Germany

***Correspondence:**
Daniel M. Sussman
daniel.m.sussman@emory.edu
Daniel A. Beller
dbeller@ucmerced.edu

Specialty section:
This article was submitted to Soft Matter Physics, a section of the journal Frontiers in Physics

Received: *15 July 2019*
Accepted: *14 November 2019*
Published: *03 December 2019*

Citation:
Sussman DM and Beller DA (2019) Fast, Scalable, and Interactive Software for Landau-de Gennes Numerical Modeling of Nematic Topological Defects. Front. Phys. 7:204. doi: 10.3389/fphy.2019.00204

1. INTRODUCTION

Nematic liquid crystals' combination of fluidity and orientational order both underlies nematics' widespread technological applications and endows them with topological defects, localized breakdowns in the orientational order stabilized by the medium's broken symmetries. The topological defects of nematics have been integral to the study of liquid crystals since the field's infancy [1].

Besides their role as tabletop physical realizations of profound topological ideas, nematic topological defects—including disclination lines, point-like hedgehogs, and surface-bound boojums—are of great interest for their importance in nematic colloidal suspensions [2]. These composite materials, formed by suspensions of colloidal particles or nanoparticles in nematics, promise new routes to directed self-assembly and self-organization. Nanoparticles in nematics are pushed by elastic forces to assemble in pre-existing defect lines, meaning that sculpted disclinations provide a path to controlled nanoparticle assembly. Applications include plasmonic properties for metamaterials [3, 4], molecular self-assembly [5], and quantum-dot assembly in microshells [6, 7]. Even greater complexity arises in the cases of colloidal particles in the size range of tens of nanometers to several microns, which often have companion topological defects and which interact through forces mediated by nematic elasticity. Self-assembled structures of colloidal particles with companion defects include bound pairs, chains [2, 8] and triclinic 3D crystals [9]; with the aid of laser tweezers, other configurations such as 3D crystals with tetragonal symmetry [10] and sophisticated disclination knots [11–14] can be stabilized. Tailored self-assembled colloidal structures hold promise as optical metamaterials for photonics applications, such as photonic bandgap crystals and microlasers [15–18].

Nematic defect configurations can also be controlled by non-trivial boundary surfaces [19]. Substrate patterning strategies include topographic variations such as "lock-and-key" docking sites for colloidal particles [20–22] and chemical patterning where the boundary condition shifts abruptly [23, 24]. Complex director fields, including disclinations, can be prescribed on a substrate by photoalignment [25] or by scribing with an atomic force microscope [26]. Confinement in geometries such as capillaries [27], droplets [28], shells [29], and thin films [30] produces a wealth of point- and line-defect behaviors stabilized by topology and energetics.

The rapidly expanding variety of experimentally created nematic defect configurations has benefited greatly from the understanding provided by robust modeling approaches. One set of approaches is based on the Frank-Oseen elastic free energy, which penalizes deformations of the nematic director $\hat{n}(\mathbf{x})$, and which in its simplest form reads

$$\mathcal{F}_{\mathrm{FO}}^{(1)} = \frac{K}{2} \int dV \sum_{i,j=1}^{3} (\partial_i n_j)^2. \tag{1}$$

The superscript (1) refers to the approximation of a single elastic constant K in this expression. However, the $\hat{n} = -\hat{n}$ symmetry of nematics presents challenges for this model in the presence of disclinations with half-integer winding number, especially if their locations are not known beforehand.

This difficulty is resolved by the Landau-de Gennes (LdG) model, the theoretical approach which is the focus of this work and which we review in section 2. The LdG framework takes as its order parameter the second-rank traceless nematic order tensor $Q_{ij}(\mathbf{x})$, and is well-suited to modeling arbitrary disclination configurations, as well as biaxial nematics and the blue phases [15, 31]. While little is known analytically about free energy minimizers in LdG theory in any but the simplest geometries [32, 33], numerical minimization of the LdG free energy has been fruitfully applied over a wide range of systems [10–12, 15, 21, 34–48]. Additionally, flow dynamics of nematics, including active nematic systems, can be modeled by supplementing the LdG free energy with hydrodynamical equations as formulated by Beris and Edwards [49] or by Qian and Sheng [50] and solved by methods such as lattice Boltzmann [51–55], multiparticle collision dynamics and related off-lattice methods [56–58], or finite difference and finite element approaches [59, 60]. Some methods incorporate a fast relaxation of the momentum compared to the director, to account for the separation in time scales for these relaxations in typical molecular liquid crystals [52, 61].

The broad usefulness of the LdG theory goes hand in hand with a significant limitation of scale: Resolving defects at *a priori* unknown locations requires the simulation lattice spacing to be comparable to or smaller than the size of the defect core, the region in which nematic order breaks down, which in thermotropic nematics is typically a few nanometers. This is often thousands of times smaller than the individual micron-scale colloidal particles of interest. Therefore, a faithful rescaling of the experimental system in numerics would require of order at least 10^9 lattice sites even for configurations involving only a small number of such colloids.

Accessing such experimentally relevant lattice sizes presents computational challenges not often seen in the simulations of glassy and polymeric soft matter systems. The demands on system memory quickly become prohibitive: simply maintaining the five independent degrees of freedom at each lattice site and storing the necessary change in those variables from one minimization step to the next at 10^9 lattice sites requires 80 GB—more than on most current commodity desktops and larger than the memory capacity of any CUDA-capable GPU[1]. Additionally, there is a large direct computational cost of even simple manipulations acting on so many degrees of freedom; this contributes to the significant wall-time required for most numerical energy minimizations and presents challenges for efficient exploration of parameter spaces and colloidal particle positions.

Consequently, LdG numerical modeling is typically applied to systems significantly scaled down, with respect to a fixed defect core size, as compared with the experiments that they are intended to model. While important qualitative insights about defects and director fields can often be obtained by scaling down the experimental dimensions, the change in size ratios makes quantitative prediction challenging. There can also be major qualitative differences. The most well-known of these is the form of the companion defect to a particle with homeotropic (normal) anchoring: Micron-scale particles typically have hyperbolic hedgehog companions (in the absence of confinement or external fields) [2], whereas particles in the few hundred nm or smaller size range have disclination loops in the "Saturn ring" configuration [62, 63]. This constitutes

---

[1] As of July, 2019.

a major challenge in modeling systems with multiple colloid-hedgehog pairs. Experimental work on high-aspect ratio colloidal particle shapes observes both hedgehogs and disclination loops, but numerical modeling has been limited to the line defect case [35, 38–43, 64, 65]. Adaptive mesh refinement in finite-element simulations can help to avoid computational and memory expense in regions not near defects [66] but typically does not remove the need to scale down.

In this work we present an open-source finite difference-based implementation of LdG free energy minimization with non-trivial boundary conditions, "*openQmin*" [67], using a combination of approaches designed to address the challenges described above. It is written for heterogeneous CPU and GPU operation to target two complementary research goals. First, it offers a user-friendly GUI environment for rapid prototyping of topological defect configurations as a function of liquid crystal parameters, boundary geometry, and the presence of colloidal inclusions. Simultaneously, it targets large-scale systems using OpenMPI [68] to support parallelization across both CPU and GPU resources to scale up to the supra-micron length scales of experimental relevance. We employ efficient minimization algorithms, such as the Fast Inertial Relaxation Engine (FIRE) method, to maintain reasonable convergence times even for large-scale parallelized calculations.

The remainder of the paper is structured as follows. We begin with a review of the LdG theory in section 2. Section 3 lays out our numerical approach, first discretizing the LdG theory for a finite-difference method, and then outlining our use of minimization algorithms and OpenMPI parallelization. In section 4 we present two sample studies demonstrating the effectiveness of this approach. We first perform a classic analysis of the companion defects to homeotropic spherical particles at varying system sizes, and then examine the effects of a boundary patterned with surface disclinations in a supra-micron-scale system. Section 5 briefly describes the GUI version of *openQmin* with an example of the rapid prototyping workflow it enables. Finally, in section 6, we discuss both the range of use we foresee for *openQmin* and some future directions for additional physics that could be studied in this framework.

2. LANDAU DE-GENNES THEORY FOR NEMATIC LIQUID CRYSTALS

Here we give a brief overview of those aspects of the LdG theory used in our numerical approach. The theory is of course well-established [69] and its use in a finite difference numerical free energy minimization scheme is described in several sources; the reader is directed to Ravnik and Žumer [47] for a thorough explanation.

Uniaxial nematic liquid crystals are characterized by orientational ordering of nematogens (molecules or suspended anisotropic particles) along a director, $\hat{n}$, which is a unit vector with the identification $\hat{n}$ = -$\hat{n}$. To respect that symmetry consistently, which is important at disclinations of half-integer winding number, we take as order parameter not a director but a second-rank tensor. This is the traceless, symmetric tensor field $\mathbf{Q}(\mathbf{x})$, whose lattice discretization is the fundamental object of the LdG modeling approach. $\mathbf{Q}$ is related to $\hat{n}$ by [70]

$$Q_{\alpha\beta} = \frac{3}{2}S\left(n_\alpha n_\beta - \frac{1}{3}\delta_{\alpha\beta}\right) + \frac{1}{2}S_B(m_\alpha m_\beta - l_\alpha l_\beta). \qquad (2)$$

Here, S is the degree of uniaxial nematic order, and S_B is the degree of biaxial order distinguishing a preferred direction $\hat{m} \equiv -\hat{m}$, perpendicular to $\hat{n}$, from $\hat{l} \equiv \hat{n} \times \hat{m}$. The nematic director can be recovered as the eigenvector corresponding to the largest eigenvalue of $\mathbf{Q}$, which equals S. Most nematics are unaxial, so the equality $S_B = 0$ is true in the absence of distortions and represents a good approximation away from defects. In this uniaxial limit, Equation (2) reduces to

$$Q_{\alpha\beta} = \frac{3}{2}S\left(n_\alpha n_\beta - \frac{1}{3}\delta_{\alpha\beta}\right). \qquad (3)$$

2.1. Phenomenological Free Energy Density

The LdG theory constructs a phenomenological free energy $\mathcal{F}$ as a functional of $\mathbf{Q}(\mathbf{x})$. We can write this functional schematically as [47, 70]:

$$\mathcal{F}[\mathbf{Q}] = \int_V \left(f_{\text{bulk}} + f_{\text{distortion}} + f_{\text{external}}\right) dv + \sum_\alpha \int_{S_\alpha} \left(f^\alpha_{\text{boundary}}\right) ds \qquad (4)$$

The first integral, over the volume of the nematic, has three free energy density terms incorporating respectively the energetic costs arising from deviations away from the thermodynamically preferred degree of nematic order $S = S_0$, from elastic distortions, and from external fields. The second integral, summing over all boundary surfaces S_α in contact with the nematic, incorporates the anchoring energy associated with each interface, including the surfaces of colloidal particles; its form may be different for different surfaces. We address each component in turn.

2.1.1. Bulk Free Energy

The first free energy density term in Equation (4) gives a Landau free energy for the isotropic-nematic phase transition, written in terms of rotational invariants of $\mathbf{Q}$ in a Taylor expansion about the isotropic, $\mathbf{Q} = 0$ state [71]:

$$f_{\text{bulk}} = \frac{A}{2}\text{tr}\left(\mathbf{Q}^2\right) + \frac{B}{3}\text{tr}\left(\mathbf{Q}^3\right) + \frac{C}{4}\left(\text{tr}\left(\mathbf{Q}^2\right)\right)^2. \qquad (5)$$

The parameter $A \propto (T - T^*_{NI})$, where T^*_{NI} is the temperature at which the isotropic phase is destabilized. In the uniaxial limit f_{bulk} becomes a polynomial in the degree of order,

$$f_{\text{bulk}} = \frac{3}{4}AS^2 + \frac{1}{4}BS^3 + \frac{9}{16}CS^4, \qquad (6)$$

which is minimized either by $S = 0$ or by

$$S = S_0 \equiv \frac{-B + \sqrt{B^2 - 24AC}}{6C}. \qquad (7)$$

In the nematic phase, the absolute value of

$$f_0 \equiv f_{\text{bulk}}(S = S_0) \tag{8}$$

provides a free energy penalty per unit volume to the melted cores of defects, where $S \to 0$.

2.1.2. Distortion Free Energy

The distortion free energy density models the elasticity of the nematic phase, and represents the LdG counterpart to the Frank-Oseen free energy density. The latter, in full generality up to second derivatives of $\hat{n}$, is

$$\begin{aligned} f_{\text{FO}} = \frac{1}{2}\big\{&K_1(\nabla\cdot\hat{n})^2 + K_2(\hat{n}\cdot(\nabla\times\hat{n}) + q_0)^2 + K_3|(\hat{n}\cdot\nabla)\hat{n}|^2 \\ &+K_{24}\nabla\cdot[(\hat{n}\cdot\nabla)\hat{n} - \hat{n}(\nabla\cdot\hat{n})]\big\}. \end{aligned} \tag{9}$$

The parameters in this expression are the splay (K_1), twist (K_2), bend (K_3), and saddle-splay (K_{24}) elastic constants, and the spontaneous chiral wavenumber q_0 which is non-zero in the cholesteric and blue phases. Other common conventions for the saddle-splay energy density replace K_{24} in Equation (9) by either $2K_{24}$ or $2(K_2 + K_{24})$. Equation (9) reduces to Equation (1) under the "one-constant approximation" $K_1 = K_2 = K_3 = K_{24} \equiv K$ and $q_0 = 0$. The one-constant approximation is a reasonable simplification for many molecular liquid crystals, where K_1, K_2, and K_3 typically differ by less than a factor of 5 [72, 73].

The most general form of $f_{\text{distortion}}$ that we employ, following Poniewierski and Sluckin [74], Mori et al. [48], and Mottram and Newton [70], includes all gradient terms of quadratic order in $\mathbf{Q}$ allowed by symmetry, plus one term at cubic order:

$$\begin{aligned} f_{\text{distortion}} \;=\; &\frac{L_1}{2}\frac{\partial Q_{ij}}{\partial x_k}\frac{\partial Q_{ij}}{\partial x_k} + \frac{L_2}{2}\frac{\partial Q_{ij}}{\partial x_j}\frac{\partial Q_{ik}}{\partial x_k} + \frac{L_3}{2}\frac{\partial Q_{ik}}{\partial x_j}\frac{\partial Q_{ij}}{\partial x_k} \\ &+ \frac{L_4}{2}\epsilon_{lik}Q_{lj}\frac{\partial Q_{ij}}{\partial x_k} + \frac{L_6}{2}Q_{lk}\frac{\partial Q_{ij}}{\partial x_l}\frac{\partial Q_{ij}}{\partial x_k}, \end{aligned} \tag{10}$$

where Einstein summation over repeated indices is implied, and ϵ is the Levi-Civita tensor. Equation (10) corresponds in the uniaxial limit to Equation (9) with the identifications [48]

$$\begin{aligned} L_1 &= \frac{2}{27S^2}\left(K_3 - K_1 + 3K_2\right), \\ L_2 &= \frac{4}{9S^2}\left(K_1 - K_{24}\right), \\ L_3 &= \frac{4}{9S^2}\left(K_{24} - K_2\right), \\ L_4 &= -\frac{8}{9S^2}q_0K_2, \\ L_6 &= \frac{4}{27S^3}(K_3 - K_1). \end{aligned}$$

The one-constant approximation in the absence of spontaneous chiral ordering sets $L_2 = L_3 = L_4 = L_6 = 0$, leaving the much simpler and more computationally efficient form

$$f^{(1)}_{\text{distortion}} = \frac{L_1}{2}\frac{\partial Q_{ij}}{\partial x_k}\frac{\partial Q_{ij}}{\partial x_k}, \tag{11}$$

which corresponds in the uniaxial limit to Equation (1) with $L_1 = 2/(9S^2)K$.

Taking this simpler form of the distortion energy density, we estimate the defect core size by considering a distorted uniaxial nematic configuration at $S = S_0$ with $\hat{n}$ varying with typical gradient $1/\ell$. Roughly speaking, the energy well depth f_0 (Equation 8) gives the threshold value for $f_{\text{distortion}}$ at which distortions become so energetically costly that a local melting of nematic order occurs instead. This length $\ell = \xi_N$, the nematic correlation length (or coherence length), sets the size of the defect core:

$$\xi_N \sim \sqrt{L_1/|f_0|}. \tag{12}$$

2.1.3. External Fields Free Energy

The response of the nematic to an external magnetic field $\mathbf{H}$ or an external electric field $\mathbf{E}$ is modeled by the free energy density term

$$f_{\text{external}} = -\tfrac{1}{3}\mu_0 H_i\Delta\chi Q_{ij}H_j - \tfrac{1}{3}\varepsilon_0 E_i\Delta\varepsilon Q_{ij}E_j \tag{13}$$

where $\Delta\chi$ and $\Delta\varepsilon$ are the anisotropic parts (difference in principal values corresponding to $\hat{n}$ and its perpendicular directions) of the magnetic susceptibility tensor and dielectric tensor, respectively [34], and μ_0 and ε_0 are respectively the magnetic permeability and electric permittivity of free space. (We omit here the terms for the isotropic parts of these tensors, as they do not couple to $\mathbf{Q}$). In the uniaxial limit, the right-hand side becomes $-\frac{1}{2}S\mu_0\Delta\chi(\mathbf{H}\cdot\hat{n})^2 - \frac{1}{2}S\varepsilon_0\Delta\varepsilon(\mathbf{E}\cdot\hat{n})^2$ (again dropping isotropic terms with no coupling to $\hat{n}$). Positive $\Delta\chi$ or $\Delta\varepsilon$ will favor alignment of $\hat{n}$ with $\mathbf{H}$ or $\mathbf{E}$.

2.1.4. Boundary Free Energy

Boundary surfaces, including the surfaces of embedded colloidal particles, generally impose an anchoring surface energy density f_{boundary} representing the surface tension's dependence on the director at the surface. In terms of the director, a common modeling choice for the anchoring energy is the Rapini-Papoular form $-\frac{1}{2}W^{\alpha}_{\text{RP}}(\hat{\nu}^{\alpha}\cdot\mathbf{n})^2$ where $\hat{\nu}^{\alpha}$ is the surface normal vector and $|W^{\alpha}|$ is the anchoring strength of surface α [75]. Homeotropic (normal) anchoring follows from $W_{\text{RP}} > 0$, whereas $W_{\text{RP}} < 0$ creates degenerate planar anchoring, which equally favors every direction perpendicular to $\hat{\nu}^{\alpha}$. The same anchoring functional can favor a different anchoring direction, for example an in-plane direction in the case of oriented planar anchoring, using $W_{\text{RP}} > 0$ with the replacement of $\hat{\nu}^{\alpha}$ by the favored direction.

In LdG theory, for homeotropic or other oriented anchoring, the Rapini-Papoular form is generalized as the Nobili-Durand surface anchoring form [76],

$$f^{\alpha}_{\text{boundary}} = W^{\alpha}_{\text{ND}}\text{tr}\left((\mathbf{Q} - \mathbf{Q}^0)^2\right) = W^{\alpha}_{\text{ND}}(Q_{ij} - Q^{\alpha}_{ij})(Q_{ij} - Q^{\alpha}_{ij}), \tag{14}$$

where $W^{\alpha}_{\text{ND}} > 0$ is the anchoring strength of surface α and the surface-preferred $\mathbf{Q}$-tensor, $\mathbf{Q}^{\alpha}$, is usually taken to be $Q^{\alpha}_{ij} = \frac{3}{2}S_0(n^{\alpha}_i n^{\alpha}_j - \frac{1}{3}\delta_{ij})$, with $\hat{n}^{\alpha} = \hat{\nu}^{\alpha}$ or some other surface-preferred director.

For degenerate planar anchoring, the Nobili-Durand form is not suitable, and we use instead the following free energy due to Fournier and Galatola [77]:

$$f^{\alpha}_{\text{boundary}} = W^{\alpha}_{\text{FG}}(\tilde{Q}_{ij} - \tilde{Q}^{\perp}_{ij})(\tilde{Q}_{ij} - \tilde{Q}^{\perp}_{ij}), \tag{15}$$

where $\tilde{Q}_{ij} = Q_{ij} + S_0\delta_{ij}/2$ and $\tilde{\mathbf{Q}}^{\perp}$ is the projection onto $\hat{\nu}^{\alpha}$ via $\tilde{Q}^{\perp}_{ij} = P_{ik}\tilde{Q}_{k\ell}P_{\ell j}$ for $P_{ij} = \delta_{ij} - \nu^{\alpha}_i \nu^{\alpha}_j$. Assuming $\mathbf{Q}$ is uniaxial with $S = S_0$, the Rapini-Papoular anchoring is recovered with $W^{\alpha}_{\text{RP}} = 9S_0^2 W^{\alpha}_{\text{ND,FG}}$.

3. NUMERICAL APPROACH

3.1. Overview

The primary contribution of this work is the presentation of an open-source numerical implementation that exploits the embarrassingly parallel structure of the lattice discretization of the above phenomenological theory. Our implementation, combining CUDA/C++ [78] and OpenMPI [68], was written with extreme flexibility in mind to allow users to accelerate simulations large and small using combinations of available CPU and GPU resources in either single- or multiple-core configurations.

The foundation of the software package, "dDimensionalSimulation," is a set of generic classes meant to execute simulations of N interacting units, each consisting of d scalar degrees of freedom, using data structures appropriate for efficient execution on either CPU or GPU resources. These generic classes serve as the template for *models* which instantiate the dN total degrees of freedom, *forces* which compute interactions between degrees of freedom, *updaters* which can change the degrees of freedom (e.g., by implementing equations of motion), and *simulations* which tie objects of these various types together. The present work focuses on implementing the details of these classes to carry out lattice-based LdG modeling to find energy-minimized configurations of equilibrium nematics in the presence of various boundary conditions. The general structure we have employed was chosen to allow flexibility in future development, for example to derive new model classes which include not only the $\mathbf{Q}$-tensor but also density and velocity degrees of freedom, as would be appropriate for modeling active nematic systems [53–55, 60].

In addition to writing efficient code to carry out the required lattice-based minimizations of the $\mathbf{Q}$-tensor field in a domain, we also advocate the use of the graphical user interface (GUI) we developed to rapidly prototype and explore the effects of particular boundaries, colloidal inclusions, and external fields that may be of experimental interest. The GUI allows a wide variety of user operations—adding boundary objects at any stage of the simulation, starting and stopping minimization, adding or removing external fields at will—all while visualizing the resulting defect structure and recording configurational details. A snapshot of the GUI is shown in **Figure 1**, and more details of the available features are given in section 5. We envision that this capability will allow for rapid prototyping of experimental geometries in the search for particular controllable defect states; running on a single GPU allows real-time visualization of lattices in the low-millions of total sites. We have also included several example files that use the code in a non-GUI mode; these can then use OpenMPI to parallelize across either CPU or GPU resources to scale up to lattices that represent supra-micron-scale liquid crystal systems.

3.2. Lattice Discretization and Energy Minimization

The finite difference lattice calculations employed in this work use a regular cubic lattice discretization of space, with a $\mathbf{Q}$-tensor defined at each site $\vec{x} = \{x, y, z\}$. The lattice spacing Δx can be related to physical quantities through a natural non-dimensionalization of the free energy density, $\tilde{f} \equiv f/|A|$, which implies a non-dimensionalization of the elastic constants $\tilde{L}_i \equiv L_i/(|A|\Delta x^2)$. In the one-constant approximation, we thus have $\Delta x^2 = L_1/(\tilde{L}_1|A|)$. In this work we set $\tilde{L}_1 = 2.32$. To model 5CB, following Ravnik and Žumer [47] we take $A = -0.172 \times 10^6\,\text{J/m}^3$, $B = -2.12 \times 10^6\,\text{J/m}^3$, $C = 1.73 \times 10^6\,\text{J/m}^3$, and $K = L_1 \cdot 9S_0^2/2 = 1 \times 10^{-11}\,\text{N}$ where $S_0 \approx 0.53$. These give a lattice spacing of $\Delta x \approx 4.5\,\text{nm}$, which is at the few-nm scale of the defect core in 5CB. Note that the non-dimensionalization of all constants by an energy scale $|A|$ and a length Δx is implicitly made for all values in *openQmin*, including in the GUI.

The symmetry and tracelessness of $\mathbf{Q}$ leaves five independent degrees of freedom, which we take to be $\vec{q} \equiv \{Q_{xx}, Q_{xy}, Q_{xz}, Q_{yy}, Q_{yz}\}$ at each of the N lattice sites in the simulation domain. We write the local free energy density $f(\vec{x})$ in terms of these five independent variables, so that the symmetry and tracelessness of $\mathbf{Q}$ are automatic (rather than being maintained by projection operations following update steps [47]). We also label each site with an integer "type," indicating whether it is a bulk site, a boundary site, or a site inside an object (for instance, the interior of a colloidal inclusion, or part of a bounding surface), depending on the geometry of the problem. Only bulk and boundary sites are "simulated sites," meaning $\mathbf{Q}$ is defined there.

We discretize the total free energy, $\mathcal{F} = \sum_{i=1}^{N} f(\vec{x}_i)$, using a finite-difference approach over the $5N$ independent variables. For the distortion terms we allow the user to select either the more general expression, Equation (10), or the more computationally efficient expression of Equation (11). For the terms in $f_{\text{distortion}}$ which contain spatial first derivatives of $\mathbf{Q}$, we consider first-order forward and backward finite difference approximations,

$$\left(\frac{\partial Q_{ij}}{\partial x_k}\right)(\vec{x}) \approx \begin{cases} Q_{ij}(\vec{x} + \hat{x}_k) - Q_{ij}(\vec{x}) & \text{(forward)} \\ Q_{ij}(\vec{x}) - Q_{ij}(\vec{x} - \hat{x}_k) & \text{(backward).} \end{cases} \tag{16}$$

Here $\hat{x}_k$ is the unit vector in the x_k direction, and $\vec{x}$ is the site where the calculation is taking place. The choice of a regular cubic lattice makes these derivative approximations straightforward to calculate. The forward and backward finite differences are each compatible with the simulation domain only if $(\vec{x} + \hat{x}_k)$, $(\vec{x} - \hat{x}_k)$, respectively, are simulated (bulk or boundary) sites. We then take, as the discretized expression of f, Equation (4) averaged over all forward and backward finite difference expressions for each of $k = 1, 2, 3$ that are allowed by the geometry of the simulation

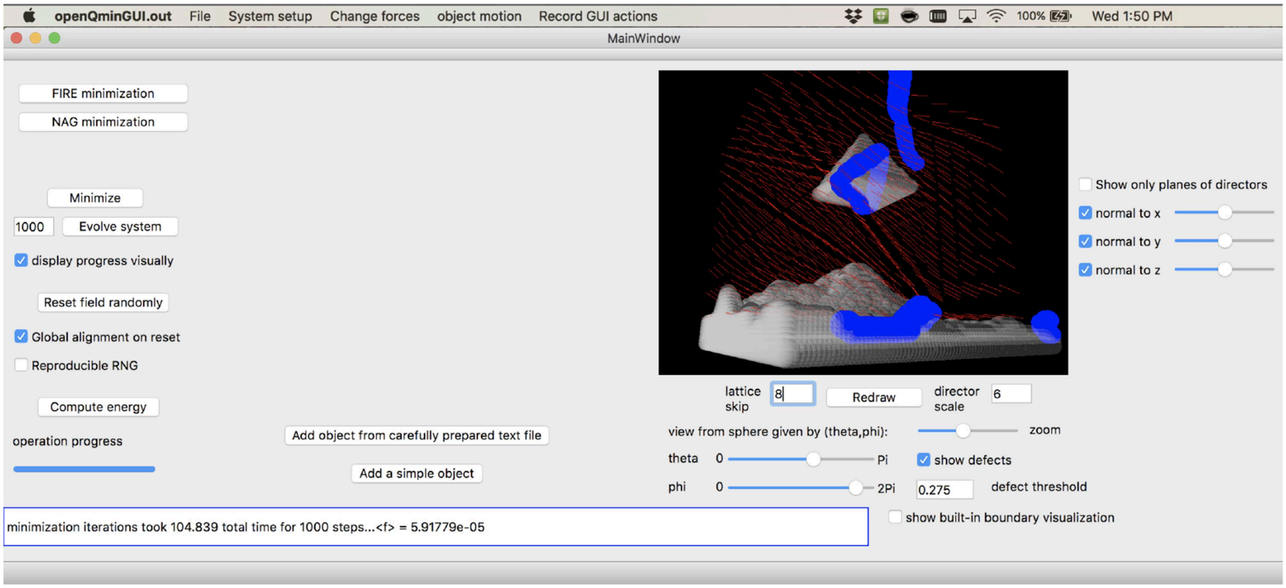

1000 Evolve system

☑ display progress visually

☑ Global alignment on reset

☐ Reproducible RNG

☐ Show only planes of directors

☑ normal to x

☑ normal to y

☑ normal to z

lattice skip: 8

director scale: 6

theta 0 — Pi

phi 0 — 2Pi

☑ show defects

defect threshold: 0.275

☐ show built-in boundary visualization

minimization iterations took 104.839 total time for 1000 steps...<f> = 5.91779e-05

FIGURE 1 | Snapshot of the graphical user interface provided by *openQmin*, here shown simulating the defect structure near a pyramidal colloid above a topographically non-trivial boundary, all with oriented anchoring along user-specified directions to approximately model homeotropic surfaces.

domain. A bulk site, therefore, has a local free energy averaged over 2^3 such combinations, while a boundary site has fewer. We use these averages over different expressions for the finite differences, rather than using a single centered finite difference formula $(\partial Q_{ij}/\partial x)(\vec{x}) \approx \frac{1}{2}[Q_{ij}(\vec{x}+\hat{x}_k)-Q_{ij}(\vec{x}-\hat{x}_k)]$, because using the latter form in Equation (11) produces no terms coupling $Q_{ij}(\vec{x})$ to its nearest neighbors, of the form $Q_{ij}(\vec{x})Q_{ij}(\vec{x}\pm\hat{x}_k)$. This use of the centered first derivative expression would therefore create an artificial (and undesirable) lattice doubling effect in our approach, with even sites and odd sites evolving independently. For curved boundaries such as on spherical colloidal particles, well-known inaccuracies are introduced in the finite difference calculations by the discretization of boundaries as sites in the cubic lattice [79]. Specifically, errors of order $O(\Delta x)$ in $Q_{ij}(\vec{x})$ are introduced, leading to truncation errors of $O(1)$ (which do not diverge as the lattice spacing is refined) in the first derivative approximations of Equation (16).

Finally, we minimize $\mathcal{F}$ as a cost function over the $5N$ independent variables $q_i(\vec{x}_j)$, $i = 1, \ldots, 5$, $j = 1, \ldots, N$. The gradient of $\mathcal{F}$ in this $5N$-dimensional space is calculated by explicitly differentiating the expression for $\mathcal{F}$ with respect to each $q_i(\vec{x}_j)$ degree of freedom. This explicit differentiation of a cost function is an alternative to the approach of analytically deriving local forces (molecular fields) from the Euler-Lagrange equations, projecting to recover symmetry and tracelessness, and then discretizing those expressions. While the Euler-Lagrange equations have separate forms for the bulk and the boundaries, in the approach used here forces are derived from the cost function in formally the same way for bulk and boundary sites.

We emphasize that by discretizing space, we can directly map the problem of solving the LdG partial differential equations to finding the minima of a complex energy landscape (where the **Q**-tensors on each lattice site are the degrees of freedom). For instance, many PDE solvers implement steepest descent relaxation, which can be directly interpreted as overdamped molecular dynamics at zero temperature. This allows us to turn to the wealth of existing algorithmic approaches from the field of non-linear optimization, including minimization techniques such as quasi-Newton methods (conjugate), gradient descent, and momentum-based techniques such as Nesterov's accelerated gradient [80]. Since our aim is to be able to scale up to large systems, we ignore minimizers which require second-order derivatives of the cost function, and we find that even limited-memory quasi-Newton methods such as L-BFGS impose too-strong a memory requirement for many of our purposes. Additionally, while conjugate gradient is appealing in having only marginal extra memory requirements and being much faster than simple gradient descent, it involves frequent line searches that require expensive repeated evaluations of the free energy density and imposes additional parallelization costs.

Thus, although we have implemented many of the above-named minimizers in *openQmin*, we focus our attention on the use of the Fast Inertial Relaxation Engine (FIRE) method of energy minimization [81]. FIRE falls into the class of "gradient plus momentum"-style minimization algorithms, and it additionally rescales the "velocity" (fictitious additional variables introduced to make the analogy with molecular dynamics even more complete and corresponding to the velocities at which the **Q**-tensor components change) of the degrees of freedom and adaptively changes the size of the time step itself based on the behavior of the force and velocity during the most recent update. For convex optimization problems the addition of inertia can be proven to enhance convergence [82], although for more complex energy landscapes

Algorithm 1: Pseudocode for FIRE minimization [81].

```
Initialize Q-tensors at each lattice site, set velocities $v_i$ to zero;
while Minimization criteria not satisfied do
    Update $q_i(\vec{x}_j)$, force $= -\nabla\mathcal{F}$, and $v_i$ using a velocity Verlet step;
    Calculate power, $P$, as the dot product of the force and velocity vectors;
    Rescale velocity by a parameter $\alpha$ which sets the inertia of the degrees of freedom;
    if $P > 0$ then
        if $P$ has been positive for more steps than a threshold, $N_{min}$ then
            Increase the time step size and increase $\alpha$.
        end
    else
        Decrease the time step size, reset velocities to zero, reset $\alpha$ to initial value;
    end
end
```

in general little can be proven. Thus, while it is a heuristic approach, FIRE has been shown to be competitive with (or even faster than) conjugate gradient minimization [81, 83, 84], all while maintaining an extremely light additional memory footprint and being highly amenable to parallelization across multiple cores or multiple GPU units. Note that FIRE was originally developed with atomistic simulations in mind, but it is increasingly being used more generally, including in the solution of PDEs [85] and in machine learning applications [86]. By the straightforward mapping mentioned above we are able to directly apply the pseudocode presented in Algorithm 1.

We first demonstrate this efficient minimization in **Figure 2**, where we compare the system energy and average norm of the force on the degrees of freedom during the minimization of a lattice of $N = 250^3$ sites in a cubic geometry with periodic boundary conditions. To make a fair comparison, we have performed both a FIRE and a gradient descent (GD) minimization on the same system using separately tuned minimization parameters for each algorithm. We use the same hardware for each simulation, and report the minimization progress in terms of the wall-clock time taken. Although it is sometimes common to report efficiency in such comparisons in units of function calls, for algorithms with very different numbers of arithmetic operations (each FIRE iteration requires more than twice the number of arithmetic operations compared to GD) such comparisons are often misleading.

As **Figure 2** makes clear, even in the trivial case of finding the uniform nematic ground state for a system with no boundary terms from a system initialized with random **Q**-tensors at each lattice site, FIRE provides orders of magnitude improvement in the time taken to find minima. This performance of our default minimizer is not restricted to simple, bulk states of the liquid crystals. As we demonstrate in **Figure 3** for a handful of simple (and well-studied) arrangements of colloidal inclusions and boundaries, FIRE is very rapidly able to find these more complex minima, too. As with any non-convex optimization solver, though, no guarantees are made by FIRE about avoiding particular local minima in favor of a true global minimum. Where this is a concern, we adopt the standard approach of minimizing from multiple different random initializations. Particularly when coupled with a GPU, the substantial acceleration of FIRE-based minimizations enables the usefulness of the GUI, as the evolution of defect structures in response to user-instigated changes can be seen in real time.

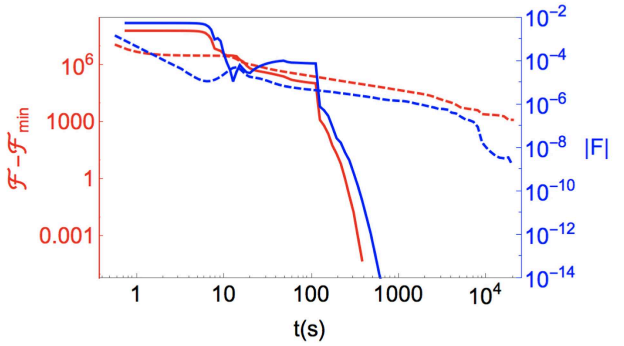

FIGURE 2 | (Red) Energy relative to the uniform texture with preferred nematic order, $\mathcal{F} - \mathcal{F}_{min}$, and (blue) the norm of the residual force vector, $|F| = \sqrt{\nabla\mathcal{F} \cdot \nabla\mathcal{F}}/N$, for bulk nematic (lattice size is $N = 250^3$), starting from a randomly initialized configuration, as a function of wall-clock time. Solid lines are minimizations using FIRE and dashed lines are those using gradient descent. As described in the text, we have tuned the minimization parameters (step size, etc.) for each algorithm separately and use identical hardware to make a one-to-one comparison.

Although numerical simulations of this size have been commonly used to make contact with experiments, in single-core operation it is impractical to simulate lattices much larger than $N \sim 300^3$, with the limiting factor being the wall-clock time required for CPUs and memory constraints for GPUs. Given a simulation with $\mathcal{N}$ degrees of freedom and spreading the work across P processing units (either GPUs or CPUs), achieving ideal $\mathcal{N}/P$ scaling requires both low-latency communication between processors and algorithms that are themselves linear in $\mathcal{N}/P$. Fortunately, lattice-based models with only nearest- and next-nearest-neighbor interactions are trivial to parallelize using a pattern common to, e.g., spin glasses [87]. We use a standard spatial decomposition of the total number of lattice sites into rectilinear sub-regions (typically cubes, although other spatial partitions are easily implemented and may be preferable for some simulation geometries). Each processing unit is assigned to one of these subregions, and is responsible for controlling and updating the lattice sites in that subregion. It also maintains information about the state of the "halo" of lattice sites that are neighbors, nearest-neighbors, and next-nearest neighbors of lattice sites at the boundary of the subregion it controls. Standard OpenMPI protocols [68] are used during each simulation step to communicate information about the state of these halo sites

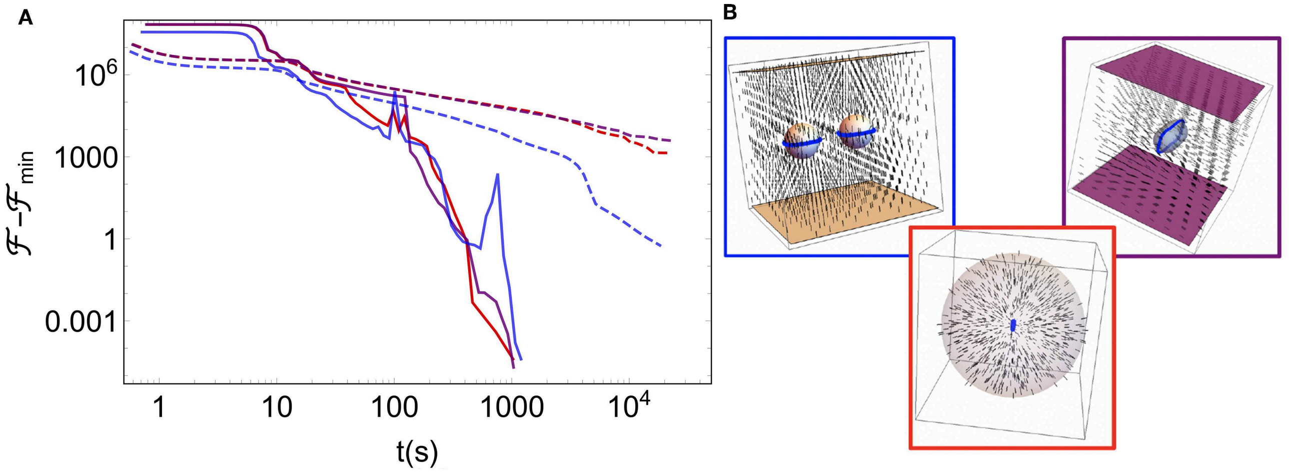

FIGURE 3 | (A) Energy relative to the minimized energy for three different geometries as a function of wall-clock time, in a lattice of size $N = 250^3$ and starting from a randomly initialized configuration. As in **Figure 2**, solid lines are minimizations using FIRE and dashed lines are those using gradient descent. As depicted in **(B)** showing the minimized configurations, the three sets of lines correspond to (Blue) two spherical colloids between parallel plates, all with homeotropic anchoring, (Red) the interior of a spherical droplet with homeotropic anchoring, and (Purple) a spherocylinder with homeotropic anchoring between parallel plates with degenerate planar anchoring. These images were created using the "multirankImages.nb" Mathematica file included in the repository for making simple visualizations.

to and from each processing unit in optimized sequences of uni-directional transfers.

We now assess how our method's efficiency scales as the problem size is increased. Although *strong scaling* (Amdahl's law)—in which the total problem size is kept fixed and P is increased—is often important, it is well-established that the structure of the near-neighbor lattice interactions we simulate is embarrassingly parallel. Our real aim is to scale up the problem size itself and use many processors to simulate lattices that approach experimental scales. As such, *weak scaling* (Gustafson's law)—in which the amount of work per processing unit is kept constant—is the relevant test.

One challenge to mention here is that when targeting energy minima—as opposed to simply advancing a molecular dynamics simulation for a fixed number of time steps—the number of minimization steps itself grows with the total system size. In general the convergence properties of different minimizers in non-convex settings are highly non-trivial. For simple geometries we are able to numerically probe this scaling—for instance, we find that in the absence of any boundary the number of minimization steps to achieve a target small force tolerance scales with the linear size of the system, whereas in the presence of a spherical colloid it scales roughly with $L^{3/2}$. In general, though, the approximate scaling may be hard to ascertain (and may depend on the target threshold for declaring a configuration to be in a minimum).

Turning instead, then, to the per-minimization-step timings, we present the weak scaling performance of *openQmin* in **Figure 4**, where we compute the total number of lattice-site updates (i.e., N times the number of simulated time steps) during a minimization in which we fix N_p, the number of lattice sites per processing unit, at several values and vary P. Consistent with a globally cubic simulation, we parallelized across $P = 1^3, 2^3, 3^3, 4^3, 5^3, 6^3, 7^3, 8^3, 9^3, 10^3$ processors on the Comet XSEDE cluster, and studied computational performance for $N_p = 75^3, 100^3, 125^3, 150^3, 250^3$. As expected, there are systematic drops due to increased communication costs as one goes from 1 core to multiple cores to multiple nodes, but *openQmin* recovers ideal linear scaling of lattice updates with P as P grows very large. Additionally, there is a systematic degradation of performance for *small* N_p, since in that case there is a more unfavorable ratio of halo sites to controlled sites for each processor.

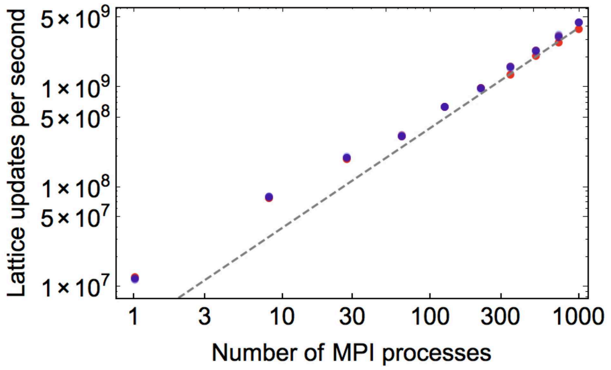

FIGURE 4 | Weak scaling performance of *openQmin* on Comet, in total number of lattice site updates [i.e., (time steps)×(ranks)×(N_p)] per second vs. the number of CPU processes, P, for a constant number of lattice sites per process. The points from dark red to light blue correspond to $N_p = 75^3, 100^3, 125^3, 150^3, 250^3$ lattice sites per rank. The dashed gray line corresponds to ideal $\propto P$ scaling.

Note that when we set the characteristic lattice spacing to correspond to 4.5 nm, the largest system simulated in this study,

$N_p \times P = (250^3) \times 10^3$, corresponds to a simulation domain of volume 1,424 μm^3.

4. SAMPLE STUDIES

4.1. Companion Defects to Homeotropic Spherical Colloids

In this section we apply *openQmin* to the question of whether a hyperbolic hedgehog or a Saturn ring disclination loop provides the minimum-energy form of the topological companion defect to a homeotropic spherical colloid. As mentioned above, a larger colloid radius a favors the dipolar configuration with a hedgehog, whereas smaller a favors the quadrupolar configuration with a Saturn ring. As a result, the common rescaling of experimental dimensions to smaller a/ξ_N in numerical modeling risks obtaining qualitatively different topological defect configurations. Besides increasing the simulation box size, altering the modeled material constants can restore qualitative agreement between experiment and simulation. Here we explore the issue in detail, using *openQmin* to systematically investigate the stability of hedgehogs relative to Saturn rings over a range of sizes and material parameters.

The dipolar configuration with a hyperbolic hedgehog is the ground state for homeotropic colloidal particles near or above the micron scale [2]. Terentjev's prediction of the alternative quadrupolar director field configuration with a Saturn ring disclination loop [62] can be stabilized for large particles by confinement or external fields [88, 89]. Stark [63] demonstrated numerically using the Frank-Oseen free energy that the Saturn ring becomes metastable relative to the dipole for $a \lesssim 720$ nm, with a defect core size $r_c = 10$ nm. For $a \lesssim 270$ nm, the Saturn ring becomes the global ground state.

While the elastic energies of the two configurations are complicated to express, the Saturn ring is additionally penalized by a simple core energy per unit length, or line tension, $\gamma = \pi K/8$ [63, 69]. Because the Saturn ring maintains a radius r_d just slightly larger than that of the colloidal particle, $r_d \approx 1.1a$ [63], the total defect core energy penalty $E_c = 2\pi r_d \gamma \propto K r_d$ of the Saturn ring grows linearly with the colloid radius. In contrast, the hyperbolic hedgehog has no defect core dimension growing in size with the colloidal particle, helping to stabilize the dipole over the Saturn ring at larger colloid sizes.

In order to numerically model multi-particle configurations in the dipolar size regime—if we cannot exploit crystal symmetries to obtain a small unit cell [10, 45]—we must either scale up the simulation volume to larger lattices, or stabilize the dipole at smaller particle sizes. We can achieve the latter by altering the materials-constant ratios $\tilde{B} \equiv B/A$, $\tilde{C} \equiv C/A$ in Equation (5). Together, these two ratios determine S_0 via Equation (7), as well as the non-dimensionalized free energy density of the nematic ground state $\tilde{f}_0 \equiv f_0/A$ with the energy well depth f_0 defined as in Equation (8).

By varying $\tilde{B}$ and $\tilde{C}$ such that S_0 remains fixed, we alter the energetic cost per unit volume of melted nematic order in defect cores, $|f_0|$. The defect core size r_c varies with the nematic correlation length ξ_N, which, from Equation (12), scales as $\sim \sqrt{L_1/|f_0|}$. Thus, an increase in $|f_0|$ implies a decrease in the defect core size, which means effectively that the ratio a/r_c of the particle size to the defect core size is increased without changing the size of the simulation lattice. The dipolar configuration is therefore expected to remain stable at smaller particle sizes. This technique was used in Luo et al. [37] to model a dynamical transition from Saturn ring to dipole as a colloidal particle approaches an undulated boundary, at simulation box sizes up to 50 times smaller than the experimental dimensions.

The results of this study are shown in **Figure 5**, which we parameterize by varying $\tilde{B}$ at fixed $S_0 = 0.53$ [i.e., setting $\tilde{C} = (-2 - \tilde{B}S_0)/(3S_0^2)$], along with the size of the spherical colloid and the lattice size. We test the stability of hyperbolic hedgehogs by initializing the surrounding lattice sites in the dipolar defect configuration suggested by Lubensky et al. [90], performing an energy minimization, and testing whether the resulting configuration has remained in the hedgehog state or transitioned to a Saturn ring configuration (thus, testing the meta-stability of the dipolar defect state as a function of system parameterization). At the values $\tilde{B} \approx 12$, $\tilde{C} \approx -10$ commonly used in modeling of 5CB [47], we find that the lower limit of hedgehog meta-stability is $a \approx 74$ lattice spacings, or about 330 nm. In this sample study we have imposed a large but finite anchoring strength at the colloid's surface. Weaker anchoring strength will affect the results, with a "surface ring" configuration replacing the dipole at low anchoring strength [63].

We have also tested the meta-stability of the quadrupolar defect configuration by initializing the system in a Saturn ring configuration and minimizing, but we have not observed the spontaneous appearance of hedgehog defects from such simulations, indicating at least the meta-stability (if not absolute stability) of Saturn rings over the entire parameter range studied here. In addition to the effect of defect core size mentioned above, slight deviations in hedgehog meta-stability as a function of lattice size at fixed $\tilde{B}$ and a seen in **Figure 5** indicate the importance of far-field distortion terms on the (meta-) stability of defect configurations.

4.2. Patterned Boundary Conditions

To demonstrate the modeling of patterned boundaries in *openQmin*, we examine a square array of alternating ±1 disclinations imprinted as a spatially varying anchoring direction on a planar substrate. Such an array was created experimentally by the authors of Murray et al. [26], by scribing lines into a polyimide surface with an atomic force microscope. As in that experiment, we give the opposing surface degenerate planar anchoring. In *openQmin*, these boundary conditions are specified at each boundary lattice site through a user-prepared text file (see section 5 below). We employ periodic boundary conditions in the horizontal directions, and the anchoring strength W at both surfaces is set to make the extrapolation length K/W roughly equal to the lattice spacing.

Figure 6A shows the result of minimizing a cell of thickness $h = 224$ lattice spacings, corresponding to ≈ 1 μm for 5CB, and a spacing d between defects equal to h. We create an 8×8 array of defects, so the total volume modeled is 64 μm^3, larger than the maximum size achievable with single core minimizations

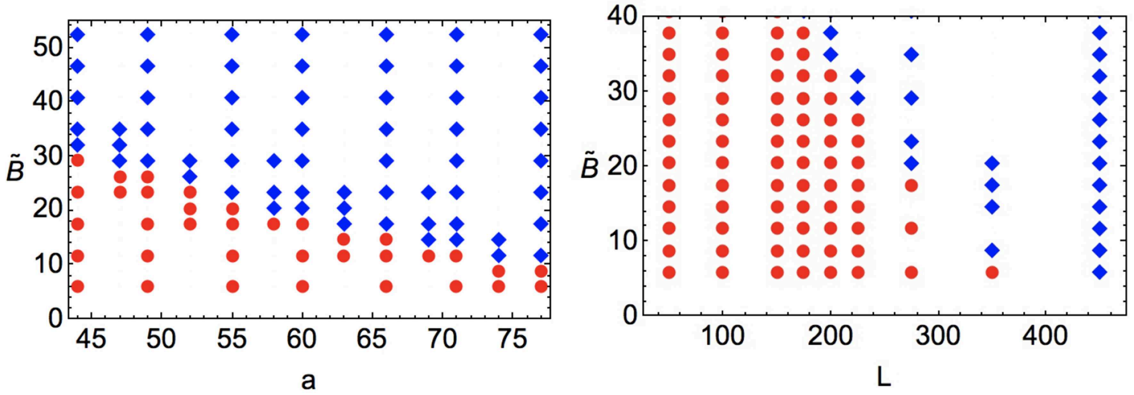

FIGURE 5 | Stability of dipolar defects around a spherical colloidal inclusion at fixed $S_0 = 0.53$ as a function of dimensionless bulk free energy density constant $\tilde{B}$, colloid size a, and linear system size L, with a and L in units of the lattice spacing. Regions of parameter space with (meta-)stable dipolar configurations are shown with blue diamonds, stable quadrupolar configurations are shown with red circles. **(Left)** For fixed lattice size of $N = 275^3$, we vary the dimensionless bulk free energy density constant $\tilde{B}$ and the colloidal radius a. **(Right)** For fixed ratio of colloidal radius to linear system size, $a = 0.22 \times L = 0.22 \times N^{1/3}$, we vary $\tilde{B}$ and L. Particularly for the larger values of a, one can see dependence of hedgehog meta-stability on L, indicating the importance of far-field distortions and boundary conditions (here, periodic).

on a typical CPU ($\approx 10 - 20\ \mu\text{m}^3$). Simulating several unit cells of the substrate patterning in this way allows us to observe a labyrinthine configuration of half-integer disclination lines near the plane of the substrate, connecting neighboring surface-defects. Meanwhile, some disclination lines are vertical, traveling between the two surfaces and imprinting a $+\frac{1}{2}$ or $-\frac{1}{2}$ defect profile on the top surface. The stopping condition for the minimization here was a somewhat modest force tolerance, allowing these large-system-size studies to be completed in less than 24 hours. While clearly not completely equilibrated, the horizontal disclination labyrinth is similar to a domain wall texture observed experimentally in Murray et al. [26], which may also be kinetically trapped. Absent from the texture in **Figure 6A** is the ±1 non-singular escaped configuration, which did appear in the experiments.

The energetic cost per unit length of disclination lines implies that the vertical configuration is favored by smaller cell thickness h. Indeed, as shown in **Figure 6B**, when we decrease h/d from 1 to $\frac{1}{6}$, only vertical disclinations appear, in pairs of $+\frac{1}{2}$ or $-\frac{1}{2}$ disclinations from the "splitting" of the ±1 surface defects. This defect splitting was sometimes observed in Murray et al. [26] in place of the escaped configuration. Conversely, as shown in **Figure 6C**, only horizontal disclinations appear when h/d is increased to 2. Extensions to even larger defect arrays, to curved boundaries, and to spatially non-uniform anchoring types can be explored in the same manner in *openQmin*.

5. RAPID PROTOTYPING WITH GUI INTERFACE

Figure 1 shows a screenshot of the graphical user interface in action; the **Supplemental Video** and accompanying narrative transcript of the video in **Supplementary Data Sheet 1** shows a representative demonstration of its use. Here we discuss some of its current functionality. Initialization dialog boxes allow the user to set the simulation size, the computational resource to use (CPU or GPU, auto-detecting whether CUDA-capable resources are available for use), and parameters for the bulk and distortion free energy density. This generates a random bulk configuration of **Q**-tensor lattice sites with periodic boundary conditions. For the visualization pane the user can specify the density and magnitude of directors to draw (taken to be the direction of the largest eigenvector of **Q** at each site), and can freely rotate and zoom in on the configuration, as well as highlight in blue defects defined locally by regions where the largest eigenvalue of **Q** falls below some threshold.

In the top left are buttons allowing the user to specify parameters from one of two energy minimization techniques to use (FIRE and Nesterov's Accelerated Gradient Descent); the resulting dialog boxes are populated with values that we typically find to be efficient for default parameter choices in the bulk and distortion energies, although some amount of tuning may be quite beneficial (particularly when changing the distortion terms L_2 through L_6). The "Minimize" button performs the requested energy minimization (either until a target force tolerance is attained or the maximum number of iterations is reached), with the option to visualize the results only at the end or to watch the minimization proceed. The "File" dialog box allows the currently visualized state of the system to be saved for separate analysis or processing.

Note that menu items allow any of the terms in the energy functional governing the simulation, Equation (4), to be changed on the fly. This allows, for example, the user to first minimize a system with some values of the distortion constants and then perform repeated minimizations as those values are changed, observing the stability or meta-stability of defect structures as this is done.

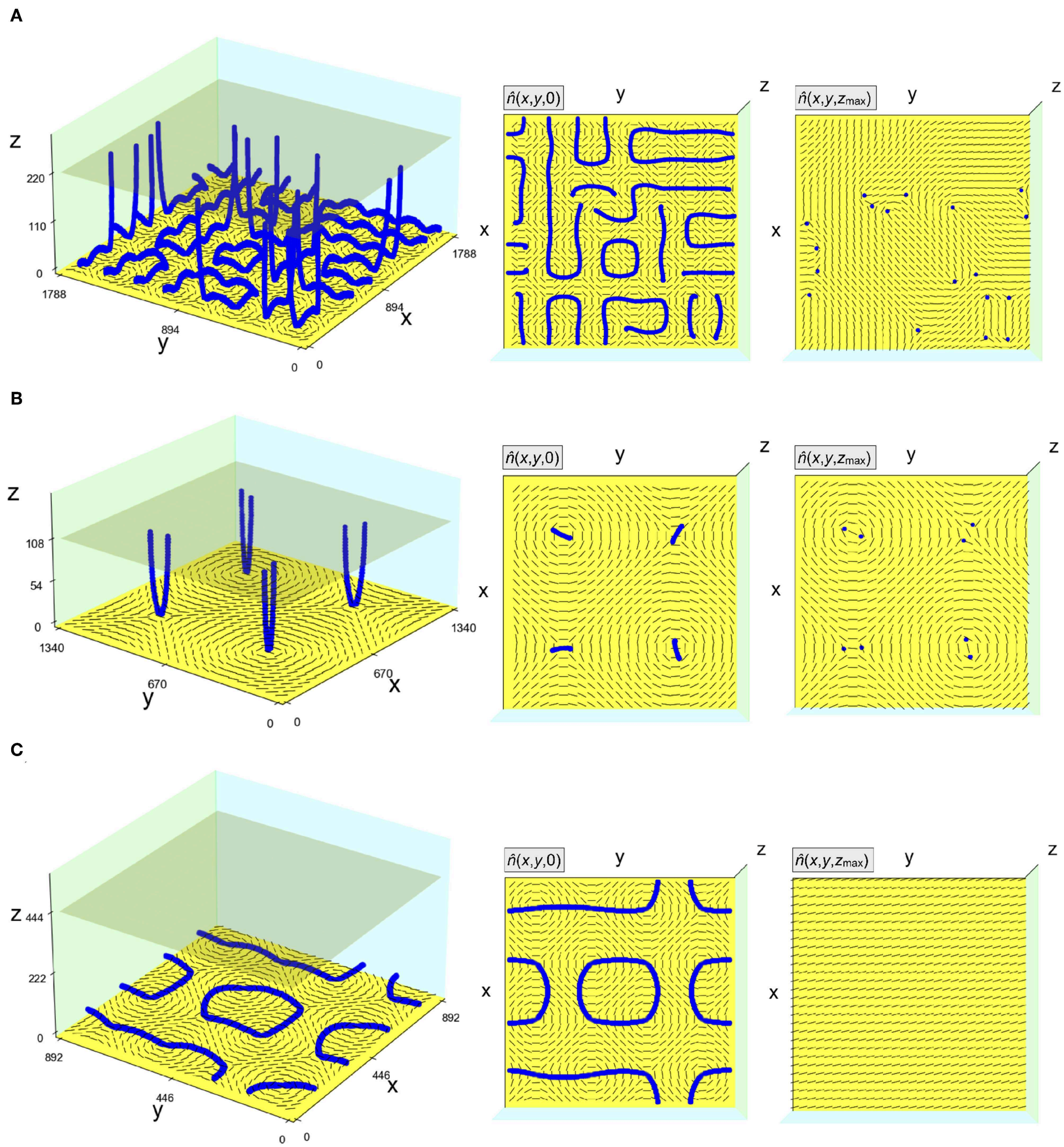

FIGURE 6 | Numerically computed disclination configurations near planar substrates patterned with square arrays of alternating ±1 surface disclinations. The opposite planar boundary (transparent square) has degenerate planar anchoring. **(A)** An 8 × 8 array of surface disclinations with spacing equal to the cell thickness. **(B)** A 2 × 2 array of surface disclinations with spacing equal to six times the cell thickness. **(C)** A 4 × 4 array of surface disclinations with spacing equal to half the cell thickness. Configurations in **(A–C)** are partially energy-minimized. Disclinations are colored blue. Axes values are given in units of the lattice spacing. In each row, the second panel shows a top view of the disclinations in bulk and the director field in the plane of the patterned substrate; the third panel shows a top view of the director field on the opposite surface, along with the half-integer disclination points (if any) in that surface. These images were made using the "visualize.py" Python script included in the repository for taking saved configurations and making simple visualizations from the command line.

Two buttons allow the user to introduce boundaries and colloidal inclusions into the system. "Simple" objects are spheres and flat walls with either normal homeotropic or degenerate planar anchoring conditions. Arbitrarily complex boundary conditions (taking any shape, with degenerate planar and homeotropic anchoring conditions not restricted by the direction of the surface normal) can be added by preparing a simple text file that the program can read in – an example script that generates the custom boundary file used in **Figure 1** is included in the "/tools" directory of the project's GitHub repository [67].

With boundaries and colloids ("objects") in place, some manipulations of these objects are accessible via drop-down menus. The positions of these objects within the simulation can be directly modified, so the user could place an ellipsoidal particle, perform a minimization, change the position, re-minimize the system, and record the different energy minima attained. We include an option to automate this type of operation (which can be used to build up the potential of mean force from the liquid crystal and colloid interactions) for convenience. A near-term addition will be allowing objects to move according to the integrated stresses at their surface (or according to the energetic results of various trial moves); the user will then be able to separately "Minimize" just the liquid crystal sites or "Evolve [the] system" by allowing both liquid crystalline and colloidal degrees of freedom to change simultaneously.

Finally, to facilitate moving from GUI prototyping to larger-scale MPI studies, we have included the ability to record system initialization and sequences of commands entered in the graphical user interface, and then save this sequence of commands as a new file that can be separately compiled and executed in non-GUI operation. This file has its own set of command line options, primarily so that it can be made to work as an MPI executable and so that the system size of the simulation it represents can be rescaled to a larger value. We highlight this GUI-prototyping approach as a visual alternative to the scripting-language approaches of molecular-dynamics packages like LAMMPS [91] or HOOMD-blue [92] for specifying complex sequences of system initialization, energy minimizations, and the introduction of objects, fields, and boundary conditions. We believe that this seamless visual-prototyping-to-MPI-scalable pipeline will be beneficial to researchers interested in accessing experimental-scale simulations.

6. DISCUSSION

As demonstrated in our sample study, *openQmin* utilizes MPI to enable LdG modeling at typical size scales of experimental relevance, at the $\sim 10\ \mu$m range, with fast convergence enabled by the FIRE algorithm. Besides the colloidal defect configurations and patterned boundaries discussed here, another immediate use is for the study of cholesterics, where typically fewer than ten pitches can fit inside a simulation box using a single processor, but using *openQmin* tens of pitches can be modeled. While it may not be realistic at present to *frequently* conduct simulations with 10^3 processors, using *openQmin* on computer clusters will facilitate demonstration of how numerical results scale with system size, allowing reasonable extrapolations to experimental scales.

For modeling at the $\sim 1\ \mu$m range or smaller, *openQmin*'s combination of FIRE with GPU computing offers a substantial speedup, enabling users to manipulate the simulated conditions in a GUI environment and observe the change in energy-minimized configurations. The GUI is useful for running "real-time" tests of proposed configurations which can then be modeled at larger scales with MPI.

Likewise, the GUI will also be useful to experimentalists in quickly identifying more optimal properties of nematics, colloidal particles, boundaries, etc. in order to achieve targeted topological or self-assembled configurations. In general, numerical modeling can aid experimental studies not only in developing theoretical understanding of nematic structures and energy landscapes, but also in performing high-throughput searches through these design spaces. For example, geometric compatibility conditions favoring lock-and-key assembly of particles and patterned walls [21, 37], or particle design promoting assembly into photonic crystals, can be optimized more efficiently in numerics, to help guide the increasingly sophisticated uses of fabrication techniques such as photolithography and two-photon polymerization [93]. An ambitious but important direction for future development is therefore to efficiently explore design parameter spaces in numerical modeling, possibly employing genetic algorithms and techniques from machine learning.

There are some near-term directions for future development of *openQmin* that we anticipate will increase the usefulness of this open-source software to the liquid crystals research community. An expanded library of **Q**-initialization options will facilitate investigations of chiral liquid crystals, topologically entangled or knotted defect configurations [11–14], and periodic defect arrays [26, 94], for example. A major advance would be adding a flow field coupled to **Q** by Beris-Edwards nematodynamics, for investigations of microfluidic geometries and active nematics.

Incorporating motion of colloidal particles into the modeling is another area for useful developments. In the experimental system, energy is minimized not only over **Q** but also over the positions and (if applicable) orientations of colloidal particles. At present, *openQmin* takes these latter degrees of freedom as input parameters, and a free energy landscape can be mapped either informally using the GUI or more systematically on a computer cluster. Thus one desired future improvement is to allow overdamped translation and rotation of colloidal particles within the program, downhill in the energy landscape, based on trial moves or on estimated nematic elastic stresses felt by the particle [46]. The trial move approach, requiring several re-minimizations of **Q** at each time step, is made less cumbersome by improved convergence speed of the FIRE algorithm.

Finally, we hope that *openQmin*'s GUI interface will be useful in physics education. Interacting with a fast and "hands-on" version of the numerical modeling, students at the undergraduate or beginning graduate level can quickly gain experience and intuition for liquid crystals. This will help to capitalize on the position of liquid crystals as one of the most accessible, and visualizable, physical realizations of abstract topological ideas relevant to many areas of physics.

DATA AVAILABILITY STATEMENT

The open source code described in this work can be found at Reference [67] and used to reproduce all data in the manuscript. Documentation for the software is maintained at Reference [95], and can also be generated with doxygen from the source code.

AUTHOR CONTRIBUTIONS

DS and DB designed the study, developed the open-source software, and wrote the manuscript.

FUNDING

DS was supported by NSF-POLS-1607416 as well as Simons Foundation Grant Number 454947. The Tesla K40s used for this research were donated by the NVIDIA Corporation. We acknowledge computing support via an XSEDE allocation on Comet through Grant No. NSF-TG-PHY190027, and from the Multi-Environment Computer for Exploration and Discovery (MERCED) cluster at UC Merced, which was funded by National Science Foundation Grant No. ACI-1429783.

ACKNOWLEDGMENTS

DB thanks Gareth Alexander for introducing him to LdG numerical modeling, and gratefully acknowledges illuminating discussions with Simon Čopar, Miha Ravnik, and Slobodan Žumer.

SUPPLEMENTARY MATERIAL

The Supplementary Material for this article can be found online at: https://www.frontiersin.org/articles/10.3389/fphy.2019.00204/full#supplementary-material

REFERENCES

1. Friedel G. Les états mésomorphes de la matière. *Ann Phys*. (1922) **18**:273–474. doi: 10.1051/anphys/192209180273
2. Poulin P, Stark H, Lubensky TC, Weitz DA. Novel colloidal interactions in anisotropic fluids. *Science*. (1997) **275**:1770–3. doi: 10.1126/science.275.5307.1770
3. Dickson W, Wurtz GA, Evans PR, Pollard RJ, Zayats AV. Electronically controlled surface plasmon dispersion and optical transmission through metallic hole arrays using liquid crystal. *Nano Lett*. (2008) **8**:281–6. doi: 10.1021/nl072613g
4. Liu Q, Cui Y, Gardner D, Li X, He S, Smalyukh II. Self-alignment of plasmonic gold nanorods in reconfigurable anisotropic fluids for tunable bulk metamaterial applications. *Nano Lett*. (2010) **10**:1347–53. doi: 10.1021/nl9042104
5. Wang X, Miller DS, Bukusoglu E, De Pablo JJ, Abbott NL. Topological defects in liquid crystals as templates for molecular self-assembly. *Nat Mater*. (2016) **15**:106–12. doi: 10.1038/nmat4421
6. Rodarte AL, Pandolfi RJ, Ghosh S, Hirst LS. Quantum dot/liquid crystal composite materials: self-assembly driven by liquid crystal phase transition templating. *J Mater Chem C*. (2013) **1**:5527–32. doi: 10.1039/c3tc31043d
7. Rodarte A, Cisneros F, Hein J, Ghosh S, Hirst L. Quantum dot/liquid crystal nanocomposites in photonic devices. *Photonics*. (2015) **2**:855–64. doi: 10.3390/photonics2030855
8. Muševič I, Škarabot M, Tkalec U, Ravnik M, Žumer S. Two-dimensional nematic colloidal crystals self-assembled by topological defects. *Science*. (2006) **313**:954–8. doi: 10.1126/science.1129660
9. Mundoor H, Senyuk B, Smalyukh II. Triclinic nematic colloidal crystals from competing elastic and electrostatic interactions. *Science*. (2016) **352**:69–73. doi: 10.1126/science.aaf0801
10. Nych A, Ognysta U, Škarabot M, Ravnik M, Žumer S, Muševič I. Assembly and control of 3D nematic dipolar colloidal crystals. *Nat Commun*. (2013) **4**:1489. doi: 10.1038/ncomms2486
11. Ravnik M, Škarabot M, Žumer S, Tkalec U, Poberaj I, Babič D, et al. Entangled nematic colloidal dimers and wires. *Phys Rev Lett*. (2007) **99**:247801. doi: 10.1103/PhysRevLett.99.247801
12. Tkalec U, Ravnik M, Čopar S, Žumer S, Muševič I. Reconfigurable knots and links in chiral nematic colloids. *Science*. (2011) **333**:62–5. doi: 10.1126/science.1205705
13. Tasinkevych M, Campbell MG, Smalyukh II. Splitting, linking, knotting, and solitonic escape of topological defects in nematic drops with handles. *Proc Natl Acad Sci USA*. (2014) 111:16268–73. doi: 10.1073/pnas.1405928111
14. Machon T, Alexander GP. Knotted defects in nematic liquid crystals. *Phys Rev Lett*. (2014) **113**:027801. doi: 10.1103/PhysRevLett.113.027801
15. Ravnik M, Alexander GP, Yeomans JM, Žumer S. Three-dimensional colloidal crystals in liquid crystalline blue phases. *Proc Natl Acad Sci USA*. (2011) **108**:5188–92. doi: 10.1073/pnas.1015831108
16. Lavrentovich OD. Liquid crystals, photonic crystals, metamaterials, and transformation optics. *Proc Natl Acad Sci USA*. (2011) **108**:5143–4. doi: 10.1073/pnas.1102130108
17. Humar M, Muševič I. 3D microlasers from self-assembled cholesteric liquid-crystal microdroplets. *Opt Express*. (2010) **18**:26995–7003. doi: 10.1364/OE.18.026995
18. Muševič I. Interactions, topology and photonic properties of liquid crystal colloids and dispersions. *Eur Phys J Spec Top*. (2019) **227**:2455–85. doi: 10.1140/epjst/e2019-800107-y
19. Serra F. Curvature and defects in nematic liquid crystals. *Liq Cryst*. (2016) **43**:1920–36. doi: 10.1080/02678292.2016.1209698
20. Hung FR, Gettelfinger BT, Koenig GM Jr, Abbott NL, de Pablo JJ. Nanoparticles in nematic liquid crystals: interactions with nanochannels. *J Chem Phys*. (2007) **127**:124702. doi: 10.1063/1.2770724
21. Eskandari Z, Silvestre N, da Gama MT, Ejtehadi M. Particle selection through topographic templates in nematic colloids. *Soft Matter*. (2014) **10**:9681–7. doi: 10.1039/C4SM02231A
22. Luo Y, Serra F, Stebe KJ. Experimental realization of the "lock-and-key" mechanism in liquid crystals. *Soft Matter*. (2016) **12**:6027–32. doi: 10.1039/C6SM00401F
23. Guillamat P, Sagués F, Ignés-Mullol J. Electric-field modulation of liquid crystal structures in contact with structured surfactant monolayers. *Phys Rev E*. (2014) **89**:052510. doi: 10.1103/PhysRevE.89.052510
24. Kos Ž, Ravnik M. Relevance of saddle-splay elasticity in complex nematic geometries. *Soft Matter*. (2016) **12**:1313–23. doi: 10.1039/C5SM02417J
25. Peng C, Guo Y, Conklin C, Viñals J, Shiyanovskii SV, Wei QH, et al. Liquid crystals with patterned molecular orientation as an electrolytic active medium. *Phys Rev E*. (2015) **92**:052502. doi: 10.1103/PhysRevE.92.052502
26. Murray BS, Pelcovits RA, Rosenblatt C. Creating arbitrary arrays of two-dimensional topological defects. *Phys Rev E*. (2014) **90**:052501. doi: 10.1103/PhysRevE.90.052501
27. Williams C, Cladis P, Kleman M. Screw disclinations in nematic samples with cylindrical symmetry. *Mol Cryst Liquid Cryst*. (1973) **21**:355–73. doi: 10.1080/15421407308083329
28. Volovik G, Lavrentovich O. Topological dynamics of defects: boojums in nematic drops. *Zh Eksp Teor Fiz*. (1983) **85**:1997–2010.
29. Nelson DR. Toward a tetravalent chemistry of colloids. *Nano Lett*. (2002) **2**:1125–9. doi: 10.1021/nl0202096

30. Lavrentovich O, Nastishin YA. Defects in degenerate hybrid aligned nematic liquid crystals. *Europhys Lett.* (1990) **12**:135. doi: 10.1209/0295-5075/12/2/008
31. Wright DC, Mermin ND. Crystalline liquids: the blue phases. *Rev Modern Phys.* (1989) **61**:385. doi: 10.1103/RevModPhys.61.385
32. Alama S, Bronsard L, Lamy X. Minimizers of the Landau–de Gennes energy around a spherical colloid particle. *Arch Ration Mech Anal.* (2016) **222**:427–50. doi: 10.1007/s00205-016-1005-z
33. Alama S, Bronsard L, Lamy X. Analytical description of the Saturn-ring defect in nematic colloids. *Phys Rev E.* (2016) **93**:012705. doi: 10.1103/PhysRevE.93.012705
34. Kralj S, Žumer S. Fréedericksz transitions in supra-um nematic droplets. *Phys Rev A.* (1992) **45**:2461–70. doi: 10.1103/PhysRevA.45.2461
35. Tkalec U, Škarabot M, Muševič I. Interactions of micro-rods in a thin layer of a nematic liquid crystal. *Soft Matter.* (2008) **4**:2402–9. doi: 10.1039/b807979j
36. Emeršič T, Zhang R, Kos Ž, Čopar S, Osterman N, de Pablo JJ, et al. Sculpting stable structures in pure liquids. *Sci Adv.* (2019) **5**:eaav4283. doi: 10.1126/sciadv.aav4283
37. Luo Y, Beller DA, Boniello G, Serra F, Stebe KJ. Tunable colloid trajectories in nematic liquid crystals near wavy walls. *Nat Commun.* (2018) **9**:3841. doi: 10.1038/s41467-018-06054-y
38. Tasinkevych M, Mondiot F, Mondain-Monval O, Loudet JC. Dispersions of ellipsoidal particles in a nematic liquid crystal. *Soft Matter.* (2014) **10**:2047–58. doi: 10.1039/c3sm52708e
39. Hashemi SM, Ejtehadi MR. Equilibrium state of a cylindrical particle with flat ends in nematic liquid crystals. *Phys Rev E.* (2015) **91**:012503. doi: 10.1103/PhysRevE.91.012503
40. Hung FR, Bale S. Faceted nanoparticles in a nematic liquid crystal: defect structures and potentials of mean force. *Mol Simul.* (2009) **35**:822–34. doi: 10.1080/08927020902801563
41. Hung FR. Quadrupolar particles in a nematic liquid crystal: effects of particle size and shape. *Phys Rev E.* (2009) **79**:021705. doi: 10.1103/PhysRevE.79.021705
42. Hung FR, Guzmán O, Gettelfinger BT, Abbott NL, de Pablo JJ. Anisotropic nanoparticles immersed in a nematic liquid crystal: defect structures and potentials of mean force. *Phys Rev E.* (2006) **74**:011711. doi: 10.1103/PhysRevE.74.011711
43. Beller DA, Gharbi MA, Liu IB. Shape-controlled orientation and assembly of colloids with sharp edges in nematic liquid crystals. *Soft Matter.* (2015) **11**:1078–86. doi: 10.1039/C4SM01910E
44. Araki T, Tanaka H. Colloidal aggregation in a nematic liquid crystal: topological arrest of particles by a single-stroke disclination line. *Phys Rev Lett.* (2006) **97**:127801. doi: 10.1103/PhysRevLett.97.127801
45. Škarabot M, Ravnik M, Žumer S, Tkalec U, Poberaj I, Babič D, et al. Interactions of quadrupolar nematic colloids. *Phys Rev E.* (2008) **77**:031705. doi: 10.1103/PhysRevE.77.031705
46. Škarabot M, Ravnik M, Žumer S, Tkalec U, Poberaj I, Babič D, et al. Hierarchical self-assembly of nematic colloidal superstructures. *Phys Rev E.* (2008) **77**:061706. doi: 10.1103/PhysRevE.77.061706
47. Ravnik M, Žumer S. Landau–de Gennes modelling of nematic liquid crystal colloids. *Liq Cryst.* (2009) **36**:1201–14. doi: 10.1080/02678290903056095
48. Mori H, Gartland EC, Kelly JR, Box PJ. Multidimensional director modeling using the Q tensor repre- sentation in a liquid crystal cell and its application to the π cell with patterned electrodes. *Jpn J App Phys.* (1999) **38**:135. doi: 10.1143/JJAP.38.135
49. Beris AN, Edwards BJ. *Thermodynamics of Flowing Systems: With Internal Microstructure.* New York, NY; Oxford: Oxford University Press (1994).
50. Qian T, Sheng P. Generalized hydrodynamic equations for nematic liquid crystals. *Phys Rev E.* (1998) **58**:7475. doi: 10.1103/PhysRevE.58.7475
51. Denniston C, Orlandini E, Yeomans J. Lattice Boltzmann simulations of liquid crystal hydrodynamics. *Phys Rev E.* (2001) **63**:056702. doi: 10.1103/PhysRevE.63.056702
52. Spencer T, Care C. Lattice Boltzmann scheme for modeling liquid-crystal dynamics: zenithal bistable device in the presence of defect motion. *Phys Rev E.* (2006) **74**:061708. doi: 10.1103/PhysRevE.74.061708
53. Carenza LN, Gonnella G, Lamura A, Negro G, Tiribocchi A. Lattice Boltzmann methods and active fluids. *Eur Phys J E.* (2019) **42**:81. doi: 10.1140/epje/i2019-11843-6
54. Marenduzzo D, Orlandini E, Cates M, Yeomans J. Steady-state hydrodynamic instabilities of active liquid crystals: hybrid lattice Boltzmann simulations. *Phys Rev E.* (2007) **76**:031921. doi: 10.1103/PhysRevE.76.031921
55. Cates M, Henrich O, Marenduzzo D, Stratford K. Lattice Boltzmann simulations of liquid crystalline fluids: active gels and blue phases. *Soft Matter.* (2009) **5**:3791–800. doi: 10.1039/b908659p
56. Lee KW, Mazza MG. Stochastic rotation dynamics for nematic liquid crystals. *J Chem Phys.* (2015) **142**:164110. doi: 10.1063/1.4919310
57. Shendruk TN, Yeomans JM. Multi-particle collision dynamics algorithm for nematic fluids. *Soft Matter.* (2015) **11**:5101–10. doi: 10.1039/C5SM00839E
58. Mandal S, Mazza MG. Multiparticle collision dynamics for tensorial nematodynamics. *Phys Rev E.* (2019) **99**:063319. doi: 10.1103/PhysRevE.99.063319
59. James R, Willman E, Fernandez FA, Day SE. Computer modeling of liquid crystal hydrodynamics. *IEEE Trans Magn.* (2008) **44**:814–7. doi: 10.1109/TMAG.2007.916029
60. Giomi L, Mahadevan L, Chakraborty B, Hagan M. Excitable patterns in active nematics. *Phys Rev Lett.* (2011) **106**:218101. doi: 10.1103/PhysRevLett.106.218101
61. Svenšek D, Žumer S. Hydrodynamics of pair-annihilating disclination lines in nematic liquid crystals. *Phys Rev E.* (2002) **66**:021712. doi: 10.1103/PhysRevE.66.021712
62. Terentjev EM. Disclination loops, standing alone and around solid particles, in nematic liquid crystals. *Phys Rev E.* (1995) **51**:1330. doi: 10.1103/PhysRevE.51.1330
63. Stark H. Physics of colloidal dispersions in nematic liquid crystals. *Phys Rep.* (2001) **351**:387–474. doi: 10.1016/S0370-1573(00)00144-7
64. Gharbi MA, Cavallaro M Jr, Wu G, Beller DA, Kamien RD, Yang S, et al. Microbullet assembly: interactions of oriented dipoles in confined nematic liquid crystal. *Liq Cryst.* (2013) **40**:1619–27. doi: 10.1080/02678292.2012.755223
65. Luo Y, Yao T, Beller DA, Serra F, Stebe KJ. Deck the walls with anisotropic colloids in nematic liquid crystals. *Langmuir.* (2019) **35**:9274–85. doi: 10.1021/acs.langmuir.9b01811
66. Bajc I, Hecht F, Žumer S. A mesh adaptivity scheme on the Landau–de Gennes functional minimization case in 3D, and its driving efficiency. *J Comput Phys.* (2016) **321**:981–96. doi: 10.1016/j.jcp.2016.02.072
67. Sussman DM, Beller DA. Available online at: https://github.com/sussmanLab/open-Qmin (2019).
68. Gabriel E, Fagg GE, Bosilca G, Angskun T, Dongarra JJ, Squyres JM, et al. Open MPI: goals, concept, and design of a next generation MPI implementation. In: *European Parallel Virtual Machine/Message Passing Interface Users' Group Meeting.* Berlin: Springer (2004). p. 97–104. doi: 10.1007/978-3-540-30218-6_19
69. de Gennes PG, Prost J. *The Physics of Liquid Crystals.* 2nd Edn. Oxford: Clarendon Press (1993).
70. Mottram NJ, Newton CJ. Introduction to Q-tensor theory. *arXiv [Preprint]. arXiv:14093542* (2014).
71. Schophol N, Sluckin TJ. Defect core structure in nematic liquid crystals. *Phys Rev Lett.* (1987) **59**:2582. doi: 10.1103/PhysRevLett.59.2582
72. Jeu WHD, Claassen WAP, Spruijt AMJ. The determination of the elastic constants of nematic liquid crystals. *Mol Cryst Liq Cryst.* (1976) **37**:269–80. doi: 10.1080/15421407608084362
73. Madhusudana NV, Pratibha R. Elasticity and orientational order in some cyanobiphenyls: part IV. Reanalysis of the data. *Mol Cryst Liq Cryst.* (1982) **89**:249–57. doi: 10.1080/00268948208074481
74. Poniewierski A, Sluckin T. On the free energy density of non-uniform nematics. *Mol Phys.* (1985) **55**:1113–27. doi: 10.1080/00268978500101931
75. Rapini A, Papoular M. Distorsion d'une lamelle nématique sous champ magnétique conditions d'ancrage aux parois. *Le J Phys Coll.* (1969) **30**:C4–54. doi: 10.1051/jphyscol:1969413
76. Nobili M, Durand G. Disorientation-induced disordering at a nematic-liquid-crystal–solid interface. *Phys Rev A.* (1992) **46**:R6174. doi: 10.1103/PhysRevA.46.R6174
77. Fournier JB, Galatola P. Modeling planar degenerate wetting and anchoring in nematic liquid crystals. *Europhys Lett.* (2005) **72**:403. doi: 10.1209/epl/i2005-10253-5

78. Nvidia C. *Nvidia CUDA C Programming Guide.* Nvidia Corporation (2011).
79. Noye B, Arnold R. Accurate finite difference approximations for the Neumann condition on a curved boundary. *Appl Math Modell*. (1990) **14**:2–13. doi: 10.1016/0307-904X(90)90157-Z
80. Nocedal J, Wright S. *Numerical Optimization.* New York, NY: Springer Science & Business Media (2006).
81. Bitzek E, Koskinen P, Gähler F, Moseler M, Gumbsch P. Structural relaxation made simple. *Phys Rev Lett*. (2006) **97**:170201. doi: 10.1103/PhysRevLett.97.170201
82. Polyak BT. Some methods of speeding up the convergence of iteration methods. *USSR Comput Math Math Phys.* (1964) **4**:1–17. doi: 10.1016/0041-5553(64)90137-5
83. Sheppard D, Terrell R, Henkelman G. Optimization methods for finding minimum energy paths. *J Chem Phys*. (2008) **128**:134106. doi: 10.1063/1.2841941
84. Herbol HC, Stevenson J, Clancy P. Computational implementation of nudged elastic band, rigid rotation, and corresponding force optimization. *J Chem Theor Comput*. (2017) **13**:3250–9. doi: 10.1021/acs.jctc.7b00360
85. Zhou Y, Moseler M, Müser MH. Solution of boundary-element problems using the fast-inertial-relaxation-engine method. *Phys Rev B*. (2019) **99**:144103. doi: 10.1103/PhysRevB.99.144103
86. Wang Y, Jia Z, Wen Z. The Search direction Correction makes first-order methods faster. *arXiv [Preprint]. arXiv:190506507* (2019).
87. Lulli M, Bernaschi M, Parisi G. Highly optimized simulations on single-and multi-GPU systems of the 3D Ising spin glass model. *Comput Phys Commun*. (2015) **196**:290–303. doi: 10.1016/j.cpc.2015.06.019
88. Gu Y, Abbott NL. Observation of saturn-ring defects around solid microspheres in nematic liquid crystals. *Phys Rev Lett*. (2000) **85**:4719. doi: 10.1103/PhysRevLett.85.4719
89. Loudet J, Poulin P. Application of an electric field to colloidal particles suspended in a liquid-crystal solvent. *Phys Rev Lett*. (2001) **87**:165503. doi: 10.1103/PhysRevLett.87.165503
90. Lubensky TC, Pettey D, Currier N, Stark H. Topological defects and interactions in nematic emulsions. *Phys Rev E.* (1998) **57**:610. doi: 10.1103/PhysRevE.57.610
91. Plimpton S. Fast parallel algorithms for short-range molecular dynamics. *J Comput Phys*. (1995) **117**:1–19. doi: 10.1006/jcph.1995.1039
92. Anderson JA, Lorenz CD, Travesset A. General purpose molecular dynamics simulations fully implemented on graphics processing units. *J Comput Phys*. (2008) **227**:5342–59. doi: 10.1016/j.jcp.2008.01.047
93. Martinez A, Ravnik M, Lucero B, Visvanathan R, Žumer S, Smalyukh II. Mutually tangled colloidal knots and induced defect loops in nematic fields. *Nat Mater*. (2014) **13**:258–63. doi: 10.1038/nmat3840
94. Suh A, Gim MJ, Beller D, Yoon DK. Topological defects and geometric memory across the nematic-smectic A liquid crystal phase transition. *Soft Matter*. (2019) **15**:5835–41. doi: 10.1039/C9SM00781D
95. Sussman DM, Beller DA. Available online at: https://dmsussman.gitlab.io/landaudegui/ (2019).

Conflict of Interest: The authors declare that the research was conducted in the absence of any commercial or financial relationships that could be construed as a potential conflict of interest.

frontiers
in Physics

ORIGINAL RESEARCH
published: 14 January 2020
doi: 10.3389/fphy.2019.00238

On Generation, Motions, and Collisions of Dowsons

Pawel Pieranski[1]* *and Maria Helena Godinho*[2]

[1] *Laboratoire de Physique des Solides, Université Paris-Saclay, Orsay, France,* [2] *CENIMAT, Faculdade de Ciências e Tecnologia - Universidade Nova De Lisboa, Caparica, Portugal*

Dowsons are $\pm 2\pi$ point singularities of the unitary complex order parameter $e^{i\varphi}$ characterizing the so-called dowser texture in a thin nematic layer with homeotropic boundary conditions. Dowsons are therefore similar to disclinations in freely-standing smectic C films or to vortices in two-dimensional superfluids or superconductors. Using especially tailored setups called dowsons' colliders, pairs of dowsons of opposite signs are generated and set into motion on counter-rotating trajectories leading to collisions. In a first approximation, the velocity of dowsons is orthogonal and proportional to the local phase gradient $\vec{\nabla}\varphi$. The outcome of collisions, i.e., either annihilation or bypass, depends on the distance of trajectories $\Delta\varphi$ in terms of the phase: for $\Delta\varphi < \pi$ a collision of a pair of dowsons leads to their annihilation, while for $\Delta\varphi > \pi$ the dowsons are passing by. This rule is valid only for quasi-static stationary wound up textures and can be easily broken by application of a Poiseuille flow in an appropriate direction.

Keywords: nematic, topological defects, dowser texture, complex order parameter, collider, annihilation

Edited by:
Teresa Lopez-Leon,
École Supérieure de Physique et de Chimie Industrielles de la Ville de Paris, France

Reviewed by:
Simon Čopar,
University of Ljubljana, Slovenia
Thomas Machon,
University of Bristol, United Kingdom

Correspondence:
Pawel Pieranski
pawel.pieranski@u-psud.fr

Specialty section:
This article was submitted to Soft Matter Physics, a section of the journal Frontiers in Physics

Received: *11 September 2019*
Accepted: *16 December 2019*
Published: *14 January 2020*

Citation:
Pieranski P and Godinho MH (2020) On Generation, Motions, and Collisions of Dowsons. Front. Phys. 7:238. doi: 10.3389/fphy.2019.00238

1. DOWSONS: DEFECTS OF THE DOWSER TEXTURE

1.1. The Dowser Texture

As stressed by de Gennes in his pioneering paper on classification of topological defects [1], superfluids (or superconductors) (**Figure 1A**) and smectics A (**Figure 1B**) are characterized by complex order parameters $|\Psi|e^{i\varphi}$. Later, smectics C (**Figure 1C**) have been added to this list. Beside phases in the thermodynamic sense, the complex order parameter characterizes also textures of a homeotropic nematic layer above the Freedericks transition (**Figure 1D**) as well as the so called dowser texture in a nematic layer with homeotropic boundary conditions (**Figure 1E**).

The dowser texture, known as the quasi-planar texture for decades [3], was believed unduly to be unstable, with respect to the homogeneous homeotropic texture, so that it has been scarcely studied in past. Recent work [4] proved that in practice the quasi-planar texture is only metastable and can be preserved indefinitely in certain conditions. Experiments with this persistent version of the quasi-planar texture have unveiled its remarkable qualities such as its sensitivity to magnetic [5], mechanical [6], or electric [7] perturbations. For this reason, as well because of the resemblance with the wooden dowser tool, the persistent version of the quasi-planar texture was dubbed "the dowser texture."

1.2. Dowsons d_+ and d_-: the $+2\pi$ and -2π Singularities of the Phase Field $\varphi(x, y, t)$ of the Dowser Texture

The dowser texture is fully characterized by the azimuthal angle φ of the unitary two-dimensional dowser field $\mathbf{d} = (\cos\varphi, \sin\varphi)$ (**Figure 1E**) which is equivalent to the phase φ of the complex order parameter $e^{i\varphi}$.

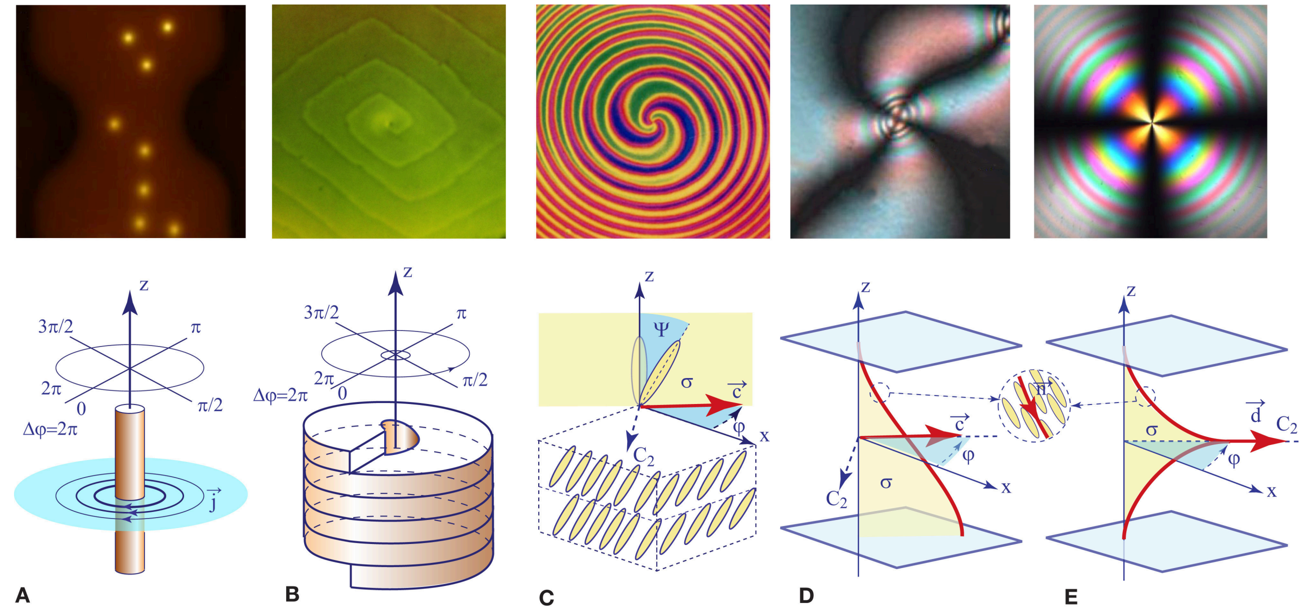

FIGURE 1 | Topological defects in systems characterized by complex order parameters: **(A)** vortices in a superconductor [2], **(B)** dislocation in a BPI crystal, **(C)** disclination in a smectic C free-standing film, **(D)** umbilic in a homeotropic nematic layer above the Freedericks transition, **(E)** dowson in the dowser texture.

Thanks to the birefringence of nematics, the phase $\varphi(x,y,t)$ of the dowser field $\mathbf{d}(x,y,t)$ is directly observable in polarized light so that its $+2\pi$ and -2π topological singularities are easily identifiable [5]. Let us note that when considered in three dimensions of the nematic layer, these singularities of the 2D dowser field $\mathbf{d}(x,y)$ appear as nematic monopoles [8], that is to say, point singularities of the 3D director field $\mathbf{n}(x,y,z,t)$.

In the present work, devoted to motions and collisions of topological singularities of the dowser field we will call them shortly "dowsons." Moreover, for the sake of concision, we will use notations "d_+" and "d_-" corresponding to the $+2\pi$ and -2π versions of dowsons.

Let us stress that in contradistinction with the dowser texture, the phase $\varphi(x,y)$ of the complex order parameter in superconductors is not an observable quantity and only its $+2\pi$ and -2π singularities, that is to say vortices, can be imaged, for example, with a squid-tip AFM because they carry in their normal core the quanta of the magnetic flux h/(2e) [2].

1.3. Trajectories and Collisions of Dowsons

Previous experiments with dowsons [4, 5] have shown that pairs of dowsons "d_+" and "d_-" can be easily generated, set into motion and brought into collisions. In certain conditions collision of pairs of dowsons (d_+,d_-) can result in their annihilation. Here, we will explore these processes by means of especially tailored setups called "dowsons' colliders" (see section 2.1 and **Figure 4**).

The principal role of dowsons' colliders consists in driving motions of dowsons which is achieved by a controlled winding of the phase of the dowser field. Indeed, like vortices in superconductors which are set in motion by phase gradients (the Lorentz force is exerted on a flux quantum by a transport current proportional to the phase gradient), the motion of dowsons is also driven by phase gradients.

1.4. Single Dowsons Inserted in a Wound Up Dowser Field

This is explained on the first example shown in **Figure 2** where one dowson d_+ is imbedded in a wound up dowser texture. Before considering forces involved in the motion of this dowson d_+, let us emphasize that its structure depends on the phase $\varphi_i = \varphi(x_i, y_i)$ at the insertion point (x_i, y_i). **Figures 2A–C** show that for $\varphi_i = 0$ the structure of the dowson d_+ is radial with the field $\mathbf{d}$ directed outward. For $\varphi_i = \pi/2$ the structure becomes circular anticlockwise (see **Figures 2D–F**) and for $\varphi_i = \pi$ it is radial directed inward (see **Figures 2G–I**).

In **Figure 2** the dowser field is wound up in the y direction ($\overrightarrow{\nabla}\varphi // \overrightarrow{y}$) so that the phase $\varphi_i = \varphi(x_i, y_i)$ does not depend on the coordinate x_i of the insertion point. Therefore, lines defined by $y_i = const$ are isophasic and can be considered as isophasic trajectories of the dowson. In the general case of an arbitrarily wound up dowser field, one can still define isophasic lines by equation

$$\varphi(x_i, y_i, t) = const \tag{1}$$

When the dowson d_+ is moving on such isophasic trajectories, its structure (radial, circular, or spiral) remains the same. Therefore, the isophasic trajectories can be alternatively called isoform. This second denomination is more convenient in practice: when the orientation of the cross-shaped isogyres of a dowson remains the same, its trajectory is isophasic.

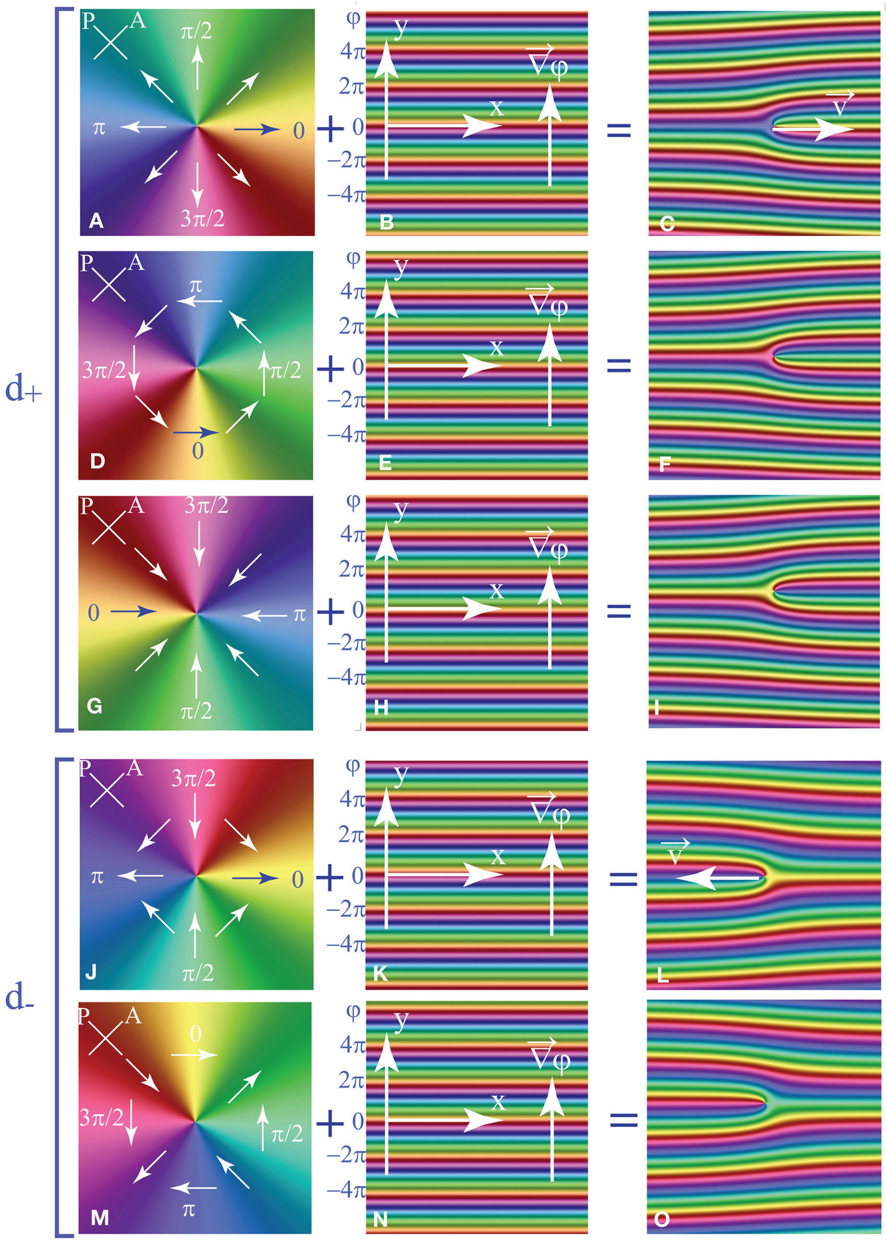

FIGURE 2 | (A–I) Dowson +2π imbedded in a wound up dowser texture. **(A,D,G)** Radial, orthoradial, and antiradial configurations of the dowson d_+ alone. The orthoradial configuration has the lowest elastic energy [5]. **(B,E,H)** Phase field of the dowser texture wound up in y direction: $\varphi = 2\pi y/\lambda$. **(C,F,I)** The wound up phase field with the dowson d_+ imbedded respectively at y = 0 **(C)**, y = $\lambda/4$ **(F)**, and y=$\lambda/2$ **(I)**. **(J–O)** Dowson -2π imbedded in a wound up dowser texture. **(J,M)** Configurations of the dowson d_- depend on the phase $\varphi_i = \varphi(x_i, y_i)$ at the insertion point (x_i, y_i). They result from rotation by the angle φ_i. **(K,N)** Phase field of the dowser texture wound up in y direction: $\varphi = 2\pi y/\lambda$. **(L,O)** The wound up phase field with the dowson d_- imbedded respectively at y = 0 **(L)** and y=$\lambda/4$ **(O)**.

Similar consideration on the insertion of one dowson d_- into a wound up dowser field (illustrated by **Figures 2J–O**) leads to the conclusion that the "hyperbolic" structure of the dowson d_- rotates as a whole when φ_i varies. Such a transformation of the dowson d_- does not change its elastic energy so that trajectories of the dowson d_- are not submitted to elastic constraints.

On the contrary, as stated above, the structure of the dowson d_+ varies with φ_i. Therefore, due to the elastic anisotropy, the elastic energy of the dowson d_+ depends on φ_i so that its trajectories are submitted to an elastic constraint. As we will point out below, dowsons d_+ tend to follow isophasic trajectories.

In **Figure 2C**, the dowson d_+ is located at the left extremity of a 2π wall. The elastic energy stored in this wall is relaxed when the dowson d_+ moves to the right because the wall is shortened by this means.

Qualitatively, a wall of width λ exerts on the dowson d_+ the force which is of the order of the elastic energy per unit length stored in it:

$$\tau_{el} = \frac{1}{2} K_{eff} h \int_0^{\lambda} \left(\frac{\partial \varphi}{\partial \xi} \right)^2 d\xi \approx K_{eff} \frac{2\pi^2 h}{\lambda} \tag{2}$$

During the motion of the dowson with velocity v, the driving force τ_{el} is opposed by another one τ_{visc} resulting from the viscous dissipation:

$$\tau_{visc} \approx \pi \gamma_1 h v \tag{3}$$

Therefore, the velocity of the dowson is given by:

$$v \approx 2\pi \frac{K_{eff}}{\gamma_1} \frac{1}{\lambda} \tag{4}$$

In conclusion, the velocity of the dowson should be independent of the local thickness but should decrease as $1/\lambda$ with the local width λ of the wall.

When instead of the dowson d_+, the dowson d_- is imbedded in the same wound un dowser field (see **Figure 2J**), it is positioned at a right extremity of the 2π wall and therefore will move to the left.

1.5. Pair of Dowsons (d_+,d_-) Inserted in a Wound Up Dowser Field

Figure 3 represents the case of a pair of dowsons d_+ and d_- inserted in the same wound up dowser field. Analytically, the phase field of the wound up dowser texture with the pair of d_+ and d_- dowsons inserted respectively at points $(x_\pm, y_\pm)$ can be expressed as

$$\varphi(x, y) = \frac{2\pi}{\lambda} y + arctan \left(\frac{y - y_+}{x - x_+} \right) + arctan \left(- \frac{y - y_-}{x - x_-} \right) \tag{5}$$

When the two dowsons are far enough, i.e., when $|x_+ - x_-| > \lambda$, they move on trajectories defined by $y(t) = y_+$ and $y(t) = y_-$. We can thus define the distance of trajectories as

$$\delta = y_+ - y_- \tag{6}$$

in terms of the length or as

$$\Delta\varphi = 2\pi \frac{y_+ - y_-}{\lambda} \tag{7}$$

in terms of the phase. The set of seven pictures in **Figures 3A–G** illustrates graphically this concept of the distance of trajectories leading to collisions.

1.6. Aims of Experiments With Dowsons' Colliders

One of aims of our experiments performed with dowsons' colliders is to find conditions which determine the outcome of collisions [9, 10]. When $\Delta\varphi = 0$ (see **Figure 3A**), the two dowsons are located at extremities of the same 2π wall. It seems therefore that annihilation of the (d_+,d_-) pair must occur. Inversely, when $\Delta\varphi > \pi$ (see **Figure 3G**), the two dowsons are located at extremities of two distinct 2π walls so that the annihilation of such a pair will be avoided. We will thus generate experimentally numerous pair collisions with the aim to find the annihilation cross section of dowsons.

Before that, we will focus on the primary aim of our experiments which consists in observing motions of dowsons and measuring their velocities. Knowing that the elastic force driving their motion is inversely proportional to the wave length λ of the wound up texture, we have to wind up the dowser texture more or less expecting that the velocity of dowsons should increase when the phase gradient grows.

2. DOWSONS' COLLIDERS

2.1. Experimental Setups

2.1.1. The Double Dowsons' Collider

The first setup shown in **Figure 4A**, called here "Double Dowson Collider" or DDC, was developed during the study of the rheotropism of the dower texture [6]. It consists mainly of a convex lens (50 mm in diameter) and of a glass slide ($25 \times 75 \times 1 mm$) supported at one end by a translation stage as shown in **Figure 4A**. The radius of curvature of the convex lens is 140 mm. A droplet of a nematic (5CB) is held by capillarity in the gap between the lens and the slide. Typically the diameter of the squeezed droplet is 10 mm and its thickness in the center (regulated by means of the translation stage) is of the order of a few μm. The glass slide is set into vibrations by the force exerted on small magnets by the magnetic field of the coil. Due to the mirror symmetry [with respect to the (x,z) plane] of this device, only the flexural modes of vibration $\zeta = \zeta(x, t)$ are excited in it.

As explained in Pieranski et al. [6], vibration of the slide (in its flexural modes) results in two harmonic motions at the drop center: 1—modulation of the gap thickness and 2—rotation around the y axis. By this means, two Poiseuille flows, radial and dipolar, shifted in phase by $\pi/2$, are driven simultaneously. The resulting effective flows are elliptical: clockwise and anticlockwise in the two halves of the droplet symmetrical with respect to the mirror plane (x,z).

The rheotropic (weathercock-like) behavior of the dowser field results in rotation of the dowser field **d** with the angular velocity $\omega(x, y, t) = d\varphi/dt$ depending on the (x,y) position in the droplet. In the DDC, the torque Γ(x,y,t) exerted by the elliptical Poiseuille flow on the dowser field can be approximated, heuristically, by the function $f_{DDC}(r)\cos(\theta)$, with $f_{DDC}(r) = re^{-r^2}$, $r = \sqrt{x^2 + y^2}$ and $\theta = \arctan(y/x)$, plotted in **Figure 4C**. A typical pattern of a wound up dowser texture observed in experiments between crossed polarisers is shown in **Figure 4E**. It is symmetrical with respect to the (x,z) plane.

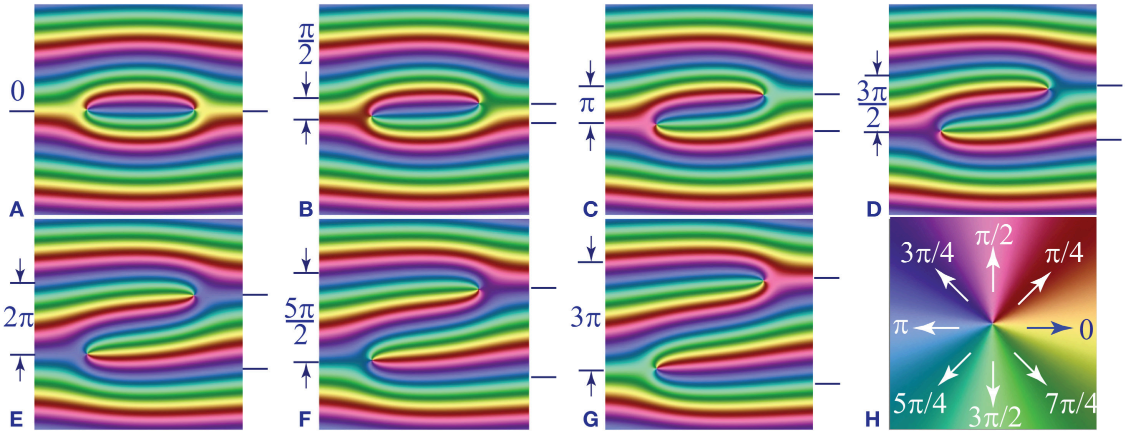

FIGURE 3 | Collision of a pair of dowsons d_+ and d_- imbedded in a wound up dowser texture. The distance of their trajectories in terms of the phase difference $\Delta\varphi$ varies between 0 to 3π from **(A–G)**. The color code for the phase is given in **(H)**.

2.1.2. The Circular Dowsons' Collider

For the purpose of the present study of collisions of dowsons, we developed a second setup (see **Figure 4B**) tailored for production of a circularly wound up pattern. As we will see below, trajectories of dowsons in this Circular Dowsons' Collider are circular and respectively clockwise and anticlockwise for the d_+ and d_- defects.

In this second setup, the mirror symmetry is broken by its structure. The magnet is now located at one extremity of an additional glass slide ($10 \times 75 \times 1mm$) which is attached at its second extremity to the principal glass slide. The force f_{exc} exerted by the coil on the magnet produces now also a torque $f_{exc}\Delta y$ which drives the torsional mode of the principal glass slide. As the flexural and torsional modes have different eigenfrequencies, the $\pi/2$ phase shift between them can be obtained by an appropriate choice of the excitation frequency, which typically is of the order of 360–440 Hz. In such a case, the motion of the principal glass slide at the center of the drop is conical: the normal to it $\vec{\nu}$ precesses on a cone centered on the z axis. The Poiseuille flow in the droplet is now circular (orthonormal) with the amplitude (and sense) depending on the distance r from the drop center.

In the first approximation, the torque Γ(x,y,t) exerted by the elliptical Poiseuille flow on the dowser field can be represented, heuristically, by the function $f_{CDC}(r) = d(f_{DDC}/dr)$ which plotted in **Figure 4D**.

2.2. Experiments With the Double Dowsons' Collider

2.2.1. Velocity of Single Dowsons on Straight Trajectories

As shown in **Figure 5E** the isogyres' pattern of the dowser field wound up in the double dowsons' collider is (almost) symmetrical with respect to the mirror plane (x,z). Therefore, when a single dowson is imbedded in the wound up dowser field in the vicinity of this plane, the 2π wall to which it is attached is parallel to the x axis as discussed in the Introduction (see **Figure 2**). This is the case in the series of five pictures in **Figures 5A–E** showing the motion of a single dowson d_+ "pulled" by a 2π wall along the x axis.

These pictures are extracted from a video containing 55 pictures recorded at intervals of 20 s. Using all of them, we measured the velocity v of the dowson and the width λ of the 2π wall to which it is attached. The result, $v(\lambda)$, is plotted in **Figure 5F**. Arrows labeled from a to e indicate measurement points corresponding to the five picture above.

From the Equation (4) in the section 1.4 we expect that the velocity of the dowson should grow as $v \sim \lambda^{-1}$ with the local wave length λ of the wound up phase field. The dashed line in the diagram of **Figure 5F** represents the best fit to this law. Clearly, the slope of the measured variation $v(\lambda)$ is slightly steeper. We have therefore tempted to fit experimental results with a more general power law $v \sim \lambda^{\alpha}$. The continuous line represents the fit with $\alpha = -1.24$ which clearly is better than the one with $\alpha = -1$.

2.2.2. Dowsons' Sprint

In the search for reasons of this discrepancy, we performed another experiment which could be called "the dowsons sprint." It starts with a simultaneous generation of a row of (d_+,d_-) pairs in a wound up dowser texture by means of a shear flow applied in the y direction (see **Figures 6A,B**). (We postpone the detailed discussion of this issue to another paper.) At t = 0 s, the dowsons d_+ "*in statu nascendi*" are aligned on a slightly curved line AB while the dowsons d_- are aligned on another line CD parallel to AB. As expected, all dowsons d_+ start to move to the left while the dowsons d_- move to the right.

For the purpose of the further discussion we will label seven neighboring dowsons d_+ on the start line AB with an integer index i = 1,2,3,... (see **Figure 6C**).

At the very beginning of this race, the motion of dowsons is driven exclusively by shortening of the 2π walls connected to them, as discussed in the section 1.4. Therefore, they have therefore the same velocity $v_i = const$ and conserve their alignment on the curved line which is moving to the left as a whole.

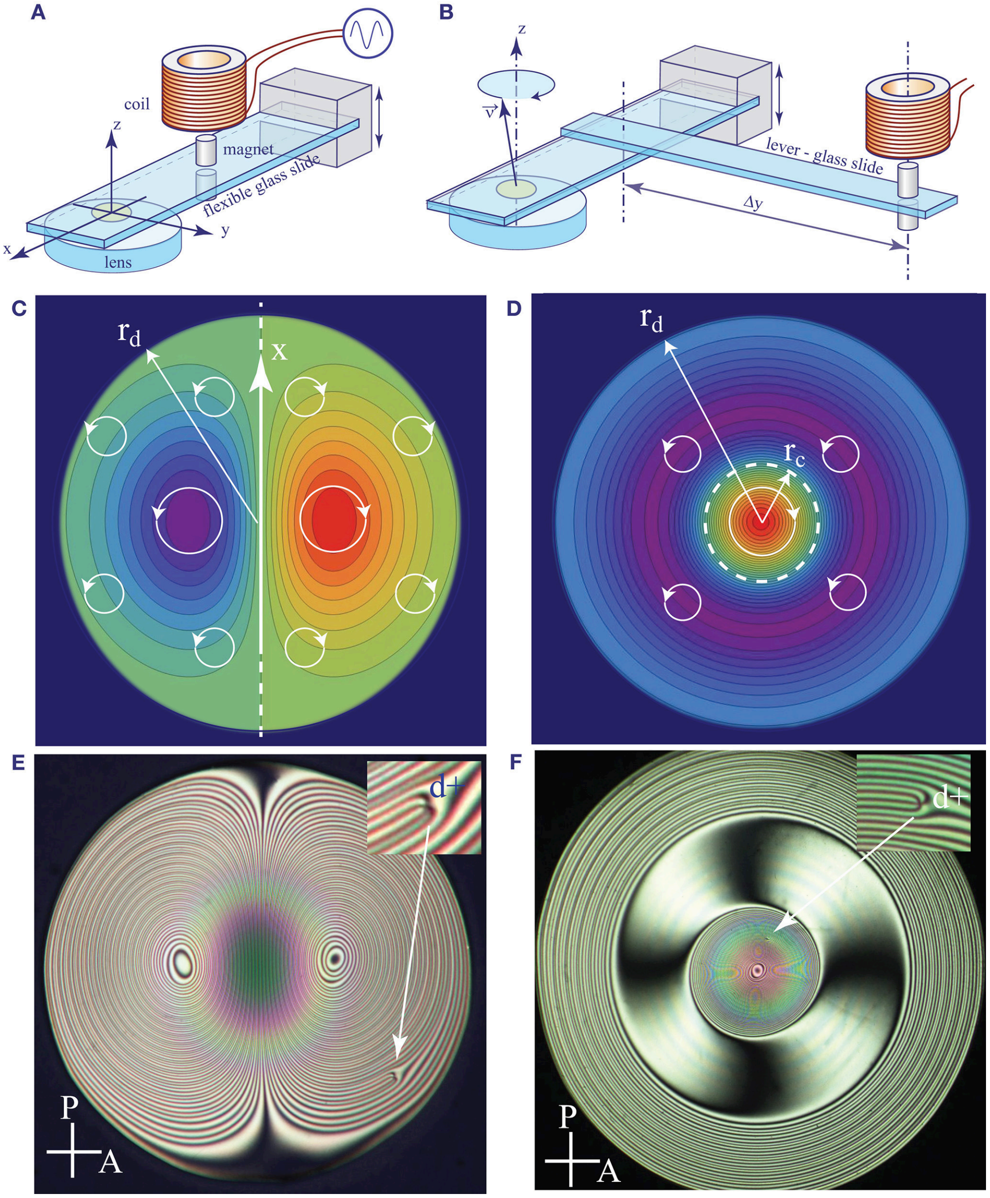

FIGURE 4 | Dowsons' colliders. **(A)** The first version developed during studies of the rheotropism of the dowser texture [6]. Here, we will call it the Double Dowson Collider (DDC). **(B)** The second version tailored for production of circular trajectories of dowsons. We refer to it as the Circular Dowsons' Collider (CDC). **(C,D)** Approximative representations of the rheotropic torque $\Gamma(x, y)$ in DDC and CDC. **(E,F)** Typical wound up dowser textures obtained with DDC and CDC.

However, soon after the departure, an instability occurs: the set of all dowsons is split into two subsets defined by the parity of the index i and, for example, dowsons with i odd (see **Figure 6D**) begin to move more slowly than those with i even. This retardation of odd dowsons (with i = 2n+1) is easy to understand: the width λ_{2n+1} of the 2π walls to which they are attached is twice larger then that of the even dowsons λ_{2n}.

If the force f_i pulling dowsons was determined only by the width λ_i of the 2π walls to which they are attached, the ratio of velocities v_{2n}/v_{2n+1} should be 2. However, measurements of the dowsons' velocity have shown that $v_{2n}/v_{2n+1} \approx 3$.

Explanation of this apparent discrepancy involves a more detailed evaluation of the elastic energy released during the motion of dowsons. If the "lanes" left behind faster dowsons stayed free of distortion, the force acting on them would remain constant during the race. However, as shown in **Figure 6D**, these lanes are filled by enlargement of the lanes of slower dowsons. The corresponding amount of the released elastic energy per unit length is equal to the force f_{2n+1} pulling slower dowsons. In conclusion, the elastic force f_{2n} acting on faster dowsons is not two but three times larger than f_{2n+1}. A more detailed

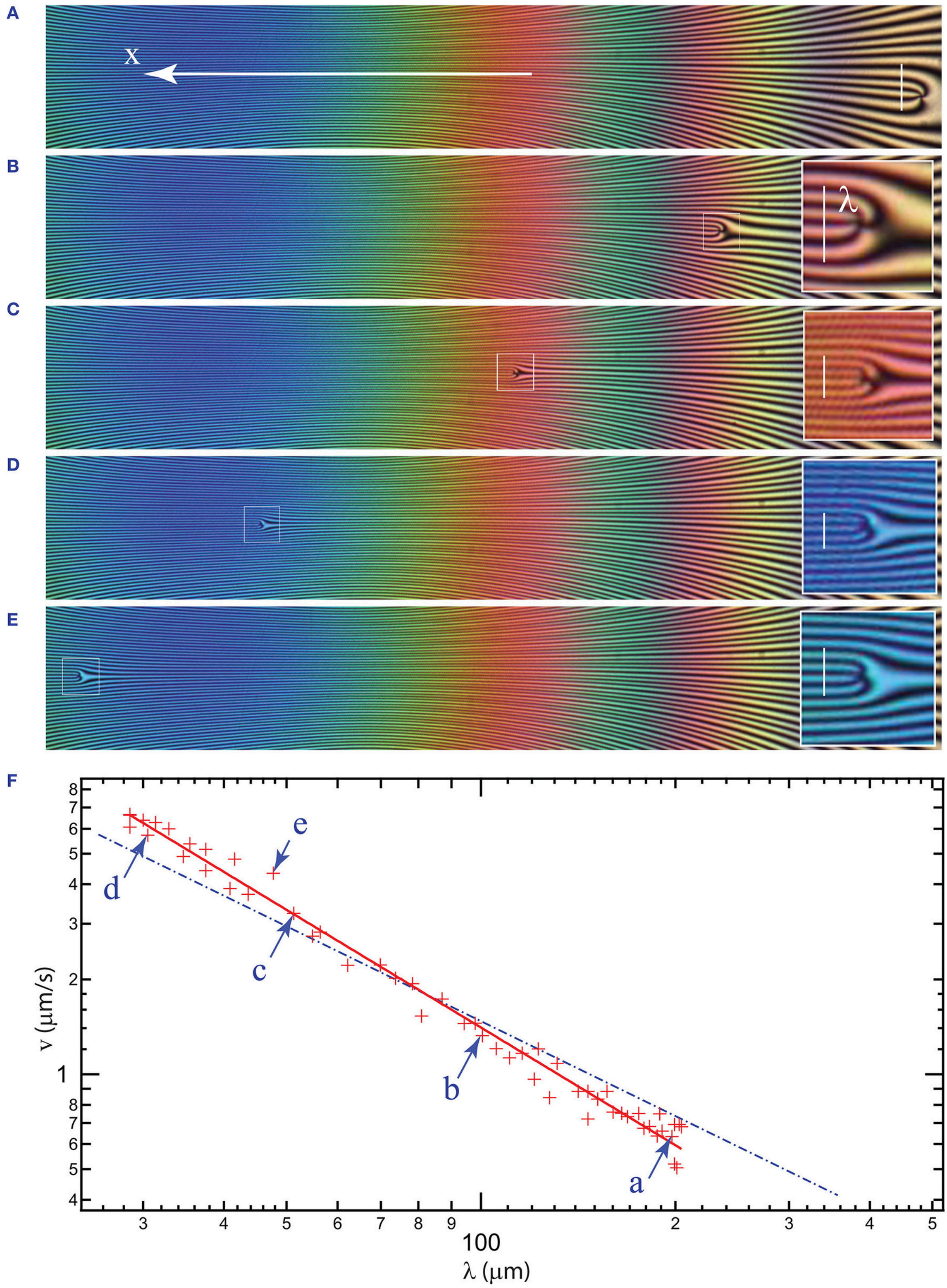

FIGURE 5 | Motion of the dowson d_+ in the phase gradient generated in the dowson collider DDC. The series of five pictures shows successive positions of the dowson d_+ at: **(A)** t = 0 s, **(B)** t = 380 s, **(C)** 520 s, **(D)** 620 s, and **(E)** 700 s. For a better visibility, small areas in vicinity of the dowson have been enlarged in pictures **(B–E)**. **(F)** Plot of the velocity of the dowson d_+ vs. the local wave length of the wound up dowser texture. The continuous red line represents the fit to the power law $v = A\lambda^{\alpha}$ with $\alpha = -1.24$. The dashed blue line corresponds to $\alpha = -1$.

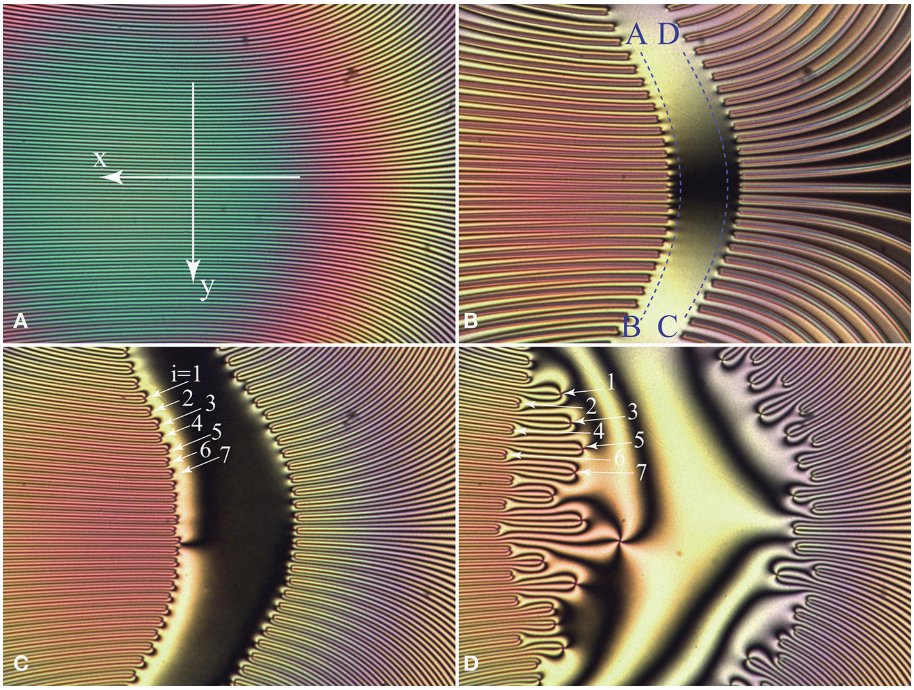

FIGURE 6 | Dowsons race. **(A)** Central portion of the dowser texture wound up in the DDC. It can be seen as a stack of 2π walls. **(B)** Collective generation of (d_+,d_-) pairs by application of a transient shear flow (in y direction) which "breaks" simultaneously all 2π walls. **(C)** At the beginning of the race, dowsons d_+ (or d_-) are moving with the same velocity. **(D)** Odd-even instability: odd dowsons (i = 2n+1) stay behind even dowsons (i = 2n) because they become about three times slower. (Collaboration with Elise Hadjefstatiou and Lisa-Marie Montagnat).

discussion of the dowsons' race is postponed to another article.

2.2.3. Are Trajectories of Dowsons Isophasic?

In experiments with dowsons' colliders, the 2π walls can be defined as bundles of four adjacent isogyres; when one crosses one of such bundles, the phase varies by 2π.

In the vicinity of the mirror symmetry plane (x,z) of the Double Dowson Collider, the 2π walls are parallel to the x axis so that the dowsons d_+ and d_- are moving on straight isophasic trajectories. However, as we know already from section 2.1 (see **Figure 4C**), the whole dowser texture, wound up in the Double Dowsons' Collider, can be seen as made of 2π walls forming closed loops in the absence of defects. Let us suppose that a pair (d_+,d_-) of dowsons has been generated by breaking one of these 2π walls. Pulled in opposite directions by the broken 2π wall these dowsons will move apart. Will their trajectories remain isophasic? If it was the case, they would remain connected to the same 2π wall which would became shorter and shorter so that, finally, the two dowsons would meet and annihilate. Such a behavior was indeed observed in first experiments with the dowser texture wound up by a rotating magnetic field [5].

As we will see below, experiments with dowsons' colliders have shown that trajectories of dowsons are not necessarily isophasic so that they do not remain connected to the same 2π wall. Therefore, when after a half turn of the wound up dowser texture the two dowsons of the pair meet again, the distance of their trajectories $\Delta\varphi$ in terms of the phase is not necessarily zero so that their annihilation is not granted.

2.2.4. The First Evidence for Non-isophasic Trajectories of Dowsons

The issue of non isophasic trajectories of dowsons was raised for the first time in experiments with the DDC. Let us consider a typical experiment illustrated in the **Figures 7A,B** by a view of one of the two target patterns of the wound up dowser texture. We identify here four dowsons d_+ and three dowsons d_-. On this background we represented by rows of circular markers successive positions, recorded at intervals of 30 s, of dowsons d_+ (**Figure 7A**) and d_-(**Figure 7B**).

Several conclusions can be drawn from this figure:

1. Dowsons d_+ and d_-, pulled by 2π walls, circulate in opposite directions, as expected.
2. The velocity of dowsons is correlated to the local width λ of 2π walls, as expected.
3. The trajectory of the dowson d_+ is parallel to isogyres while the one of the dowson d_- is crossing isogyres. In other words, the trajectory of the dowson d_+ seems to be isophasic while that of the dowson d_- is not isophasic.
4. The non isophasic behavior of dowsons d_- is even more obvious when one considers the one labeled with a dashed circle in **Figure 7**. It is located in the center of the target pattern and this central position is dynamically stable during the phase winding. Now, as during the phase winding, the

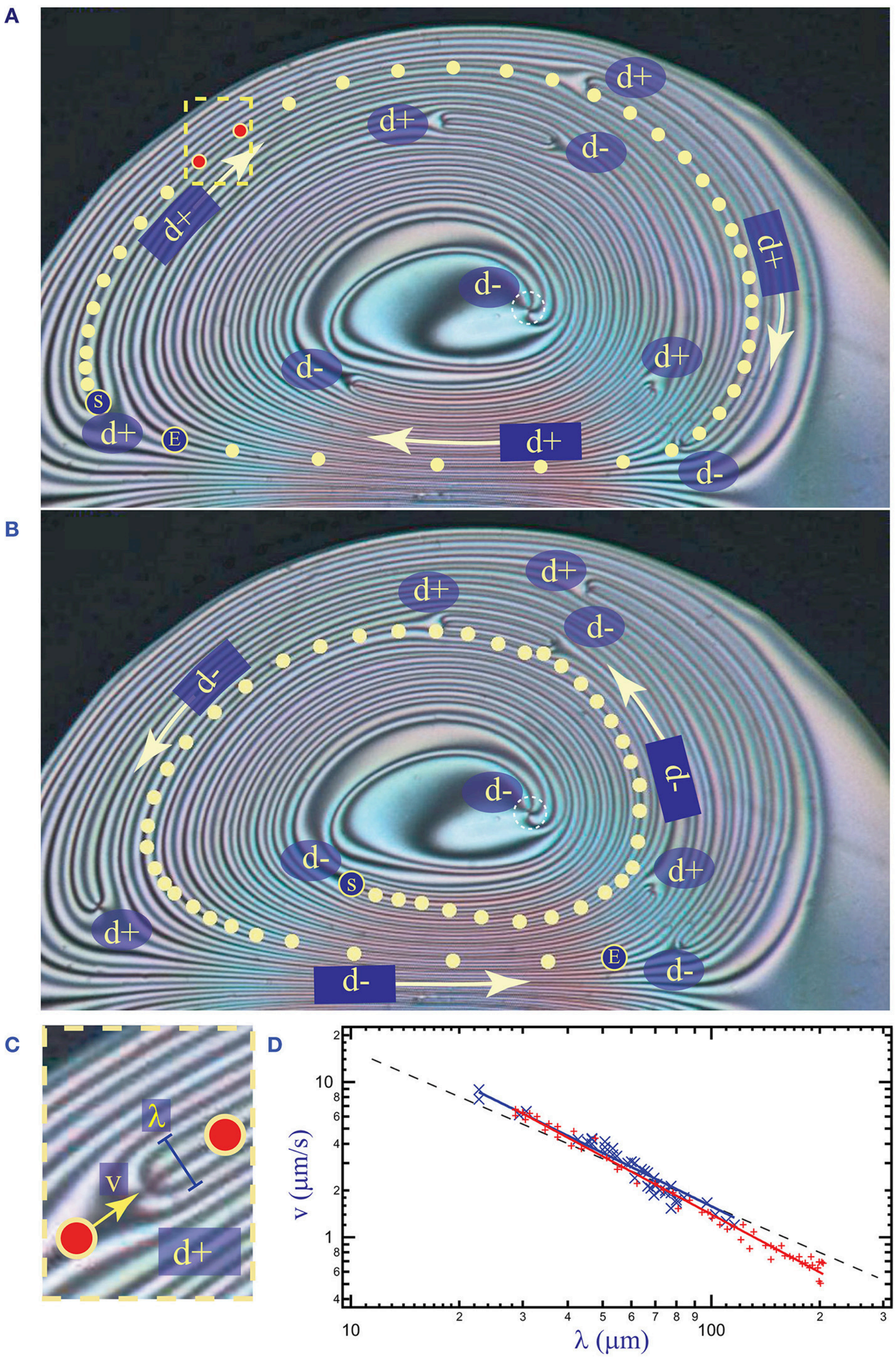

FIGURE 7 | Trajectories of two dowsons, d_+ and d_-, in the DDC. Circular markers indicate successive positions of dowsons at time intervals of 30 s. Trajectories start from larger markers labeled "S" and end at markers labeled "E." **(A)** The dowson d_+ circulates in the clockwise direction of the phase winding. **(B)** The dowson d_- circulates in the opposite, anticlockwise direction. Its trajectory starts in the vicinity of the center of the target pattern and ends at the periphery. Clearly such a trajectory is not isophasic. **(C)** Segment of the trajectory inside the dashed frame displayed in **(A)**. **(D)** Blue crosses: velocity of the dowson d_+ from **(A)** plotted vs. the width λ of the 2π wall pulling on it. Continuous blue line: the best fit to the power law with the exponent $\alpha = -1.14$. Red crosses and the red line: reminder of the data from **Figure 5**. The dashed black line corresponds to $\alpha = -1$.

angular velocity $\omega = d\varphi/dt$ is the largest here, this central position is obviously not isophasic. Consequently, the maltese cross (formed by four isogyres) of this dowson is rotating as a whole with the angular velocity ω.

Knowing that the circular markers in **Figure 7** indicate successive positions of dowsons at time intervals of 30 s, the velocity v of dowsons has been determined. Simultaneously the local width λ of the 2π walls pulling on dowsons has been measured in this

Figure 7A. Results obtained with the dowson d_+ are plotted with blue crosses in **Figure 7D**. The best fit to the power law $v \sim \lambda^\alpha$ plotted with the blue plain line was obtained with $\alpha = -1.14$. On the same diagram of **Figure 7D** we have plotted once again (with red crosses and a red line) results shown previously in **Figure 5**.

2.3. Experiments With the Circular Dowsons' Collider

The most recent experiments performed with the Circular Dowsons' Collider confirmed these conclusions but also unveiled other remarkable properties of the dowsons dynamics. In particular, we have found that the result of the phase winding process in the Circular Dowsons' Collider depends on the initial state of the dowser field as well as on the amplitude of the excitation. In general, for topological reasons (homeotropic boundary conditions at the nematic/air interface of the meniscus), the dowser field can contain only an odd number 2n+1 of dowsons d_+ and an even number 2n of dowsons d_-. We will show below that two different dynamically stable states C-B1 or C-B2 can be reached when, respectively, $n = 0$ and $n > 0$.

2.3.1. Cladis-Brand Stationary State C-B1: One Dowson d_+ Orbiting Around the Target Pattern

In the simplest case of $n = 0$, one dowson d_+ is located initially at the center O of the drop and the dowser field has the radial configuration imposed by the cuneitropisme [4] of the dowser texture. This radial configuration also satisfies the homeotropic boundary conditions at the nematic/air interface on the edge of the droplet (see **Figure 8A**).

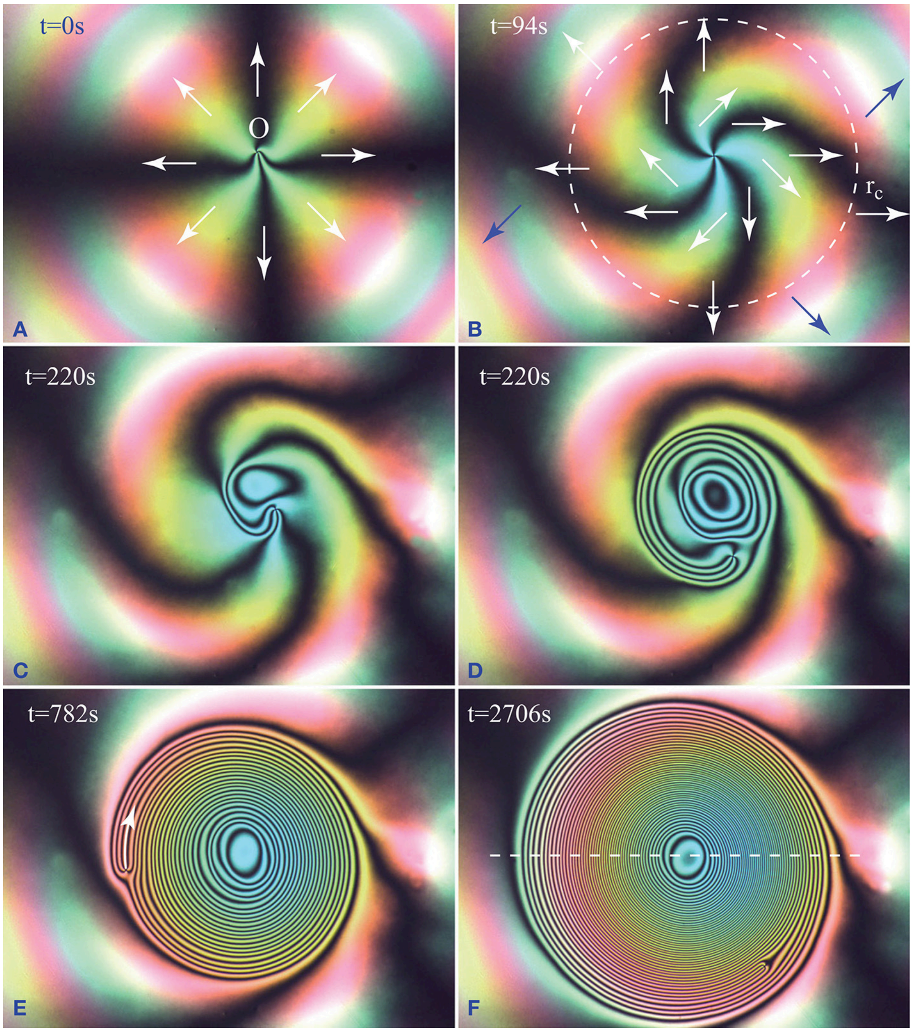

FIGURE 8 | Cladis-Brand state C-B1 obtained by winding of the dowser texture in the Circular Dowsons' Collider. **(A)** Initial radial configuration of the dowser field. **(B)** Beginning of the winding in the anticlockwise direction. The initial configuration is slightly perturbed by a $-\pi/2$ rotation in the center. **(C)** The first isogyre nucleated in the center is growing. **(D,E)** Continuation of the winding. Remark: As for energetic reasons the dowson d_+ cannot change easily its configuration, it conserves its phase staying at the periphery of the growing target pattern. **(F)** Dynamically stable Cladis-Brand state C-B1. The continuing phase growth in the center of the target pattern is absorbed by the orbiting dowson which acts as a phase sink.

When the rheotropic driving torque due to the circular Poiseuille flow is applied to the dowser field, it starts to rotate with the angular velocity $\omega(r, t)$, varying with the distance r from the center as shown in **Figure 4D**. Rotation of the dowser field is thus clockwise in the center at r=0, then the angular velocity $\omega(r, t)$ decreases and changes its sign at $r = r_c$ (dashed circle in **Figure 8B**). As a result, the maltese cross formed by four isogyres shown in **Figure 8A** is deformed: its four arms become spiral as shown in **Figure 8B**. Later, the dowson d_+ leaves the center O and a target pattern of loop-like isogyres starts its growth from the center O: one after another, new isogyres' loops are nucleated at the center O and their radii are growing (see **Figure 8**).

If $\omega(0, 0, t)$ is the phase growth rate at the center O, then the rate of nucleation of 2π walls (each made of four isogyres) is $\omega(0, 0, t)/(2\pi)$.

During this winding process, the dowson d_+ is pushed (elastically) by isogyres toward the periphery of the target pattern as shown in **Figure 8**. By this means, its position inside the evolving phase field $\varphi(x, y, t)$ remains isophasic. This behavior results from the elastic anisotropy of the nematic. Indeed, as shown in **Figure 2** the configuration of the dowson d_+ depends on the phase φ_i at the point of its insertion into the wound up phase field. From Pieranski et al. [5] we know that the elastic energy of the dowson d_+ depends on its configuration. As energetically the orthoradial configurations (clockwise or anticlockwise) are the best ones, the dowson tends to conserve its position at $\varphi = \pi/2(mod\pi)$.

Simultaneously, pulled by the 2π wall to which it is attached, the dowson d_+ begins its orbiting motion with velocity **v** (see **Figure 8E**) around the target pattern made of concentric 2π walls. The orbiting dowson d_+ can be seen as a "phase sink": after each whole turn around the target pattern, one 2π wall is "swollen." If T is the period of the orbit, then we can define the phase sinking rate as $2\pi/T$.

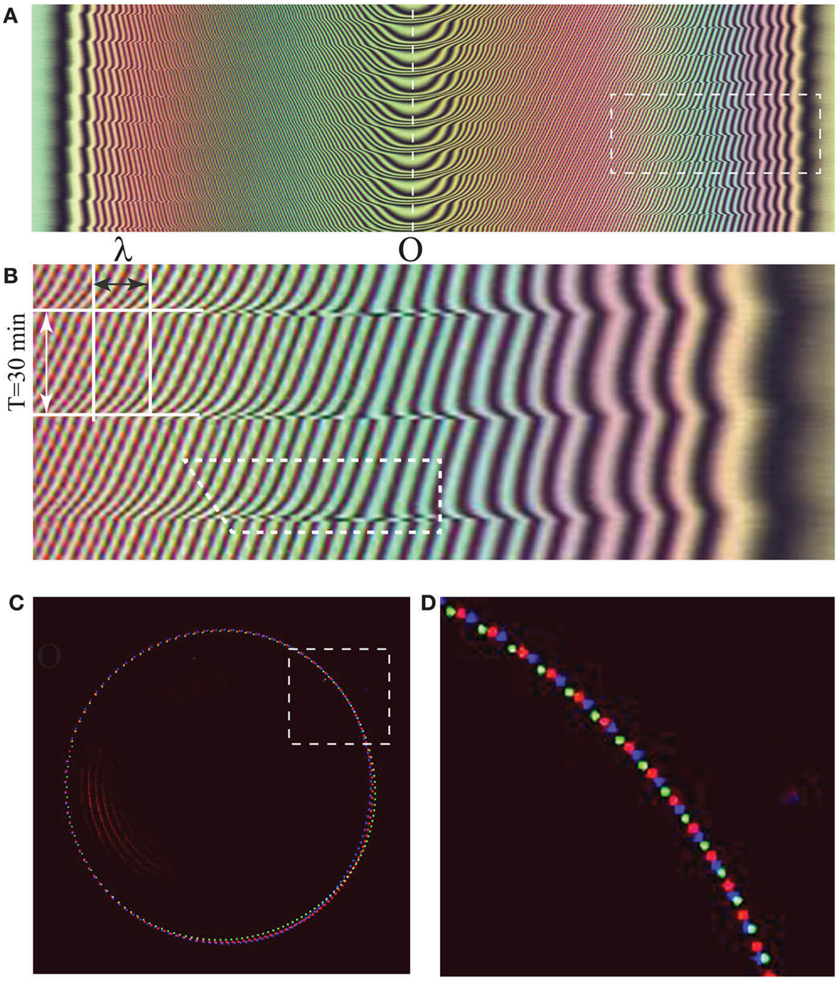

FIGURE 9 | Cladis-Brand [11] dynamically stable state C-B1 of the phase winding in the Circular Dowsons' Collider. **(A)** Spatio-temporal cross section taken along the dashed line defined in **Figure 8F**. Four new isogyres are nucleated at the center O during one period T of the orbiting motion of the dowson d_+. **(B)** Blow up of the rectangular domain defined with a dashed line in **(A)**. λ is the width of a 2π wall composed of four oblique trajectories of isogyres. During one period T = 30 min, the 2π wall is shifted by λ to the right. **(C)** Successive positions of the dowson d_+ recorded as colored dots at intervals of 10 s during three periods of its orbital motion. The three colors of dots correspond to the three periods T of the orbital motion. **(D)** Blow up of the rectangular domain defined with dashed line in **(C)**.

During the winding process, the phase growth rate $\omega(r,t)$ decreases because the rheotropic torque is opposed by the growing elastic torque. Simultaneously, the sinking rate increases because the orbiting dowson is moving faster pulled by the narrowing 2π wall.

The dynamically stable (stationary) phase field $\varphi(x,y,t)$ is achieved when the phase growth rate at the center equals the sinking rate due to the orbiting dowson d_+ : $\omega(0,0,t) = 2\pi/T$ (see **Figure 9**). As Cladis and Brand have formerly discovered in free standing smectic C films the same configuration of a $+2\pi$ defect orbiting around a target pattern [11] we propose to call it "The Cladis-Brand state 1" or shortly C-B1.

2.3.2. C-B2: Second Version of the Cladis-Brand Stationary State

At first sight, upon the action of the rheotropic torque $\Gamma_r(r)$, the dowser field should rotate in the anticlockwise direction for $r > r_c$, r_c being defined in **Figure 4D**. It seems therefore that new isogyres could nucleate also in the annular area near the second extremum of the torque $\Gamma_r(r)$. In the experiment discussed above and illustrated by the series of six pictures in **Figure 8**, this is not the case: new isogyres nucleate only at the first extremum of $\Gamma_r(r)$ located in the center O at r = 0.

Explanation of this experimental fact is very simple. Beside the rheotropic torque driving the rotation of the dowser field,

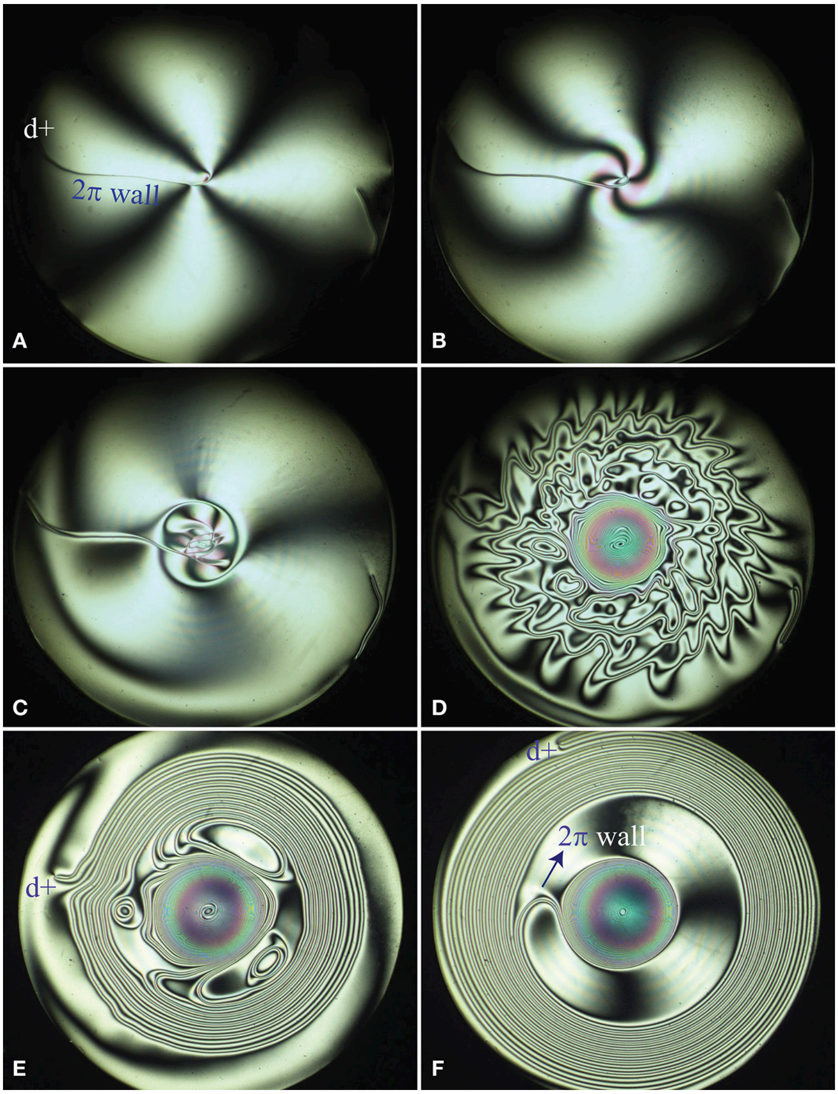

FIGURE 10 | Generation of the second Cladis-Brand dynamically stable state by the phase winding in the Circular Dowsons' Collider. **(A)** At the beginning of the winding, the "residual" d_+ dowson is close to the edge of the droplet. It is connected to the center O by a 2π wall. **(B–D)** Upon application of a strong excitation, the phase is wound up simultaneously in clockwise direction for $r < rc$ and anticlockwise direction for $r > rc$. **(E,F)** Emergence of the second Cladis-Brand dynamically stable state with the dowson d_+ orbiting around an extended double target pattern. The outer and inner target patterns are made of one spiral-shaped 2π wall connecting the dowson d_+ with the center of the droplet.

there is also the cuneitropic torque $\Gamma_c = (\pi K/h)\mathbf{g} \times \mathbf{d}$ (see [4]) tending to orient the dowser field **d** in the direction of the thickness gradient **g**, that is to say in the radial direction **r** of the sphere/plane geometry of the sample (this is the case in **Figure 8A**). This cuneitropic torque vanishes at r=0 for symmetry reasons but is finite at $r > r_c$. For a given r, it reaches its maximum value $\Gamma_{cmax} = (\pi K/h(r))|\mathbf{g}(r)|$ when **d** is orthogonal to **g**. In the experiment of **Figure 8**, for $r > r_c$ the rheotropic torque is smaller than Γ_{cmax} so that rotation of the dowser field is hindered there. In another experiment illustrated by the series of six pictures in **Figure 10**, the rheotropic torque was much larger so that nucleation of new isogyres occurred also in the secondary extremum of the rheotropic torque.

2.3.3. Triplet Stationary State: Two Dowsons d_+ Orbiting Around One d_- in the Center

Experiments with the Circular Dowsons' Collider unveiled a third stationary state (see **Figure 11**). To reach it, the winding process has to be applied to the dowser field with n>0, that is to say containing at least two dowsons d_- and one dowson d_+ when $n = 1$.

For reasons which so far have been not fully understood, during the winding, the dowson d_- is attracted to the center O [maximum of $\omega(r, t)$] and stays there while the two dowsons d_+, on the contrary, are pushed to the periphery of the growing pattern. Let us emphasize that in this new configuration the winding process does not require nucleation of new isogyres. The phase growth in the center is now due to rotation of

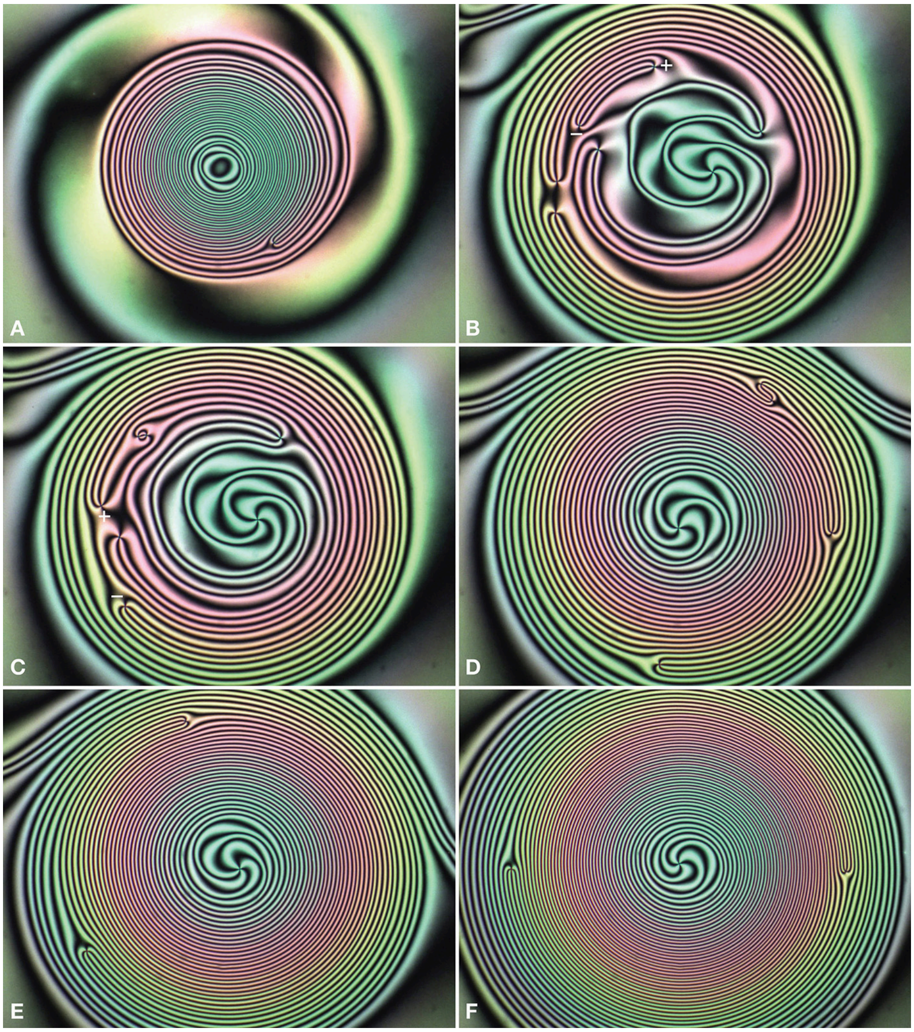

FIGURE 11 | Generation of the dynamically stable "triplet" configuration of dowsons during the phase winding in the Circular Dowsons' Collider. **(A)** First, the Cladis-Brand configuration of one orbiting d_+ dowson is generated as shown in **Figure 8**. **(B)** Application of a transitory shear flow to the Cladis-Brand state results in generation of three additional dowsons pairs (d_+,d_-). One these pairs is labeled as "+" and "−." **(C)** Annihilation of the (d_+,d_-) pair labeled in **(B)**. The second (d_+,d_-) pair is labeled as "+" and "−." **(D)** Annihilation of the (d_+,d_-) pair labeled in **(C)**. Only three dowsons are left. **(E)** Continuation of the winding process. **(F)** Dynamically stable trio of three dowson: two dowsons d_+ are orbiting around the dowson d_- which stays in the center.

the dowson d_- located there. This mechanism is similar to the Frank-Read model of crystal growth in which a spiral step, attached to a dislocation emerging on a crystal facet, is rotating.

When n is larger than 1, the (d_+,d_-) pairs in excess with respect to $n = 1$ are eliminated by annihilation during the winding process as shown in **Figures 11B–D**.

Like in the Cladis-Brand process, the stationary triplet state is reached when the phase growth rate in the center, due to the rotation of the dowson d_-, is fully compensated by the orbital motion of the two dowsons d_+ acting as phase sinks. In this stationary state, the two dowsons d_+ are located on the same orbit (see **Figure 12D**) and have therefore the same angular velocity ω_{d_+}. The total phase absorption rate is therefore $2\omega_{d_+}$. Therefore, if the d_- dowson in the center rotates with the angular velocity ω_{d-} then in the stationary state one has:

$$\frac{d\varphi}{dt} = \omega_{d-} + 2\omega_{d_+} = 0 \tag{8}$$

so that

$$\omega_{d-} = -2\omega_{d_+} \tag{9}$$

This equality is illustrated by in **Figures 12A,B**.

3. GENERATION, COLLISIONS, AND ANNIHILATION OF DOWSONS' PAIRS

The dynamically stable states of the Circular Dowsons' Collider are convenient for studies of generation of dowsons and of their subsequent collisions which can lead to annihilation. Indeed,

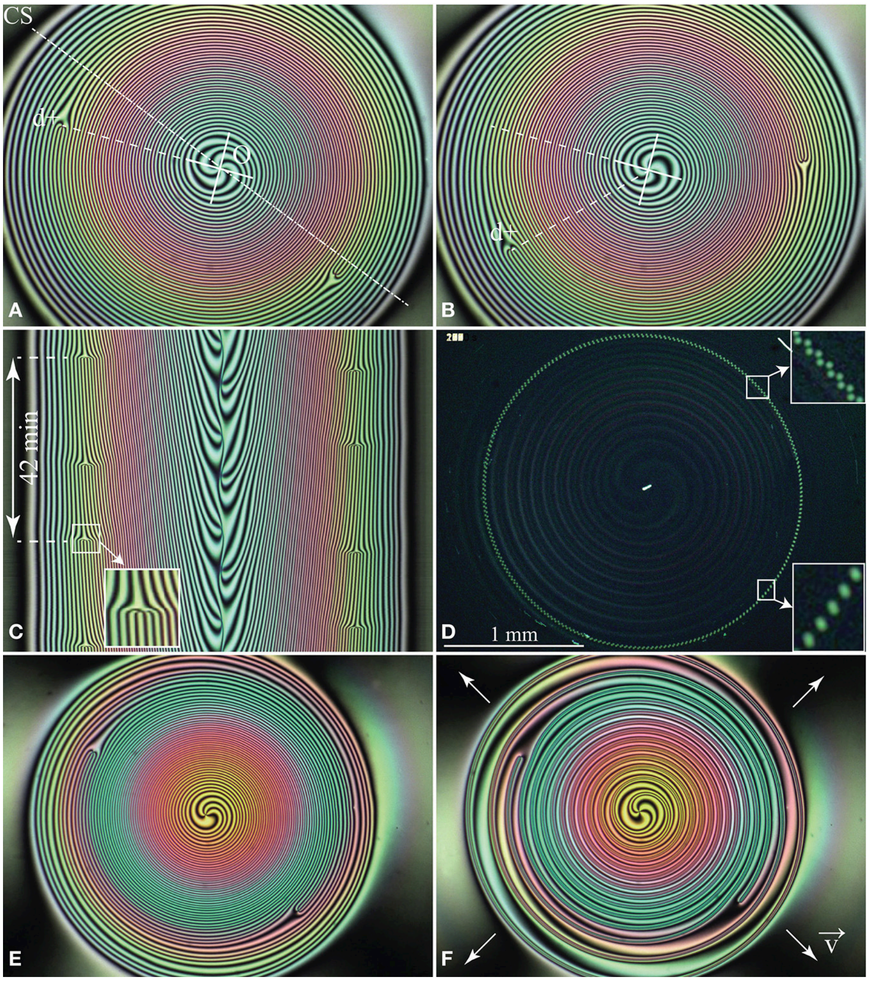

FIGURE 12 | Dynamics of the stable triplet configuration of dowsons. **(A,B)** Two pictures of the wound up dowser texture taken at an interval of 5 min. In this interval, the dowson d_- in the center rotated by $\pi/2$, while the dowson d_+ on their orbits made only 1/8th of the whole turn. **(C)** Spatio-temporal cross section taken along the dashed line CS defined in **(A)**. The inset shows that the orbiting dowson d_+ acts as a phase sink: after each crossing of the line CS by one of orbiting dowsons d_+, four isogyres are suppressed. Simultaneously four new isogyres are emitted by the dowson d_- rotating in the center O. **(D)** Successive positions of the two dowsons d_+ recorded at intervals of 10 s during one period of their orbital motions. The two inset show that velocities of the two dowsons d_+ are the same. **(E,F)** To check that the two dowsons d_+ are isophasic, a divergent Poiseuille flow was applied to the wound up dowser field shown in **(E)**.

like positrons and electrons in a hadron collider, dowsons d_+ and d_- are moving in the Circular Dowsons' Collider on respectively clockwise and anticlockwise trajectories so that they can undergo collisions that can result in annihilation of dowsons pairs.

By a collision we mean an event during which the linear distance l_{+-} between two dowsons, d_+ and d_-, decreases and becomes of the order of the winding wave length λ.

3.1. Generation of One (d_+,d_-) Pair

For the purpose of clarity of the forthcoming discussion, let us consider the example represented in **Figure 13** which shows in the **Figure 13A**, a view of the wound up dowser field shortly after generation of just one dowsons pair. The process of generation itself is illustrated by the series of five pictures **(Figures 13C–G)**. It is triggered by a rapid and short forth-and-back motion of the oscillating glass slide applied to the wound up texture visible in **Figure 13C**. During the motion, the image of the isogyres' pattern becomes fuzzy (**Figure 13D**) but shortly after that, at the beginning of the relaxation (**Figure 13E**), one can distinguish seven 2π walls thinned by the perturbation.

As discussed in Pieranski et al. [6] thinning of 2π walls is due to the rheotropism of the dowser texture, that-is-to-say, to its sensitivity to Poiseuille flows. Anticipating a more detailed discussion in section 3.5 we infer that at the beginning of the relaxation a transitory Poiseuille flow 2π walls occurred.

An excessive thinning of one of the 2π walls leads to its breaking shown in **Figure 13E**. Subsequently the two dowsons generated by this means are moving in opposite directions on initially isophasic trajectories.

3.2. Collision of a (d_+,d_-) Pair

As the isogyres pattern in the wound up Cladis-Brand state is made of concentric rings, one could think that after a half turn of their orbits (see **Figure 13B**), the freshly generated dowsons should come to a collision on isophasic trajectories. The series of five pictures **(Figures 13H–I)**, shows clearly that this is not the case: there is a $\Delta\varphi \approx 2\pi$ distance (see **Figure 13H**), in terms of the phase, between trajectories of the two dowsons coming to their collision. We postpone discussion of this paradox to another paper.

In meantime, let us just say that the two dowsons coming to collision are pulled by two distinct 2π walls so that annihilation is avoided.

3.3. Rules for Collisions of (d_+,d_-) Pairs

When more than one pair of dowsons is generated simultaneously, the subsequent collisions occur at variable distances $\Delta\varphi$ of trajectories. From observations of many of such collisions with $-2\pi < \Delta\varphi < +2\pi$ we inferred the following rules:

1. **Bypass**: When $|\Delta\varphi| > \pi$, the annihilation is avoided and the dowsons are passing by (see **Figures 14A–I**).

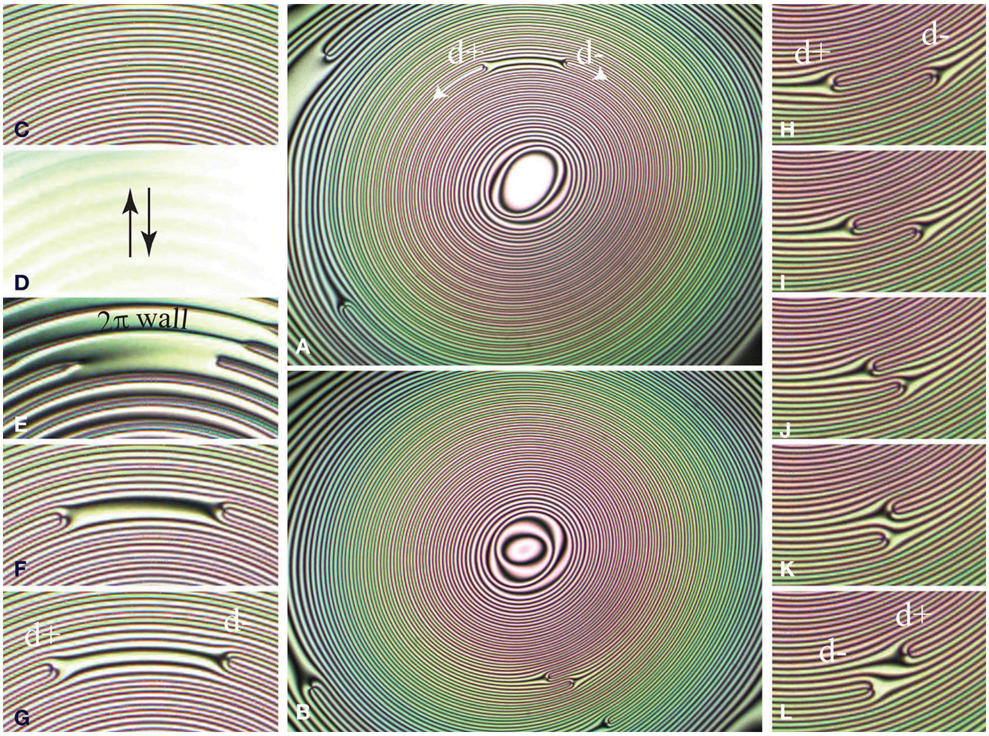

FIGURE 13 | Generation and collision of a dowsons' pair in the Circular Dowsons Colider. **(A)** Wound up dowser field with a pair of dowsons "in statu nascendi." **(B)** After a half turn of their orbits, the d_+ and d_- dowsons are coming to a collision. **(C–G)** Generation of the dowsons pair. **(H–L)** Collision of the pair without annihilation.

2. **Annihilation**: When $|\Delta\varphi| < \pi$, the annihilation occurs (see **Figures 14J–R**).
3. **Critical**: When $|\Delta\varphi| = \pi$, the outcome of the collision is random.

3.4. Influence of Poiseuille Flows on Collisions of Dowsons Pairs, Experiment

The rules formulated above apply to pairs of dowsons moving inside a very slowly evolving stationary wound up dowser field.

Knowing from former experiments that the dowser texture is very sensitive to Poiseuille flows [6] we used this property, called rheotropism, to influence the outcome of dowsons collisions. As an example we point out in the series of 20 pictures in **Figures 15A–T** that the annihilation, which should occur in terms of the collisions' rules applied to the pair of dowsons in **Figure 15A**, can be avoided by application of a Poiseuille flow in an appropriate direction.

Indeed, at the beginning of the experiment (see **Figures 15A–D**) dowsons d_+ and d_- coming to collision are almost isophasic and are connected by a 2π wall which is shortening. The outcome of the forthcoming collision seems unavoidable: an annihilation. However, an application of the Poiseuille flow $\vec{v}$ in the left direction [parallel to the dowser field in the middle of the wall (d_+,d_-)], has a very striking effect well visible in pictures **Figures 15E–L**: the wall connecting the dowsons pair as well as the whole system of isogyres is split in such a manner that the two dowsons are reconnected to two new, different 2π walls. These walls, narrowed by the Poiseuille flow, pull strongly on dowsons which move rapidely on distinct trajectories separated now by 2π, in terms of the phase. After cessation of the flow (**Figures 15M–T**) the system of isogyres relaxes: the trajectories of the two dowsons become almost isophasic again but they diverge now.

3.5. Influence of Poiseuille Flows on Collisions of Dowsons Pairs, a Model

Theoretically, this experiment can be modeled as follows. At the beginning of the experiment, the phase field can be is expressed

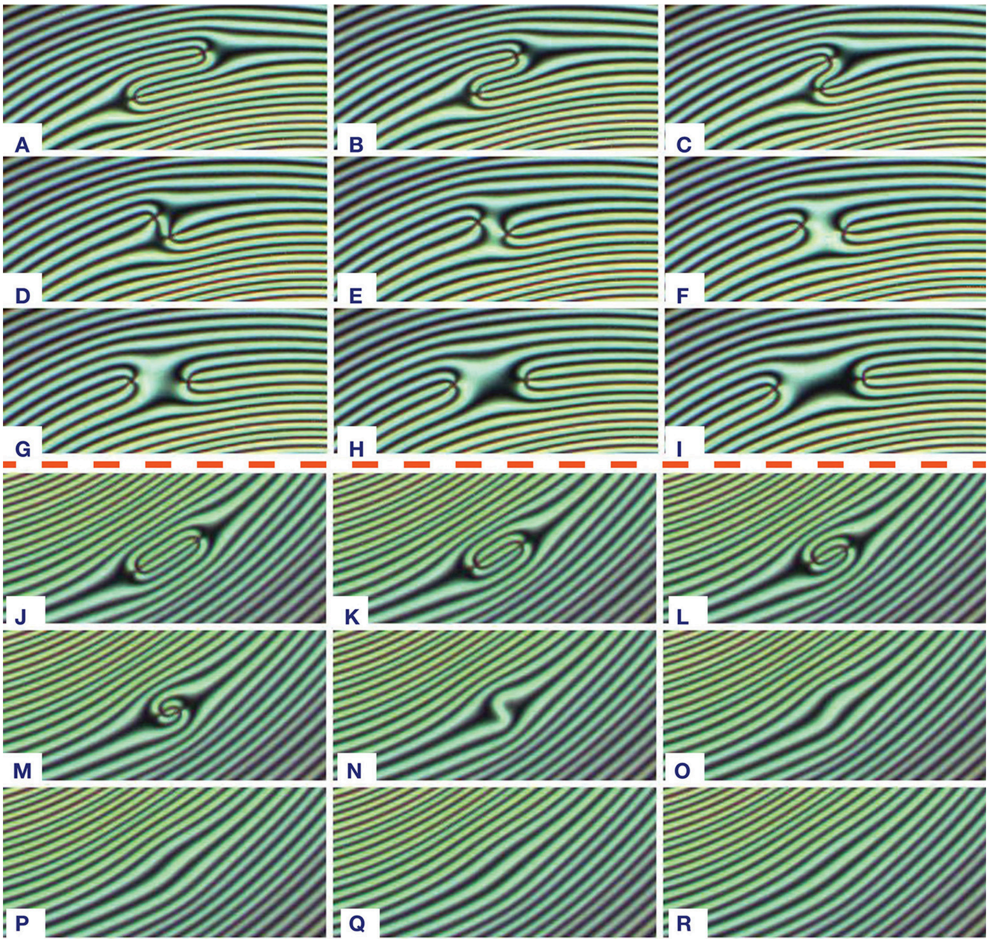

FIGURE 14 | Criterium for the outcome of collisions. **(A–I)** When $|\Delta\varphi| > \pi$, annihilation is avoided. Here, $|\Delta\varphi| \approx 3\pi/2$. Pictures taken at intervals of 10 s. **(J–R)** When $|\Delta\varphi| < \pi$, annihilation occurs. Here, $|\Delta\varphi| \approx \pi/2$. Pictures taken at intervals of 5 s.

as before (see Equation 5):

$$\varphi_o(x,y) = \frac{2\pi}{\lambda} y + arctan\left(\frac{y-y_+}{x-x_+}\right) + arctan\left(-\frac{y-y_-}{x-x_-}\right) \tag{10}$$

with $(x_+, y_+) = (-5, -\pi/4)$ and $(x_-, y_-) = (5, \pi/4)$ so that

$$\Delta\varphi = 2\pi \frac{y_+ - y_-}{\lambda} = \frac{\pi}{2} \tag{11}$$

This initial field is depicted in **Figure 15U** using the color code defined in **Figure 2A**. Application of the Poiseuille flow of the amplitude v_{max} in the -x direction perturbs the field $\varphi_o(x,y)$. The rheotropic torque exerted by this Poiseuille flow on the field $\varphi(x,y)_o$ can be written as:

$$\vec{\Gamma}_{rt} = \frac{2\alpha_2}{\pi} v_{max} \sin\varphi_o(x,y) \vec{e}_z \tag{12}$$

In the first approximation, the resulting elastic distortion is proportional to this torque so that the perturbed phase field can be written as:

$$\varphi_{pert}(x,y) \approx \varphi_o(x,y) + \delta\varphi \sin(\varphi_o(x,y)) \tag{13}$$

with $\delta\varphi \sim v_o$. The graphic representation of $\varphi_{pert}(x,y)$ in **Figure 15V** shows an agreement with the experimental picture in **Figure 15I**.

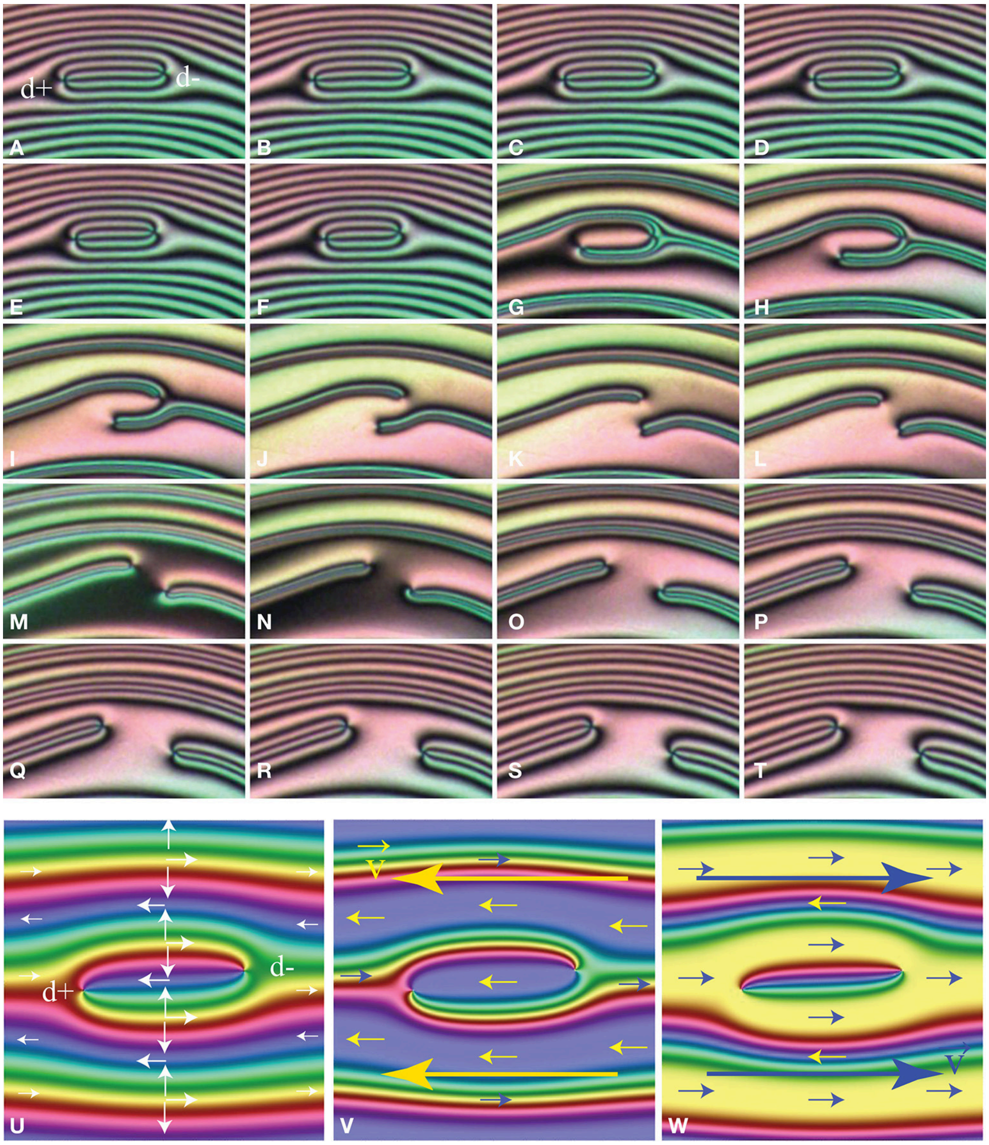

FIGURE 15 | Influence of Poiseuille flows on collisions of dowsons. **(A–T)** Experiment. Evolution of the dowser field before, during and after application of a Poiseuille flow. **(U–W)** Simulation. Pair of dowsons without flow **(U)** and in the presence of flows in left and right drections.

Let us stress that when the Poiseuille flow is applied in the inverse, +x direction, our model predicts that the 2π wall connecting the dowsons' pair is no split but narrowed as shown in **Figure 15W** so that the annihilation is accelerated.

These simulations are in agreement with our experiments: the outcome of the forthcoming collisions can be chosen at will by application of Poiseuille flows in appropriate directions.

4. CONCLUSIONS

The present paper is by no means exhaustive in the matter of generation, motions, and collisions of dowsons. Nevertheless, it raises new issues concerning (1) laws of motion of dowsons driven by phase gradients and (2) laws ruling the outcome of dowsons' collisions.

In particular, there is a huge difference in the behavior of dowsons d_+ and d_- during phase winding. The dowsons d_+ cannot rotate because of the elastic anisotropy so that they tend to escape from the winding up phase field and are going to areas where the phase growth rate is zero. In the case of a unique dowson d_+, this leads to the Cladis-Brand stationary states in which the orbiting dowson d_+ absorbs the phase generated by the dowsons' collider.

The behavior of the dowson d_- seems to be a contrary one and much more enigmatic. Indeed, experiments showed that during the winding process the dowsons d_- is attracted to the area in which the phase growth rate is maximal. By this means another stationary state, with the dowson d_- in the center (acting as a phase source) and two dowsons d_+ orbiting around it (acting as phase sinks), can be reached. This gyrophilic behavior of the dowson d_- remains to be explained.

The law ruling translational motion of dowsons on their orbits needs also further clarification. Theoretically, in the first approximation, the velocity v of dowsons should be proportional to the local phase gradient $\nabla\varphi = 2\pi/\lambda$: $v \sim \lambda^{\alpha}$ with $\alpha = -1$. Experiments have shown however that in practice the exponent α is smaller than -1. This discrepancy is probably due to interactions between moving dowsons which certainly play the major role during the dowsons sprint discussed in section 2.2.2.

From observations of dowsons pairs (d_+d_-) moving on counter-rotating orbits, a rule for the outcome of their collisions, i.e., either annihilation or bypass, was inferred. The distance of trajectories $\Delta\varphi$ in terms of the phase appeared as the pertinent parameter: for $\Delta\varphi < \pi$ a collision of a pair of dowsons leads to their annihilation, while for $\Delta\varphi > \pi$ the dowsons are passing by. However, this rule is valid only for quasi-static stationary wound up textures and can be easily broken by application of a Poiseuille flow in an appropriate direction.

DATA AVAILABILITY STATEMENT

The datasets generated for this study are available on request to the corresponding author.

AUTHOR CONTRIBUTIONS

All authors listed have made a substantial, direct and intellectual contribution to the work, and approved it for publication.

FUNDING

PP was indebted to S. Ravy for a financial support. MG thanks FCTPortuguese Foundation for Science and Technology under projects UID/CTM/50025/2013, and PTDC/CTM-BIO/6178/2014 and M-ERA-NET2/0007/2016 (CellColor).

ACKNOWLEDGMENTS

Our interest in physics of dowsons was stimulated by fruitful interactions with L. Giomi [12], T. Lubensky, and V. Vitelli during the Lorentz Workshop on Topology in Complex Fluids hold in Leiden in 2018. We acknowledge a fruitful collaboration with Elise Hadjefstatiou and Lisa-Marie Montagnat during experiments on the dowsons' race. This work benefited from the technical assistance of I. Settouraman, V. Klein, S. Saranga, J. Sanchez, M. Bottineau, J. Vieira, I. Nimaga, and C. Goldmann.

REFERENCES

1. de Gennes PG. Types de singularités permises dans une phase ordonnée. *CRAS*. (1972) **275**:319–21.
2. Embon L, Anahory Y, Jelić ZL, Lachman EO, Myasoedov Y, Huber ME, et al. Imaging of super-fast dynamics and flow instabilities of superconducting vortices. *Nat Commun.* (2017) **8**:85. doi: 10.1038/s41467-017-00089-3
3. Gilli JM, Thiberge S, Vierheilig A, Fried F. Inversion walls in homeotropic nematic and cholesteric layers. *Liquid Cryst.* (1997) **23**:619–28. doi: 10.1080/026782997207894
4. Pieranski P, Godinho MH, Čopar S. Persistent quasi-planar nematic texture: its properties and topological defects. *Phys Rev E.* (2016) **94**:042706. doi: 10.1103/PhysRevE.94.042706
5. Pieranski P, Čopar S, Godinho MH, Dazza M. Hedgehogs in the dowser state. *Eur Phys J E.* (2016) **39**:121. doi: 10.1140/epje/i2016-16121-7
6. Pieranski P, Hulin JP, Godinho MH. Rheotropism the dowser state. *Eur Phys J E.* (2017) **40**:109. doi: 10.1140/epje/i2017-11598-0
7. Pieranski P, Godinho MH. Flexo-electric polarisation of the dowser texture. *Soft Matter*. (2019) **15**: 1459–694. doi: 10.1039/C8SM02329H
8. Kleman M, Lavrentovich OD. Topological point defects in nematic liquid crystals. *Philos Mag.* (2006) **86**:4117–37. doi: 10.1080/14786430600593016
9. Cladis PE, Brand HR. Hedgehog-antihedgehog pair annihilation to a static soliton. *Phys A.* (2003) **326**:322–32. doi: 10.1016/S0378-4371(03)00254-1

10. Svetec M, Kralj S, Bradač Z, Žumer S. Annihilation of nematic point defects: pre-collision and post-collision evolution. *EPJE*. (2006) **20**:71–9. doi: 10.1140/epje/i2005-10120-9
11. Cladis PE, Finn PL, Brand HR. Stable coexistence of spiral and target patterns in freely suspended films of smectic-C liquid crystals. *Phys Rev Lett*. (1995) **75**:1518–21. doi: 10.1103/PhysRevLett.75.1518
12. Giomi L, Kos Ž, Ravnik M, Sengupta A. Cross-talk between topological defects in different fields revealed by nematic microfluidics. *Proc Natl Acad Sci USA*. (2017) **114**:E5771–7. doi: 10.1073/pnas.1702777114

Conflict of Interest: The authors declare that the research was conducted in the absence of any commercial or financial relationships that could be construed as a potential conflict of interest.

ORIGINAL RESEARCH
published: 06 February 2020
doi: 10.3389/fphy.2019.00234

Interactions Between Topological Defects and Nanoparticles

Syou-P'heng Do[1], Amine Missaoui[1], Alessandro Coati[2], Andrea Resta[2], Nicolas Goubet[1], Sébastien Royer[1], Geraldine Guida[3], Emrick Briand[1], Emmanuel Lhuillier[1], Yves Garreau[2,4], David Babonneau[5], Michel Goldmann[1,2], Doru Constantin[6], Bernard Croset[1], Bruno Gallas[1] and Emmanuelle Lacaze[1]*

[1] Sorbonne Université, Faculté des Sciences, CNRS, Institut des Nano-Sciences de Paris (INSP), Paris, France, [2] Synchrotron Soleil, BP 48, L'Orme des Merisiers, Gif sur Yvette, France, [3] LEME, EA 4416, Universite Paris Nanterre, Nanterre, France, [4] Université de Paris, Laboratoire Matériaux et Phénomènes Quantiques, CNRS, Paris, France, [5] Institut Pprime, Département Physique et Mécanique des Matériaux, UPR 3346 CNRS, Université de Poitiers, Poitiers, France, [6] Laboratoire de Physique des Solides, Bat. 510, UMR-CNRS 8502, Université Paris-Sud, Université Paris-Saclay, Orsay, France

Liquid Crystal (LC) topological defects have been shown to trap nanoparticles (NPs) in the defect cores. The LC topological defects may thus be used as a matrix for new kinds of NP organizations templated by the defect geometry. We here study composites of LC smectic dislocations and gold NPs. Straight NP chains parallel to the dislocations are obtained leading to highly anisotropic optical absorption of the NPs controlled by light polarization. Combining Grazing Incidence Small Angle X-ray scattering (GISAXS), Rutherford Back Scattering (RBS), Spectrophotometry and the development of a model of interacting NPs, we explore the role of the Np size regarding the dislocation core size. We use NPs of diameter $D = 6$ nm embedded in an array of different kinds of dislocations. For dislocation core larger than the NP size, stable long chains are obtained but made of poorly interacting NPs. For dislocation core smaller than the NP size, the disorder is induced outside the dislocation cores and the NP chains are not equilibrium structures. However we show that at least half of these small dislocations can be filled, leading to chains with strongly enhanced electromagnetic coupling between the NPs. These chains are more probably stabilized by the elastic distortions around the defect cores, the distortion being enhanced by the presence of the grain boundary where the dislocations are embedded.

Keywords: liquid crystals, nanoparticles, topological defects, smectic dislocations, gold, LSP resonance

Edited by:
Uroš Tkalec,
University of Ljubljana, Slovenia

Reviewed by:
Ingo Dierking,
University of Manchester,
United Kingdom
Julio Cesar Armas-Perez,
University of Guanajuato, Mexico

***Correspondence:**
Emmanuelle Lacaze
emmanuelle.lacaze@insp.upmc.fr

Specialty section:
This article was submitted to
Soft Matter Physics,
a section of the journal
Frontiers in Physics

***Received:** 19 September 2019*
***Accepted:** 16 December 2019*
***Published:** 06 February 2020*

Citation:
Do S-P, Missaoui A, Coati A, Resta A, Goubet N, Royer S, Guida G, Briand E, Lhuillier E, Garreau Y, Babonneau D, Goldmann M, Constantin D, Croset B, Gallas B and Lacaze E (2020) Interactions Between Topological Defects and Nanoparticles. Front. Phys. 7:234. doi: 10.3389/fphy.2019.00234

1. INTRODUCTION

Composites made of liquid crystals (LCs) and nanoparticles (NPs) are studied a lot nowadays [1–5]. One idea is to allow for controlled modification of the LC properties, which can be photonic properties but also elasticity, conductivity, magnetic properties or phase transition of LC [6–10]. The other idea is to take advantage of the anisotropy of the LC matrix or of its easy activation under external parameters (temperature, electric field) to build original anisotropic NP organizations [11, 12] or/and activable NP organizations [13]. Controlled NP organizations can allow for a control of plasmonic resonance when metallic NPs are concerned through the control of the nanorod orientation [14] or of the electromagnetic coupling between NPs for nanospheres and nanorods [11, 15]. In such a context LCs with topological defects have attracted attention because they might serve as templates for specific nanoparticle (NP) assemblies. Trapping of NPs within topological defect cores indeed allows for the release of the defect energy and the stabilization of the composite systems [16–20]. As a result LC topological defects may be used for new kinds of NP organizations templated by the defect geometry [21–24]. In return the study of composites made of a LC matrix with topological defects and NPs can bring information on the topological defects themselves, in particular on the size, structure and energy of the defect core [3, 25], still mainly unknown [26].

In this article, we focus on smectic dislocations. Oriented arrays of smectic dislocations are formed in the so-called smectic oily streaks [27]. Composites made of smectic oily streaks and gold NPs have been shown to lead to the formation of NP chains, for gold nanospheres [11, 21] and end-to-end oriented gold nanorods [15], trapped in the linear and oriented dislocation cores. NP chains are interesting specific assemblies because of their anisotropy but are not easy to obtain since under Van der Waals interactions nanospheres form hexagonal networks, whereas nanorods form side by side assemblies. In the case of metallic NP chains, Localized Surface Plasmon (LSP) resonance becomes highly anisotropic and controlled by light polarization [11, 15, 21]. The trapping process by topological defect cores can be not only generalized to different NP shapes (from NP spheres to NP rods) but also to different NP natures. It has been shown that semiconducting nanorods also are oriented along a single direction in smectic oily streaks. The release of disorder core energy does not depend on the shape and on the NP nature. It thus allowed for the control of the polarization of semiconducting single-photon emitters [12]. We now explore the role of the NP size. The trapping efficiency by defect cores is expected to decrease when the NP size becomes larger than the defect core [28]. We study composites made of gold NPs of diameter $D =$ 6 nm in smectic oily streaks composed of an array of different kinds of dislocations in order to confront the respective roles of NP size and dislocation core size. Using combined Grazing Incidence Small Angle X-ray scattering (GISAXS), Rutherford Back Scattering (RBS), Spectrophotometry and the development of a model of interacting NPs, we compare the structure and stability of NP chains formed in dislocations of different core sizes. Different features are revealed depending on the respective sizes of NPs and dislocation cores. For large dislocations, larger than the NP size, long and stable NP chains are formed but with poorly interacting NPs. For small dislocations, a strong electromagnetic coupling between NPs occurs due to the disorder induced outside the dislocation core. However the NP chains maybe not an equilibrium state but instead a metastable state stabilized by the large elastic distortion around the dislocation core.

2. MATERIALS AND METHODS

2.1. NP Synthesis

1, 2, 3, 4-tetrahydronaphthalene (tetralin, 99% Aldrich), Chlorotriphenylphosphine Au (I) (98%) and tert-butylamine borane (97%) were obtained from STEM chemicals. Dodecanethiol (DDT), oleylamine, HAuCl4 (98%), hexane, were obtained from Sigma-Aldrich, Toluene (98%) from Riedel de Haen. Ethanol (99.85%), chloroform (99.2%) from VWR. All reagents were used as received without further purification. For the NPs of diameter $D = 6$ nm the synthesis is based on reference [29]. Fifty mg of HauCl4 are mixed in a three neck flask with 5 mL of oleyalmine and 5 mL of tetralin and degassed at room temperature. The flask is dipped in an ice bath. The temperature controller is put in the ice bath rather than in the three neck flask. Meanwhile, 22 mg of tertbutylborane is mixed with 0.5 mL of oleylamine and 0.5 mL of tetratlin. The mixture is sonicated until the full dissolution of the salt. The three neck flask is put under Ar. The borane solution is injected promptly. The solution changes color to brown and then to purple. Sonication is continued for 36 min. 0.5 mL of DDT is added to stop the reaction growth. The content of the flask is mixed with 5 mL of ethanol and then centrifuged. The formed pellet is redispersed in toluene. NPs of diameter $D = 6$ nm and polydispersity 9% were obtained as shown by SAXS measurements performed on synchrotron Soleil.

2.2. Composite Film Preparation

The samples were created by depositing a droplet of a mixture of 8CB (4-n-octyl-4′-cyanobiphenyl, smectic LC at room temperature, $c = 0.02$ M) and gold NPs in toluene (concentration varying from 5.5×10^{10} NPs μL^{-1} to 1.6×10^{11} NPs μL^{-1}) onto a polyvinyl alcohol (PVA) polymer film, initially spin-coated and rubbed on a glass substrate (1.8 cm^2).

2.3. Optical Microscopy and Micro-Spectroscopy Techniques

We measure the extinction properties of the samples using a Maya 2000 pro spectrometer coupled to an upright optical microscope (Leica DMRX) to probe 40×40 μm^2 areas. The signal was collected through an air objective (×50, NA = 0.85). The composite films were excited with linearly polarized light either along or perpendicular to the oily streaks. To extract the wavelength associated with the LSPR, the normalized spectra were fitted with a gaussian curve.

2.4. Dipole Coupling Model

The distance between the nanoparticles associated with a given LSP resonance wavelength, λ was calculated using a dipole coupling model in the quasistatic approximation (NPs diameter $D \ll \lambda$) [30]. In this approximation the multipolar interactions between the nanoparticles as well as the retardance effect are not considered, this latter assumption being obviously correct due to the small size of the NPs. In this case the resonance condition is characterized by [30]:

$$\epsilon = \epsilon_m \frac{\sum +8\left(\frac{S}{D}+1\right)^3}{\sum -4\left(\frac{S}{D}+1\right)^3} \tag{1}$$

with ϵ the Au NP dielectric function, ϵ_m the dielectric function of an homogeneous surrounding medium. S is the lattice sum of the NPs assembly, the NPs being associated with punctual dipoles. S depends on the geometry of the assembly and accounts for the electromagnetic coupling between the NPs [31]. For an infinite chain of NPs with a polarization parallel to the chains, the sum in equation (1) is $S \approx 4.8$. For monolayers associated with an infinite hexagonal network, the sum S is $S \approx 5.5$ [31, 32].

The Au NP dielectric function was recalculated based on Johnson and Christy data [33] to take into account the small size effect and the influence of the chemical interface, leading to broadening and blue-shifted LSPR of the isolated NPs in toluene (**Figure S1**) [21, 34].

2.5. Finite Element Calculations

For the calculations based on finite elements we have used the commercial software HFSS by ANSYS. Different chains of N nanoparticles with a diameter $D = 6$ nm and separated by a gap s were modeled. The number of particles was varied between 2 and 10 and the gap between 1 and 6 nm. The nanoparticles were modeled as spheres with the optical constants of gold and placed in the centre of a $400 \times 400 \times 400\,\mathrm{nm}^3$ box filled with a medium with a constant refractive index of 1.51. Radiating boundaries were applied to the box and a plane wave polarized along the chain of nanoparticles was used as illumination. The optical response was calculated between 460 and 660 nm then the ohmic losses integrated over all the nanoparticles were computed to determine the position of the plasmon resonance.

2.6. X-Ray Diffraction

X-ray diffraction measurements were carried out at the SIXS beamline on the SOLEIL synchrotron facility. On SIXS beamline, the photon energy was fixed to 18 keV and the X-ray beam size to $300 \times 300\ \mu\mathrm{m}^2$. The measurements were performed with the substrate almost parallel to the X-ray beam, in GISAXS (Grazing Incidence Small Angle X-ray Scattering) configuration [11].

2.7. Rutherford Backscattering Spectroscopy

The Rutherford Backscattering Spectrometry measurements were performed with the 2.2 MV Van de Graaff accelerator of the SAFIR platform of Sorbonne Université. RBS measurements were performed by positioning the samples perpendicularly to a beam of alpha particles with an energy of 1,800 keV, a diameter of 0.5 mm, a current of 40 nA and a charge of 4 μC. The measurements were performed with the ion beam incident normal to the sample surface and the backscattered ions were detected by a surface-barrier detector placed at a scattering angle of 165°. The energy calibration and solid angle of the detector are deduced from the measurement of a reference sample of 5.64×10^{15} bismuth atoms cm^{-2} implanted into silicon.

3. SMECTIC OILY STREAKS

We have used arrays of oriented defects of 8CB (4′-octyl-4-biphenylcarbonitrile) thin films deposited on rubbed poly(vinyl alcohol) (PVA) surfaces, the so-called smectic oily streaks. Due to hybrid anchoring at the two interfaces (air/8CB and 8CB/PVA, respectively), the smectic layers become curved in flattened hemicylinders perpendicular to the anchoring on the substrate, itself defined by the rubbing of the PVA substrate (**Figure 1**) [35–37]. These flattened hemicylinders, with a typical periodicity of several hundreds of nanometers, can be detected by polarized optical microscopy between crossed polarizers, leading to the observation of parallel stripes (**Figure 1A**). Their internal structure has been determined using combined X-ray diffraction and ellipsometry measurements [27]. It is characterized by the presence of two rotating grain boundaries per hemicylinder, buried within the smectic film, which profile has been precisely established by X-ray diffraction (in red in **Figure 1B**) [27]. Along each rotating grain boundary, three edge dislocations parallel to the hemicylinder axis (i.e., oriented along the Ox direction—**Figure 1B**) are expected (blue points in **Figure 1B**). This is due to a different number of rotating and flat smectic layers from each part of the grain boundary. They are of different Burgers vector depending on their localization along the rotating grain boundary. A first dislocation of Burgers vector, b with $b/d = 2$ (d is the intra-smectic layer spacing) is located in the first half of the rotating grain boundary, the nearest to the substrate. The two other dislocations lie close to the summit of the rotating grain boundary ($b/s \approx 6$). They are separated from each other by a distance of ~50 nm and it has been shown that the rotating grain boundary profile does not depend on the thickness of the smectic film [27].

4. CHAIN FORMATION

Gold NPs of diameter $D = 6$ nm, covered by dodecanethiol ligands, have been first deposited on rubbed PVA. As shown by GISAXS measurements obtained on Soleil synchrotron facility (SIXS beamline - see the section Materials and Methods) and in agreement with electron microscopy measurements (**Figure 2**), the NPs form an hexagonal network on the substrate. Three pairs of rods are observed, (10), $(\overline{1}0)$, (11), $(\overline{11})$ and (20), $(\overline{2}0)$, being in the ratio 1, $\sqrt{3}$ and 2. They are the signature of the hexagonal network. The position of the (10) rod at 0.92 nm^{-1} leads to an inter-NP gap $s = 1.93 \pm 0.05$ nm, in perfect agreement with other measurements from the literature [38–40]. s is slightly larger than the length of the straight dodecanethiol, 1.8 nm, showing that within the NP network the ligands could be not too distorted but at least they are strongly interdigitated. The light extinction curve (**Figure 2B**) displays the LSP resonance of the NPs organized in an hexagonal network at $\lambda = 558$ nm. In comparison with the LSP resonance of gold NPs dispersed in toluene ($\lambda_o = 516$ nm, **Figure S1**), a red-shift is evidenced, in relation with the electromagnetic coupling between the NPs in the hexagonal network. It can be used to extract the inter-NP gap value in the dipolar approximation considering that the hexagonal networks are large enough to be considered as infinite for the LSP properties (see Materials and Methods) [41–43]. The 1.9 nm value consistent with X-ray results is recovered by using an optical index of $n = 1.51$ indeed close to the one of disordered dodecanethiol ($n = 1.46$). This is in agreement with an optical index dominated by the grafted dodecanethiol ligands around the NPs [11, 44].

In contrast with NPs deposited on rubbed PVA without LC, when NPs are inserted in 8CB smectic oily streaks (see section Materials and Methods), the light extinction becomes anisotropic. **Figure 3A** shows a typical extinction spectrum (probed area of $40 \times 40\ \mu m^2$). For a polarization of the incident light perpendicular to the oily streaks (black spectrum), the extinction maximum is slightly shifted to a lower wavelength compared to the one of NPs dispersed in toluene ($\lambda_o = 516$ nm, **Figure S1**), with LSP resonance at $\lambda_\perp \approx 500$ nm. In contrast,

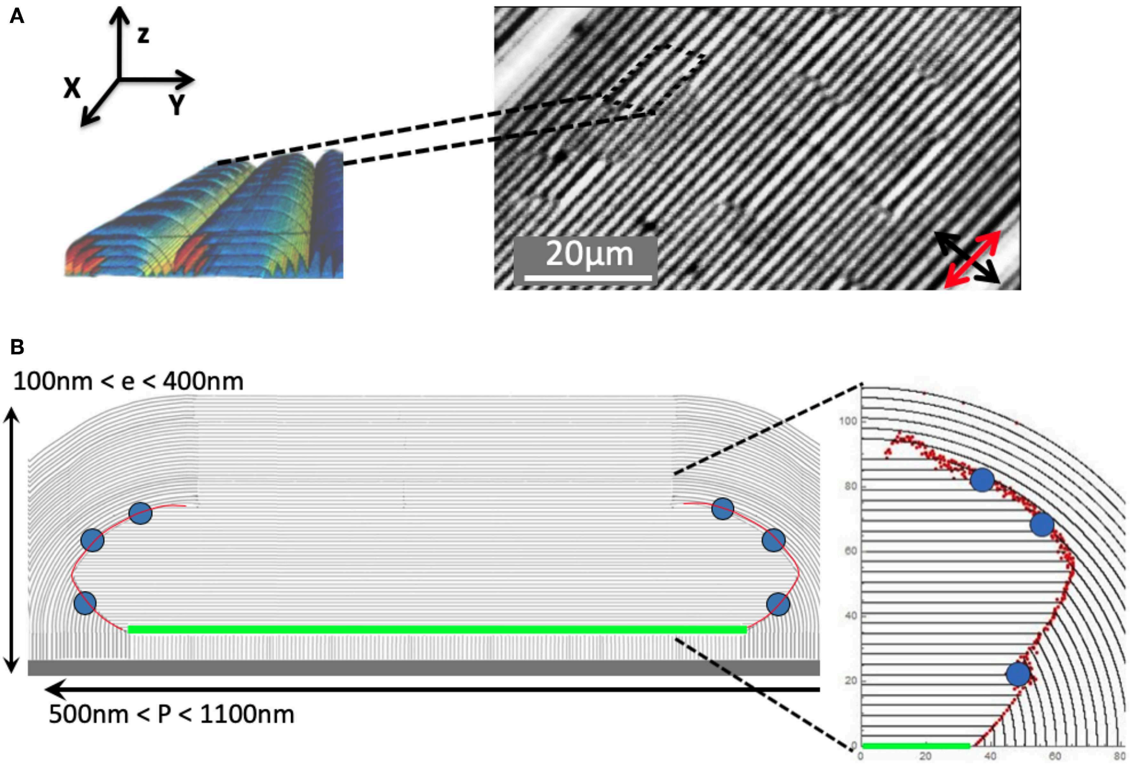

FIGURE 1 | (A) Polarized optical microscopy image of oily streaks observed from the top of a 150 nm-thick sample. Each stripe along OX corresponds to one hemicylinder and two hemicylinders in perspective are represented **(B)** Detail in side-view [in the (Y, Z) plane] of the smectic layers stacked in one given flattened hemicylinder for a typical thickness of 230 nm. Two rotating grain boundaries are shown in red, including dispersed edge dislocations (blue spots). A central grain boundary is underlined in green [27].

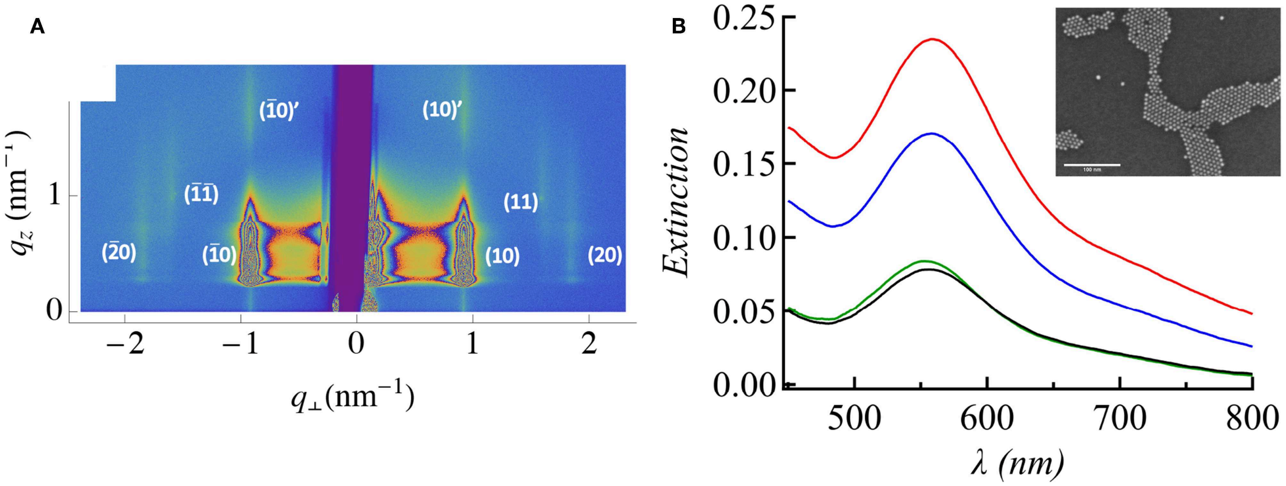

FIGURE 2 | (A) GISAXS signal of the NPs without LC, revealing the rods associated with the NP hexagonal network. **(B)** Light extinction of a network of NPs deposited on rubbed PVA substrate without LC. The LSP intensity varies depending on the measured area but not the wavelength resonance value (λ = 558 nm) except for the smallest intensity associated with the smallest NP domains. This demonstrates that, for λ = 558 nm, the hexagonal networks are large enough to be considered as infinite for the LSP properties. In inset is shown a Scanning Electron Microscopy (SEM) picture obtained with the same NPs when they were deposited on a Si substrate covered by rubbed PVA, also showing formation of an hexagonal network of NPs.

a clear red-shift of the LSP resonance is observed for a parallel polarization, with $\lambda_{\parallel} \approx 550$ nm. This indicates that a significant coupling between NPs occurs only in the direction parallel to the oily streaks, in relation with the formation of chains all parallel from each other and parallel to the dislocations [11, 21]. The spectral positions of extinction maxima taken from different zones of two samples are represented in red in the graph of $\lambda_{\parallel}$ as a function of $\lambda_{\perp}$ (**Figure 3B**). It appears that while $\lambda_{\perp}$ varies only little from one area to another, $\lambda_{\parallel}$ changes substantially, with a maximum for $\lambda_{\parallel}$ equal to 562 nm. This value for the chains is larger than the value obtained for the 2D monolayer without LC, $\lambda_{\parallel} = \lambda_{\perp} = 558$ nm. However for the same inter-NP gap and the same optical index, we would expect a higher LSP resonance wavelength for infinite NP hexagonal networks with respect to infinite NP chains. This latter wavelength is itself higher than for finite NP chains. The assumption of a same optical index in LC and without LC is very likely to be valid for two reasons: firstly it is known that the optical index is dominated by the grafted ligands with respect to the environment beyond the ligands [11, 44]. Secondly the optical index $n = 1.51$ should not be modified by the surrounding 8CB because the optical index expected in LC for a parallel polarization is close to the ordinary index of 8CB, $n_o = 1.52$, itself close to $n = 1.51$. The inter-NP gap in the NP chains formed in oily streaks is consequently in average smaller than without LC. There is a LC-induced shortening of the inter-NP gap in the NP chains. This result is in contrast with the same measurements made with smaller NPs of diameter $D = 4$ nm [11]. Either an equal or a larger inter-NP gap, depending on the preparation conditions, was obtained in the LC with respect to the network formed on rubbed PVA without LC [11].

5. CHAIN MODEL

In order to interpret these results, we consider that NP chain formation corresponds to a trapping of NPs in dislocations. The strength and efficiency of the linear trapping by dislocation cores has been previously highlighted by the fact that nanorods are aligned parallel to 8CB oily streaks. They are thus perpendicular to the nematic director but parallel to the defect cores, which is a strong indication of trapping by the linear defect cores [12, 15]. This is confirmed by the formation of NP chains, either made of nanorods [15] or of nanospheres of diameter $D = 4$ nm [11, 21]. We now observe the same phenomenon with larger NPs of diameter $D = 6$ nm but with a LC-induced shortening between NPs in contrast with NPs of diameter $D = 4$ nm. Trapping of NPs by dislocation cores may be kinetically favored by the known gradient of elastic distortion that attracts the NPs within the topological defect core [3, 19, 45]. However are the NP chains formed in the dislocation cores stable? In order to understand the structure and stability of NP chains, being trapped in dislocations, in particular the induced inter-NP gap that drives the electromagnetic coupling between the NPs, we have built a simple model that considers interacting NPs in LC. This model specifically takes into account the role of the LC in presence of topological defects. It is a model that has been built in order to understand the key parameters at the origin of the observed phenomena: NP chain formation and LC-induced shortening of the inter-NP gap. However since the interpretation of the details of the observed phenomena is not required, we have decided to only crudely consider the interaction of the NP chains with the surrounding LC, considering only two components: the favorable expulsion of disordered matter in the dislocation core; the unfavorable disorder induced by the NPs in LC if the NP size is larger than the dislocation core. We neglect in particular the details of the LC order variation and of the LC distortion around the defect core.

The energy of a NP chain made of N NPs separated by an inter-NP gap s, each NP being covered by a monolayer of ligands of length l (**Figure 4A**) can be estimated as follows: In a network of NPs, the equilibrium distance between the NPs is primarily controlled by the usual Van der Waals attraction between two NPs, balanced by the steric repulsion, both being mostly managed by the ligands around the NPs [46, 47]. We also have to take into account the mixing between the ligands leading to a model

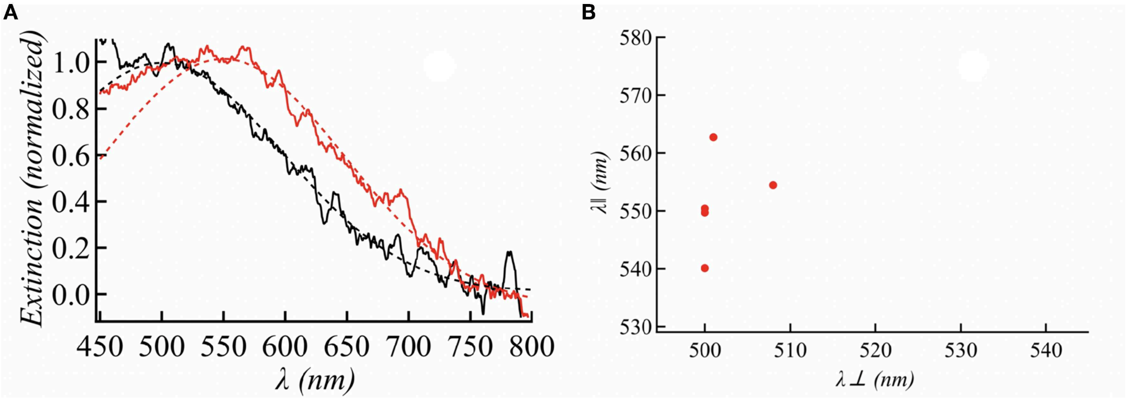

FIGURE 3 | (A) Normalized light extinction spectrum obtained in 8CB oily streaks containing gold NPs of diameter $D = 6$ nm. Superimposed gaussian fits are shown for the determination of the resonance wavelength. In black is the extinction for light polarization perpendicular to the 8CB oily streak stripes, in red for parallel polarization. **(B)** The different obtained extinction resonance measurements for NP chains represented by the $(\lambda_{\perp}, \lambda_{\parallel})$ values, obtained for NPs with diameter $D = 6$ nm embedded in 8CB oily streaks.

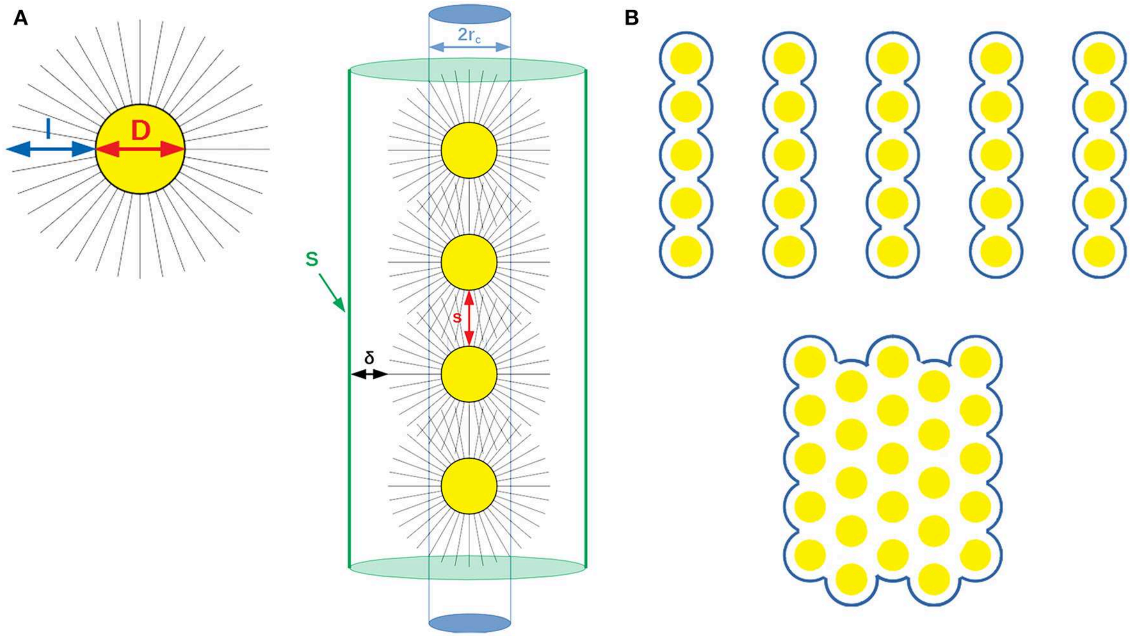

FIGURE 4 | (A) Model of the NPs with dodecanethiol ligands of length *l* and model of the NP chain with the disordered zone along the length δ shown beyond the ligands, of surface *S* shown in green. The dislocation core is schematically shown in blue. **(B)** Comparison of the surfaces of NP chains and NP FCC cube facets.

of interacting soft spheres [48]. In the case of ligands swollen by the solvent during the growth of the NP network, the usual parabolic curve of the energy of two interacting NPs is obtained as a function of *s*, the inter-NP gap [48]. If we consider toluene as solvent and gold NPs of diameter $D = 6$ nm covered by dodecanethiol, this leads to a well-marked equilibrium at $s = 1.9$ nm [38], in agreement with our combined X-ray and optical absorption measurements (**Figure 2**). In the presence of LC, two additional terms must be considered.

Firstly the energy related to the localization of the NP chain within the dislocation core, E_{Def}. This localization is favorable for the NPs since it allows the release of the disordered LC molecules of the core [16–18, 20]. As a result we expect the NPs to occupy the largest space as possible in the dislocation core to save the maximum of the dislocation core energy per unit of length, E_{DC} [11]. The length of the NP chain is $((N-1)(s+D)+D+2l)$ (**Figure 4A**). If the NP chain is embedded in the dislocation core of radius r_c, the volume of disordered matter, V_{DC} expelled by the presence of the NP chain is:

$$V_{DC} = \begin{cases} ((N-1)(s+D)+D+2l)\pi(D/2+l)^2, & if(D+2l) < 2r_c \\ ((N-1)(s+D)+D+2l)\pi r_c^2, & if(D+2l) > 2r_c \end{cases}$$

We can write:

$$E_{Def} = \begin{cases} -((N-1)(s+D)+D+2l)\frac{(D+2l)^2}{(2r_c)^2}E_{DC}, & if(D+2l) < 2r_c \\ -((N-1)(s+D)+D+2l)E_{DC}, & if(D+2l) > 2r_c \end{cases}$$

Secondly, the energy term related to the disorder induced by the NP within LC, E_{Dis}. It has already been shown that gold NPs of diameter $D = 4$ nm, covered by dodecanethiol ligands, may induce some disorder in a LC without topological defects. This disorder in return leads to a shortening of the inter-NP gap, in order to decrease in average the size of the LC disordered zone [49]. This disorder may be at the origin of the easy aggregation of NPs in LC, depending obviously on the nature of the ligands around the NPs [3, 50–52]. When the NP chains are embedded in the dislocation core, if the NP size $(D + 2l)$ is strictly larger than the defect core diameter $2r_c$, we expect that some disorder may be created in the LC around the dislocation core. The volume of the disordered zone created in the LC, beyond the NP ligands is schematized on **Figure 4A**. The disorder may extend along a distance δ in the LC beyond the ligands. The disordered volume is thus equal to $\delta \times S_{chain}$, with S_{chain}, the surface of the disorder zone (see **Figure 4A**). If we neglect the surfaces at the extremities of the disordered cylinder since it may mainly correspond to the surface of the dislocation core, $S_{chain} = \pi(D+2l)(N-1)(D+s) + \pi(D+2l)^2$. There is an energy to pay for the creation of this disordered volume: $E_{dis} = \delta \times e_{dis} \times S_{chain}$, with e_{dis} the disorder energy per unit of volume. Consequently:

$$E_{dis} = \delta \times e_{dis} \times (\pi(D+2l)(N-1)(D+s) + \pi(D+2l)^2). \quad (2)$$

If $(D + 2l) \leq 2r_c$, there is no disorder induced in LC in relation with NPs of size smaller or equal to the dislocation core, $E_{dis} = 0$. We only have to consider the overall energy $E(s) = (N-1)e(s) + E_{Def}$, with $e(s)$ the energy corresponding to the soft sphere model for a given inter-NP gap, s [38, 48]. $dE/ds = 0$ and $dE_{Def}/ds = -(N-1)\frac{(D+2l)^2}{(2r_c)^2}E_{DC} < 0$ leading to a decrease of $de(s)/ds$ with respect to the equilibrium at $s = 1.9$ nm without LC. As a result, we expect an increase of s, the inter-NP gap, the NPs occupying the largest possible space within the dislocation core. This is the case of gold nanospheres covered by dodecanethiol of diameter $D = 4$ nm [11].

If $(D + 2l) > 2r_c$, the NP size is larger than the dislocation core size, disorder is induced outside the core. The equilibrium established without NPs becomes differently modified in LC. If $d/ds(E_{Def} + E_{dis}) = (N-1)(\pi(D+2l)\delta e_{dis} - E_{DC}) < 0$, s is increased; if $\pi(D+2l)\delta e_{dis} - E_{DC} > 0$, s is decreased. With NPs of diameter $D = 6$ nm, we find a decrease of s with respect to NP networks formed without LC in contrast with NPs pf diameter $D = 4$ nm. This brings two conclusions:

- In smectic oily streaks there are dislocations of core size intermediate between the NP sizes associated with gold diameters $D = 4$ nm and $D = 6$ nm.
- The corresponding dislocation core energy per unit of length, $E_{DC} < \pi(D+2l)\delta e_{dis}$, with $D = 6$ nm and l the length of the dodecanethiol in LC.

A second issue is: Are the NP chains equilibrium structures?

If $(D + 2l) \leq 2r_c$, they are obviously equilibrium structures. The energy of N NPs potentially inducing disorder in LC is reduced when they are embedded in the dislocation core.

If $(D + 2l) > 2r_c$, this is not obvious. As shown by **Figure 4B**, the surface of the disordered zone induced by a FCC cube of edge made of N NPs is clearly smaller than the one of N^2 chains made of N NPs. This should favor aggregation of NPs instead of formation of NP chains trapped in dislocation cores, except if the dislocation core energy per unit of length, E_{DC} is large enough to compensate the disorder induced by a chain outside the defect core. To obtain formation of stable chains, we expect for N^2 chains made of N NPs, neglecting the variation of entropy between N^2 chains and a single FCC cube:

$$N^2(S_{chain}\times e_{dis}\times\delta-((N-1)(s+D)+D+2l)\times E_{DC}) < S_{FCC}\times e_{dis}\times\delta. \tag{3}$$

In other words:

$$\begin{aligned}N^2((\pi(D+2l)(N-1)(D+s)+\pi(D+2l)^2)e_{dis}\delta\\ -((N-1)(s+D)+D+2l)E_{DC}) < S_{FCC}\times e_{dis}\times\delta\end{aligned} \tag{4}$$

S_{FCC} being the surface of a FCC cube made of N^3 NPs. This suggests that:

$$\begin{aligned}N^2((n-1)(s+D)+D+2l)E_{DC} > (N^2(\pi(D\\ +2l)(N-1)(D+s)+\pi(D+2l)^2)-S_{FCC})e_{dis}\delta\end{aligned} \tag{5}$$

The calculation of the surface of a FCC cube thus leads to:

$$\begin{aligned}\pi(D+2l)\delta e_{dis} - E_{DC} <\ \delta e_{dis}\frac{N^2(D+s)^2(3/2+2\sqrt{3})+N((\sqrt{3}+1)(s+D)\pi(D+2l)-2(D+s)^2(3/2+2\sqrt{3}))}{N^3(s+D)+N^2(2l-s)+2(s+D)}\\ +\delta e_{dis}\frac{(D+s)^2(3/2+2\sqrt{3})-(\sqrt{3}+1)(s+D)\pi(D+2l)+2\pi(D+2l)^2}{N^3(s+D)+N^2(2l-s)+2(s+D)}\end{aligned} \tag{6}$$

If N is large enough this transforms into:

$$\begin{aligned}\pi(D+2l)\delta e_{dis} - E_{DC} <\ \delta e_{dis}(\frac{(D+s)(3/2+2\sqrt{3})}{N}\\ +\frac{(\sqrt{3}+1)\pi(D+2l)-3(D+s)(3/2+2\sqrt{3})}{N^2})\end{aligned} \tag{7}$$

With the other inequality obtained above, we finally have:

$$\begin{aligned}0 < \pi(D+2l)\delta e_{dis} - E_{DC} <\ \delta e_{dis}(\frac{(D+s)(3/2+2\sqrt{3})}{N}\\ +\frac{(\sqrt{3}+1)\pi(D+2l)-3(D+s)(3/2+2\sqrt{3})}{N^2})\end{aligned} \tag{8}$$

This result shows that it is not possible to create very long chains (N close to infinity) being equilibrium structures. The decreasing of the inter-NP gap in the NP chains observed in the smectic oily streaks is indeed driven by the value of $\pi(D+2l)\delta e_{dis} - E_{DC}$ that can not be strictly zero. To create equilibrium long chains (N large), the dislocation core energy per unit of length, E_{DC} must be close to $e_{dis}\delta\pi(D+2l)$. In order to satisfy both inequalities e_{dis} and E_{DC} must be large enough.

6. DISCUSSION

Smectic oily streaks are composed of 2 similar dislocations at the summit of the rotating grain boundary (Burgers vector b, $b/d \approx 6$, with d the inter-smectic layer spacing, $d = 3.16$ nm in 8CB), coexisting with another dislocation, of smaller Burgers vector (Burgers vector b, $b/d \approx 2$) nearer to the substrate (**Figure 1B**). The diameter of the dislocation cores, $2r_c$ is generally expected to be close to the dislocation Burgers vector [53, 54]. With a Burgers vector $b/d = 1$, $2r_c$ has indeed been shown to be very close to d for smectic C edge dislocations [55] and for smectic A screw dislocations [56]. If the NPs would induce disorder outside the defect core for the three dislocations of the oily streaks, this would imply that all the dislocation core radii would be smaller than the half of the NP size $D + 2l$ with l the dodecanethiol length in 8CB. The dodecanethiol length in 8CB is not known but can be considered as ranging between 1 nm, its highly stretched value [46] and 1.8 nm its extended value. $(D + 2l) \approx 8$–10 nm is not more than 3 times d, the 8CB inter-smectic layer spacing. This is largely too small to account for two times the core radius of a dislocation of Burgers vector b such that $b/d \approx 6$. This demonstrates that the hypothesis of only one kind of dislocation inducing disorder outside the core is highly more probable. It must be the smallest one, the dislocation of Burgers vector b, with $b/d \approx 2$ and we finally obtain an estimation of the corresponding dislocation core radius, r_c. $2r_c$ may range between the NP size associated with the gold diameter $D = 4$ nm and the NP size with the diameter $D = 6$ nm. Considering the dodecanethiol length as ranging between 1 and 1.8 nm, this leads to 6 nm $< 2r_c <$ 9.6 nm. The fact that similar LC-induced decrease in the inter-NP gap has been observed for NP diameters $D = 5$ nm (see **Figure S2**) even allows to decrease the inequality to 6 nm $< 2r_c <$ 8.6 nm. This is in very good agreement with the presence of dislocations of core radius, r_c such that $2r_c \approx 2d = 6.3$ nm, in smectic oily streaks, associated with a Burgers vector b, with $b/d = 2$.

As a result, the preferred dislocations for NP trapping are the largest dislocations where the largest amount of disorder energy is saved in the presence of NPs and no disorder is induced outside the defect core. They are equilibrium structures for NPs of diameter $D = 6$ nm. The smallest dislocations may be filled by NPs at high NP concentration only when the largest dislocations may be already significantly filled. A large number of NPs is thus required to explain the observed decrease of inter-NP gap revealed by the $\lambda_{\parallel}$ measurements of the NP chains shown in **Figure 3B**. We have used Rutherford Backscattering Spectroscopy (RBS) experiments (see Materials and Methods) to obtain the average number of gold atoms in the smectic oily streaks. We have found in average 1300 NPs μm^{-2} for one of the two samples presented in **Figure 3B**. Assuming an inter-NP distance of $D + 1.4 = 7.4$ nm, 1.4 nm being the average inter-NP gap in the chains (see below), it can be calculated that a linear defect of length 1 μm contains up to approximately 140 NPs. As a result, for the LC thickness of 170 nm found for the corresponding composite oily streak sample, the period of oily streaks being of the order of 550 nm [27], the critical concentration necessary to entirely fill the 6 dislocations of one hemicylinder (**Figure 1B**) is 1530 NPs μm^{-2}. 1300 NPs μm^{-2} corresponds to 85% of the 6 linear dislocations shown in **Figure 1B** being fully filled by NPs confirming a significant filling of the small dislocations in addition to the large ones. If we consider the large dislocations as being almost fully filled by NPs, this leads to a half filling on average for the small dislocations.

Despite the larger NP filling in large dislocations, the average LSP measurements of highest $\lambda_{\parallel}$ presented in **Figure 3** are expected to be dominated by the NP chains in the small dislocations. These latter chains are the only ones subjected to strong electromagnetic coupling between NPs. $\lambda_{\parallel} = 550$ nm is the LSP resonance value calculated in the dipolar approximation with infinite chains of inter-NP gap $s = 1.9$ nm and with a dipolar index $n = 1.51$, 1.9 nm corresponding to the equilibrium inter-NP gap without LC. The expected increase of the inter-NP gap in the large dislocations without induced disorder outside the defect core should lead to $\lambda_{\parallel}$ significantly smaller than $\lambda_{\parallel} = 550$ nm. In agreement with coexisting NP chains of large inter-NP gaps in large dislocations together with NP chains of small inter-NP gaps in small dislocations, all extinction data are enlarged toward the low wavelength values (**Figure 3A**), the low wavelength values being associated with the NP chains in the large dislocations. In contrast the maximum $\lambda_{\parallel}$ shown in **Figure 3B**, $\lambda_{\parallel} = 562$ nm may be dominated by the NP chains trapped in the small dislocations. $\lambda_{\parallel}$ ranging between 540 and 562 nm as shown on **Figure 3B** may be associated with different local concentrations of NPs in the small dislocations. This may be associated with different lengths of NP chains in the small dislocations for a same sample of average filling of the dislocations of 85%.

The average length of the NP chains in the small dislocations is not known. In order to use the maximum $\lambda_{\parallel}$ of 562 nm to extract an inter-NP gap value and use it for an estimation of the energy per unit of length of the small dislocations, E_{DC}, with the assumption that they form equilibrium structures, we have considered different possible average lengths for the NP chains. If the chains are long enough to be considered as infinite for LSP properties [41–43], the dipolar approximation with a dipolar index $n = 1.51$ leads to $s = 1.4$ nm. For numbers of NPs in the chains, N, which can not be considered as infinite, the wavelengths of the LSP resonances of chains of gold NPs were calculated with finite element methods (see Materials and Methods). The variations $\Delta\lambda$ of the position of the LSP resonance of the NP chains with respect to the position for isolated NPs λ_o were then fitted to a plasmon ruler [57]:

$$\Delta\lambda = \lambda_o \beta e^{-\frac{\left(\frac{2s}{D(n-1)}\right)^{\nu}}{\tau}} \tag{9}$$

where the decay rate $\tau = 0.324$ the exponent $\nu = 0.55$ and the scaling parameter $\beta = 0.16$ were adjustable parameters. **Figure S3** gives the variations of the calculated $\Delta\lambda$ in nm as a function of $\frac{2s}{D(n-1)}$ together with the plasmon ruler.

We obtain $s = 1.3$ nm for $N = 10$. It is hard to account for an inter-NP gap smaller than $s = 0.6$ nm, the value that has been found without topological defects in cholesteric films with NPs of diameter $D = 4$ nm. This latter case, $s = 0.6$ nm, corresponds to $N = 5$. We can then use the previously calculated energy curve of interacting NPs without LC, $e(s)$, as a function of the inter-NP gap, s, for gold NPs of diameter $D = 6$ nm with grafted dodecanethiol in toluene [38]. It leads to the observed equilibrium inter-NP gap of $s = 1.9$ nm without LC but also gives the evolution of $e(s)$ in case of departure of s with respect to $s = 1.9$ nm. Using in LC the fact that:

$$\frac{d(e(s))}{ds} = -(\pi(D + 2l)\delta e_{dis} - E_{DC}) \tag{10}$$

allows to obtain:

If N = 10 and s = 1.3 nm [38], $\pi(D + 2l)\delta e_{dis} - E_{DC} = 16kTnm^{-1}$

If N = 5 and s = 0.6 nm [38], $\pi(D+2l)\delta e_{dis} - E_{DC} = 42kTnm^{-1}$

If the NP chains in the small dislocations are equilibrium structures they must also respect inequality (8), leading (with $l = 1.8$ nm) to:

$$\begin{cases} \pi(D + 2l)\delta e_{dis} > 145kTnm^{-1}, E_{DC} > 129kTnm^{-1}, \ if \ N = 10 \\ \pi(D + 2l)\delta e_{dis} > 160kTnm^{-1}, E_{DC} > 118kTnm^{-1}, \ if \ N = 5. \end{cases}$$

e_{dis} and E_{DC} necessary to obtain equilibrium NP chains consistent with the measured optical absorption in the composites oily streaks/gold NPs, $\lambda_{\parallel} = 562$ nm, finally only poorly depend on the NP chain length. They appear very large. With the rough assumption that the zone around the dislocation core is transformed into a nematic zone, in agreement with recent results obtained with a screw dislocation [56] and neglecting the elastic nematic distortion within this zone, e_{dis} is the Landau-de Gennes penalty: e_{dis} = 0.73 kT nm^{-3}, for 8CB at 25°C [58]. Taking l as 1.8 nm, we need $\delta \approx 6nm$ to reach $\pi(D+2l)\delta e_{dis} >$ 145kT nm^{-1} which is two times the intra-layer spacing. Measurements of the core energy of dislocations are still scarce. The total energy of dislocations, including the core energy, has been measured as a function of the Burgers vector in 8CB free standing films. It confirmed that it is proportional to the Burgers vector [59]. For a Burgers vector $b/d = 1$ the energy per unit of length is 5 kT nm^{-1} [59]. Here we find E_{DC} at least 16 times larger for a Burgers vector only two times larger. Such a large value may be due to the complex structure of oily streak dislocations associated with a large disorientation of the smectic layers from each part of the dislocation (**Figure 1**). Another assumption is that the NP chains in the small dislocations are not an equilibrium structure in relation with the induced disorder outside the core. They could be only kinetically favored by the attraction toward the defect core occurring due to the elastic distortion around the dislocations [3, 19, 45]. The fact that the dislocations are embedded in rotating grain boundaries may strongly enhance this phenomenon, through the presence of additional elastic distortion.

7. CONCLUSION

Combining GISAXS, spectrophotometry, RBS measurements and the development of a model of interacting NPs, we present a comprehensive description of composites made of gold NPs with a given diameter $D = 6$ nm in an array of different kinds of smectic dislocations (with different Burgers vectors). If the NP concentration is small, only the large dislocations are filled and long chains may be formed. They are favorable equilibrium structures because no disorder is induced outside the defect core but they consist of only poorly interacting NPs. If the NP concentration is large enough, the small dislocations can also be filled and we demonstrate up to 85 % of the dislocations being filled without any aggregation outside the core. We demonstrate that such high filling of the dislocations by the NPs leads to the coexistence of different NP chains in the smectic film, long NP chains with large inter-NP gap coexisting with smaller chains with a shortened inter-NP gap that can become as small as 1.4 nm. As a result the plasmonic properties of the composite are dominated by the small chains due to the LC-induced enhanced electromagnetic coupling between the NPs in the small dislocations. Using a model that takes into account the modifications of the interactions between NPs associated with their localization in the smectic dislocations, we confirm the presence of dislocations of Burgers vector b, $b/d = 2$, the "small" dislocations. We also demonstrate that the NP chains formed in the "small" dislocations are most probably not equilibrium structures. This is due to the disorder outside the defect core which is responsible for the observed LC-induced shortening inter-NP gap. However these NP chains might remain stable over time due to the elastic distortion around the rotating grain boundary that might play the role of the energy barrier for the trapped NPs.

DATA AVAILABILITY STATEMENT

The datasets generated for this study are available on request to the corresponding author.

AUTHOR CONTRIBUTIONS

All authors listed have made a substantial, direct and intellectual contribution to the work, and approved it for publication.

ACKNOWLEDGMENTS

We thank D. Limagne, C. Rafaillac, and B. Voisin for technical support. D. Demaille and L. Becerra for the electronic Microscopy; Y. Vickridge for the analysis of the RBS data. We thank CNES (Centre National d'Etudes Spatiales) for supporting this project. Concerning the financial funding, SD, AM, and EL thank the French state funds managed by the ANR within the Investissements d'Avenir programme under reference ANR-11-IDEX-0004-02, and more specifically within the framework of the Cluster of Excellence MATISSE. We also thank Synchrotron SOLEIL for providing the beam on SixS beamline.

SUPPLEMENTARY MATERIAL

The Supplementary Material for this article can be found online at: https://www.frontiersin.org/articles/10.3389/fphy.2019.00234/full#supplementary-material

Figure S1 | Extinction in toluene of the NPs of diameter 6 nm.

Figure S2 | The different obtained extinction measurements for NP chains represented by the ($\lambda_{\perp}$; $\lambda_{\parallel}$) values, obtained for NPs with diameter $D = 5$ nm, for which the extinction of hexagonal networks without LC is at $\lambda_{\perp} = \lambda_{\parallel} = 558$ nm.

Figure S3 | $2s/(N-1)D$ as a function of Delta lambda, calculated (in blue) with finite element method compared with the plasmon ruler (in red).

REFERENCES

1. Bisoyi HK, Kumar S. Liquid-crystal nanoscience: an emerging avenue of soft self-assembly. *Chem Soc Rev*. (2011) **40**:306–19. doi: 10.1039/B901793N
2. Lagerwall JPF, Scalia G. A new era for liquid crystal research: applications of liquid crystals in soft matter nano-, bio- and microtechnology. *Curr Appl Phys*. (2012) **12**:1387–412. doi: 10.1016/j.cap.2012.03.019
3. Blanc C, Coursault D, Lacaze E. Ordering nano-and microparticles assemblies with liquid crystals. *Liquid Cryst Rev*. (2013) **1**:83–109. doi: 10.1080/21680396.2013.818515
4. Lewandowski W, Wojcik M, Górecka E. Metal nanoparticles with liquid-crystalline ligands: controlling nanoparticle superlattice structure and properties. *ChemPhysChem*. (2014) **15**:1283–95. doi: 10.1002/cphc.201301194

5. Choudhary A, Singh G, Biradar AM. Advances in gold nanoparticle–liquid crystal composites. *Nanoscale*. (2014) **6**:7743–56. doi: 10.1039/C4NR01325E
6. Sridevi S, Prasad SK, Nair GG, D'Britto V, Prasad BLV. Enhancement of anisotropic conductivity, elastic, and dielectric constants in a liquid crystal-gold nanorod system. *Appl Phys Lett*. (2010) **97**:151913. doi: 10.1063/1.3499744
7. Mishra M, Kumar S, Dhar R. Effect of dispersed colloidal gold nanoparticles on the electrical properties of a columnar discotic liquid crystal. *RSC Adv*. (2014) **4**:62404–12. doi: 10.1039/C4RA11541D
8. Tomašovičová N, Timko M, Mitróová Z, Koneracká M, Rajňak M, Éber N, et al. Capacitance changes in ferronematic liquid crystals induced by low magnetic fields. *Phys Rev E*. (2013) **87**:014501. doi: 10.1103/PhysRevE.87.014501
9. Mouhli A, Ayeb H, Othman T, Fresnais J, Dupuis V, Nemitz IR, et al. Influence of a dispersion of magnetic and nonmagnetic nanoparticles on the magnetic Fredericksz transition of the liquid crystal 5CB. *Phys Rev E*. (2017) **96**:012706. doi: 10.1103/PhysRevE.96.012706
10. Ramanuj M, Jayanta H, Anil H, Binod G, Ragini D, Debanjan B, et al. Dielectric properties of a strongly polar nematic liquid crystal compound doped with gold nanoparticles. *Liquid Cryst*. (2018) **45**:1661–71. doi: 10.1080/02678292.2018.1478995
11. Coursault D, Blach JF, Grand J, Coati A, Vlad A, Zappone B, et al. Towards a control of anisotropic interactions between soft nanospheres using dense arrays of smectic liquid crystal edge dislocations. *ACS Nano*. (2015) **9**:11678–89. doi: 10.1021/acsnano.5b02538
12. Pelliser L, Manceau M, Lethiec C, Coursault D, Vezzoli S, Lemenager G, et al. Alignment of rod-shaped single photon emitters driven by line defects in liquid crystals. *Adv Funct Mater*. (2015) **25**:1719–26. doi: 10.1002/adfm.201403331
13. Lee E, Xia Y, Ferrier RC Jr, Kim HN, Gharbi MA, Stebe KJ, et al. Fine golden rings: tunable surface plasmon resonance from assembled nanorods in topological defects of liquid crystals. *Adv Mater*. (2016) **28**:2731–6. doi: 10.1002/adma.201506084
14. Liu Q, Yuan Y, Smalyukh II. Electrically and optically tunable plasmonic guest Host liquid crystals with long-range ordered nanoparticles. *Nanoletters*. (2014) **14**:4071. doi: 10.1021/nl501581y
15. Rozic B, Fresnais J, Molinaro C, Calixte J, Umadevi S, Lau-Truong S, et al. Oriented gold nanorods and gold nanorod chains within smectic liquid crystal topological defects. *ACSNano*. (2017) 11:6728–38. doi: 10.1021/acsnano.7b01132
16. Yoshida H, Tanaka Y, Kawamoto K, Kubo H, Tsuda, Fujii A, et al. Nanoparticle-stabilized cholesteric blue phases [Article]. *Appl Phys Express*. (2009) **2**:121501. doi: 10.1143/APEX.2.121501
17. Karatairi E, Rozic B, Kutnjak Z, Tzitzios V, Nounesis G, Cordoyiannis G, et al. Nanoparticle-induced widening of the temperature range of liquid-crystalline blue phases. *Phys Rev E*. (2010) **81**:041703. doi: 10.1103/PhysRevE.81.041703
18. Rozic B, Tzitzios V, Karatairi E, Tkalec U, Nounesis G, Kutnjak Z, et al. Theoretical and experimental study of the nanoparticle-driven blue phase stabilisation. *Eur Phys J E*. (2011) **34**:1–11. doi: 10.1140/epje/i2011-11017-8
19. Senyuk B, Evans JS, Ackerman PJ, Lee T, Manna P, Vigderman L, et al. Shape-dependent oriented trapping and scaffolding of plasmonic nanoparticles by topological defects for self-assembly of colloidal dimers in liquid crystals. *Nano Lett*. (2012) **12**:955–63. doi: 10.1021/nl204030t
20. Cordoyiannis G, Rao J i VS, Kralj S, Dhara S, Tzitzios V, Basina G, et al. Different modulated structures of topological defects stabilized by adaptive targeting nanoparticles. *Soft Matt*. (2013) **9**:3956–64. doi: 10.1039/c3sm27644a
21. Coursault D, Grand J, Zappone B, Ayeb Hand L'evi G, F'elidj N, Lacaze E. Linear self-assembly of nanoparticles within liquid crystal defect arrays. *Adv Matt*. (2012) 24:1461–5. doi: 10.1002/adma.201103791
22. Evans JS, Ackerman PJ, Broer DJ, van de Lagemaat J, Smalyukh II. Optical generation, templating, and polymerization of three-dimensional arrays of liquid-crystal defects decorated by plasmonic nanoparticles. *Phys Rev E*. (2013) **87**:032503. doi: 10.1103/PhysRevE.87.032503
23. Gharbi MA, Manet S, Lhermitte J, Brown S, Milette J, Toader V, et al. Reversible nanoparticle cubic lattices in blue phase liquid crystals. *ACS Nano*. (2016) **10**:3410–15. doi: 10.1021/acsnano.5b07379
24. Mundoor H, Sheetah GH, Park S, Ackerman PJ, Smalyukh II, van de Lagemaat J. Tuning and switching a plasmonic quantum dot sandwiched in a nematic line defect. *ACS Nano*. (2018) **12**:2580–90. doi: 10.1021/acsnano.7b08462
25. Lacaze E, Coursault D. Control of nanoparticle self-assemblies using distorted liquid crystals. In: Lagerwall JPF, Scalia G, editors. *Liquid Crystals with Nano and Microparticles. Series in Soft Condensed Matter*. Singapore: World Scientific (2016). p. 186–222.
26. Rahimi M, Ramezani-Dakhel H, Zhang R, Ramirez-Hernandez A, Abbott NL, de Pablo JJ. Segregation of liquid crystal mixtures in topological defects. *Nat Commun*. (2017) **8**:15064. doi: 10.1038/ncomms15064
27. Coursault D, Zappone B, Coati A, Boulaoued A, Pelliser L, Limagne D, et al. Self-organized arrays of dislocations in thin smectic liquid crystal films. *Soft Matter*. (2016) **12**:678–88. doi: 10.1039/C5SM02241J
28. Ravnik M, Alexander G, Yeomans J, Zumer S. Three-dimensional colloidal crystals in liquid crystalline blue phases. *Proc Natl Acad Sci USA*. (2011) **108**:5188–92. doi: 10.1073/pnas.1015831108
29. Peng S, Lee Y, Wang C, Yin H, Dai S, Sun S. A facile synthesis of monodisperse Au nanoparticles and their catalysis of CO oxidation. *Nano Res*. (2008) **1**:229–34. doi: 10.1007/s12274-008-8026-3
30. Kreibig U, Vollmer M. *Optical Properties of Metal Clusters*. Vol. 25. Springer Series in Materials Science. Springer (1995).
31. Topping J. On the mutual potential energy of a plane network of doublets. *Proc R Soc London A*. (1927) **114**:67–72. doi: 10.1098/rspa.1927.0025
32. Van der Hoff BME, Benson GC. A method for the evaluation of some lattice sums oocurring in calculations of physical properties of crystals. *Can J Phys*. (1953) 31:1087–04. doi: 10.1139/p55-064
33. Johnson PB, Christy RW. Optical constants of the noble metals. *Phys Rev B*. (1972) 6:4370–9. doi: 10.1103/PhysRevB.6.4370
34. Garcia MA, de Ia Venta J, Crespo P, LLopis J, Penades S, Fernandez A, et al. Surface plasmon resonance of capped au nanoparticles. *Phys Rev B*. (2005) 72:241403. doi: 10.1103/PhysRevB.72.241403
35. Michel JP, Lacaze E, Alba M, de Boissieu M, Gailhanou M, Goldmann M. Optical gratings formed in thin smectic films frustrated on a single crystalline substrate. *Phys Rev E*. (2004) **70**:011709. doi: 10.1103/PhysRevE.70.011709
36. Michel JP, Lacaze E, Goldmann M, Gailhanou M, de Boissieu M, Alba M. Structure of smectic defect cores: x-ray study of 8CB liquid crystal ultrathin films. *Phys Rev Lett*. (2006) **96**:027803. doi: 10.1103/PhysRevLett.96.027803
37. Zappone B, Lacaze E. Surface-frustrated periodic textures of smectic- a liquid crystals on crystalline surfaces. *Phys Rev E Stat Nonlin Soft Matt Phys*. (2008) **78**:061704. doi: 10.1103/PhysRevE.78.061704
38. Goubet N, Richardi J, Albouy PA, Pileni MP. Which forces control supracrystal nucleation in organic media? *Adv Funct Mater*. (2011) **21**:2693–704. doi: 10.1002/adfm.201100382
39. Gauvin M, Wan YF, Arfaoui I, Pileni MP. Mechanical properties of Au supracrystals tuned by flexible ligand interactions. *J Phys Chem C*. (2014) **118**:5005–12. doi: 10.1021/jp411896c
40. Wen T, Zhang D, Wen Q, Liao Y, Zhang C, Li J, et al. Enhanced optical modulation depth of terahertzWaves by self-assembled monolayer of plasmonic gold nanoparticles. *Adv Opt Mat*. (2016) **4**:1974–80. doi: 10.1002/adom.201600248
41. Lin S, Li M, Dujardin E, Girard C, Mann S. One-dimensional plasmon coupling by facile self-assembly of gold nanoparticles into branched chain networks. *Adv Mater*. (2005) **17**:2553–9. doi: 10.1002/adma.200500828
42. Bonell F, Sanchot A, Dujardin E, Péchou R, Girard C, Li M, et al. Processing and near-field optical properties of self-assembled plasmonic nanoparticle networks. *J Chem Phys*. (2009) **130**:034702. doi: 10.1063/1.3046291
43. Barrow SJ, Funston AM, Gómez DE, Davis TJ, Mulvaney P. Surface plasmon resonances in strongly coupled gold nanosphere chains from monomer to hexamer. *Nano Lett*. (2011) **11**:4180–7. doi: 10.1021/nl202080a
44. Mulvaney P. Surface plasmon spectroscopy of nanosized metal particles [Review]. *Langmuir*. (1996) **12**:788–800.
45. Voloschenko D, Pishnyak OP, Shiyanovskii SV, Lavrentovich OD. Effect of director distortions on morphologies of phase separation in liquid crystals. *Phys Rev E*. (2002) **65**:060701. doi: 10.1103/PhysRevE.65.060701
46. Schapotschnikow P, Pool R, Vlugt TJ. Molecular simulations of interacting nanocrystals. *Nano Lett*. (2008) **8**:2930–4. doi: 10.1021/nl8017862

47. Schapotschnikow P, Vlugt TJH. Understanding interactions between capped nanocrystals: Three-body and chain packing effects. *J Chem Phys*. (2009) **131**:124705. doi: 10.1063/1.3227043
48. Khan SJ, Pierce F, Sorensen CM, Chakrabarti A. Self-assembly of ligated gold nanoparticles: phenomenological modeling and computer simulations. *Langmuir*. (2009) **25**:13861–8. doi: 10.1021/la9008202
49. Pendery JS, Merchiers O, Coursault D, Grand J, Ayeb H, Greget R, et al. Gold nanoparticle self-assembly moderated by a cholesteric liquid crystal. *Soft Matt*. (2013) **9**:9366–75. doi: 10.1039/c3sm51736e
50. Qi H, Hegmann T. Multiple alignment modes for nematic liquid crystals doped with alkylthiol-capped gold nanoparticles. *ACS Appl Mater Interfaces*. (2009) **1**:1731–8. doi: 10.1021/am9002815
51. Khatua S, Manna P, Chang WS, Tcherniak A, Friedlander E, Zubarev ER, et al. Plasmonic nanoparticles liquid crystal composites. *J Phys Chem C*. (2010) **114**:7251–7. doi: 10.1021/jp907923v
52. Draper M, Saez I, Cowling S, Gai P, Heirich B, Donnio B, et al. Self-assembly and shape morphology of liquid-crystalline gold metamaterials. *Adv Funct Mat*. (2011) **21**:1260–78. doi: 10.1002/adfm.201001606
53. Kléman M. *Points, Lignes, Parois dans les Fluides Anisotropes et les Solides Cristallins. No. vol. 1 in Points, lignes, parois dans les fluides anisotropes et les solides cristallins.* Orsay: Éditions de physique (1977).
54. Holyst R, Oswald P. Dislocations in uniaxial lamellar phases of liquid crystals, polymers and amphiphilic systems. *Int JMod Phys*. (1995) **9**:1115–573.
55. Zhang C, Grubb AM, Seed AJ, Sampson P, Jákli A, Lavrentovich OD. Nanostructure of edge dislocations in a smectic-C^* liquid crystal. *Phys Rev Lett*. (2015) **115**:087801. doi: 10.1103/PhysRevLett.115.087801
56. Repula A, Grelet E. Elementary edge and screw dislocations visualized at the lattice periodicity level in the smectic phase of colloidal rods. *Phys Rev Lett*. (2018) **121**:097801. doi: 10.1103/PhysRevLett.121.097801
57. Jain PK, Huang W, El-Sayed MA. On the universal scaling behavior of the distance decay of plasmon coupling in metal nanoparticle pairs: a plasmon ruler equation. *Nano Lett*. (2007) **7**:2080–8. doi: 10.1021/nl071008a
58. Thoen J, Marynissen H, Van Dael W. Temperature dependence of the enthalpy and the heat capacity of the liquid-crystal octylcyanobiphenyl (8CB). *Phys Rev A*. (1982) **26**:2886–905.
59. Géminard JC, Laroche C, Oswald P. Edge dislocation in a vertical smectic film: line tension versus film thickness and Burgers vector. *Phys Rev E*. (1998) **58**:5923–5.

Conflict of Interest: The authors declare that the research was conducted in the absence of any commercial or financial relationships that could be construed as a potential conflict of interest.

frontiers in Physics

ORIGINAL RESEARCH
published: 21 April 2020
doi: 10.3389/fphy.2020.00094

Geometric-Phase Waveplates for Free-Form Dark Hollow Beams

Bruno Piccirillo[1]*, *Ester Piedipalumbo*[1,2] *and Enrico Santamato*[1]

[1] *Department of Physics "E. Pancini", Università di Napoli Federico II, Naples, Italy,* [2] *Istituto Nazionale di Fisica Nucleare (INFN)-Sezione di Napoli, Naples, Italy*

We demonstrate the possibility of creating optical beams with phase singularities engraved into exotic intensity landscapes imitating the shapes of a large variety of diverse plane curves. To achieve this aim, we have developed a method for directly encoding the geometric properties of a selected curve into a single azimuthal phase factor without passing through indirect encryption methods involving lengthy numerical procedures. The outcome is utilized to mold the optic axis distribution of a liquid-crystal-based inhomogeneous waveplate. The latter is finally used to sculpt the wavefront of an input optical gaussian beam via the Pancharatnam-Berry phase.

Keywords: geometric phase, wavefront sculpting, optical angular momentum, optical singularities, liquid crystals

Edited by:
Uroš Tkalec,
University of Ljubljana, Slovenia

Reviewed by:
Nina Kravets,
UMR5798 Laboratoire Ondes et Matière d'Aquitaine (LOMA), France
Qi-Huo Wei,
Southern University of Science and Technology, China

***Correspondence:**
Bruno Piccirillo
bruno.piccirillo@fisica.unina.it

Specialty section:
This article was submitted to Soft Matter Physics, a section of the journal Frontiers in Physics

Received: *30 November 2019*
Accepted: *12 March 2020*
Published: *21 April 2020*

Citation:
Piccirillo B, Piedipalumbo E and Santamato E (2020) Geometric-Phase Waveplates for Free-Form Dark Hollow Beams. Front. Phys. 8:94. doi: 10.3389/fphy.2020.00094

1. INTRODUCTION

Light sculpting has gained increasing importance in both fundamental and applied optics [1]. Engraving singularities in optical beams, in particular, has paved the way for multiple applications in both classical and quantum optics, most of which relate to the angular momentum of light. Singular Optics has gradually become an independent research field and now aspires to become a fundamental cornerstone of modern photonics. Optical singular beams have proven to be invaluable for non-contact manipulation over micro- and nanoscale [2, 3], which has enormous implications for modern nanophysics, crystal growth, and metamaterials, to give just a few examples. Furthermore, the infinite dimensionality of the orbital angular momentum (OAM) space has paved the way for increasing the data capacity of both free-space and fiber-optic communications [4] and for developing novel efficient protocols for classical [5] as well as quantum information processing [6–8]. No less important, optical singularities have been successfully utilized for super-resolution imaging [9, 10], on-chip optical switching [11–13], advanced microscopy [14, 15], and material machining [16–18].

Needless to say, the great potential of singular optics—and, more generally, of sculpted light—has been progressively unlocked over time, through the development of increasingly efficient and versatile tools for shaping the optical wavefronts. The most prominent technologies currently available for shaping spatial modes are computer-generated holograms (CGHs) displayed on spatial light modulators (SLMs)—based on dynamic phase control—and Pancharatnam-Berry phase (or geometric phase) Optical Elements (PBOEs). Indeed, several methods are nowadays available to fabricate geometric-phase optical elements for wavefront shaping, ranging from subwavelength metal stripe space-variant gratings [19] to multilayer plasmonic metasurfaces [20] and Spatially Varying Axis Plates (SVAPs) based on liquid crystals [21–26].

In the present paper, we introduce a method for designing SVAPs enabling the generation of scalar optical beams with non-linear azimuthal phase structures, giving birth to phase singularities engraved within non-cylindrically symmetric intensity profiles. Indeed, the cylindrical symmetry typical of the intensity profile of helical beams springs from their linear azimuthal phase profile,

$e^{\mathrm{i}\,\ell\phi}$. Helical beams have helical wavefronts —hence the name—and carry an OAM of $\hbar\ell$ per photon, ℓ being an integer, and ϕ the azimuthal polar angle around the beam propagation direction.There are multiple families of helical beams, which differ in their radial dependencies. Well-known examples are Laguerre-Gaussian (LG) beams [27, 28], Bessel and Bessel-Gaussian (BG) beams [29], and the wider class of Hypergeometric-Gaussian (HyG) beams [30], to name just a few. A helical beam with an azimuthal index ℓ has an ℓ-fold rotational symmetry, and its OAM spectrum accordingly includes only the component ℓ. With the light beam wavevector denoted as $\boldsymbol{k}$, the azimuthal component of the linear momentum is $\hbar k_\phi$ per photon: it does not depend on ϕ but only on the distance from the beam axis. The energy flux is therefore rotationally invariant around the beam axis, yielding the well-known cylindrically symmetric doughnut-shaped profile. An azimuthally non-uniform k_ϕ, in contrast, will break such symmetry and will give birth to an optical wavefront with a non-uniform helical phase structure, which will result, in its turn, in a non-cylindrically symmetric intensity profile. An OAM spectrum will broaden as a consequence of such symmetry breaking.

To impart a non-linear azimuthal structure, we have developed a phase design method aimed at encoding the geometric properties of a plane curve in order to create an intensity profile imitating the shape of the curve. We presently demonstrate that such an approach enables the direct determination of the phase profile required to reshape the intensity profile of a light beam as well as its OAM spectrum according to one's wishes. Here, in fact, we avoid passing through indirect methods for encoding the amplitude and phase of the target field into a single phase function [31], though the price to be paid is that only some features of the intensity profile and of the OAM spectrum will be precisely determined. Despite these apparent limitations, our method spontaneously leads us to introduce the concept of dark hollow beams with tailored intensity profiles or "Free-Form Dark-Hollow" (FFDH) Beams. A detailed study of the optical properties of FFDH beams will be reported elsewhere. Here, we focus on the generation of such beams by using the aforementioned SVAPs, of which q-plates [32] are probably the most famous examples. Liquid crystal-based SVAPs combine high conversion efficiency with exceptional manageability for overall high performance. Our SVAPs were fabricated by adopting a "direct-write approach," as defined in Kim et al. [21]. However, we would like to emphasize that our focus is presently on the method developed to determine the transmittance phase function. Specifically, an arbitrary superposition of azimuthal modes amounts to a complex function of ϕ with both an amplitude and a phase, i.e.,

$$\sum_{\ell} c_\ell \mathrm{e}^{\mathrm{i}\ell\phi} = A(\phi)\mathrm{e}^{\mathrm{i}\Psi(\phi)}. \tag{1}$$

Several approaches, mostly based on the Gerchberg-Saxton algorithm, are usually adopted to obtain a pure phase function providing an acceptable approximation for Equation (1) [33]. In what follows, we describe a method to directly generate a dark hollow beam in which the shape of the dark zone is basically inherited from the shape of a selected plane curve. This is achieved without resorting to inverse algorithms such as those mentioned above. They can be proved to be promising devices of potential interest for multiple applications ranging from super-resolution microscopy to directional selective trapping [34], as well as material processing and optical coronagraphy, not to mention the applications in classical and quantum communications [35, 36]. As an example, we consider the case of Stimulated Emission Depletion (STED) microscopy, in which super resolution is achieved by the selective deactivation of fluorophores through an excitation beam filling the internal zone of a doughnut-shaped de-excitation spot. Replacing the doughnut with an FFDH beam, the illumination area would acquire a non-circular shape, suitable for optimally sending photons to zones where they are really required and/or to prevent them from damaging the surrounding areas.

2. FREE-FORM AZIMUTHAL PHASE SHAPING

The question arises of to what extent the transverse intensity profiles or the OAM spectrum of a light beam can be molded by manipulating a purely azimuthal phase factor $e^{\mathrm{i}\psi(\phi)}$, $\psi(\phi)$ being an arbitrary function of the azimuthal coordinate ϕ. Such a phase factor does not enable the exploration of all the possible field distributions, even approximately, since ψ is assumed to be independent of the distance r from the beam axis [31, 37]. As above mentioned, in this work, we aim at introducing a *toy* method based on geometric intuition to determine the most appropriate azimuthal phase factor $e^{\mathrm{i}\psi(\phi)}$ required to generate dark hollow beams with arbitrary shapes or, as we have baptized them, FFDH beams. To this purpose, we need a "dough cutter" for partitioning the plane around the beam axis into a number of sectors—"slicing the doughnut." One can then distribute the transverse intensity of light among the several sectors according to one's wishes and necessities. Molding the intensity of light within each sector is necessary for tailoring the boundaries of the dark region around the axis—"shaping the hole of the doughnut." The portions of light within different sectors can be disconnected from each other or not. Metaphors aside, our "dough cutter" is the azimuthal component $\hbar k_\phi(\phi)$ of the photon linear momentum as a function of ϕ, i.e.,

$$k_\phi(\phi) = \frac{1}{r}\frac{d\psi(\phi)}{d\phi}. \tag{2}$$

Assuming $\psi(\phi)$ is proportional to the orientation angle $\Theta(\phi)$ of the unit normal to some plane curve γ described by ϕ-dependent parametric equations, then all the relevant features of $k_\phi(\phi)$ can be gathered from the rotational symmetry properties of γ and from the local radius of curvature—the latter being related to both k_ϕ and its derivative. Such a geometric approach has the advantage that $\Theta(\phi)$—and therefore the plane curve it comes from—needs not to be determined, on a case-by-case basis, as a solution of an inverse problem. Rather, it can be helpful to use a representation of the curve in polar coordinates, with some free parameters that can be tuned to match as much as possible the target intensity profile.

2.1. Curve Selection

Multiple choices are available. Good options are Lamé curves or their generalizations. A Lamé Curve, also known as a superellipse [38], is a closed curve retaining the geometric properties of semi-major axis and semi-minor axis, typical of an ellipse, but with a different shape. In polar coordinates it is described by the equation

$$(a\cos\phi)^{\frac{n}{n-1}} + \left(b\sin\phi\right)^{\frac{n}{n-1}} = \rho(\phi)^{\frac{n}{n-1}}\,, \tag{3}$$

where a, b, and n are positive reals.

In 2003, J. Gielis introduced a single parametric equation—dubbed the "superformula"—describing multiple plane curves of the most varied kinds to study forms in plants and other living organisms [39]. The mathematical expression of the superformula, in polar coordinates, is

$$\rho(\phi) = \left(\left|\frac{\cos\frac{m\phi}{4}}{a}\right|^{n_2} + \left|\frac{\sin\frac{m\phi}{4}}{b}\right|^{n_3}\right)^{-\frac{1}{n_1}}\,, \tag{4}$$

where ρ is the distance of a point of the curve γ from the origin of the coordinate system as a function of the azimuthal angle ϕ, m is an integer, n_1, n_2, and n_3 are three integers controlling its local radius of curvature, and, finally, the positive real numbers a and b parameterize the radii of the circumferences respectively inscribed and circumscribed to the curve γ. For even $m = 2\,k$, Equation (4) describes a curve $\gamma_{2\,k}$ closing over the interval $[0, 2\pi)$. $\gamma_{2\,k}$ is rotationally symmetric by an angle $2\pi/k$. For odd $m = 2\,k+1$, $\gamma_{2\,k+1}$ closes over the interval $[0, 4\pi)$. When $a = b$ and $n_1 = n_2$, γ_m exhibits an m-fold rotational symmetry C_m. As all the free parameters in Equation (4) can vary, the generated curves can be deeply diverse. No doubt the curves could be grouped according to a criterion based on the order of the their rotational symmetry. For $m = 4$, $a = b$, and $n_2 = n_3 > 2$, for instance, the superformula simply returns the superellipses first introduced by G. Lamé in 1818 [38]. For fixed values of m, a, and b, however, the signs and the absolute values of n_1, n_2, and n_3 can dramatically change the topological properties of the curves. Besides, a peculiar feature of the superformula is the fact that, independently of m, when $n_2 = n_3 = 2$, it always degenerates into a circumference when $a = b$ or into an ellipse otherwise. Here, we are not interested in the mathematical peculiarities of the superformula but rather in taking advantage of its "shape-shifter" capabilities.

Encrypting the geometrical properties of the selected curves into the optical phase. Assume $\gamma(a, b, m, n_1, n_2, n_3)$ is the curve described by the superformula for some values of the free parameters. The normal unit vector $\boldsymbol{n} = \left(n_x, n_y\right)$ of the curve is given by

$$\left(n_x + \mathrm{i}\,n_y\right)^2 = \frac{\rho(\phi) - \mathrm{i}\,\dot{\rho}(\phi)}{\rho(\phi) + \mathrm{i}\,\dot{\rho}(\phi)}e^{2\,\mathrm{i}\phi}, \tag{5}$$

where $\dot{\rho}$ is the derivative of ρ with respect to ϕ. Denoting as $\Theta(\phi)$ the angle that $\boldsymbol{n}$ forms with the $x-$axis, we set the optical phase $\psi(\phi)$ to be

$$\psi(\phi) = 2\,\Theta(\phi;\, a, b, m, n_1, n_2, n_3). \tag{6}$$

Consequently, by varying the free parameters in Equation (4), multiple phase profiles can be designed and FFDHs accordingly generated. The realized phase profiles exhibit a modulation with the same symmetry properties as the curve γ. In the following, we show that the m-fold symmetry characterizing the phase modulation also affects the intensity profile of the generated beam. Light intensity, indeed, is expected to be equally partitioned among the m equally spaced sectors of the phase profile.

In **Figure 1**, this geometry-to-phase transfer procedure is sketched in the case $a = b = 1$, $m = 5$, $n_1 = 1/2$, and $n_2 = n_3 = 4/3$. The rippled helical wavefront arising from Equation (6) is shown in **Figure 2B** for the same values of the parameters and is compared to the smooth helical wavefront corresponding to a doughnut beam with $\ell = 2$ (**Figure 2A**). The latter can be easily shown to come from a circumference.

This structure primarily affects the OAM spectrum, which includes only the components $(\ell - m) \pm k\,m$, with k being an integer (**Figure 3**) and ℓ being the OAM index corresponding to the background helical mode. Specifically, in **Figure 3**, the OAM power spectrum $|c_l|^2$ of the generated FFDH is presented. In classical optics, the quantity $|c_l|^2$ is the fraction of the total power of the optical field component carrying an OAM proportional to l. In quantum optics, it is the probability that a photon in the beam carries an OAM of $\hbar l$. The actual values of $|c_l|^2$, as reported in **Figure 3**, have been determined numerically, by Fourier expansion of the azimuthal phase factor reported in Equation (5). The skew rays follow the paths dictated by k_ϕ.

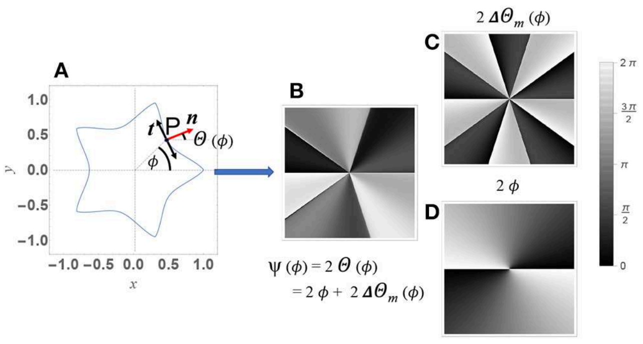

FIGURE 1 | Schematic of the encryption procedure of the symmetry properties of a plane curve into the azimuthal phase of a light beam. In **(A)**, as an example, we show $\boldsymbol{t}$ and $\boldsymbol{n}$, i.e., the tangent and the normal unit vectors to the curve at the point P, respectively. $\boldsymbol{n}$ forms an angle $\Theta(\phi)$ with the horizontal axis. In **(B)**, we show the transverse phase profile $\psi(\phi) = 2\,\Theta(\phi;\, 1, 1, 5, 1/2, 4/3, 4/3)$ (Equation 6). The latter can be regarded as the superposition of the phase modulation $2\,\Delta\Theta_m(\phi)$ **(C)** and the helical phase profile $2\,\phi$ **(D)**.

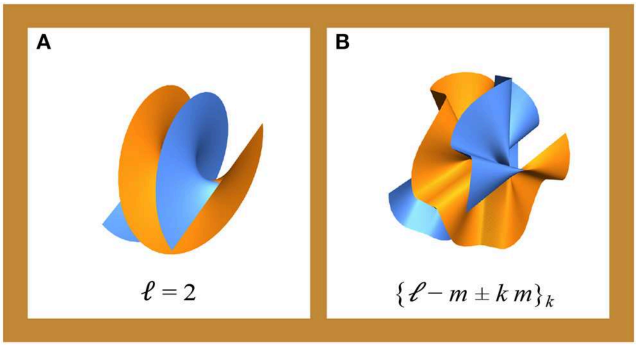

FIGURE 2 | Helical wavefronts corresponding to a circumference **(A)** and to the curve represented in **Figure 1A(B)**.

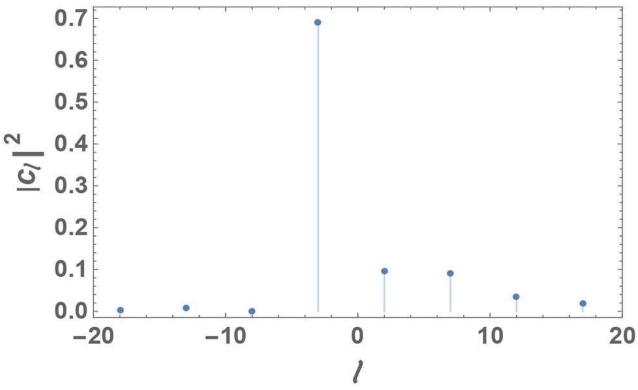

FIGURE 3 | OAM power spectrum arising from the azimuthal phase profile corresponding to the parameter values $a = b = 1$, $m = 5$, $n_1 = 1/2$, and $n_2 = n_3 = 4/3$.

3. FREE-FORM AZIMUTHAL (FFA) SVAPS

We now focus on the experimental methods for generating optical beams with the phase structure prescribed by Equation (6). To reshape a TEM_{00} laser beam according to our wishes, we opted for a properly tailored SVAP. The latter is a half-wave retardation plate in which the direction-angle of $\bar{\Theta}(r, \phi)$ of the optic axis is spatially variant [23, 24, 26]. When a circularly polarized input beam passes through the plate, it acquires a *geometric phase* factor $e^{\pm i2\bar{\Theta}(r,\phi)}$. The sign in the exponent depends on the handedness of the incident beam polarization $\boldsymbol{C}_{\pm} = (\boldsymbol{x} \pm i\boldsymbol{y})/\sqrt{2}$, which is reversed by the SVAP [25]. For a comprehensive view of the mechanism underlying wavefront reshaping via the Geometric or Pancharatnam-Berry Phase, we address the reader to Piccirillo et al. [25]. In essence, molding the phase of a SVAP amounts to patterning the optic-axis so that its direction-angle is locally equal to half the prescribed optical phase. In order to fabricate a liquid-crystal SVAP for generating FFDH beams, the optic-axis angular distribution must be set to

$$\bar{\Theta}(r, \phi) = \frac{\psi(\phi)}{2} = \Theta(\phi; a, b, m, n_1, n_2, n_3). \tag{7}$$

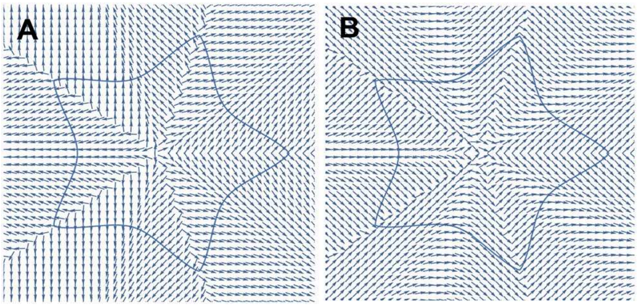

FIGURE 4 | Optic axis patterns deduced from Equation (7) for the parameter values $a = b = 1$, $m = 5$, $n_1 = 1/2$, and $n_2 = n_3 = 4/3$. **(A)** Optic axis pattern for a SVAP imparting to an input beam the geometric phase $2\phi + 2\Delta\Theta_m(\phi)$ (**Figure 1B**). **(B)** Optic axis pattern for a SVAP imparting the geometric phase $2\Delta\Theta_m(\phi)$ (**Figure 1C**).

In **Figure 4**, we show the optic-axis pattern of a SVAP corresponding to $\Theta(\phi; a = 1, b = 1, m = 5, n_1 = 1/2, n_2 = 4/3, n_3 = 4/3)$ (**Figure 4A**) and, for comparison, the contribution to such a pattern of the modulation only (**Figure 4B**). **Figure 5A** shows a microscope image of the SVAP under crossed polarizers, with a birefringent λ-compensator inserted between the SVAP and the analyzer. The λ-compensator has a path difference of 550 nm and therefore introduces a π retardation at that wavelength. The fast axis forms a 45° angle to the axis of the analyzer. When the compensator is put in, the sample changes its color depending on its orientation. The changes in color are based on optical interference. This method fully unveils the optic axis pattern underlying the SVAP (**Figure 4A**) because, differently from the simple crossed-polarizers method, it enables the orthogonal orientations of the optic axis to be distinguished between.

Though pure-phase holograms displayed on SLM could be used to create FFDH beams, fabricating optical devices based on Geometric Phase has proved to be not only the best-performing choice but also the most natural, since the unit normal distribution deduced from a generating curve is directly translated into an optic axis pattern. As an example, we have here chosen curves generated via the superformula to take advantage of a large variety of shapes grouped under the same equation. A similar method, however, can be applied to any other curve or family of curves.

4. INTENSITY PROFILES

As mentioned above, by adding a periodical azimuthal phase modulation to the phase of a helical beam, the cylindrical symmetry typical of the intensity profile of a doughnut is broken. In fact, each photon at distance r from the beam axis suffers a change in its azimuthal linear momentum k_ϕ that depends periodically on the orientation of the meridional plane it starts from. As k_ϕ has the same period as $\rho(\phi)$ in Equation (4), the

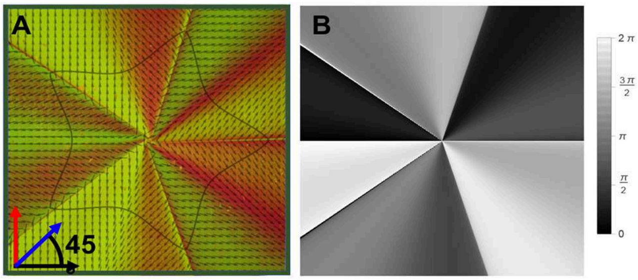

FIGURE 5 | Experimental observation of the optic axis distribution of the SVAP ($a = b = 1$, $m = 5$, $n_1 = 1/2$, and $n_2 = n_3 = 4/3$). **(A)** Microscope image of the SVAP between crossed polarizers + birefringent compensator plate at 45°. This image reveals the optic axis pattern underlying the SVAP (**Figure 4A**), which is displayed in the image overlay. The image was recorded when illuminating the sample with white light, sandwiched between crossed polarizers, and inserting, between the sample and the analyzer, a birefringent λ-compensator ($\lambda = 550$ nm) with the optic axis rotated by 45°. The arrows in the lower left corner sketch the axes orientations of the input linear polarizer (black arrow), the output analyzer (red arrow), and the λ-compensator (blue arrow). **(B)** Optical transverse phase profile associated with the optic axis pattern in **(A)**—the same as in **Figure 1B**—here replicated for the sake of comparison.

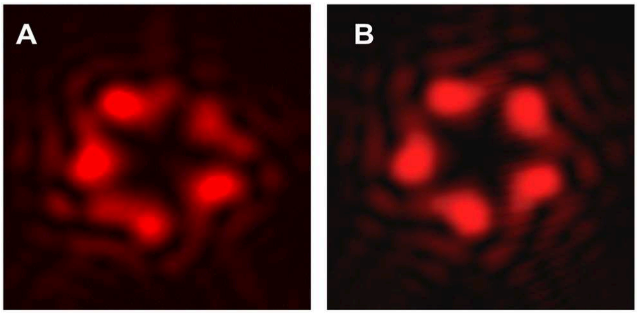

FIGURE 6 | Comparison between the experimental **(A)** and theoretical **(B)** intensity profiles of the beam generated through the SVAP with the optic axis pattern shown in **Figure 4A** at distance $z = 1$ m, for the values $a = b = 1$, $m = 5$, $n_1 = 1/2$, and $n_2 = n_3 = 4/3$ of the curve parameters and for an input gaussian beam with a plane wavefront and radius $w_0 = (1.50 \pm 0.04)$ mm.

resulting transverse intensity profile becomes periodic as well. What's more, the details of the profile of k_ϕ are inherited from the azimuthal rate of change of the unit vector normal to the curve, also meaning that the inflections of the intensity profiles will be inherited from the local curvature of the generating curve. This enables a one-to-one correspondence to be set between the geometric properties of the generating curve and the transverse intensity profile of the beam, especially as far as the dark region is concerned. In **Figure 6A**, we show the intensity profile of the beam experimentally generated for the parameter values $a = b = 1$, $m = 5$, $n_1 = 1/2$, and $n_2 = n_3 = 4/3$ at distance $z = 1$ m from the SVAP for a circularly polarized input TEM$_{00}$ Gaussian mode with a plane wavefront and radius $w_0 = (1.50 \pm 0.04)$ mm. For comparison, **Figure 6B** shows the theoretical intensity profile predicted by calculating the Fresnel transform of the optical field

$$E_0\, e^{-\frac{x^2+y^2}{w_0^2}+2\,i\,\Theta(\phi;1,1,5,1/2,4/3,4/3)}, \qquad (8)$$

for the same parameter values. The faint striped structure surrounding the core profile originates by diffraction from the abrupt azimuthal changes in the transverse phase profile shown in **Figure 5B**.

5. CONCLUDING REMARKS

We have shown the possibility of generating dark hollow beams with a large variety of intensity landscapes by using a single azimuthal phase factor without passing through numerical methods for optical field encryption. The method is based on a geometric approach in which the intensity profile around the beam axis is supposed to imitate the shape of a selected closed curve. Also, the OAM spectrum is affected by the shape of the generating curve. If the generating curve has m-fold rotational symmetry, the OAM spectrum will include only components with multiple of m within a global shift determined by the OAM index of the unperturbed helical mode. Liquid-crystal SVAPs turn out to be the most natural choice for implementing such a method, since the unit vector normal to the generating curve comes to be copied over the axis pattern. Applications of FFA SVAPs can be easily devised, in particular, for manipulating non-spherical objects trapped by optical tweezers—as unwanted rotations of micro-objects could then be avoided—as well as for increasing contrast in optical coronagraphy—as properly tailored dark-hollow beams with line singularities along radial directions could be exploited to split the intensity distribution around the optical axis.

DATA AVAILABILITY STATEMENT

All datasets generated for this study are included in the article/supplementary material.

AUTHOR CONTRIBUTIONS

All of the authors contributed to developing the method for designing Free-Form SVAPs introduced in this paper. BP fabricated and tested the SVAPs. All of the authors contributed to writing the paper.

FUNDING

This work was supported by the University of Naples Research Funding Program (DR no. 3425-10062015) and by the European Research Council (ERC) under grant no. 694683 (PHOSPhOR).

ACKNOWLEDGMENTS

The authors thank Prof. L. Marrucci from the Department of Physics E. Pancini of the University of Naples for useful discussions.

REFERENCES

1. Rubinsztein-Dunlop H, Forbes A, Berry MV, Dennis MR, Andrews DL, Mansuripur M, et al. Roadmap on structured light. *J Opt.* (2016) **19**:013001. doi: 10.1088/2040-8978/19/1/013001
2. Taylor MA, Waleed M, Stilgoe AB, Rubinsztein-Dunlop H, Bowen WP. Enhanced optical trapping via structured scattering. *Nat Photon.* (2015) **9**:669–73. doi: 10.1038/nphoton.2015.160
3. Dholakia K, Čižmár T. Shaping the future of manipulation. *Nat Photon.* (2011) **5**:335–42. doi: 10.1038/nphoton.2011.80
4. Bozinovic N, Yue Y, Ren Y, Tur M, Kristensen P, Huang H, et al. Terabit-scale orbital angular momentum mode division multiplexing in fibers. *Science.* (2013) **340**:1545–8. doi: 10.1126/science.1237861
5. Willner AE, Huang H, Yan Y, Ren Y, Ahmed N, Xie G, et al. Optical communications using orbital angular momentum beams. *Adv Opt Photon.* (2015) **7**:66–106. doi: 10.1364/AOP.7.000066
6. Mair A, Vaziri A, Weihs G, Zeilinger A. Entanglement of the orbital angular momentum states of photons. *Nature.* (2001) **412**:313–6. doi: 10.1038/35085529
7. Molina-Terriza G, Torres JP, Torner L. Twisted photons. *Nat Phys.* (2007) **3**:305–10. doi: 10.1038/nphys607
8. Peacock AC, Steel MJ. The time is right for multiphoton entangled states. *Science.* (2016) **351**:1152–3. doi: 10.1126/science.aaf2919
9. Maurer PC, Maze JR, Stanwix PL, Jiang L, Gorshkov AV, Zibrov AA, et al. Far-field optical imaging and manipulation of individual spins with nanoscale resolution. *Nat. Phys.* (2010) **6**:912–8. doi: 10.1038/nphys1774
10. D'Aguanno G, Mattiucci N, Bloemer M, Desyatnikov A. Optical vortices during a superresolution process in a metamaterial. *Phys Rev A.* (2008) **77**:043825. doi: 10.1103/PhysRevA.77.043825
11. Boriskina SV, Reinhard BM. Molding the flow of light on the nanoscale: from vortex nanogears to phase-operated plasmonic machinery. *Nanoscale.* (2012) **4**:76–90. doi: 10.1039/C1NR11406A
12. Boriskina SV, Reinhard BM. Adaptive on-chip control of nano-optical fields with optoplasmonic vortex nanogates. *Opt Express.* (2011) **19**:22305–15. doi: 10.1364/OE.19.022305
13. Kim H, Park J, Cho S-W, Lee S-Y, Kang M, Lee B. Synthesis and dynamic switching of surface plasmon vortices with plasmonic vortex lens. *Nano Lett.* (2010) **10**:529–36. doi: 10.1021/nl903380j
14. Hell SW, Wichmann J. Breaking the diffraction resolution limit by stimulated emission: stimulated-emission-depletion fluorescence microscopy. *Opt Lett.* (1994) **19**:780–2. doi: 10.1364/OL.19.000780
15. Novotny L, Beversluis MR, Youngworth KS, Brown TG. Longitudinal field modes probed by single molecules. *Phys Rev Lett.* (2001) **86**:5251–4. doi: 10.1103/PhysRevLett.86.5251
16. Nivas JJ, Cardano F, Song Z, Rubano A, Fittipaldi R, Vecchione A, et al. Surface structuring with polarization-singular femtosecond laser beams generated by a q-plate. *Sci Rep.* (2017) **7**:42142. doi: 10.1038/srep42142
17. Meier M, Romano V, Feurer T. Material processing with pulsed radially and azimuthally polarized laser radiation. *Appl Phys A.* (2007) **86**:329–34. doi: 10.1007/s00339-006-3784-9
18. Rose P, Diebel F, Boguslawski M, Denz C. Airy beam induced optical routing. *Appl Phys Lett.* (2013) **102**:101101. doi: 10.1063/1.4793668
19. Bomzon Z, Kleiner V, Hasman E. Pancharatnam-Berry phase in space-variant polarization-state manipulations with subwavelength gratings. *Opt Lett.* (2001) **26**:1424–6. doi: 10.1364/OL.26.001424
20. Liu C, Bai Y, Zhao Q, Yang Y, Chen H, Zhou J, et al. Fully controllable pancharatnam-berry metasurface array with high conversion efficiency and broad bandwidth. *Sci Rep.* (2016) **6**:34819. doi: 10.1038/srep34819
21. Kim J, Li Y, Miskiewicz MN, Oh C, Kudenov MW, Escuti MJ. Fabrication of ideal geometric-phase holograms with arbitrary wavefronts. *Optica.* (2015) **2**:958–64. doi: 10.1364/OPTICA.2.000958
22. Jiang M, Yu H, Feng X, Guo Y, Chaganava I, Turiv T, et al. Liquid crystal pancharatnam–berry micro-optical elements for laser beam shaping. *Adv Opt Mater.* (2018) **6**:1800961. doi: 10.1002/adom.201800961
23. Piccirillo B, D'Ambrosio V, Slussarenko S, Marrucci L, Santamato E. Photon spin-to-orbital angular momentum conversion via an electrically tunable q-plate. *Appl Phys Lett.* (2010) **97**:241104. doi: 10.1063/1.3527083
24. Piccirillo B, Kumar V, Marrucci L, Santamato E. Pancharatnam-Berry phase optical elements for generation and control of complex light: generalized superelliptical q-plates. In: Galvez EJ, Glückstad J, Andrews DL, editors. *Complex Light and Optical Forces IX*, Vol. 9379. International Society for Optics and Photonics (SPIE) (2015). p. 22–30. doi: 10.1117/12.2078372
25. Piccirillo B, Picardi MF, Marrucci L, Santamato E. Flat polarization-controlled cylindrical lens based on the pancharatnam-berry geometric phase. *Eur J Phys.* (2017) **38**:034007. doi: 10.1088/1361-6404/aa5e11
26. Alemán-Castaneda LA, Piccirillo B, Santamato E, Marrucci L, Alonso MA. Shearing interferometry via geometric phase. *Optica.* (2019) **6**:396–9. doi: 10.1364/OPTICA.6.000396
27. Allen L, Beijersbergen MW, Spreeuw RJC, Woerdman JP. Orbital angular momentum of light and the transformation of Laguerre-Gaussian laser modes. *Phys Rev A.* (1992) **45**:8185–9.
28. Allen L, Barnett SM, Padgett MJ. *Optical Angular Momentum.* Bristol: Institute of Physics Publishing (2003).
29. Jáuregui R, Hacyan S. Quantum-mechanical properties of bessel beams. *Phys Rev A.* (2005) **71**:033411. doi: 10.1103/PhysRevA.71.033411
30. Karimi E, Piccirillo B, Marrucci L, Santamato E. Improved focusing with hypergeometric-gaussian type-II optical modes. *Opt Express.* (2008) **16**:21069–75. doi: 10.1364/OE.16.021069
31. Bolduc E, Bent N, Santamato E, Karimi E, Boyd RW. Exact solution to simultaneous intensity and phase encryption with a single phase-only hologram. *Opt Lett.* (2013) **38**:3546–9. doi: 10.1364/OL.38.003546
32. Marrucci L, Manzo C, Paparo D. Optical spin-to-orbital angular momentum conversion in inhomogeneous anisotropic media. *Phys Rev Lett.* Berlin (2006) **96**:163905. doi: 10.1103/PhysRevLett.96.163905
33. Lu TH, Huang TD, Wang JG, Wang LW, Alfano RR. Generation of flower high-order poincarésphere laser beams from a spatial light modulator. *Sci Rep.* (2016) **6**:39657. doi: 10.1038/srep39657
34. Porfirev A, Skidanov R. Dark-hollow optical beams with a controllable shape for optical trapping in air. *Opt Express.* (2015) **23**:8373–82. doi: 10.1364/OE.23.008373
35. Piccirillo B, Piedipalumbo E, Marrucci L, Santamato E. Electrically tunable vector vortex coronagraphs based on liquid-crystal geometric phase waveplates. *Mol Crystals Liquid Crystals.* (2019) **684**:15–23. doi: 10.1080/15421406.2019.1581707
36. Rubano A, Cardano F, Piccirillo B, Marrucci L. Q-plate technology: a progress review (invited). *J Opt Soc Am B.* (2019) **36**:D70–87. doi: 10.1364/JOSAB.36.000D70
37. Forbes A, Dudley A, McLaren M. Creation and detection of optical modes with spatial light modulators. *Adv Opt Photon.* (2016) **8**:200–27. doi: 10.1364/AOP.8.000200
38. Sokolov D. *Lamé Curves.* Encyclopedia of Mathematics. Springer Science+Business Media B.V.; Kluwer Academic Publishers (2001).
39. Gielis J. A generic geometric transformation that unifies a wide range of natural and abstract shapes. *Am J Bot.* (2003) **90**:333–8. doi: 10.3732/ajb.90.3.333

Conflict of Interest: The authors declare that the research was conducted in the absence of any commercial or financial relationships that could be construed as a potential conflict of interest.

frontiers in Physics

REVIEW
published: 25 May 2020
doi: 10.3389/fphy.2020.00112

Topological Point Defects of Liquid Crystals in Quasi-Two-Dimensional Geometries

Kirsten Harth[1,2]* *and Ralf Stannarius*[1]

[1] *Department of Nonlinear Phenomena, Institute of Physics, Otto von Guericke University, Magdeburg, Germany,*
[2] *Department of Computer Oriented Theoretical Physics, Institute of Physics, Otto von Guericke University, Magdeburg, Germany*

We review the interactions and dynamics of topological defects in liquid crystals (LCs) in quasi-two-dimensional (2D) geometries. Such spatial restrictions can be realized in thin freely suspended smectic C films, in thin sandwich cells filled with nematic LCs, and under specific boundary conditions in LC shells embedded in aqueous solutions. Random defect patterns can be created by thermal quenching of the samples from lower ordered into higher ordered phases. On the other hand, well-defined isolated defect configurations for the study of elementary interaction steps can be prepared by using simple mechanical techniques. Observation by polarizing microscopy is straightforward. Spatial dimensions of the experimental systems as well as time scales are convenient for observation. The continuum theory of LCs is well-developed so that, in addition to the experimental characterization, an analytical or numerical description is feasible. From interactions and dynamic features observed in these LC systems, general conclusions on defect dynamics can be drawn.

Keywords: defects, disclinations, liquid crystals, two-dimensional systems, continuum theory, freely suspended films, fluid mechanics, phase transitions

Edited by:
Francesca Serra,
Johns Hopkins University,
United States

Reviewed by:
Julio Cesar Armas-Perez,
University of Guanajuato, Mexico
Roberto Cerbino,
University of Milan, Italy

Correspondence:
Kirsten Harth
kirsten.harth@ovgu.de

Specialty section:
This article was submitted to
Soft Matter Physics,
a section of the journal
Frontiers in Physics

Received: *28 November 2019*
Accepted: *23 March 2020*
Published: *25 May 2020*

Citation:
Harth K and Stannarius R (2020)
Topological Point Defects of Liquid
Crystals in Quasi-Two-Dimensional
Geometries. Front. Phys. 8:112.
doi: 10.3389/fphy.2020.00112

1. INTRODUCTION

Topological defects occur in a wide variety of physical systems, ranging from soft matter [1–6] to quantum systems [7–10], superfluid liquids [11–14], and thin magnetic films [15–17] to cosmology [18–22]. Often, the coarsening of defect patterns that form after symmetry-breaking phase transitions determines the establishment of long-range order in the system. The dynamical properties of such patterns are far from being trivial. A promising concept to find a universal description is to look for general features of defect patterns and their interactions in different systems [20–25]. For that purpose, a system in which universal features of defects can be studied relatively easily and in a quantitative way is of great advantage. Some liquid crystal (LC) phases are promising candidates by virtue of their easy handling, straightforward observation, convenient relaxation time scales, and diversity of structures. They allow for studying defect interactions and coarsening dynamics of topological defect patterns with conventional optical polarizing microscopy. Ensembles of very different kinds of defects in LC phases have been described (e.g., [1–5, 26–33]). The observation of pattern coarsening by mutual annihilations of topological point defects in such systems allows for the direct study of "scaling solutions," providing models for the evolution of monopoles, multipoles, and textures. Isolated defect pairs can be created to study their mutual interactions as the elementary steps of pattern coarsening. Beyond such defect interactions, mixed structures of defects and inclusions of various shapes and sizes or influences of container boundaries can add further levels of complexity. It is possible to add a mass (of attached inclusions) to defects, to set spatial restrictions, and to exploit defects for structural stabilization of two-dimensional or three-dimensional colloids.

A considerable simplification for the analysis of basic features of defect dynamics is the restriction to quasi-two-dimensional (2D) systems, i.e., samples in which the extension in the third dimension is negligible with respect to the typical defect distances and core sizes and samples that can be considered uniform in the third dimension. We focus here on defects in this category of 2D systems, even though this excludes the rich variety of three-dimensional defect structures found in colloidal systems with nematic hosts in flat cells [3, 4, 34, 35] or other geometrical restrictions [36–39]. We also disregard dislocations, which are 3D defect structures formed by smectic phases, but restrict ourselves to disclinations. Finally, we have limited this review to conventional, "passive" LC materials and disregard active nematics (e.g., [41, 42]). The focus of this review is on smectic LCs in thin-film geometry, but we also discuss some quasi-2D nematic systems in sandwich cells, where the character of the director field is sufficiently 2D. Examples of optical images of topological defects in LC films are seen in **Figure 1**. Topologically, they are classified by the defect strength or topological charge S, which is equal to the number of full rotations of the liquid-crystal director on a closed path around the defect core. Defects of a given strength S may be further distinguished by a phase θ_1 (**Figure 2**). An advantage of smectic freely suspended films over nematics is that experiments with nematics in sandwich cells are not easy to interpret because of the three-dimensionality of the geometric problem. Defects, even if they are well-localized in the cell midplane, usually extend from one glass plate to the other. Interactions with the boundaries, such as pinning, and a preferential alignment or 3D director field distortions near the cell walls have to be taken into account. No-slip boundary conditions for material flow will make the dynamics much more complex than in freely suspended films, for which we can neglect coupling to a surrounding fluid in most cases. The same applies if the defects are located at a confining boundary; their geometry will, in this case, be more 3D in nature. Smectic C mesogens, on the other hand, can form stable, quasi-two-dimensional (2D) freely suspended films (FSFs) similar to soap films when they are stretched across a solid frame [45]. Since their first detailed description by Young et al. [46], they have proven very useful in manifold investigations. Stable films can be as thin as two molecular layers.

2. FUNDAMENTALS

2.1. Liquid Crystal Phases and Their Continuum Description

Since there are excellent textbooks that describe the physics of liquid crystals, we recollect here only a few basic features that are necessary to understand the nature, structure and dynamics of defects in LC phases. For a deeper introduction into the properties and theoretical description of LCs, the reader is referred to standard books (e.g., [47, 48]).

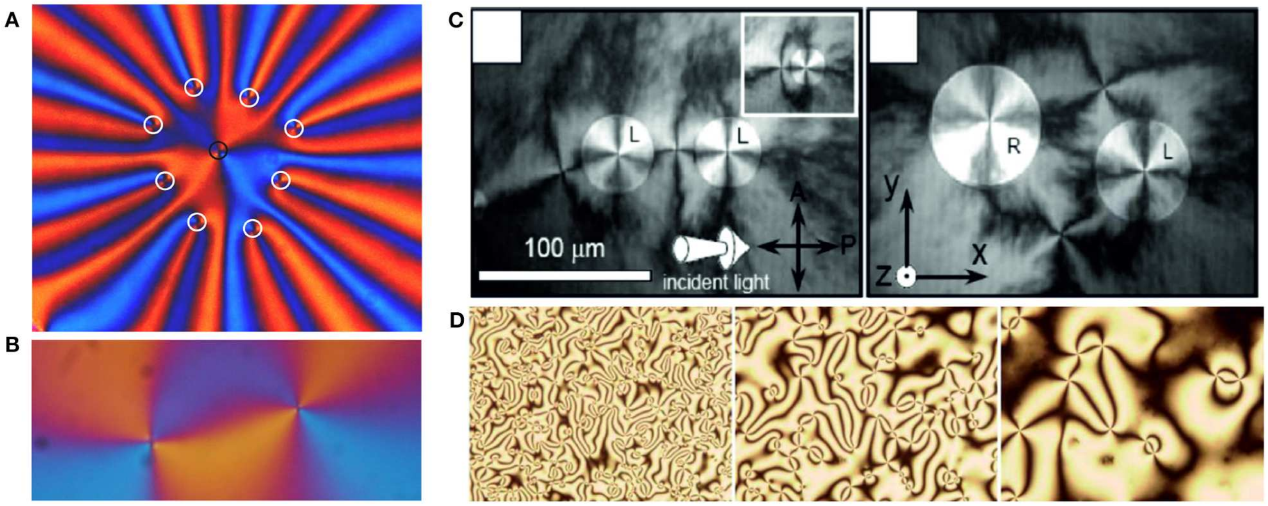

FIGURE 1 | (A) Snapshot of a non-equilibrium arrangement of nine defects in a SmC freely suspended film, all with topological strength +1. The defects repel each other, and the pattern rapidly expands, with eight defects moving radially outward and one remaining in the center. The defect cores are labeled by small circles (see text). Figure adapted from Stannarius and Harth [32]. **(B)** Pair of two defects of opposite topological strengths, −1 (left) and +1 (right) in a SmC freely suspended film. The defects attract each other and finally annihilate, leaving a defect-free uniform texture. Figure adapted from Missaoui et al. [43]. Both images were recorded with crossed polarizers and a diagonally inserted wave plate. **(C)** Depolarized reflected microscope images of islands in a SmC freely suspended film. The islands contain tangential clockwise (L) and counterclockwise (R) c-director fields and central +1 defects, each island has an accompanying outer −1 defect. Reproduced from Silvestre et al. [29] with permission, copyright American Physical Society. **(D)** Coarsening of umbilical defect patterns in a nematic cell with homeotropic anchoring and an electric field normal to the cell plane. The director of the material with negative $\Delta\varepsilon$ is driven into the cell plane, forming numerous umbilic ±1 disclinations. Reproduced with permission from Dierking et al. [44], copyright American Physical Society.

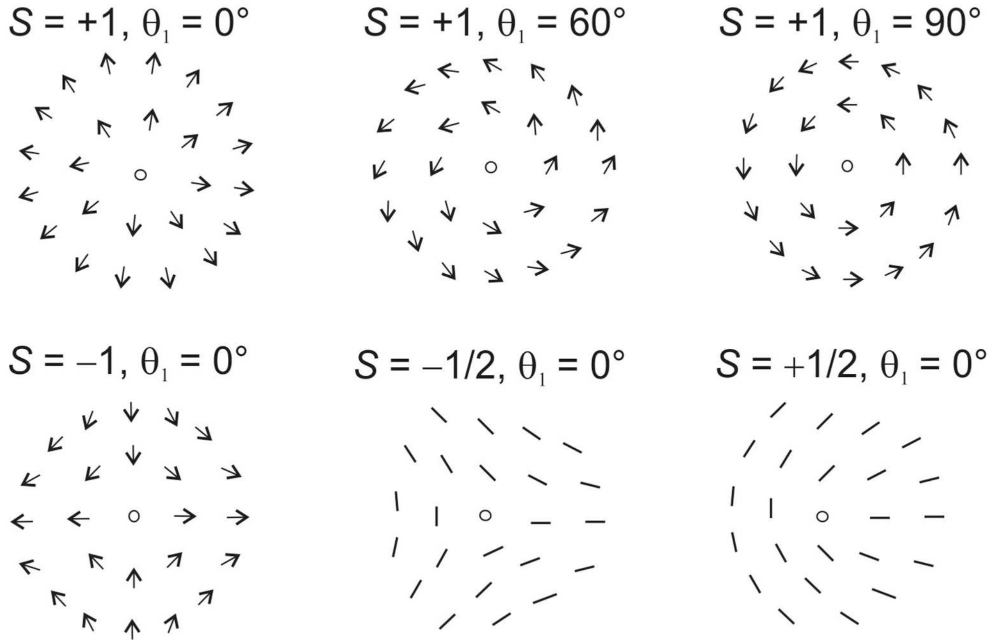

FIGURE 2 | Sketches of topological defects with strengths ±1 and ±1/2 with different phases θ_1. The phase of +1 defects changes their structure qualitatively (see top row images), left: "radial," right: "tangential" configuration. For all defects of strengths $S \neq 1$, a non-zero phase θ_1 is equivalent to a simple rotation of the defect by an angle $\theta_1/(1-S)$. The half-integer defects are prohibited in vector fields such as the $\vec{c}$ director field of smectic C phases.

The relevant thermotropic LC phases in the context of this review are nematic (N), smectic C (SmC), and smectic C* (SmC*) liquid crystals. Nematics have a molecular arrangement without long-range positional order, and the local preferential orientation of the molecular long axes (the optical axis) is characterized by the director field $\hat{n}(x, y, z)$. Conventional nematic phases are non-polar, belong to the symmetry group $D_{\infty h}$, and the directions $\hat{n}$ and $-\hat{n}$ are equivalent. The ground state of a conventional non-chiral, infinitely extended nematic sample is a spatially uniform alignment of $\hat{n}$. Spatial distortions of the director lead to contributions to the elastic free energy density w in the form

$$w = \frac{1}{2}K_{11}(\nabla \cdot \hat{n})^2 + \frac{1}{2}K_{22}(\hat{n} \cdot \nabla \times \hat{n})^2 + \frac{1}{2}K_{33}(\hat{n} \times \nabla \times \hat{n})^2 \quad (1)$$

with the elastic constants for splay, K_{11}, twist, K_{22}, and bend, K_{33}, of the order of a few pN. Such distortions can be caused, for example, by the boundary conditions in finite samples, by the existence of topological defects, by application of electromagnetic fields, or by shear flow.

At solid or liquid boundaries, or at free surfaces, the director may adopt preferential orientations. Those are described by boundary conditions, which may be strong (analogous to Dirichlet type boundary conditions), fixing the orientation of the director, or weak (analogous to Robin boundary conditions), fixing a certain relation between the director and its spatial derivatives. For weak anchoring, the director can deviate from its preferred orientation at the cost of an increased elastic energy.

Additional terms may occur in chiral or polar phases. Another term with the saddle-splay elastic constant K_{24} can be transformed into a surface integral of the free energy, it is thus only dependent on the director orientation at boundaries and can be neglected when the director is rigidly anchored. It may play a role in the vicinity of defect cores. Except near singular points of this director field, one can assume that $|\hat{n}| = 1$. In 2D geometry, with $\hat{n} = (\cos\theta, \sin\theta, 0)$, the free energy density equation reduces to

$$\begin{aligned} w &= \frac{K_{11}}{2}(\nabla \cdot \hat{n})^2 + \frac{K_{33}}{2}(\nabla \times \hat{n})^2 \quad (2) \\ &= \frac{K_{11}}{2}\left(-\sin\theta\frac{\partial\theta}{\partial x} + \cos\theta\frac{\partial\theta}{\partial y}\right)^2 + \frac{K_{33}}{2}\left(\sin\theta\frac{\partial\theta}{\partial y} + \cos\theta\frac{\partial\theta}{\partial x}\right)^2. \end{aligned}$$

In one-constant approximation, where the elastic constants are set equal to $K_{11} = K_{33} = K$,

$$w = \frac{K}{2}\left(\left(\frac{\partial\theta}{\partial x}\right)^2 + \left(\frac{\partial\theta}{\partial y}\right)^2\right), \quad (3)$$

and the minimum of the free energy can be found from the solutions of the Laplace equation $\Delta\theta = 0$. Singular points of the director field mark defects. In their vicinity, the nematic order parameter goes down and the continuum model requires the introduction of a tensor order parameter [49–53]. We will not consider the nanoscopic structure of the defect cores here. In many situations, it is practical to make the reasonable approximation that the director is pinned at the boundary of a circle with radius r_c around the defect core, and the actual core region is omitted.

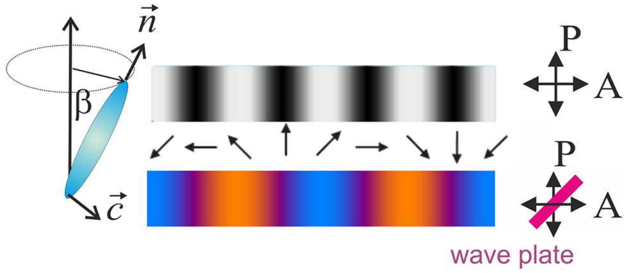

FIGURE 3 | C-director and optical appearance when the planar film is observed with crossed polarizers (top) and with crossed polarizers and diagonally inserted phase plate (bottom).

Another important property of nematics is their electric and magnetic anisotropy. In the simplest case of uniaxial nematics, the dielectric permittivity adopts the form

$$\hat{\varepsilon} = \begin{bmatrix} \varepsilon_\perp & 0 & 0 \\ 0 & \varepsilon_\perp & 0 \\ 0 & 0 & \varepsilon_\parallel \end{bmatrix}.$$

In the case $\Delta\varepsilon = \varepsilon_\parallel - \varepsilon_\perp > 0$, the electric torque drives the director toward a parallel or antiparallel orientation respective to the electric field; in the opposite case, the director is pushed toward a perpendicular orientation. Similarly, the diamagnetic susceptibility $\hat{\chi}$ is a tensor that governs the reorientation of the director in an external magnetic field. Finally, the uniaxial nematic phase is birefringent, with different ordinary and extraordinary refractive indices. This allows optical studies with polarizing microscopy (see section 2.3 below).

Thin SmC films can be treated with the same concept, where a unit vector along the projection of $\hat{n}$ onto the film plane takes over the role of the nematic director. This is appropriate as long as the director orientation is uniform along the film normal, which is fulfilled in micrometer or sub-micrometer thin SmC films and in SmC* films that are much thinner than their helical pitch. We now consider the projection $\vec{n}_0 = (n_x, n_y, 0)$ of $\hat{n}$ onto the film plane, with variable length depending on the tilt angle β (see **Figure 3**). The free energy expansion in the film is [54, 55]

$$w = A|\vec{n}_0|^2 + C|\vec{n}_0|^4 + K_{11}(\nabla \cdot \vec{n}_0)^2 + \left[K_{22}(\hat{n} - \vec{n}_0)^2 + K_{33}\,\vec{n}_0^2\right](\nabla \times \vec{n}_0)^2, \tag{4}$$

where the Landau parameters $A < 0$ and $C > 0$ set the equilibrium length of $\vec{n}_0$, viz. the equilibrium tilt angle $\beta_0 = \arcsin\sqrt{-A/(2C)}$ of $\hat{n}$ respective to the layer normal. Their magnitude describes the resistance against changes of β. At non-zero tilt, one can define a unit vector $\vec{c} = \vec{n}_0/|\vec{n}_0|$, the c-director (**Figure 3**), which is a true vector [1]. Approaching the core of a defect in the c-director field, $|\vec{n}_0|$ drops to zero, i.e., the material in the core is locally in the smectic A (SmA) phase ($\beta \to 0$). Note that there are only splay and bend of $\vec{c}$ in the 2D system. With the new constants $K_S = \sin^2\beta K_{11}$, $K_B = K_{22}\sin^2\beta\cos^2\beta + K_{33}\sin^4\beta$, and $\vec{c} = (\cos\theta, \sin\theta, 0)$ one obtains

$$w_C = \frac{K_S}{2}(\mathrm{div}\,\vec{c})^2 + \frac{K_B}{2}(\mathrm{rot}\,\vec{c})^2 = \frac{K_S}{2}\left(-\sin\theta\frac{\partial\theta}{\partial x} + \cos\theta\frac{\partial\theta}{\partial y}\right)^2 + \frac{K_B}{2}\left(\sin\theta\frac{\partial\theta}{\partial y} + \cos\theta\frac{\partial\theta}{\partial x}\right)^2. \tag{5}$$

This free energy density is similar to Equation (2). In one-constant approximation, $K_S = K_B = K$, the SmC free energy density has the same form as in the nematic case (Equation 3).

2.2. Geometries

The conventional geometry to study nematics is that of thin sandwich cells, with cell gaps between few μm and several hundred μm. The director can be anchored homeotropically at both cell plates, or planarly at one plate, homeotropically at the other (hybrid anchoring), or anchored planarly at both plates. The planar anchoring can have a preferential direction in the plane, or it can be azimuthally degenerate. Two examples are depicted in **Figure 4A**.

There are various methods to produce defects in nematic cells. The easiest one is a rapid phase transition from the isotropic into the nematic phase across the clearing point, either by a temperature quench or by application of high pressure to trigger this transition [20, 21]. It is advantageous in such experiments to have either homeotropic anchoring conditions at the cell plates (director normal to the surfaces) or planar, azimuthally degenerate anchoring. A rich pattern of string defects occurs after the disorder–order transition. These are three-dimensional and of complex geometry. The problem in this experiment is to achieve a well-defined temperature quench. In Chuang's studies [20, 21], no particular surface treatment was reported. Pargellis et al. [56] improved the experiment by well-defined surface treatment of the sapphire windows to ensure homeotropic boundary conditions of the director in the nematic phase. The temperature was quenched by cooling one of the plates below the clearing point and keeping the second one above that point so that a phase boundary between isotropic and nematic states was established and kept in the middle between the cell plates. After this temperature quench, the director adopted degenerate planar boundary conditions at the nematic-isotropic (N-I) interface. Defects that form spontaneously in the nematic move to the N-I interface. Owing to broken mirror symmetry of the anchoring conditions on both interfaces, the 3D director field includes tilt, and only integer-strength defects can form.

This experimental technique was further improved by Nagaya et al. [57, 58] and later employed by Dierking et al. [44, 59]. Their experiments were performed under isothermal conditions in a homeotropic cell within the nematic phase. The authors used materials with negative dielectric anisotropy $\Delta\varepsilon = \varepsilon_\parallel - \varepsilon_\perp < 0$ and applied an electric field along the cell normal. The director remained anchored homeotropically at the cell plates but was driven out of the field direction in the cell center. The maximum director deflection toward the planar orientation was then in the cell midplane. It was not necessary to fix temperature gradients in a sophisticated way to keep the phase boundary in the cell center

---

[1] For simplicity, we will use the term *director* in smectic films synonymously to denote the c-director.

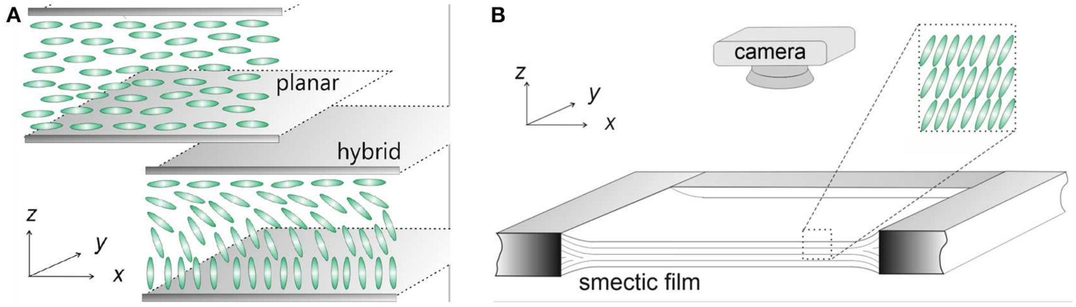

FIGURE 4 | (A) Geometry of nematic cells with planar (top) and hybrid (bottom) anchoring. The mesogens are sketched as ellipsoids. **(B)** Geometry of a planar freely suspended SmC film in air. The front edge of the solid film support has been omitted for visualization of the layered film structure.

as in Pargellis et al. [56]. The geometry of the umbilics that form was such that only integer-strength disclinations were possible (**Figure 1D**). We note that umbilics are, strictly speaking, not defects because they do not contain singularities of the director field. In a 2D projection, however, they behave in many respects like point defects and show similar interactions.

In all these types of nematic sandwich cells, one has to consider the peculiar boundary conditions for the nematic at the glass plates. The director field is therefore in general three-dimensional. Not only is the director anchored at the plates, but the flow field also has 3D character because of its no-slip boundary conditions. Even though many studies of defect dynamics have been performed in nematic cells (e.g., [20, 21, 44, 59–67]), these limitations must be clearly recognized [62, 68, 69]. A different geometry for nematics is that of spherical shells of few μm thickness and diameters of the order of 100 μm, which are filled with, and suspended in, surfactant solutions [40, 70]. There, one can adjust planar, degenerate, or hybrid boundary conditions to create defect structures of the director field. The spherical geometry requires a total topological charge of $+2$ in the director field at any surface with planar components of $\hat{n}$. The closed nature of the nematic layer imposes special restrictions to the arrangements of topological defects [71–77]. In smectic shells with homeotropic anchoring, layers arrange in an onion-like structure. The layer arrangement is usually more complex for hybrid or planar anchoring of $\hat{n}$ [40, 73]. This special geometry of LC shells will not be considered in the following because of its many peculiarities that are unrelated to defect behavior in the flat 2D geometry.

Smectic C phases offer several advantages over nematics when one is interested in a quantitative determination of defect interactions, dynamics, and annihilation processes. These materials can form FSFs with huge aspect rations, either as planar films (**Figure 4B**) or bubbles. These films are ideal model systems to study defect dynamics: they can be prepared with thicknesses that are uniform on a molecular scale. The local orientation is well-described by a continuum theory of a 2D unit vector field $\vec{c}(x, y)$. Film thicknesses are between a few nanometers and several micrometers depending on the preparation conditions. Since all relevant forces scale linearly with the film thickness, the dynamics of the point disclinations are independent of film thickness as long as air drag can be neglected. Lateral widths of the films can be chosen in the millimeter and centimeter ranges so that influences of the boundaries on the local defect dynamics can be controlled. Spatial dimensions of defect patterns in the micrometer range and time scales of annihilation experiments of few seconds offer convenient observation conditions.

The spatially uniform alignment of the c-director is the ground state. Boundary conditions at the film holder may impose certain c-director distortions or even require the necessity of a defect in the film. If the film is disturbed, e.g., by quenching it into a lower symmetry phase [78–81], by a sudden air blow causing complex shear flow patterns in the film plane [82–84], or by rapid changes of the film geometry in presence of inhomogeneous director fields [32, 43, 85], point disclinations can be generated.

Pargellis et al. [78] performed experiments in SmC FSF. Defects were created by temperature quenches from SmA into SmC. Some of the disadvantages of this technique are difficulties to avoid spatial temperature inhomogeneities during the quench, which may evoke Marangoni effects, and advection of the film with airflow. In order to avoid these complications, Muzny [80] studied defects produced with a mechanically induced phase transition from SmA to SmC. Films were spanned across a circular frame and could be deflected by an overpressure of a few Pascal to SmC sphere caps. Upon sudden release of the overpressure, the caps collapsed to flat films, thereby reducing their surface. The consequence was a rapid transition from SmC to the SmA phase. Upon reducing the mesogen tilt angle β very quickly to zero, the film thickened and partially compensated for surface area reductions. Within few milliseconds after collapse, the SmC phase was re-established, and a c-director texture with multiple defects appeared. Wachs [81] performed similar experiments with the same technique in very thin (two-layer) SmC films.

An alternative is the preparation of islands (circular thicker film regions), which can be achieved by air flushes [84] or by a reduction of the film area of very thin films [86, 87]. Since the c-director is anchored at the island borders, each island necessarily contains a $+1$ defect in equilibrium. A compensating -1 defect is formed in the film surrounding the island. Defects can also form spontaneously, starting from a periodically distorted director structure in film menisci [88–91]. Such defects can migrate into a

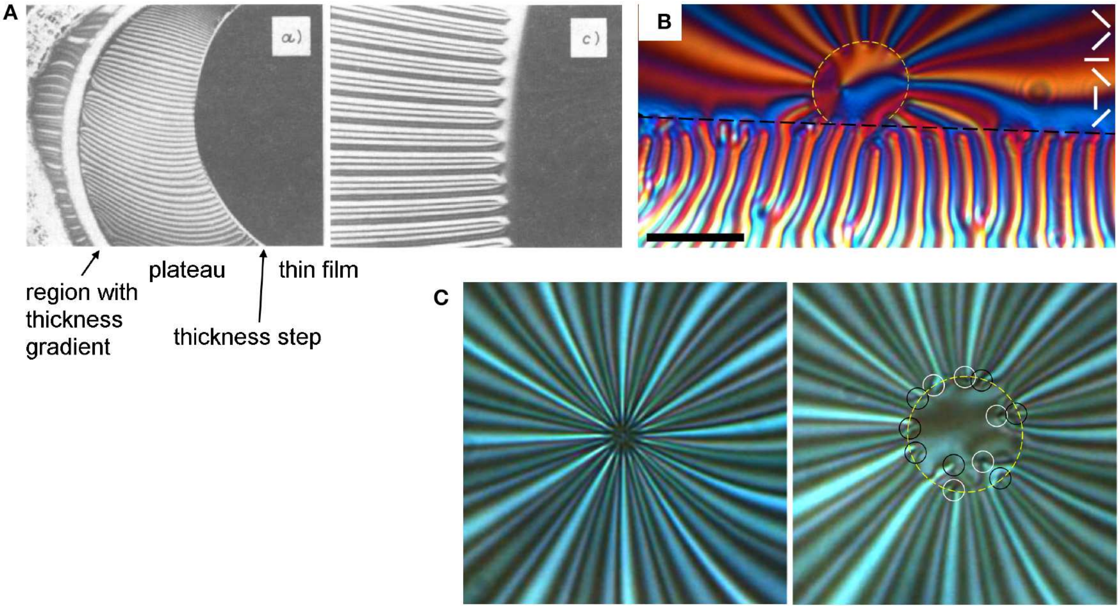

FIGURE 5 | Arrays of $+1$ point defects pinned at layer steps of free-standing SmC films: **(A)** A continuous director distortion extends from a stripe pattern in a band of decreasing thickness (white arc in a), connected to the meniscus at the film holder, across a plateau of homogeneous thickness (striped region in the middle of a), and ending in several $+1$ point defects at a thickness step toward the thinner film seen in black on the right. The region near the stripe ends is enlarged in (c). Image size of (c) $455 \times 367\ \mu\text{m}^2$. Figure reproduced from Maclennan [88], copyright IOP Publishing. **(B)** Defects trapped around a circular film thickness step (yellow dashes), with its connection to the meniscus (below the black dashed line). Crossed polarizers parallel to the edges, with wave plate at 45°, scale bar 50 μm. Adapted from Harth [91]. **(C)** Stripe array with 12 trapped $+1$ defects in the central region, left: in equilibrium (the thinner region enclosed by the film thickness step is not resolved); right: after the film is slightly expanded, the 12 individual defects are visible. Because of $K_S > K_B$, they are all tangential. Black and white circles mark $+1$ with opposite sense of rotation of $\vec{c}$, yellow dashes indicate the main layer step trapping the defects. Crossed polarizers parallel to the edges, image dimensions $72 \times 72\ \mu\text{m}^2$. Microscopy images taken from Stannarius and Harth [32], copyright American Physical Society, annotations from Harth [91].

uniform film region (see **Figure 5A**). Multiple $+1$ defects can be pinned in small thinner regions ("holes") of an otherwise uniform film [32], as in **Figures 5B,C**.

A simple technique to produce defect pairs is to touch the films with a thin fiber [43]. At the contact spot, the fiber circumference may enforce a preferential tangential or radial anchoring of the c-director and a compensating nearby -1 defect. If one moves the fiber far enough away from the latter defect before the film is released, a conjugated pair remains.

A very peculiar exception are materials that exhibit a sign change of one of the elastic constants, for example, the bend elastic constant. In such a material, the uniform ground state is no longer energetically favored, a film with uniform texture will spontaneously develop defect pairs connected by inversion walls [93]. A similar spontaneous formation of defects in a uniform film was described by Dolganov et al. [94] and attributed to a spontaneous bend term in a chiral smectic C* material.

2.3. Observation Techniques

The optical anisotropy in the film plane is determined by the orientation of the c-director, which reflects the tilt azimuth. This allows optical observation of the c-director field by means of polarizing microscopy in transmission or reflection. **Figure 3** sketches the c-director and the optical appearance of a SmC film when observed with crossed polarizers (top), or crossed polarizers and a diagonal λ wave plate (bottom). Without the phase plate, the texture is fourfold degenerate, and with the phase plate it is two-fold.

The c-director field is extracted from transmission images under crossed polarizers as in **Figure 5C**, or with an additional diagonally inserted full wave plate (550 nm, slow axis from top right to bottom left), as in the examples shown in **Figures 1A,B, 5B**. With the phase plate, the films appear bluish where the c-director is diagonal bottom-left to top-right or vice versa, and they appear orange where the c-director is oriented diagonal from bottom-right to top-left or vice versa. It is impossible to distinguish the directions $\vec{c}$ and $-\vec{c}$ at normal incidence. When the c-director field corresponding to a certain texture is plotted in the following, the sense of direction of $\vec{c}$ was chosen arbitrarily in each experiment. This is no problem as long as this selection is consistently maintained within each experiment, because the free energy, force, and torque equations do not depend upon the sign of $\vec{c}$. An alternative is Depolarized Reflected Light Microscopy (DRLM), with the same limitations (see images in **Figure 1C**).

In nematic cells, the situation is in principle similar, but the director is usually not uniform along the cell normal. The optical axis may thus have spatially varying polar and azimuthal angles. The optical intensity in transmission depends in a more complex fashion on $\hat{n}(x, y, z)$. In a crude approximation, one may usually presuppose that textures under crossed polarizers reflect the orientation of the in-plane components of $\hat{n}$. This is fulfilled when the director field is uniform along the cell normal.

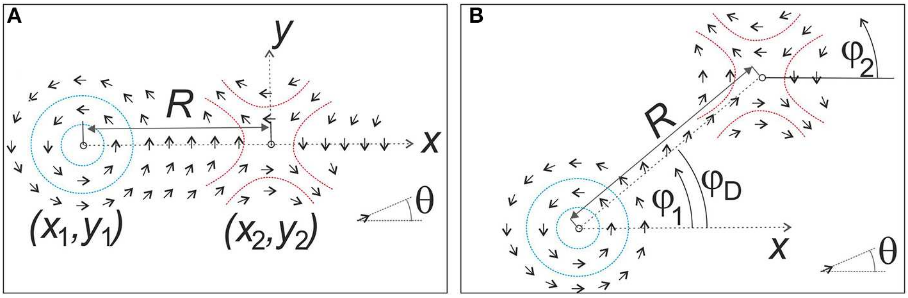

FIGURE 6 | (A) Two defects with matching director fields, i.e., they can be written as a simple superposition of the solutions for two single conjugate defects. **(B)** Two defects whose phases do not match: the director changes along the straight line connecting the two cores.

Then, textures and defects have appearances very similar to those of the c-director given in **Figure 3**, with the c-director replaced by the director projection: Dark regions indicate that the projection of the nematic director onto the cell plane is along one of the polarizers. Bright regions reflect diagonal projections. If $\hat{n}(x, y, z)$ is perpendicular to the cell plane everywhere, the texture under crossed polarizers is uniformly black.

A more elaborate analysis reveals that the transmitted intensity does not only vary with the phase lag between ordinary and extraordinary wave in the cell and the polarizer orientations. One also has to take into account that in-plane variations of $\hat{n}$ modulate the spatial refractive index profile. In contrast to thin smectic films, this may generate refraction and intensity modulations of transmitted light even in absence of polarizers so that defects may be visible even in unpolarized light.

3. THEORETICAL MODELS

3.1. Quasi-Equilibrium Configurations and Forces of Defect Pairs

Continuum models of the nematic and smectic C phases form the theoretical basis of the description of defect dynamics. The simplest assumption made in many models is that the motion of the defects is overdamped and adiabatic. There is no inertia related to the director reorientation or defect core motion. Defects move with a velocity determined by the balance of elastic forces that arise from the gradients in the potential and counteracting viscous forces caused by director reorientations and possible coupling to flow. Each snapshot of the director field can be assumed to represent a free energy minimum under the condition of fixed defect core positions (sometimes including a given flow field). Such interaction forces can be generated, e.g., by fixed anchoring conditions of the director at a boundary near the defect. In a pair of defects of equal or opposite topological charges, their elastic interaction forces drive mutual attraction or repulsion.

The interaction between two disclinations was first calculated under the simplifying assumption of equal splay and bend elastic constants, i.e., $K_S = K_B = K$, in the absence of material flow. The director field is taken as a linear superposition of the single-defect solutions of the director field [95]. For individual defects with topological charge S_i positioned at the origin $(0, 0)$, these individual solutions have the form

$$\theta(\vec{r}) = S_i \varphi(\vec{r}) + \theta_i, \tag{6}$$

where φ is the angle between $\vec{r}$ and the x axis, and θ_i is the phase of the defect. For two defects of topological charges S_1 and S_2 at positions $\vec{R_1} = (x_1, y_1)$ and $\vec{R_2} = (x_2, y_2)$, this yields

$$\theta(\vec{r}) = S_1 \arctan\left(\frac{y - y_1}{x - x_1}\right) + S_2 \arctan\left(\frac{y - y_2}{x - x_2}\right) + \theta_\infty. \tag{7}$$

The two arctan functions yield the angles of the position vectors $(\vec{r} - \vec{R}_1)$ and $(\vec{r} - \vec{R}_2)$ with the x axis. This solution is sketched in **Figure 6A** for $S_1 = +1$ (left), $S_2 = -1$ (right) and $\theta_\infty = -\pi/2$ (the c-director angle in infinity). The problem with this type of solutions is that it produces only defect pairs whose phases match, i.e., the c-director along a straight line connecting the defects is constant, since the arguments of the two arctan functions in Equation (7) remain constant on the straight line connecting the defect cores. This is only a specific subset of the solutions of the general problem, where defects can have any phases.

For two such specific defects with strengths S_1 and S_2, separated by a distance R, the mutual attractive or repulsive force per film thickness is [96, 97]

$$F_e = 2\pi S_1 S_2 \frac{K}{R}. \tag{8}$$

It acts along the separation vector $\vec{R} = \vec{R}_2 - \vec{R}_1$, where $\vec{R}_i$ are the positions of the two cores. Thus, the two defects are expected to approach or move away from each other on straight paths. In nematics, the defect strengths can have integer or half-integer values. In SmC films, owing to the polar character of the c-director, point defects can only have integer strengths. Disclinations of the same sign repel, those of opposite signs attract each other, with forces inversely proportional to the distance R.

Equations (7), (8) describe defect pairs with "ideal" orientations respective to each other, and with "ideal" orientation of $\vec{R}$ to the far director field. The basic models that led to Equation (7) assume that the superposition of two

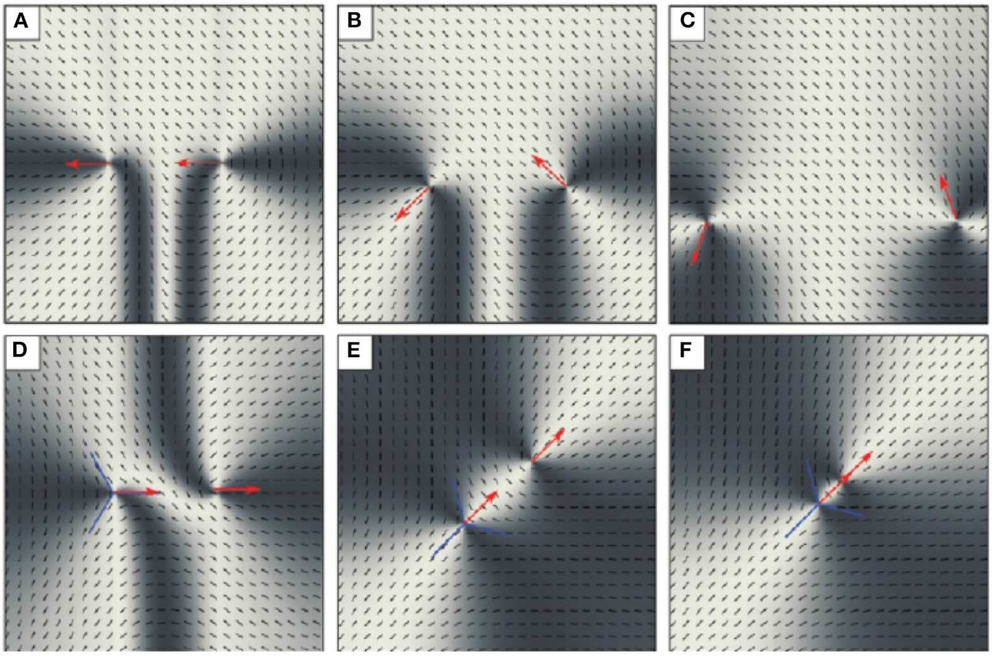

FIGURE 7 | Temporal evolution of a pair of mutually repelling +1/2 defects **(A–C)** and mutually attracting ±1/2 defects **(D–F)**, simulated with Neumann boundary conditions, and an initial separation of the defects of 1/3 of the computed region. Red arrows indicate the "tilt," a quantity introduced to describe the defect orientations. Even though the interconnection vector is initially horizontal in the images, the defect trajectories are curved, and the direction of defect motion noticeably differs from that vector. The image was reproduced from Vromans and Giomi [99], with permission of the Royal Society of Chemistry.

interacting defects is the only director field deformation present. This is correct only if the orientations "match," i.e., the θ is constant along the line connecting the two cores, as sketched in **Figure 6A**. These models cannot describe the effects of mutual orientation mismatches (with regard to the phase angles $\theta_{1,2}$ of both defects) such as those sketched in **Figure 6B**. In practice, one has to take into account that phases of interacting defects in general do not match. The effects of these mutual orientations were first discussed by Vromans and Giomi [99]. They argued that half-integer defects have a generic orientation (*"tilt"*), which affects their interactions qualitatively. It changes the trajectories of mutually attracting or repelling pairs so that their motion is no longer along the interconnecting line (**Figure 7**).

Tang and Selinger [100] extended this idea and generalized it to arbitrary defect strengths. They introduced tensors of rank $n|1-S|$ to characterize the orientation of defects of strength S in n-atic phases (phases with an orientational order parameter of n-fold symmetry). In the non-polar nematic phase, $S = +1/2$ defects are described by a vector, $-1/2$ defects by a tensor of rank 3. In polar nematics and SmC, the $+1$ defect is a scalar, the -1 defect is a tensor of rank 2. Tang and Selinger derived explicit expressions for the director field around defect pairs with different orientations and for the elastic energy depending on the defect orientation parameters. The analytical solutions were found using a conformal mapping technique [100], which works only under the condition of elastic isotropy ($K_S = K_B$).

We use their concept to discuss effects of defect orientations on interactions of conjugated pairs, $S_1 = -S_2 = S$. The equilibrium solutions are [100]

$$\begin{aligned} \theta(\vec{r}) &= S\arctan\left(\frac{y-y_1}{x-x_1}\right) - S\arctan\left(\frac{y-y_2}{x-x_2}\right) \\ &\quad + \frac{\delta\theta}{2}\left[1 + \frac{\ln(|\vec{r}-\vec{R}_1|) - \ln(|\vec{r}-\vec{R}_2|)}{\ln(R)-\ln(r_c)}\right] + \theta_0, \\ \delta\theta &= \theta_2 - \theta_1 - 2S\varphi_D - S\pi, \\ \theta_0 &= \theta_1 + S(\varphi_D + \pi), \end{aligned} \tag{9}$$

where the angle φ_D defines the direction of $\vec{R}$ respective to the x axis (**Figure 6B**), and r_c is the defect core radius. It is assumed that r_c is very small compared to R. The director field at circles with radius r_c around the cores is described by equations of the form of Equation (6). The terms $-S\pi$ and $+S\pi$ in the definitions of $\delta\theta$ and θ_0 arise from the correct choice of the quadrants of the arctan functions used in Tang and Selinger [100]. The first line of Equation (9) plus θ_0 reproduces the solution for pairs with mutually matching orientations (Equation 7). The second line with the parameter $\delta\theta/2$ is a solution of the Laplace equation with fixed boundary conditions $\theta = 0$ at the core of the S_1 defect and $\theta = \delta\theta$ at the core of the S_2 defect.

These equilibrium solutions are exact, but they lead to a boundary condition of the director field at infinity $\theta_\infty = \delta\theta/2 + \theta_0 = (\theta_1 + \theta_2 + S\pi)/2$ that depends upon the phase angles of the two defects. This is no problem unless one wants to describe realistic experimental systems where the director far from the conjugated pair is usually homogeneous and independent of the

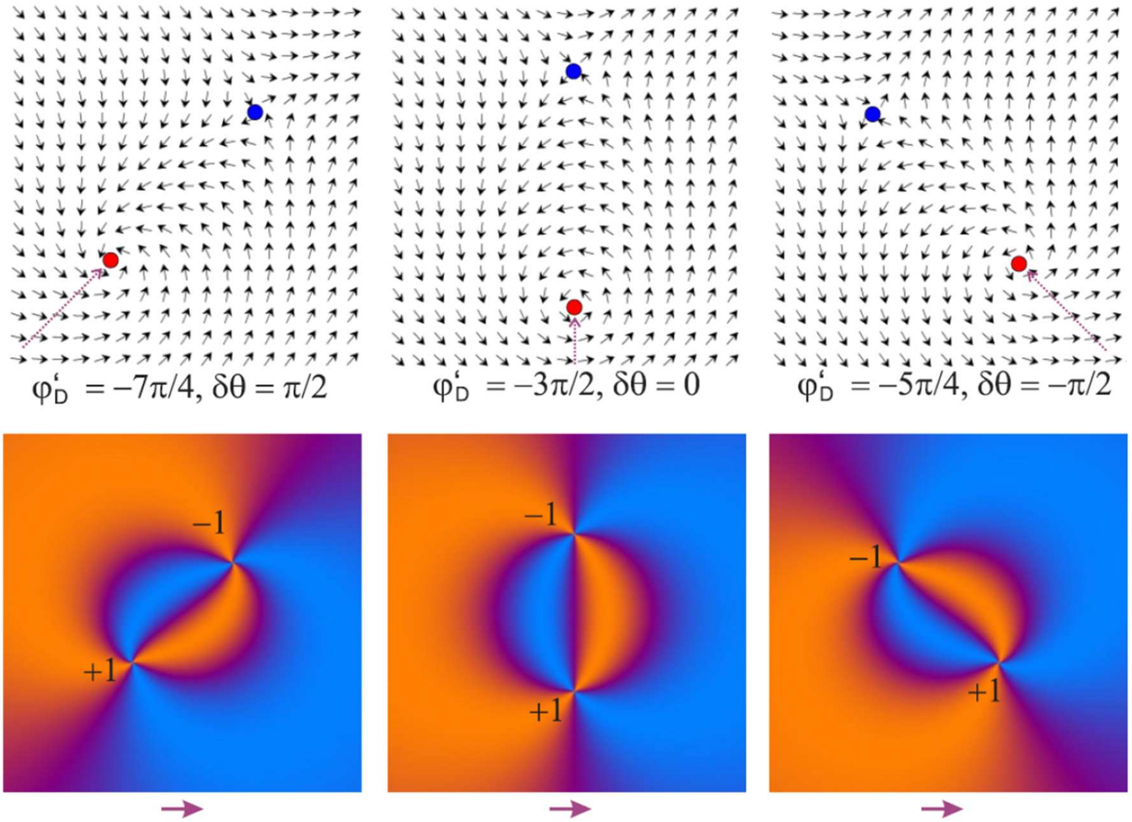

FIGURE 8 | Static director fields around matching and mismatching defect pairs obtained by Equation (9) (top) with $\delta\theta = (\pi/2, 0, -\pi/2)$ from left to right in a homogeneous external director field indicated by the pink arrow below the plots. The red dot marks the +1 defect and the blue dot the −1 defect. The bottom row shows their appearance between crossed polarizers with diagonal phase plate. The image was reproduced from Missaoui et al. [43].

defect positions and orientations. In order to realize such fixed boundary conditions, we rotated the solutions of Equation (9) to fix θ_∞. Without loss of generality, we chose $\theta'_\infty = 0$ [primed angles refer to the rotated system (x', y')]. In the primed system rotated by $-\theta_\infty$, the defect phases become

$$\begin{aligned} \theta'_1 &= \frac{S+1}{2}\theta_1 + \frac{S-1}{2}\theta_2 + \frac{S-1}{2}S\pi, \\ \theta'_2 &= -\frac{S+1}{2}\theta_1 - \frac{S-1}{2}\theta_2 - \frac{S+1}{2}S\pi. \end{aligned} \tag{10}$$

Some representative solutions are visualized in **Figure 8** for ±1 defect pairs and more in Missaoui et al. [43]. In the special case $S = 1$, the equations simplify to $\theta'_1 = \theta_1$ and $\theta'_2 = -\theta_1 - \pi$, the phase angle of the scalar +1 defect is preserved. One can easily verify that $\theta'_1 + \theta'_2 + S\pi = 0$ gives the correct boundary condition $\theta'_\infty = 0$ in all cases. The phase mismatch $\delta\theta$, i.e., the angle by which the director reorients on the straight line connecting the two cores, remains invariant under rotations of the coordinates. It is one of the two essential parameters for the pair orientation. The second important parameter describing the defect pair is the orientation of the connection vector $\vec{R}$ with respect to the far director. We will refer to φ'_D as the misalignment angle. It becomes

$$\varphi'_D = -\frac{\delta\theta}{2S} - \frac{1}{S}\theta'_1 - \pi. \tag{11}$$

It is useful to introduce the misalignment parameter $\delta\phi = \varphi'_D + \theta'_1/S + \pi$. The most important result of this analysis is that according to Equation (11), the mismatch $\delta\theta$ and the misalignment $\delta\phi$ are not independent of each other in equilibrium. The mutual phases of the conjugated defects and the orientation of the defect pair in the external director field are strictly related. Defect pairs in equilibrium adopt a mismatch angle in accordance with their positions in a given external director field.

The elastic free energy of a film of thickness h, associated with the distorted configurations of a defect pair, is [100]

$$W_{\text{pair}} = 2\pi KhS^2 \ln\left(\frac{R}{2r_c}\right) + \frac{\pi Kh\delta\theta^2}{2}\frac{\ln(R/(2r_{r_c}))}{[\ln(R/r_c)]^2} \tag{12}$$

where the first term represents the usual elastic energy for matching defects with topological charges ±S. The second term is the effect of mismatch, which generates a torque. Again, the equilibrium also fixes φ'_D, the orientation of the topological dipole in the surrounding director field, thus the rotation of the −1 defect and the orbit of both defects around the annihilation center cannot be separated in this model. At defect separations that are large compared to r_c, the torque is

$$T = -\frac{\pi K h}{\ln(R/r_c)}\,\delta\theta. \tag{13}$$

The previous derivation presupposed one-constant approximation. Two aspects have to be considered: Already Chandrasekhar [101] noticed that an elastic anisotropy causes a torque if the predominant elastic deformation between the defects is unfavorable. This holds true even if this pair is aligned and has matching phases. Second, defects with topological charge $S = +1$ have a peculiarity: the director field in the vicinity of the core can either be pure splay for $\theta_1 = \{0, \pm\pi\}$, or pure bend for $\theta_1 = \pm\pi/2$. Since the deformation energy diverges near the core, the director will be pinned there, either radially or tangentially. All other types of defects are less affected by elastic anisotropy. The director field structure slightly changes when $K_S \neq K_B$, but the energy of isolated defects does not depend on their phase angle θ_i. Because of their symmetry, director fields near the $S = +1$ defect core are unaffected by elastic anisotropy, but all other types contain splayed and bent regions in their vicinity. Regions related to the smaller elastic constant are compressed, while those related to the larger elastic constant expand to minimize the elastic energy. The director field around an isolated $S = -1$ defect in presence of an elastic anisotropy $\alpha = (K_S - K_B)/(K_S + K_B)$ changes to [102]

$$\varphi(\theta) = q\int_0^{\theta}\sqrt{\frac{1+\alpha\cos(2x)}{1+\alpha q^2\cos(2x)}}\,dx, \tag{14}$$

with a prefactor q determined by $(S-1)\varphi[\pi, q] = -2\,\varphi[\pi, q] = \pi$. We note here that the combination of defect phase match and alignment concepts with elastic anisotropy, with material flow and with finite system size is currently almost unexplored. This requires further theoretical effort. Gartland et al. [98] derived a general energy-based framework to determine the force acting on point defects in nematics. They noted that the static director fields considered above will, in general, not be identical to the dynamic director field configurations during defect annihilation, particularly not in presence of backflow (see next section). Tang and Selinger [103] exemplarily calculated a correction term describing the director field change due to a motion of $\pm 1/2$ defects at constant velocity in presence of material flow. Thus, simply deducing the annihilation dynamics from the energy landscapes of static solutions for the director field may not be adequate.

3.2. Defect Dynamics

After having obtained the equilibrium director configurations for defect pairs in given distances and orientations, we now discuss their dynamics: It is a widely used concept to assume that interacting defects moving in the LC system pass equilibrium configurations of the director fields in an adiabatic way. The specific drag force (per film thickness) on a defect of topological strength S moving with velocity v in a film at rest is [104]

$$F_{\text{drag}} = \pi\gamma_1 S^2 v \ln(L/r_c), \tag{15}$$

L is a characteristic system size. Flow is neglected here, the one-constant approximation is used, and γ_1 is the rotational viscosity. Pleiner [105] derived an equivalent equation for a defect moving in a SmC film, with γ_1 as the rotational viscosity of the c-director. The problem with this equation is its logarithmic divergence with L, which requires setting some long-distance cut-off. Ryskin and Kremenetsky [106] proposed a correction that leads to

$$F_{\text{drag}} = \pi\gamma_1 S^2 v \ln(3.6/Er), \tag{16}$$

with the Ericksen number $Er = \gamma_1 v r_c/K$. Note that, since the defect is an immaterial object, it does not involve material transport in this approximation. Thus, shear viscosities do not enter the drag force equation.

The balance of the elastic force F_e and the drag forces F_{drag} on both defects yields the velocity

$$v = \pm\frac{K}{\gamma_1 \ln(3.6/Er)\,R} = \pm\frac{D_1}{R} \tag{17}$$

for each defect. According to Equation (17), two disclinations of opposite charge approach each other with velocities essentially inversely proportional to the separating distance R (disregarding the velocity dependence of Er). With $\dot{R} = 2v$, one obtains

$$R(t) = \sqrt{4D_1(t_0 - t)}, \tag{18}$$

where t_0 is the annihilation time.

A more accurate model has to incorporate several aspects: first, the approximation that a moving defect has the same director configuration as a defect at rest needs to be checked [107]. Second, the defect velocities are influenced by the elastic anisotropy $\alpha = (K_S - K_B)/(K_S + K_B) \neq 0$ [6, 55]. Third, backflow effects cannot be neglected in most situations (except in Langmuir films where the subphase effectively inhibits such material transport).

An elastic anisotropy $\alpha \neq 0$ will cause a difference in the velocities of the defects of the pair, even when the film material is at rest. Because of their symmetry, $+1$ defects are unaffected. The altered director configuration around a -1 disclination (Equation 14), however, influences the specific drag force in Equation (15). Brugues et al. [6] obtained for ± 1 defects moving with velocity v in a restricted domain with radius R_d

$$\begin{aligned}
F^{(+)}_{\text{drag}} &\simeq \pi\gamma_1 v \ln\frac{R_d}{r_c},\\
F^{(-)}_{\text{drag}} &\simeq \frac{1}{2}\gamma_1 v \ln\frac{R_d}{r_c}\int_0^{2\pi}\left[1+\frac{1}{q}\sqrt{\frac{1+\alpha q^2\cos(2\theta)}{1+\alpha\cos(2\theta)}}\right]^2 d\varphi,
\end{aligned} \tag{19}$$

respectively, independent of the direction of motion. This effect was already observed in simulations by Svenšek and Žumer [55]: The $+1$ defect will move faster toward the annihilation point than the -1 defect, irrespective of the sign of the elastic anisotropy α.

However, the differences in defect velocities caused by elastic anisotropy are small compared to flow-coupling effects in SmC FSFs or effectively 2D nematic films. In particular, as the defects

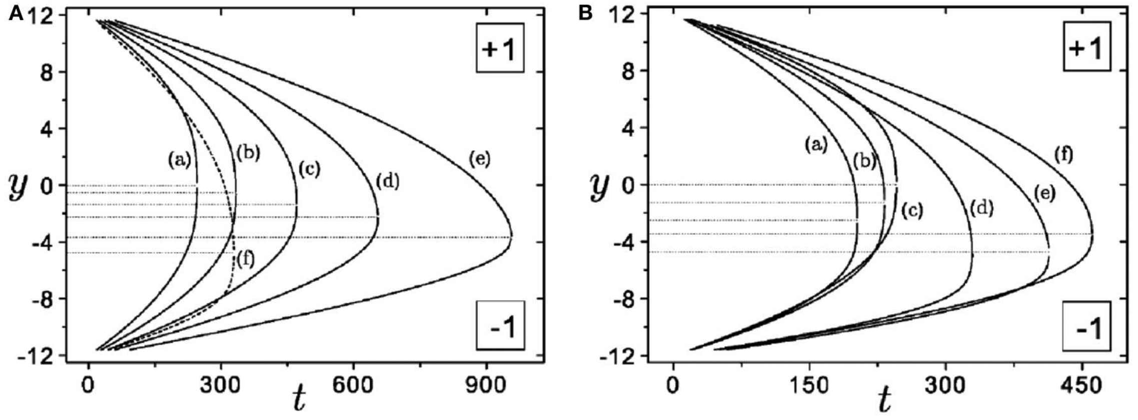

FIGURE 9 | Effect of elastic anisotropy (left) and flow parameters (right) on defect annihilation of a $(+1/-1)$ pair. **(A)** no flow, (a) $\alpha = 0$, (b) $\alpha = 1/3$, (c) $\alpha = 3/5$, (d) $\alpha = 7/9$ (e) $\alpha = 15/17$, (f) same as (d) in right image, for comparison. **(B)** (a) $\theta_1 = 0, \alpha = 0$, (b) $\theta_1 = \pi/2, \alpha = 0$, (c) without flow, $\alpha = 0$, (d) $\theta_1 = 0, \alpha = 0$ with rotational viscosity γ_1 doubled, (e) $\theta_1 = 0, \alpha = 2/3$, (f) $\theta_1 = \pi/2, \alpha = -2/3$. Images reproduced from Svenšek and Žumer [55], copyright American Physical Society.

move, coupling between the inhomogeneously changing director field and the velocity field (so-called backflow) plays a significant role. Defects of different strength couple to the flow field in different ways. Using a tensor order parameter description, simulations of Toth et al. [51] showed that, in a 2D nematic, the $+1/2$ defect moves faster than its $-1/2$ counterpart.

The coupled problem of director reorientation and flow is described by the Ericksen-Leslie equations, see, for example, Stewart [108] for a comprehensive discussion. These equations have to be treated numerically in general. Few analytical results exist [109–111] regarding the asymmetry of the motion of the defects in a conjugated pair [109, 111] and the *qualitative* structure of the backflow field [110]. The sign of the velocity field at the defect position depends on the topological charge: the fastest flow occurs in front of the positive defect *toward* and behind the negative defect *away from* the partner [110]. Coupling director reorientation and flow can speed up the relaxation significantly and it induces vortices in the flow field accompanying the moving defects, as first predicted by Denniston et al. [52]. The qualitative effect of backflow on the defect velocities is similar for defect lines and umbilics in nematics and point defects in SmC FSFs: while backflow increases the velocity of the positively charged defect, motion of the negative defect is hardly affected by backflow, often even reduced [51, 53, 55, 112, 113]. Due to the structure of the equations, the scaling of the defect separation $R \propto \sqrt{t_0 - t}$ with time to annihilation is preserved until the defects approach so closely that their core regions start overlapping. Svenšek and Žumer [55] studied the influence of the Ericksen-Leslie viscosities and elastic anisotropy on ± 1 defect pair annihilation in a SmC film numerically on a short spatial scale of initial separations.

Qualitative results are summarized in **Figure 9B**. Compared to the reference case without flow [**Figure 9A**, graph (a), and **Figure 9B**, graph (c)], both elastic anisotropy and flow slow down the -1 defect and accelerate the $+1$ defect. The annihilation points are shifted toward the initial position of the -1 defect. In general, symmetric terms of the stress tensors, e.g., the complete elastic stress tensor in one elastic constant approximation, affect motion of both defects in the same way, thus they do not contribute to an asymmetric annihilation process [55]. The γ_1 term in the viscous stress tensor is antisymmetric. It dominates the flow coupling during annihilation: the generated flow carries both defects with the same velocity in the same direction [55]. This enhances flow near the $+1$ defect while reducing flow near the -1 defect. The efficiency of backflow increases with the ratio of γ_1 to the isotropic viscosity α_4. The flow driven by the above terms does not depend on the phase θ_1 of the $+1$ defect (Equation 6). The viscosity coefficient $\gamma_2 = \alpha_2 + \alpha_3$ becomes relevant when the phase of the $+1$ defect is varied: a tangential $+1$ defect annihilates faster than a radial one with its partner (compare curves e and f in **Figure 9B**). For general phase angles θ_1, the induced flow field even breaks the symmetry respective to the axis connecting the defects [53]. The situation is qualitatively the same for annihilating $\pm 1/2$ lines in 2D nematics [53]. The coarsening of defect patterns is only slightly accelerated by hydrodynamic effects, and the $R(t)$ scaling behavior is unchanged [114], at least when $R \gg r_c$. It is also common to 2D nematics and SmC models that initialization of the simulation with an equilibrium director field of given defect positions causes significant transient deviations from the expected scaling behavior [53, 55].

An alternative, coarse-grained approach to describe defect dynamics is based on Rayleigh dissipation functions, as outlined by Vertogen [115], Sonnet and Virga [116], and Tang and Selinger [103]. Tang and Selinger [103] recently employed this technique to predict the motion of disclinations, including their reorientation, treating the defects as effective "particles". The authors considered passive nematics where the drag on $\pm 1/2$ disclinations is shown to depend upon the orientation of the defects relative to the surrounding director field (a feature that is closely connected with the mismatch and misalignment angles discussed above). The study describes a coupling of translations and rotations in the defect dynamics. In addition, an extension of the model to active nematics was developed by introduction of an activity coefficient.

The influence of an in-plane aligning electric field on the annihilation of $\pm 1/2$ disclinations was described for 2D nematics with weak degenerate planar anchoring [63, 117]. The director distortion in-between the pair is compressed to a wall of relatively constant width along the connecting axis. This leads to a different scaling regime where the energy decreases linearly with decreasing wall length, and the defects approach each other at constant velocity [63]. Speed anisotropy between the defects is caused mainly by backflow and not by elastic anisotropy.

Umbilic distortions in nematics with negative $\Delta\varepsilon$ in homeotropically aligned cells with an electric field normal to the cell are in many respects similar to SmC defects. However, in the former, one always has to consider 3D effects due to the finite cell gap, evoked by boundary conditions on the director and flow fields [59]. The dynamics also depend on the electric field strength, which sets the core size of the umbilic structure [59]. When bend is favored to splay in the nematic, the elastic anisotropy speeds up the -1 umbilic [59]. Remarkably, this is opposite to the behavior of $\pm 1/2$ disclinations in nematic cells and ± 1 disclination pairs in SmC FSFs.

When the elementary process is known, one may draw conclusions from pair annihilations to the coarsening of random patterns with multiple defects. For that purpose, a distribution of defects with a given density $\rho(t)$ per unit area is considered, and its scaling with time is analyzed statistically. In a given film area, $\rho \propto \ell^{-2}$ depends upon some characteristic length ℓ related to the average defect distance. Coarsening proceeds as a sequence of individual annihilation steps of neighboring conjugated strings or point defects. From scaling arguments, considering the energy dissipation rate and the defect energy of a network of string defects in a nematic, a decay of the defect density with $\rho(t) \propto t^{-1}$ was predicted [20] in 2D. The typical length scale in such a system increases with $t^{1/2}$.

4. EXPERIMENTAL RESULTS

A number of 2D experiments were performed in nematic cells under different anchoring conditions (e.g., [20, 21, 44, 56–59, 62, 63, 118, 119]), mainly focused on pair annihilation and on coarsening statistics. Irrespective of the apparent simplicity of the experimental realization, only a few experimental studies have examined point defects and their interactions in smectic C FSFs (e.g., [32, 78–81, 86, 120]) to test the above described theoretical models and predictions. However, there has been considerable work on inclusions in SmC FSFs where self-organization caused by topological interactions has been investigated. We refer the reader to a recent review by Dolganov et al. [33] and to the review by Bohley and Stannarius [121].

Finally, there are a few publications on defects in Langmuir films (e.g., [6, 122]), which share many properties with thin smectic films, viz. their quasi-2D geometry and homogeneity in normal direction. The c-director can rotate freely at the interfaces. On the other hand, the coupling to the subphase inhibits flow. We have grouped the experiments in this section by the arrangement of defects instead of the mesophase in which they are formed.

4.1. Single Disclinations

Structure and dynamics of single disclinations in nematic and smectic phases have been studied by several techniques. While with polarizing microscopy the core structures of conventional nematics are not accessible, transmission electron microscopy (TEM) can visualize such structures after they were frozen quickly into a crystalline state [123–127]. Often, this technique is employed with polymeric liquid crystals where the structure transfer to the solid phase is easier to achieve. Recently, experiments were also reported for chromonic liquid crystals [127]. Since the long-range interactions of defects are hardly affected by the inner core, we have disregarded this aspect in the following section. At greater distances, the director structure can either be determined with polarizing microscopy or by decoration of the distortions with inclusions [26, 128].

In thin SmC films surrounded by a uniform meniscus, topology requires a total topological charge $+1$ within a flat smectic film. An energetically favorable state is a single $+1$ defect near the film center. This holds similarly for defects enclosed in smectic islands or holes (**Figure 1C**).

4.1.1. Structure of Single Disclinations

The $+1$ disclinations in LCs have a peculiarity: they are invariant to rotations, irrespective of an elastic anisotropy. In case of $\alpha \neq 0$, they choose the configuration with lower energy, which in nematics can be either splay or bend depending upon the material parameters K_{11} and K_{33}. In smectic C, non-polar materials have $K_B < K_S$ because the bend constant contains contributions from $\hat{n}$ director twist (see line above Equation 5), which are less energy costly. This may be opposite in strongly polar SmC* materials where the spontaneous polarization tends to avoid splay. When this polarization is perpendicular to $\vec{c}$, it increases the effective bend constant [129]. However, even though radial and tangential configurations represent the equilibrium states, a strong enough torque exerted by the external director field may distort the defect and may even cause the c-director to flip θ_1 by $\pm\pi$ at the defect core. For such a jump over the potential wall, a sufficiently strong distortion is needed. This can be realized by spinning the c-director in a circular film with strong anchoring at the outer meniscus by means of electric or magnetic fields [130, 131]. When the field is switched off, the $+1$ defect that is necessarily present in the film because of the boundary conditions moves to the center. The phase difference between the defect core and the film boundary (seen as a spiral pattern, **Figure 10**) can only relax if the c-director reorients at the meniscus or at the defect core. The spiral contracts toward the center and increases the torque near the core until the barrier is surmounted and the phase mismatch is relieved by π. Note the strong deformation near the core in the second image of **Figure 10**, immediately before the flip. In practically all other experimental situations where SmC defect pair or pattern dynamics are considered, such strong distortions are absent; thus the c-director remains pinned tangentially at the $+1$ core,

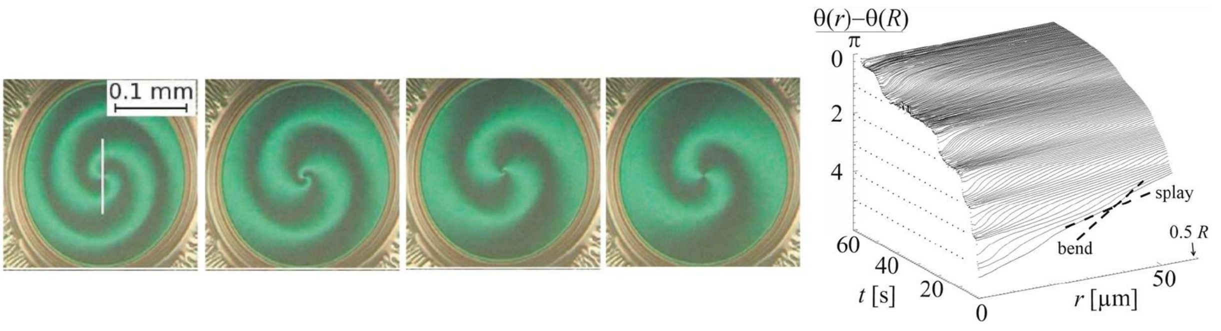

FIGURE 10 | Central +1 defect in a radially distorted director field within a SmC FSF. Images taken during relaxation in 4 s steps. The phase of the defect relative to the film border is initially 2π, it slips to π in the last image. Dark and bright green regions reflect horizontal and vertical c-director orientations, respectively, in these pictures. The relief on the right shows the time dependence of the radial phase profile in the film center. Image adapted from Eremin et al. [131].

either clockwise or counterclockwise. In **Figures 1A**, **5C**, the clockwise (CW) and counterclockwise (CCW) tangential defects are marked with black/white circles. Since the sign of $\vec{c}$ cannot be distinguished in reflection microscopy at normal incident light, the assignment is not unequivocal. The black circle may mark a CCW defect and white circles CW defects or vice versa.

4.1.2. Diffusion of Single Defects

The position of disclinations in FSFs is subject to Brownian diffusion in a potential given by the elastic energy landscape which is defined by the boundary conditions. Diffusive motion is counteracted by viscous drag due to director reorientations [79, 80, 105]. A single +1 defect in the center of a circular film shows normal diffusion with a linearly time-dependent mean square displacement (MSD) as long as this displacement is small compared to the film radius. Diffusion coefficients are of the order of $10^{-11}\mathrm{m}^2/\mathrm{s}$ [80]. At longer times, the confining potential of the film boundaries takes effect, and the MSD saturates. Central defects within islands experience particularly strong confinement. Wachs [81] showed that the diffusion constant for extremely thin films significantly increases under reduced ambient pressure, while the elastic constant remains roughly unaltered. This evidences that the material flow driven by inhomogeneous director reorientations in the film couples to flow of the ambient gas. This coupling mechanism is similar to that of the subphase of Langmuir films, yet the effect is much weaker. Similar film thickness dependent effects on the mobility of *inclusions* in quasi 2D membranes [132, 133] can be described within the Saffman-Delbrück/Hughes-Pailthorpe-White theory [134]. If this conclusion is correct, then Equations (15, 16) underestimate the drag forces on defects under normal atmosphere substantially, at least in thin FSFs.

4.2. Defect Pairs

When one analyzes the published studies of pair annihilation in nematics, it is striking that most pairs are in mutually matching orientations, which is most probably no coincidence. We do not exclude, however, the possibility that these particularly simple configurations had been intuitively selected by the experimenters. We are going to discuss the matching, aligned pairs first before returning to the mismatch problem afterwards in section 4.2.2.

4.2.1. Annihilation Dynamics

When external disturbances are negligible, the defect separation R obeys the square root law (Equation 18), in good approximation both in nematics [44, 62, 68] and in uniformly thick SmC FSFs [43, 80, 81]. However, when either strong planar anchoring with a preferential alignment is present in a cell [62], or when an aligning external electric field [59, 63] breaks the azimuthal symmetry in the cell plane, R scales linearly with $(t_0 - t)$. The distortion connecting the defects is compressed to a narrow wall and reducing the wall length is the dominant source of energy reduction.

In very thick SmC FSFs, arrays of layer dislocations can play the role of an external field [78]. Pargellis et al. studied 10–40 μm thick films that were most probably not uniform in thickness. In such films, dislocation arrays tend to force the c-director in a preferential orientation parallel to layer steps, i.e., normal to the thickness gradient. Distortions are squeezed into narrow walls [135]. The square-root law (Equation 18), describes only pairs which are separated by less than the wall widths.

Regardless of the existence of a field, the positively charged defects always move faster than the negatively charged ones, in accordance with theory. The dominance of backflow over elastic anisotropy in this asymmetry was demonstrated for umbilics in a cholesteric material [68]. The asymmetry of umbilic velocities in external fields is set by visco-elastic parameters of the material, not by field-induced structural changes [59].

Annihilation of ±1/2 disclination pairs was also analyzed in lyotropic nematics within a rather thick (100 μm) glass capillary with planar anchoring [118, 119]. Interestingly, averaging numerous experiments produced a scaling $R \propto (t - t_0)^{0.4\pm0.01}$. The reasons for the deviations can be manifold, e.g., fluctuations in the lyotropic [118, 119] or more complex defect interactions, such as mismatching mutual orientations in defect pairs (next paragraph) or inhomogeneous surrounding director fields. The defect separation was of the order of the cell thickness in these experiments, and the geometry is thus rather 3D. Defect velocities fluctuate more strongly than in thermotropic LCs, with evidence of long-range correlations [119].

Smectic C FSFs appear to be well-suited to study annihilation with full backflow coupling. Nevertheless, a quantitative analysis of annihilation dynamics and comparison to viscous and elastic material parameters to test existing models [55] is still missing. The few existing studies have confined themselves to the qualitative confirmation of the scaling law. In Missaoui et al. [43], a velocity ratio of +1 and −1 defect of about 1.8 was reported in qualitative agreement with theory. In extremely thin films, deviations from the $t^{1/2}$ scaling were found at small separations [81].

Material flow is inhibited in Langmuir films [6, 122]. This allows to quantify the velocity asymmetry caused by elastic anisotropy. In small circular islands, defect interactions and annihilation were observed after island coalescence. Qualitatively, the results agree with predictions [6, 55].

4.2.2. Defect Matching and Alignment

As the theoretical models in section 3.1 predicted, the defect orientation and the alignment of the pair in the far director field are important parameters for the quasi-equilibrium states. The previous section showed that the concept of defect pairs passing different quasi-equilibria is useful for pairs that are perfectly oriented with respect to each other. The hypothesis that the angular mismatch might play a role in the dynamics was probably first uttered by Wachs [81]. In practically all experimental studies, the problem of orientation matching was disregarded, but one can discover examples in published papers: In Pargellis' 1992 experiments ([78], Figures 10, 12 in there), the annihilation of several pairs definitely does not follow straight paths. A wall connecting the pair rotates in the film plane. Similar mismatch can be identified in Dierking et al. [44], **Figure 3B**, even though this aspect was not mentioned in those papers.

A systematic experimental study of defect pairs in different mutual orientations and different positions respective to the far field was performed by Missaoui et al. [43]: essentially, defect pairs always adopt an orientation with respect to each other that is related to their alignment with the far field. Misalignment causes curved trajectories, and, on the way to annihilation, the defects move on either clockwise or counterclockwise bent paths depending upon the sign of $\delta\theta \approx -\delta\phi$ (**Figure 11**). This differs quantitatively from the theoretical prediction $\delta\phi = -\delta\theta/2$. Possible reasons are that either the one-constant approximation $\alpha = 0$ used in Equation (9) is a too strong simplification for the material used ($\alpha \approx 0.4$), the assumption of an adiabatic approach is incorrect, or the finite film size affects the pair orientation.

The static equilibrium solutions are certainly not exact when flow is present [55]. We note that in realistic coarsening scenarios, the director field surrounding adjacent pairs is influenced by all neighbors. Then, misalignment effects may be averaged out to a certain extent, while the mismatch between the partners remains an important parameter.

4.3. Multidefect Arrays

A previous investigation [32] of repulsive interactions of defects of identical topological charges $S = +1$ has shown some limitations of the classical defect interaction models in liquid crystals [61, 95, 97] but a good agreement of the predicted square-root law of the time dependence of the characteristic quantities. Defects were collected initially in a small spot of a smectic C film: the film contained a circular area of reduced film thickness, a so-called "hole" comprising defects with total topological charge N. In this hole, N defects of charge +1 each were located along the boundary. The situation is shown in **Figure 5C**. In different experiments, N was varied between 4 and 12. The defects repel each other but cannot enter the surrounding thicker film regions because their elastic energy increases linearly with film thickness. On the other hand, they prevent the hole from shrinking and extinction because they counteract a reduction of the hole radius. By manually destroying the hole [32], the defects are freed and they explode in a regular pattern (**Figure 1A**) on straight radial trajectories. It was found that the velocities are well-described by a square-root law $R \propto t^{1/2}$ with R being the distance from the central spot that contained the defects and t the time after extinction of the hole. It was further observed that because of the pinning of the c-director at +1 defect cores, interactions to farther away defects are partially screened by nearer ones. Finally, it was demonstrated that multiple +1 defects with tangential anchoring cannot be described as a superposition of solutions of single defects. They necessarily include additional distortions of the surrounding director field that are not considered in the classical interaction models. The latter two features are not relevant in systems with elastic isotropy, where +1 defects can adjust θ_1 without barriers. They are, however, characteristic for any systems that require strictly tangential or radial vector fields around their +1 defects.

4.4. Coarsening of Complex Patterns

In an attempt to mimic cosmic string dynamics and the coarsening of complex string defect patterns, Chuang et al. [20, 21] studied nematics between sapphire plates. Rapid phase transitions from the isotropic phase were triggered either by a temperature quench or high pressure. The boundary conditions at the surfaces were not specified. They were presumably planar degenerate. In the nematic phase, a rich pattern of string defects occurred after the disorder-order transition. These defects were three-dimensional and of complex geometry. Nevertheless, the authors analyzed the 2D images and considered the mean density ρ of defects per area. They confirmed a coarsening $\rho(t) \propto t^{-1}$, as predicted by scaling arguments within an approximate model. In the late stages of coarsening, there were clear deviations from the t^{-1} scaling law, and $\rho(t)$ dropped even faster than the t^{-2} scaling predicted for 3D systems. Comparable experiments by Pargellis et al. [56] were performed under well-defined boundary conditions. Defects of strength ±1 emerged at an isotropic-nematic interface in the cell midplane. The authors were able to obtain accurate quantitative data of the 2D defect density $\rho(t)$. Approximately 1 min after the quench, this density followed the predicted t^{-1} decay. In an improved experimental geometry, Nagaya et al. [58] and Dierking et al. [44, 59] studied coarsening of defect patterns under isothermal conditions. Umbilics were formed in a material with $\Delta\varepsilon < 0$ exposed to an electric field along the cell normal. In a 2D view, the authors consider the umbilics as defect patterns. These structures can be regarded as integer-strength defects (see **Figure 1**). The $\rho \propto 1/t$ coarsening law was confirmed. Similar coarsening experiments in SmC FSFs were reported by Pargellis et al. [78].

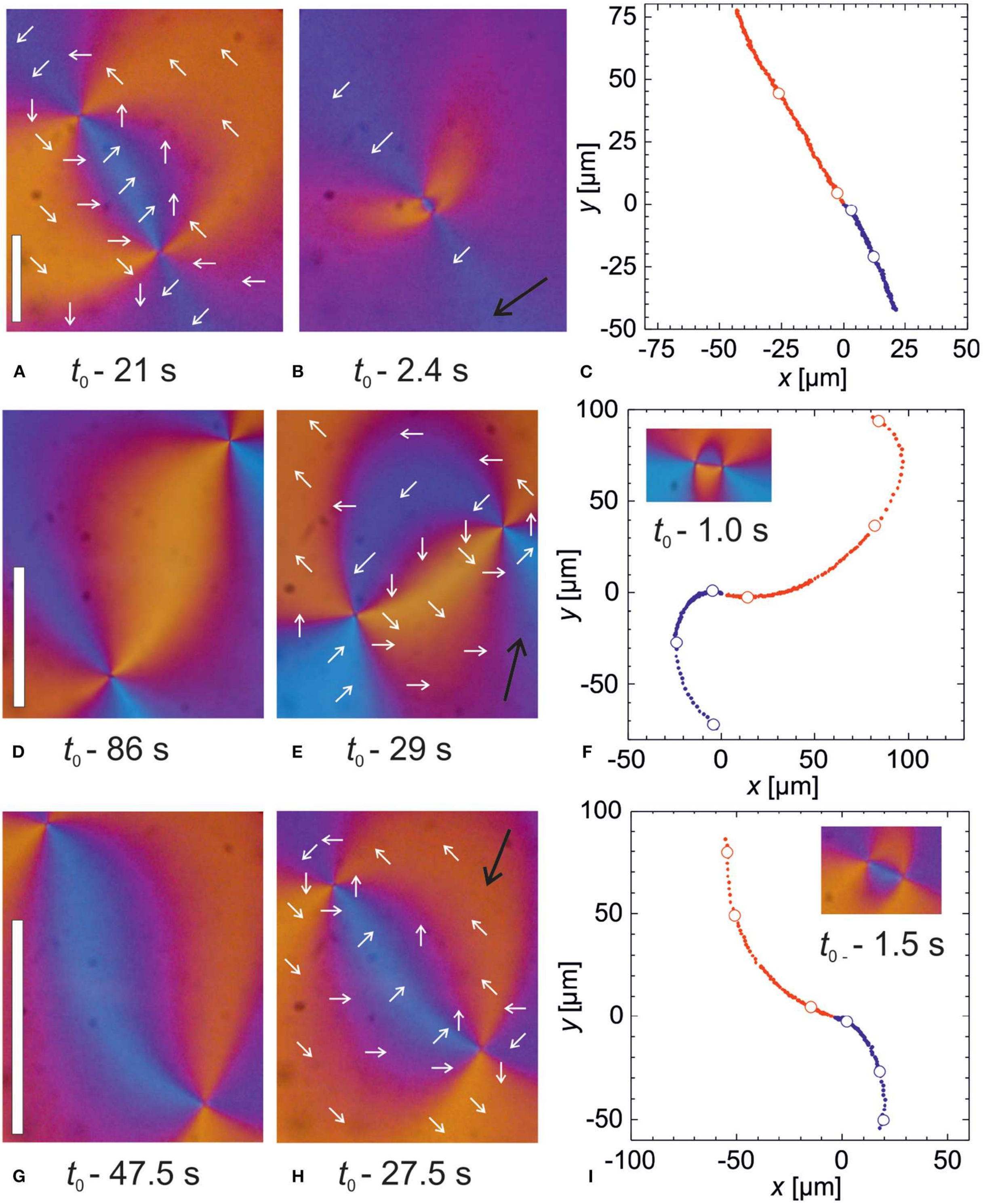

FIGURE 11 | (A–C) Matching defect pair, $\delta\theta = 0$, in perfect alignment, $\delta\phi = 0$. Times refer to the annihilation event, white circles in **(C)** mark the positions where **(A,B)** were recorded. **(D–F)** Same for mismatching, misaligned pair with initial angles $\delta\theta = +65°$, $\delta\phi = -36°$, **(G–I)** mismatching, misaligned pair with initial angles $\delta\theta = -50°$, $\delta\phi = +79°$. The white bar in **(A)** marks 50 μm, in **(D,G)** 100 μm. Black arrows indicate the orientation of the far director. Images reprinted from Missaoui et al. [43].

The films were comparably thick (of the order of 10^3 layers). Defects were created by temperature quenches. The texture between defect pairs showed an unusual appearance: instead of structures comparable to those found by other authors, the director distortions were localized in narrow inversion walls. This changes the defect dynamics qualitatively. The likely explanation of this discrepancy was given in section 4.2.1. One consequence was that the coarsening statistics changed qualitatively, the decay of $\rho(t)$ became exponential. Since a reproducible thickness profile is difficult to control in very thick films, it is preferable to study defect pattern coarsening in submicrometer thin, uniform films.

Muzny [80] studied defect pattern coarsening in homogeneously thick FSFs with a purely mechanical preparation technique that does not involve temperature changes. The decay of the defect density $\rho(t) \propto t^{-1}$ in random many-defect patterns was confirmed in these experiments. The fact that the coarsening dynamics is rather similar in all these experiments, irrespective of the sample geometries, defect preparation methods and types of defects seem to indicate that the $\rho \propto t^{-1}$ scaling is a robust result that is independent of details of the elementary annihilation steps.

5. SUMMARY

Models and experiments of 2D nematic and SmC defect interactions and dynamics were compiled in this review. The nematodynamic equations require that the defect separation R of an isolated conjugated pair scales as $R(t) \propto \sqrt{t_0 - t}$ with the time to annihilation, irrespective of the presence of flow. This holds true as long as no other length scales enter the description, such as lateral confinement, the vicinity of defect cores, the Saffman length of advected air layers, or widths of inversion walls generated by external electric fields. The square-root scaling was confirmed in many experiments with smectic films and nematics in sandwich cells. Material flow accelerates the motion of the positively charged defect and decelerates the negative counterpart; the annihilation point is thus shifted toward the negatively charged defect. The dominating term is related to the ratio γ_1/α_4. Elastic anisotropy has a similar effect, which is usually much weaker than flow coupling. Both predictions qualitatively agree with experiments. Nematics confined to sandwich cells often suffer from a more or less 3D character of the director field. Real quasi-2D systems can be realized using free-standing smectic C films or Langmuir films. The former display full flow coupling, as the surrounding fluid is often negligible, whereas the latter eliminate flow in the film plane through coupling to the bulk water phase.

Most of the existing models of defect dynamics disregard the mutual orientation of the defects and the pair's orientation in the far director field. They also do not account for the special fixed configurations of $+1$ defects (preferentially tangential or radial), which influence the relaxation dynamics qualitatively. Recent studies have brought this problem into focus [43, 99, 100]. The theory predicts curved defect trajectories and rotations of the defects on the way to annihilation. Quantitatively, there are some discrepancies between model and experiments, suggesting that a single-elastic constant approach without flow oversimplifies the physical situation. Pinning of the phase of $+1$ defects in general requires additional director distortions in configurations of multiple defects, altering the repulsion dynamics [32]. The influence of lateral confinement as well as a possible coupling to thermal fluctuations or a surrounding low-viscosity fluid still need to be incorporated in the models of thin films.

Defect diffusion has been studied in FSF [79–81]. In thick films, normal diffusion with coefficients of the order of a few $\mu m^2/s$ was observed, while in very thin films of only few molecular layers, coupling of flow to the ambient air seems to attenuate the diffusive motion.

This review has focused on systems where defect dynamics is driven by interactions with the surrounding director field and flow driven by the director dynamics. An interesting extension with promising perspectives is the study of systems where defects are generated, moved, and recombined by flow fields of external origin, such as active nematics [41, 136], and microfluidic systems where external flow can tune the topology of the samples [137]. In addition, the vast field of disclinations interacting with solid or liquid inclusions in liquid crystals has been completely left open here. Comprehensive reviews of static arrangements of solid or liquid inclusions in combination with defects can be found in Dolganov et al. [33] and Stannarius and Harth [92]. The dynamics of such symbiotic structures deserve considerable interest in future studies. Another promising perspective to consider when preparing self-assembled structures is the well-controlled creation of defect patterns with proper surface structuring of nematic cells [138]. Such structures can be switched electrically, and diffraction properties of nematic cells can be influenced by means of electric fields.

AUTHOR CONTRIBUTIONS

Both authors contributed equally to this publication.

FUNDING

The German Science Foundation DFG is acknowledged for support within projects STA 425/42-1, HA 8467/2-1, and HA 8467/3. The German Space Administration DLR is acknowledged for support within grant 50WM1744.

ACKNOWLEDGMENTS

The authors acknowledge A. Missaoui, J. Selinger, X. Tang, and E. Virga for fruitful discussions and P. Salamon for participating in some experiments.

REFERENCES

1. Poulin P, Stark H, Lubensky TC, Weitz DA. Novel colloidal interactions in anisotropic fluids. *Science*. (1997) **275**:1770–3. doi: 10.1126/science.275.5307.1770
2. Poulin P, Weitz DA. Inverted and multiple emulsions. *Phys Rev E*. (1998) **57**:626–37. doi: 10.1103/PhysRevE.57.626
3. Muševič I, Škarabot M, Tkalec U, Ravnik M, Žumer S. Two-dimensional nematic colloidal crystals self-assembled by topological defects. *Science*. (2006) **313**:954–8. doi: 10.1126/science.1129660
4. Tkalec U, Ravnik M, Čopar S, Žumer S, Muševič I. Reconfigurable knots and links in chiral nematic colloids. *Science*. (2011) **333**:62–5. doi: 10.1126/science.1205705
5. Muševič I. Interactions, topology and photonic properties of liquid crystal colloids and dispersions. *Eur Phys J ST*. (2019) **227**:2455–85. doi: 10.1140/epjst/e2019-800107-y
6. Brugues J, Ignes-Mullol J, Casademunt J, Sagues F. Probing elastic anisotropy from defect dynamics in Langmuir monolayers. *Phys Rev Lett*. (2008) **100**:037801. doi: 10.1103/PhysRevLett.100.037801
7. Weiler CN, Neely TW, Scherer DR, Bradley AS, Davis MJ, Anderson BP. Spontaneous vortices in the formation of Bose-Einstein condensates. *Nature*. (2008) **455**:948–51. doi: 10.1038/nature07334
8. Polkovnikov A, Sengupta K, Silva A, Vengalattore M. Nonequilibrium dynamics of closed interacting quantum systems. *Rev Mod Phys*. (2011) **83**:863. doi: 10.1103/RevModPhys.83.863
9. Kudo K, Kawaguchi Y. Coarsening dynamics driven by vortex-antivortex annihilation in ferromagnetic Bose-Einstein condensates. *Phys Rev A*. (2015) **91**:053609. doi: 10.1103/PhysRevA.91.053609
10. Seo SW, Kwon WJ, Kang S, Shin Y. Collisional dynamics of half-quantum vortices in a spinor Bose-Einstein condensate. *Phys Rev Lett*. (2016) **116**:185301. doi: 10.1103/PhysRevLett.116.185301
11. Abrikosov AA. On the magnetic properties of superconductors of the second group. *JETP*. (1957) **32**:1442.
12. Ruutu VMH, Eltsov VB, Gill AJ, Kibble TWB, Krusius M, Makhlin YG, et al. Vortex formation in neutron-irradiated superfluid ^{3}He as an analogue to cosmological defect formation. *Nature*. (1996) **382**:334. doi: 10.1038/382334a0
13. Bäuerle C, Bunkov YM, Fisher SN, Godfrin H, Picket GR. Laboratory simulation of cosmic string formation in the early universe using superfluid ^{3}He. *Nature*. (1996) **382**:332. doi: 10.1038/382332a0
14. Bäuerle C, Bunkov YM, Fisher SN, Godfrin H, Pickett GR. Do not try this at home. *Nature*. (1996) **383**:570. doi: 10.1038/383570b0
15. Wachowiak A, Wiebe J, Bode M, Pietzsch O, Morgenstern M, Wiesendanger R. Direct observation of internal spin structure of magnetic vortex cores. *Science*. (2002) **298**:577–80. doi: 10.1126/science.1075302
16. Hertel R, Schneider CM. Exchange explosions: magnetization dynamics during vortex-antivortex annihilation. *Phys Rev Lett*. (2006) **97**:177202. doi: 10.1103/PhysRevLett.97.177202
17. Rissanen I, Laurson L. Coarsening dynamics of topological defects in thin permalloy films. *Phys Rev E*. (2016) **94**:144428. doi: 10.1103/PhysRevB.94.144428
18. Volovik GE, Mineev VP. Particle-like solitons in superfluid ^{3}He phases. *Sov Phys*. (1977) **73**:767–73.
19. Ray R, Srivastava AM. Measuring cosmic defect correlations in liquid crystals. *Phys Rev D*. (2004) **69**:103525. doi: 10.1103/PhysRevD.69.103525
20. Chuang I, Durrer R, Yurke B, Turok N. Cosmology in the laboratory: defect dynamics in liquid crystals. *Science*. (1991) **251**:1336–42. doi: 10.1126/science.251.4999.1336
21. Chuang I, Yurke B, Turok N. Late-time coarsening dynamics in a nematic liquid crystal. *Phys Rev Lett*. (1991) **66**:2472. doi: 10.1103/PhysRevLett.66.2472
22. Zurek WH. Cosmological experiments in condensed matter systems. *Phys Rep*. (1996) **276**:177–221. doi: 10.1016/S0370-1573(96)00009-9
23. Bowick MJ, Chandar L, Schiff EA, Srivastava AM. The cosmological Kibble mechanism in the laboratory: string formation in liquid crystals. *Science*. (1994) **263**:943–5. doi: 10.1126/science.263.5149.943
24. Trebin HR. Defects in liquid crystals and cosmology. *Liq Cryst*. (1998) **24**:127–30. doi: 10.1080/026782998207659
25. Kibble T, Srivastava A. Condensed matter analogues of cosmology. *J Phys Condens Matter*. (2013) **25**:400301. doi: 10.1088/0953-8984/25/40/400301
26. Brinkman WF, Cladis PE. Defects in liquid crystals. *Phys Today*. (1982) **35**:48. doi: 10.1063/1.2915094
27. Liu C, Muthukumar M. Annihilation kinetics of liquid crystal defects. *J Chem Phys*. (1997) **106**:7822. doi: 10.1063/1.473740
28. Wang W, Shiwaku T, Hashimoto T. Experimental study of dynamics of topological defects in nematic polymer liquid crystals. *J Chem Phys*. (1997) **108**:1618. doi: 10.1063/1.475532
29. Silvestre NM, Patricio P, Telo da Gama MM, Pattanaporkratana A, Park CS, Maclennan JE, et al. Modeling dipolar and quadrupolar defect structures generated by chiral islands in freely suspended liquid crystal films. *Phys Rev E*. (2009) **80**:041708. doi: 10.1103/PhysRevE.80.041708
30. Fukuda JI, Žumer S. Quasi-two-dimensional Skyrmion lattices in a chiral nematic liquid crystal. *Nat Commun*. (2011) **2**:246. doi: 10.1038/ncomms1250
31. Pieranski P, Godinho MH, Čopar S. Persistent quasiplanar nematic texture: its properties and topological defects. *Phys Rev E*. (2016) **94**:042706. doi: 10.1103/PhysRevE.94.042706
32. Stannarius R, Harth K. Defect interactions in anisotropic two-dimensional fluids. *Phys Rev Lett*. (2016) **117**:157801. doi: 10.1103/PhysRevLett.117.157801
33. Dolganov PV, Cluzeau P, Dolganov VK. Interaction and self-organization of inclusions in two-dimensional free-standing smectic films. *Liquid Cryst Rev*. (2019) **7**:1–29. doi: 10.1080/21680396.2019.1586590
34. Tkalec U, Muševič I. Topology of nematic liquid crystal colloids confined to two dimensions. *Soft Matter*. (2013) **9**:8140–50. doi: 10.1039/c3sm50713k
35. Čopar S, Clark NA, Ravnik M, Žumer S. Elementary building blocks of nematic disclination networks in densely packed 3D colloidal lattices. *Soft Matter*. (2013) **9**:8203–9. doi: 10.1039/c3sm50475a
36. Serra F, Vishnubhatla KC, Buscaglia M, Roberto Osellame RC, Cerulloc G, Bellini T. Topological defects of nematic liquid crystals confined in porous networks. *Soft Matter*. (2011) **7**:10945. doi: 10.1039/c1sm05813d
37. Araki T, Buscaglia M, Bellini T, Tanaka H. Memory and topological frustration in nematic liquid crystals confined in porous materials. *Nat Mater*. (2011) **10**:303–9. doi: 10.1038/nmat2982
38. Araki T, Serra F, Tanaka H. Defect science and engineering of liquid crystals under geometrical frustration. *Soft Matter*. (2013) **9**:8107–20. doi: 10.1039/c3sm50468a
39. Yao X, Zhang H, Chen JZY. Topological defects in two-dimensional liquid crystals confined by a box. *Phys Rev E*. (2018) **97**:052707. doi: 10.1103/PhysRevE.97.052707
40. Urbanski M, Reyes CG, Noh J, Sharma A, Geng Y, Jampani VSR, et al. Liquid crystals in micron-scale droplets, shells and fibers. *J Phys: Cond Mat*. (2017) **29**:133003. doi: 10.1088/1361-648X/aa5706
41. Doostmohammadi A, Ignés-Mullol J, Yeomans JM, Sagués F. Active nematics. *Nat Commun*. (2018) **9**:3246. doi: 10.1038/s41467-018-05666-8
42. Kempf F, Mueller R, Frey E, Yeomans JM, Doostmohammadi A. Active matter invasion. *Soft Matter*. (2019) **15**:7538–46. doi: 10.1039/C9SM01210A
43. Missaoui A, Harth K, Salamon P, Stannarius R. Annihilation of point defect pairs in freely suspended liquid-crystal films. *Phys Rev Res*. (2020) **2**:013080. doi: 10.1103/PhysRevResearch.2.013080
44. Dierking I, Marshall O, Wright J, Bulleid N. Annihilation dynamics of umbilical defects in nematic liquid crystals under applied electric fields. *Phys Rev E*. (2005) **71**:061709. doi: 10.1103/PhysRevE.71.061709
45. Friedel G. Les états mésomorphes de la matiére. *Ann Phys*. (1922) **9**:273–474. doi: 10.1051/anphys/192209180273
46. Young CY, Pindak R, Clark NA, Meyer RB. Light-scattering study of two-dimensional molecular-orientation fluctuations in a freely suspended ferroelectric liquid-crystal film. *Phys Rev Lett*. (1978) **40**:773. doi: 10.1103/PhysRevLett.40.773
47. Oswald P, Pieranski P. *Nematic and Cholesteric Liquid Crystals: Concepts and Physical Properties Illustrated by Experiments*. Boca Raton, FL: Taylor & Francis (2005). doi: 10.1201/9780203023013
48. Oswald P, Pieranski P. *Smectic and Columnar Liquid Crystals: Concepts and Physical Properties Illustrated by Experiments*. Boca Raton, FL: Taylor & Francis (2006). doi: 10.1201/9781420036343

49. Schopohl N, Sluckin T. Defect core structure in nematic liquid-crystals. *Phys Rev Lett*. (1987) **59**:2582–4. doi: 10.1103/PhysRevLett.59.2582
50. Qian H, Sheng P. Generalized hydrodynamic equations for nematic liquid crystals. *Phys Rev E*. (1998) **58**:7475. doi: 10.1103/PhysRevE.58.7475
51. Toth G, Denniston C, Yeomans JM. Hydrodynamics of topological defects in nematic liquid crystals. *Phys Rev Lett*. (2002) **88**:105504. doi: 10.1103/PhysRevLett.88.105504
52. Denniston C, Orlandini E, Yeomans JM. Simulations of liquid crystal hydrodynamics in the isotropic and nematic phases. *Europhys Lett*. (2000) **52**:481. doi: 10.1209/epl/i2000-00463-3
53. Svenšek D, Žumer S. Hydrodynamics of pair-annihilating disclination lines in nematic liquid crystals. *Phys Rev E*. (2002) **66**:021712. doi: 10.1103/PhysRevE.66.021712
54. Harth K, Eremin A, Stannarius R. Vortex flow in free-standing smectic C films driven by elastic distortions. *Soft Matter*. (2011) **7**:2858. doi: 10.1039/c0sm01040e
55. Svenšek D, Žumer S. Hydrodynamics of pair-annihilating disclinations in SmC films. *Phys Rev Lett*. (2003) **90**:155501. doi: 10.1103/PhysRevLett.90.219901
56. Pargellis AN, Green S, Yurke B. Planar XY-model dynamics in a nematic liquid crystal system. *Phys Rev E*. (1994) **49**:4250. doi: 10.1103/PhysRevE.49.4250
57. Nagaya T, Hotta H, Orihara H, Ishibashi Y. Observation of annihilation process of disclinations emerging from bubble domains. *J Phys Soc Jpn*. (1991) **60**:1572. doi: 10.1143/JPSJ.60.1572
58. Nagaya T, Hotta H, Orihara H, Ishibashi Y. Experimental study of the coarsening dynamics of +1 and −1 disclinations. *J Phys Soc Jpn*. (1992) **61**:3511. doi: 10.1143/JPSJ.61.3511
59. Dierking I, Ravnik M, Lark E, Healey J, Alexander GP, Yeomans JM. Anisotropy in the annihilation dynamics of umbilic defects in nematic liquid crystals. *Phys Rev E*. (2012) **85**:021703. doi: 10.1103/PhysRevE.85.021703
60. Chuang I, Yurke B, Pargellis AN, Turok N. Coarsening dynamics in uniaxial nematic liquid crystals. *Phys Rev E*. (1993) **47**:3343. doi: 10.1103/PhysRevE.47.3343
61. Minoura K, Kimura Y, Ito K, Hayakawa R. Dynamics of annihilation process of disclination pairs in nematic liquid crystals. *Mol Cryst Liq Cryst*. (1997) **302**:345–55. doi: 10.1080/10587259708041847
62. Bogi A, Martinot-Lagarde P, Dozov I, Nobili M. Anchoring screening of defects interaction in a nematic liquid crystal. *Phys Rev Lett*. (2002) **89**:225501. doi: 10.1103/PhysRevLett.89.225501
63. Blanc C, Svenšek D, Žumer S, Nobili M. Dynamics of nematic liquid crystal disclinations: the role of the backflow. *Phys Rev Lett*. (2005) **95**:097802. doi: 10.1103/PhysRevLett.95.097802
64. Alexander GP, Chen BG, Matsumoto EA, Kamien RD. Colloquium: disclination loops, point defects, and all that in nematic liquid crystals. *Rev Mod Phys*. (2011) **84**:1229. doi: 10.1103/RevModPhys.84.497
65. Yanagimachi T, Yamamura SYY, Saito K. Cell gap dependence of nematic backflow around annihilating disclination pair. *J Phys Soc Jpn*. (2012) **81**:074603. doi: 10.1143/JPSJ.81.074603
66. Yanagimachi T, Yamamura SYY, Saito K. Backflow-induced asymmetric annihilation of nematic disclinations under strong anchoring condition. *J Phys Soc Jpn*. (2012) **81**:034601. doi: 10.1143/JPSJ.81.034601
67. Shen Y, Dierking I. Annihilation dynamics of topological defects induced by microparticles in nematic liquid crystals. *Soft Matter*. (2019) **15**:8749. doi: 10.1039/C9SM01710K
68. Oswald P, Ignés-Mullol J. Backflow-induced asymmetric collapse of disclination lines in liquid crystals. *Phys Rev Lett*. (2005) **95**:027801. doi: 10.1103/PhysRevLett.95.027801
69. Shahzamanian MA, Kadivar E. Disclinations dynamics in confined nematic liquid crystals: strong anchoring. *Liq Cryst*. (2006) **33**:941–5. doi: 10.1080/02678290600900660
70. Fernandez-Nieves A, Vitelli V, Utada AS, Link DR, Marquez M, Nelson DR, et al. Novel defect structures in nematic liquid crystal shells. *Phys Rev Lett*. (2007) **99**:157801. doi: 10.1103/PhysRevLett.99.157801
71. Liang HL, Schymura S, Rudquist P, Lagerwall J. Nematic-smectic transition under confinement in liquid crystalline colloidal shells. *Phys Rev Lett*. (2011) **106**:247801. doi: 10.1103/PhysRevLett.106.247801
72. Lopez-Leon T, Fernandez-Nieves A, Nobili M, Blanc C. Nematic-smectic transition in spherical shells. *Phys Rev Lett*. (2011) **106**:247802. doi: 10.1103/PhysRevLett.106.247802
73. Lopez-Leon T, Bates MA, Fernandez-Nieves A. Defect coalescence in spherical nematic shells. *Phys Rev E*. (2012) **86**:030702. doi: 10.1103/PhysRevE.86.030702
74. Liang HL, Zentel R, Rudquist P, Lagerwall J. Towards tunable defect arrangements in smectic liquid crystal shells utilizing the nematic-smectic transition in hybrid-aligned geometries. *Soft Matter*. (2012) **8**:5443. doi: 10.1039/c2sm07415j
75. Liang HL, Noh JH, Zentel R, Rudquist P, Lagerwall J. Tuning the defect configurations in nematic and smectic liquid crystalline shells. *Philos Trans R Soc A*. (2013) **371**:20120258. doi: 10.1098/rsta.2012.0258
76. Noh JH, Henx B, Lagerwall JPF. Taming liquid crystal self-assembly: the multifaceted response of nematic and smectic shells to polymerization. *Adv Mat*. (2016) **28**:10170. doi: 10.1002/adma.201603158
77. Gim MJ, Beller DA, Yoon DK. Morphogenesis of liquid crystal topological defects during the nematic-smectic A phase transition. *Nat Commun*. (2017) **8**:15453. doi: 10.1038/ncomms15453
78. Pargellis AN, Finn P, Goodby JW, Panizza P, Yurke B, Cladis PE. Defect dynamics and coarsening dynamics in smectic-C films. *Phys Rev A*. (1992) **46**:7765. doi: 10.1103/PhysRevA.46.7765
79. Muzny CD, Clark NA. Direct observation of the Brownian motion of a liquid-crystal topological defect. *Phys Rev Lett*. (1992) **68**:804–7. doi: 10.1103/PhysRevLett.68.804
80. Muzny C. *Properties of defects in freely suspended smectic C thin films* (Ph.D. Thesis). University of Colorado, Boulder, CO, United States (1994).
81. Wachs K. *Dynamics of smectic-c point disclinations infreely-suspended liquid crystal films* (B. A. Thesis). University of Colorado, Boulder, CO, United States (2014).
82. Nguyen DH. *Smectic Liquid Crystal Freely Suspended Films: Testing Beds for the Physics in Thin Membranes.* (Ph.D. Thesis) Boulder, CO: University of Colorado (2011).
83. Radzihovsky SP, Cranfill C, Nguyen Z, Park CS, Maclennan JE, Glaser MA, et al. Two-dimensional island emulsions in ultrathin, freely-suspended smectic liquid crystal films. *Soft Matter*. (2017) **13**:6314. doi: 10.1039/C7SM01584D
84. Clark NA, Eremin A, Glaser MA, Hall NR, Harth K, Klopp C, et al. Realization of hydrodynamic experiments on quasi-2D liquid crystal films in microgravity. *Adv Space Res*. (2017) **60**:737. doi: 10.1016/j.asr.2017.04.014
85. Harth K, Stannarius R. Deep holes in free-standing smectic C films. *Ferroelectrics*. (2014) **468**:92. doi: 10.1080/00150193.2014.933655
86. Dolganov PV, Shuravin NS, Fukuda A. Two-dimensional hexagonal smectic structure formed by topological defects. *Phys Rev E*. (2016) **93**:032704. doi: 10.1103/PhysRevE.93.032704
87. May K, Harth K, Trittel T, Stannarius R. Dynamics of freely floating smectic bubbles. *Europhys Lett*. (2012) **100**:16003. doi: 10.1209/0295-5075/100/16003
88. Maclennan JE. Spontaneous director rotation in freely suspended ferroelectric liquid-crystal films. *Europhys Lett*. (1990) **13**:435. doi: 10.1209/0295-5075/13/5/010
89. Harth K, Stannarius R. Corona patterns around inclusions in freely suspended smectic films. *Eur Phys J E*. (2009) **28**:265. doi: 10.1140/epje/i2008-10404-6
90. Harth K, Eremin A, Stannarius R. A gallery of meniscus patterns of free-standing smectic films. *Ferroelectrics*. (2012) **431**:59. doi: 10.1080/00150193.2012.684630
91. Harth K. *Episodes of the Life and Death of Thin Fluid Membranes.* (Ph.D. Thesis) Magdeburg: Otto von Guericke Universität Magdeburg (2016). doi: 10.25673/4391
92. Stannarius R, Harth K. Inclusions in freely suspended smectic films. In: Lagerwall S, Scalia G, editors. *Liquid Crystals With Nano and Microparticles*. Vol. 1. London: World Scientific (2016). p. 361. doi: 10.1142/9789814619264_0011
93. Eremin A, Nemeş A, Stannarius R, Pelzl G, Weissflog W. Spontaneous bend patterns in homochiral ferroelectric SmCP films: evidence for a negative effective bend constant. *Soft Matter*. (2008) **4**:2186. doi: 10.1039/b804845b
94. Dolganov PV, Kats EI, Dolganov VK, Cluzeau P. Linear defects forming the ground state of polar free standing smectic-C*

films. *Soft Matter*. (2019) **14**:7174. doi: 10.1039/C8SM01276H

95. Dafermos CM. Disinclinations in liquid crystals. *Quart J Mech Appl Math*. (1970) **23**:S49. doi: 10.1093/qjmam/23.2.49
96. Chandrasekhar S, Ranganath GS. The structure and energetics of defects in liquid crystals. *Adv Phys*. (1986) **35**:507–96. doi: 10.1080/00018738600101941
97. Kleman M, Lavrentovich OD. *Soft Matter Physics: An Introduction*. Berlin: Springer Verlag (2003). doi: 10.1007/b97416
98. Gartland EC Jr, Sonnet AM, Virga EG. Elastic forces on nematic point defects. *Continuum Mech Thermodyn*. (2002) **14**:307–19. doi: 10.1007/s00161-002-0099-8
99. Vromans AJ, Giomi L. Orientational properties of nematic disclinations. *Soft Matter*. (2016) **12**:6490–5. doi: 10.1039/C6SM01146B
100. Tang X, Selinger JV. Orientation of topological defects in 2D nematic liquid crystals. *Soft Matter*. (2017) **13**:5481. doi: 10.1039/C7SM01195D
101. Chandrasekhar S. *Liquid Crystals*. Cambridge: Cambridge University Press (1992). doi: 10.1017/CBO9780511622496
102. Landau LD, Lifschitz EM. *Elastizitätstheorie*. 6th Ed. Berlin: Akademie-Verlag (1989).
103. Tang X, Selinger JV. Theory of defect motion in 2D passive and active nematic liquid crystals. *Soft Matter*. (2019) **15**:587. doi: 10.1039/C8SM01901K
104. Imura H, Okano K. Friction coefficient for a moving disinclination in a nematic liquid crystal. *Phys Lett*. (1973) 42A:403. doi: 10.1016/0375-9601(73)90728-7
105. Pleiner H. Dynamics of a disclination point in smectic-C and -C* liquid-crystal films. *Phys Rev A*. (1988) **37**:3986. doi: 10.1103/PhysRevA.37.3986
106. Ryskin G, Kremenetsky M. Drag force on a line defect moving through an otherwise undisturbed field: disclination line in a nematic liquid crystal. *Phys Rev Lett*. (1991) **67**:1574. doi: 10.1103/PhysRevLett.67.1574
107. Radzihovsky L. Anomalous energetics and dynamics of moving vortices. *Phys Rev Lett*. (2015) **115**:247801. doi: 10.1103/PhysRevLett.115.247801
108. Stewart IW. *The Static and Dynamic Continuum Theory of Liquid Crystals*. London; New York, NY: Taylor & Francis (2004).
109. Kats EI, Lebedev VV, Malinin SV. Disclination motion in liquid crystalline films. *J Exp Theor Phys*. (2002) **95**:714–27. doi: 10.1134/1.1520604
110. Biscari P, Sluckin TJ. A perturbative approach to the backflow dynamics of nematic defects. *Eur J Appl Math*. (2012) **23**:181–200. doi: 10.1017/S0956792510000343
111. Sonnet AM, Virga EG. Flow and reorientation in the dynamics of nematic defects. *Liq Cryst*. (2009) **36**:1185. doi: 10.1080/02678290903034480
112. Denniston C, Tóth G, Yeomans JM. Domain motion in confined liquid crystals. *J Stat Phys*. (2002) **107**:187. doi: 10.1023/A:1014562721540
113. Mandal S, Mazza MG. Multiparticle collision dynamics for tensorial nematodynamics. *Phys Rev E*. (2019) **99**:063319. doi: 10.1103/PhysRevE.99.063319
114. Denniston C, Orlandini E, Yeomans JM. Phase ordering in nematic liquid crystals. *Phys Rev E*. (2001) **64**:021701. doi: 10.1103/PhysRevE.64.021701
115. Vertogen G. The equations of motion for nematics. *Z Naturforsch A*. (1983) **38**:1273–5. doi: 10.1515/zna-1983-1201
116. Sonnet AM, Virga EG. Dynamics of dissipative ordered fluids. *Phys Rev E*. (2001) **64**:031705. doi: 10.1103/PhysRevE.64.031705
117. Biscari P, Sluckin TJ. Field-induced motion of nematic disclinations. *SIAM J Appl Math*. (2005) **65**:2141. doi: 10.1137/040618898
118. Guimarães RR, Mendes RS, Fernandes PRG, Mukai H. Dynamics of topological monopoles annihilation on a fibre in a thick and thin nematic layer. *J Phys Condens Matter*. (2013) **25**:404203. doi: 10.1088/0953-8984/25/40/404203
119. Ribeiro HV, Guimarães RR, Teixeira-Souza RT, Mukai H, Fernandes PRG, Lenzi EK, et al. Antipersistent behavior of defects in a lyotropic liquid crystal during annihilation. *Phys Rev E*. (2013) **87**:054501. doi: 10.1103/PhysRevE.87.054501
120. Dolganov PV, Shuravin NS, Dolganov VK, Kats EI, Fukuda A. Topological defects in smectic islands formed in antiferroelectric freestanding nanofilms. *Surf Innov*. (2019) **7**:168. doi: 10.1680/jsuin.18.00059
121. Bohley C, Stannarius R. Inclusions in free standing smectic liquid crystal films. *Soft Matter*. (2008) **4**:683. doi: 10.1039/b715124a
122. Vallvé MA, Ignés-Mullol J. Dynamics of point defects and stripe textures in smectic-C Langmuir monolayers. *Eur Phys J E*. (2009) **30**:403–9. doi: 10.1140/epje/i2009-10539-x
123. Wang W, Hashimoto T, Lieser G, Wegner G. Elastic constant anisotropy, core structure of wedge disclinations and optical texture of main-chain P-4-BCMU liquid crystals. *J Polym Sci Pt B-Polymer Phys*. (1994) **32**:2171–86. doi: 10.1002/polb.1994.090321305
124. Gu Q, Wu C, Chen S, Huang Y. Decoration of disclinations by solidification-induced band texture and focal-conic texture for a low-molar-mass liquid crystal. *Chin Sci Bull*. (2002) **47**:1711–3. doi: 10.1007/BF03183313
125. Drummy L, Voigt-Martin I, Martin D. Analysis of displacement fields near dislocation cores in ordered polymers. *Macromolecules*. (2001) **34**:7416–26. doi: 10.1021/ma010003b
126. Zhang S, Terentjev E, Donald A. Nature of disclination cores in liquid crystals. *Liquid Cryst*. (2005) **32**:69–75. doi: 10.1080/02678290512331324057
127. Zhou S, Shiyanovskii SV, Park HS, Lavrentovich OD. Fine structure of the topological defect cores studied for disclinations in lyotropic chromonic liquid crystals. *Nat Commun*. (2017) **8**:14974. doi: 10.1038/ncomms14974
128. Cladis P, Kleman M, Pieranski P. New method for decoration of mesomorphic phase of para methoxybenzylidene para betylaniline. *Compt Rend Hebd Acad Sci Ser B*. (1971) **273**:275.
129. Lee JB, Pelcovits RA, Meyer RB. Role of electrostatics in the texture of islands in free standing ferroelectric liquid-crystal films. *Phys Rev E*. (2007) **75**:011701. doi: 10.1103/PhysRevE.75.051701
130. Cladis PE, Finn PL, Brand HR. Stable coexistence of spiral and target patterns in freely suspended films of smectic-C liquid crystals. *Phys Rev Lett*. (1995) **75**:1518. doi: 10.1103/PhysRevLett.75.1518
131. Eremin A, Bohley C, Stannarius R. Stick-slip dynamics around a topological defect in free standing smectic films. *Phys Rev E*. (2006) **74**:040701(R). doi: 10.1103/PhysRevE.74.040701
132. Nguyen ZH, Atkinson M, Park CS, Maclennan J, Glaser M, Clark N. Crossover between 2D and 3D fluid dynamics in the diffusion of islands in ultrathin freely suspended smectic films. *Phys Rev Lett*. (2016) **105**:268304. doi: 10.1103/PhysRevLett.105.268304
133. Eremin A, Baumgarten S, Harth K, Stannarius R, Nguyen ZH, Goldfain A, et al. Two-dimensional microrheology of freely suspended liquid crystal films. *Phys Rev Lett*. (2011) **107**:268301. doi: 10.1103/PhysRevLett.107.268301
134. Hughes BD, Pailthorpe BA, White LR. The translational and rotational drag on a cylinder moving in a membrane. *J Fluid Mech*. (1981) **110**:349. doi: 10.1017/S0022112081000785
135. Völtz C, Stannarius R. Self-organization of isotropic droplets in smectic-C free-standing films. *Phys Rev E*. (2004) **70**:061702. doi: 10.1103/PhysRevE.70.061702
136. Hardouin J, Hughes R, Doostmohammadi A, Laurent J, Lopez-Leon T, Yeomans JM, et al. Reconfigurable flows and defect landscape of confined active nematics. *Commun Phys*. (2019) **2**:121. doi: 10.1038/s42005-019-0221-x
137. Giomi L, Kos Ž, Ravnik M, Sengupta A. Cross-talk between topological defects in different fields revealed by nematic microfluidics. *Proc Natl Acad Sci USA*. (2017) **114**:E5771. doi: 10.1073/pnas.1702777114
138. Kim M, Serra F. Tunable dynamic topological defect pattern formation in nematic liquid crystals. *Adv Opt Mater*. (2020) **8**:1900991. doi: 10.1002/adom.201900991

Conflict of Interest: The authors declare that the research was conducted in the absence of any commercial or financial relationships that could be construed as a potential conflict of interest.

frontiers in Physics

PERSPECTIVE
published: 23 June 2020
doi: 10.3389/fphy.2020.00184

Microbial Active Matter: A Topological Framework

*Anupam Sengupta**

Physics of Living Matter Group, Department of Physics and Materials Science, University of Luxembourg, Luxembourg City, Luxembourg

Topology transcends boundaries that conventionally delineate physical, biological, and engineering sciences. Our ability to mathematically describe topology, combined with recent access to precision tracking and manipulation approaches, has triggered a fresh appreciation of topological ramifications in biological systems. Microbial ecosystems, a classic example of living matter, offer a rich test bed for exploring the role of topological defects in shaping community compositions, structure, and functions spanning orders in length and time scales. Microbial activity—characteristic of such structured, out-of-equilibrium systems—triggers emergent processes that endow evolutionary and ecological benefits to microbial communities. The scene stealer of this developing cross-disciplinary field of research is the topological defects: singularities that nucleate due to spontaneous symmetry breaking within the microbial system or within the surrounding material field. The interplay of geometry, order, and topology elicit novel, if not unexpected dynamics that are at the heart of active and emergent processes in such living systems. In this short review, I have put together a summary of the key recent advances that highlight the interface of active liquid crystal physics and the physical ecology of microbes; and combined it with original data from experiments on sessile species as a case to demonstrate how this interface offers a biophysical framework that could help to decode and harness active microbial processes in *true* ecological settings. Topology and its functional manifestations—a crucial and well-timed topic—offer a rich opportunity for both experimentalists and theoreticians willing to take up an exciting journey across scales and disciplines.

Keywords: active matter, microbial ecology, microscale biophysics, liquid crystals, anisotropy, topological defects, feedback, emergence

Edited by:
Teresa Lopez-Leon,
ESPCI ParisTech École Supérieure de Physique et de Chimie Industrielles de la Ville de Paris, France

Reviewed by:
Julio Cesar Armas-Perez,
University of Guanajuato, Mexico
Arlette Baljon Baljon,
San Diego State University, United States

***Correspondence:**
Anupam Sengupta
anupam.sengupta@uni.lu

Specialty section:
This article was submitted to Soft Matter Physics, a section of the journal Frontiers in Physics

Received: *13 December 2019*
Accepted: *28 April 2020*
Published: *23 June 2020*

Citation:
Sengupta A (2020) Microbial Active Matter: A Topological Framework. Front. Phys. 8:184. doi: 10.3389/fphy.2020.00184

INTRODUCTION

Microbes mediate and dictate a broad range of processes in ecology, medicine, and industry. The urgent need for devising better antibiotics, the development of bioremediation approaches for anthropogenic disasters such as oil spills, application of microbes toward sustainable ecosystems, and the need to coherently assess how microbes govern the dynamics of soil, plant, marine, and human ecosystems—all require an articulate understanding of the vital functions that microbes carry out. Microbial activity spans multiple scales [1–3]: from community dynamics playing over millimeter to meter scales, down to sub-cellular organelles with characteristic lengths of hundreds of nanometers (**Figure 1**). A significant proportion of these microbes—from prokaryotic bacteria making up different biotopes, to eukaryotic phytoplankton in flow—occupy highly dynamic natural habitats, where a combination of periodic and stochastic variations in their micro-environments shape the species fitness, succession, and selection [4, 5]. Since Pasteur formalized the nexus between microbiology and materials (in this case, food materials) [6], the scientific and industrial pursuit of biotechnology at the interface of microbes and materials has continued unhindered. This lasting advancement was realized in part due to the discovery of diverse microbial taxonomies within different contexts [7–9], and elucidation of the intricate community structures therein, also known as the microbiota, or more commonly, microbiome [10, 11]. Alongside, a close understanding of the biophysical attributes of the environment has enabled valuable insights into microbial behavior and physiology in a dynamic environment. At the scale of a microorganism, the local micro-environment can be generalized as a spatially structured complex soft material, with internal energies spanning equilibrium thermal energies ($k_{\mathrm{B}}T$, the product of the Boltzmann constant, k_B, and the temperature, T) [12–14], to out-of-equilibrium active environments [1, 15, 16]. Ranging from 1 nm to 100 μm—five orders of length scale—micro-structural complexity coexists with microbial complexity in vast majority of natural and nature-inspired microbial ecosystems. Key microorganisms, or the *core microbiota*, from a range of applied microbial settings, have yielded plethora of information on optimal physiology and fitness, relevant from a fundamental microbial perspective [17]. Together with the rapid progress in sequencing and *omics* tools, this has led to a systematic and high throughput analysis of microbial metabolism and response pathways [18]. Yet microbiology and microscale physics have rarely been considered as an ensemble—a single composite biophysical system—that underpins the natural and synthetic microbial processes. Bulk of the existing studies—both experimental and modeling—have considered one or the other, and thus, relatively little is known about the *active biophysics* that govern the microbiome dynamics in general, and the microbe-environment interactions in particular. Specifically, by analyzing microbial ecosystems through the lens of active matter physics, two distinct uncharted biophysical themes emerge: (1) Activity and emergence in microbial consortia: how emergent properties are triggered (or hindered) in communities of multiple players (species) with distinct biophysical traits; and (2) Microbial behavior and physiology in relation to the dynamic micro-environments they are part of. In other words, can we harness environmental dynamics to tune microbial activity and emergent properties? Both the themes, interfacing microbial ecology and active matter physics, went unexplored this far, despite their relevance and potential impact. The holy grail will be to develop a mechanistic framework that could decouple the two scenarios and reveal the relative influence of consortium species vis-a-vis the environmental attributes. In an integrative approach, the species in a consortium could be considered a part of the microbial environment itself. Nonetheless, an unambiguous understanding of each species in a microbial community, and their relation to the micro-environment, will be crucial in assessing their contribution to the environmental variables.

In a biophysical context, microbes can be generalized as microscale biological active matter that expends energy to perform tasks and processes information to execute physiological functions, ultimately enabling them to maintain biological fitness. Microbes have thus been considered as model systems, based on which theories for active matter systems have been developed [19–23]. Broadly classified under prokaryotes (unicellular organisms without membrane-bound nucleus) and eukaryotes (uni- or multicellular organisms possessing membrane-bound nucleus), microbes can be planktonic (motile), or sessile (non-motile), inhabiting different ecosystems. Motility imparts cells the ability to actively propel, aided by plethora of propulsion mechanisms [24]. On the other hand, non-motile microbes could be surface attached, or rely on passive mechanisms for locomotion. Over the recent years, there has been a growing interest to understand the dynamics of microbial systems with higher complexities: coexisting motile and non-motile species [25–27], microbes in complex fluids [28–30], and active response and feedback between microbes and their micro-environments [1, 16, 19, 31]. Despite the unprecedented progress over the last decade, the field of microbial biophysics faces conceptual challenges on the way, specifically in linking the *physics* of active matter to the *biology* of microbial ecosystems in natural or nature-inspired ecosystems. A close scrutiny would reveal that microbes, as they exist today in their natural habitats, have emerged from eons evolution, guided by the interplay of physics and genetics [32]. Thus, for a consequential application of the theory in true biological settings, an appreciation of the role of the environmental variations and the underlying molecular pathways, in addition to the material and mechanical attributes of the cells, will be vital. Engaging biomolecular approaches in tandem with microbial biophysics will trigger an iterative feedback where the knowledge of biological pathways will inform new and update existing theory, and vice versa; ultimately enabling predictive approaches for microbial biophysics [33, 34]. Furthermore, bridging theory with the biophysical experiments has been hindered by the multiplicity of microbial traits and processes that act simultaneously, affecting both the consortia members and the micro-environment [34]. Our ability to move from experiment-specific theory to general principles of microbial biophysics could garner much wider attention from both aisles of the scientific community, ultimately offering an integrative framework for microbial ecology. These challenges have offered untapped opportunities for the active matter community, which could allow existing theories to be validated and iteratively updated to capture *true* biological systems. The objective of this article is 3-fold: (1) to summarize key recent works on microbial active matter, with a focus on the role of geometric and topological features; (2) present selected original results that capture the topological facets in microbial systems, in particular sessile bacteria; and (3) conclude with a perspective on the topological framework, and its promise in future studies on microbial systems.

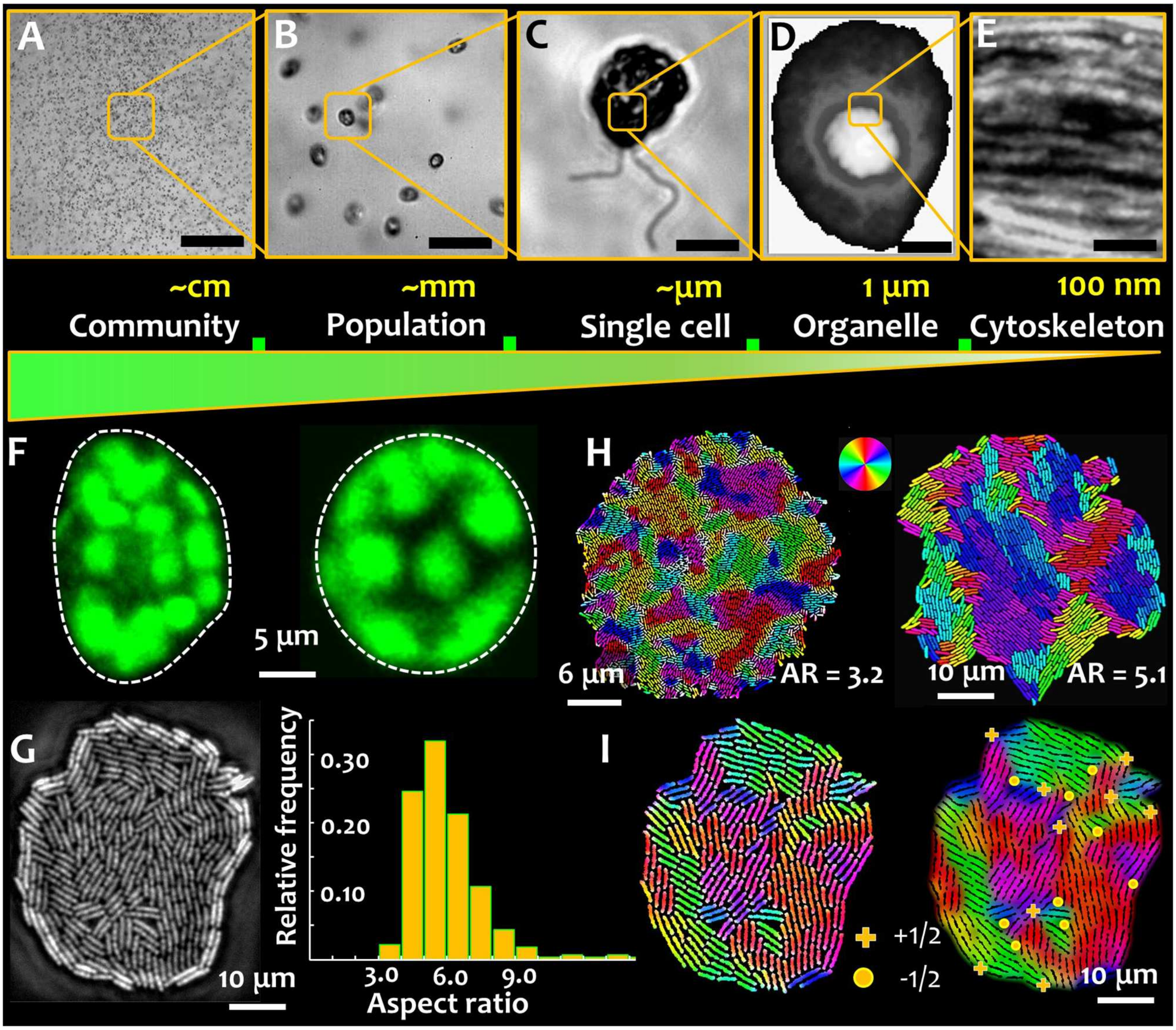

FIGURE 1 | Microbial active matter. Microbial active matter spans multiple scales: from communities comprising populations of multiple species **(A)**, to microbial populations of single species **(B)**, down to individual cells **(C)** Out-of-equilibrium physics underpins biophysical processes at sub-cellular scales, regulating phase separation, organelle compartmentalization, and microbial shape-shifting **(D)** and directional molecular transport by the cytoskeletal elements **(E)**. The scale bar in green represents the decreasing system length scales on moving from the microbial community to the cytoskeletal elements. **(F)** Microbial shape and its modulation are critical determinants of behavior and physiology, shown here for phytoplankton that can carry out rapid morphological transformation from asymmetric (left) to symmetric (right) shape as a response to hydrodynamic cues. Such transformations are mediated by the active reorganization of the cytoskeleton. Chloroplasts surrounding the cell membrane of photosynthetic phytoplankton species appear as blobs (false colored in green), imaged here using chlorophyll autofluorescence. **(G)** Microbial shape in a monoclonal culture can be intrinsically heterogeneous, as captured in an expanding colony of rod shaped bacteria. The growth conditions play a key role in tuning the aspect ratio of cells, a metric of microbial shape. **(H)** Cell aspect ratio determines the size of self-organized nematic microdomains in a growing bacterial colony. The colors denote local cell orientations, as per scheme shown in the color wheel. **(I)** Topological defects in an expanding bacterial colony. (+) sign indicates +1/2 integer defects and (•) indicates −1/2 topological defects, which appear at the intersection of nematic microdomains. (**D,H** are adapted from the author's work [1, 2], and **E** from Jin et al. [3], with permissions from the Nature Publishing Group, Creative Commons CCBY license and John Wiley and Sons, respectively).

MICROBIAL ECOLOGY: A TOPOLOGICAL PERSPECTIVE

Microbes occupy every part of our biosphere, often as a part of complex community structures, interacting closely with dynamic micro-environments via physico-chemical cues. The ability of microbes to respond and *adjust* to environmental changes spanning vastly different scales (individual to community scales; from generational to evolutionary time scales), is a conundrum that has long intrigued biologists and physicists alike. Consequently, understanding how microbes interface, exchange, and communicate with their local surroundings is central to the grand quest for a theory of microbial ecology. On the timeline of microbial ecology, it is rather recent that cellular and sub-cellular biophysics has started to emerge as a key player, propelling our understanding of microbial lifestyles and strategies under biotic and abiotic variations in their environment. Recent advances in molecular and imaging techniques have started to uncover the functional role of active biophysics in microbial ecosystems, specifically in the context of topological defects [35–37], yet we lack a mechanistic framework that could explain, generalize, and predict microbial fate under environmental fluctuations. Microbiology and microscale biophysics work in tandem in everyday ecological settings, though they have rarely been considered as an *ensemble* parameter for analyzing microbial ecology. Of particular significance to microbe-environment interactions is *phenotypic plasticity* [38]—the ability of microbes to dynamically tune biophysical attributes, namely, morphology, cell size, motility, or surface-association, without altering the genotype (i.e., the genetic makeup remains same). Variations in phenotypes, the composite of observable characteristics or traits in an organism, arise due to differential expressions of the genetic code due to interactions with the environment [39–42]. Its fundamental role in establishing a link between organisms and their environment has been reported in all forms of life: from simple unicellular bacteria [42] and photosynthetic phytoplankton [1, 3], to highly organized multicellular eukaryotes [43].

At a functional level, phenotypic plasticity imparts individual cells, or populations, the capacity to cope with physiological requirements (for instance, necessitated by cellular age), or changes in the environmental conditions (e.g., response and adaptation). In the context of active matter physics, plasticity of phenotypes is analogous to tunable activity spanning different timescales—either at individual or collective levels. **Figure 1** presents the relative scales of organization in aquatic phytoplankton. An example of phenotypic plasticity—asymmetric and symmetric morphotypes—that emerge rapidly in motile phytoplankton exposed to turbulent hydrodynamic cues is shown in **Figure 1F** [1]. The transition from an asymmetric to a symmetric cell shape depends on the properties of the external cue and the physiological state of the cells, which as depicted in **Figure 1E**, is potentially mediated by the intracellular cytoskeletal matrix. The nature of the cytoskeletal element, in combination with the orientational order of the cytoskeletal network, determine the cell geometry, playing a fundamental role in sensing and transmission mechanical perturbations [44, 45]. Physiologically, cytoskeletal organization and its dynamics mediate crucial functions in marine microorganisms [46–49]. Recent reports have suggested that cytoskeletal organization regulates biomineralization [46], and shapes mineralized [47] and labile [48, 49] forms. The secretion of biomineralized elements is tuned—in contrasting manners—by the disruption of the actin and microtubule networks. However, if and to which extent cytoskeletal order and emergent topological constraints, contribute to the transport processes involved, are yet to be explored. This could be particularly interesting in light of anisotropic diffusion in intra-cellular environments, known to facilitate the encounter and interaction of spindle-associated proteins [50]. Linking cytoskeletal order and organization to cellular physiology and functions will enable an integrative understanding of microbial behavior and lifestyles, while furthering our comprehension of multiscale complexities in nature for potential material science applications.

Phenotypic variations are commonplace among prokaryotes too, both at single cell and population scales. In absence of changes in their micro-environment, individual cells in a microbial population can exhibit intrinsic phenotypic heterogeneity [2, 51]. As shown in **Figure 1G**, within an expanding colony of bacteria under steady conditions (nutrients and temperature), cells can exhibit intrinsic differences in the cell aspect ratio, i.e., the ratio of length to width of the cell. Additionally, phenotypic heterogeneities can emerge as a consequence of the ecological constraints, with different cell morphologies competing for limited resources. Recent results suggest that microbial populations comprising morphologically distinct shapes can undergo spatial structuring [52], with potential ramifications on the cell lineage and fitness. Additional heterogeneities in phenotypes can co-exist, or co-emerge, including different cell structures (e.g., size and number of flagella), motility, surface attributes (e.g., adhesive properties), and growth rates. Taken together, phenotypic traits and variations therein, lead to a rich biophysical landscape where the interplay of microbial activity, geometry, and local order trigger emergent behavior and functions.

For surface-associated bacterial colonies, the generation and propagation of growth-induced active stress is determined by the activity (cell division rate) and the cell geometry, characterized by the ratio of cell length over width, or the aspect ratio (**Figure 1H**) [2]. The emergence of microdomains is mediated by two competing forces: the steric forces between neighboring cells and the extensile stresses due to cell growth, which, respectively, tend to favor cell alignment and disrupt the local orientational order of the system. The aspect ratio of cells in a colony determines the overall size (area) and spatial distribution of emergent nematic microdomains. Thus, for a given number of bacterial cells, an increase in the aspect ratio results in fewer number of nematic microdomains, each of which is however larger in size. The interplay of growth stresses and the steric interactions results in an exponential distribution of the domain areas, with a characteristic length scale proportional to the square root of the ratio between the orientational stiffness of the system and the magnitude of the extensile active stress. For a given size of the colony, the tradeoff between the size of the bacterial cells and that of the nematic microdomains determine the total number of topological defects. The defects nucleate at the intersection of three (or occasionally, four) distinctly oriented nematic microdomains, as shown in **Figure 1I**, where the $+1/2$ and $-1/2$ topological defects are indicated by the (**+**) and (•) signs. The position and nature of the defects can be determined using a two-step analysis involving identification of the microdomain intersections (step 1), and then evaluating the angular rotation of bacterial cells around this intersection

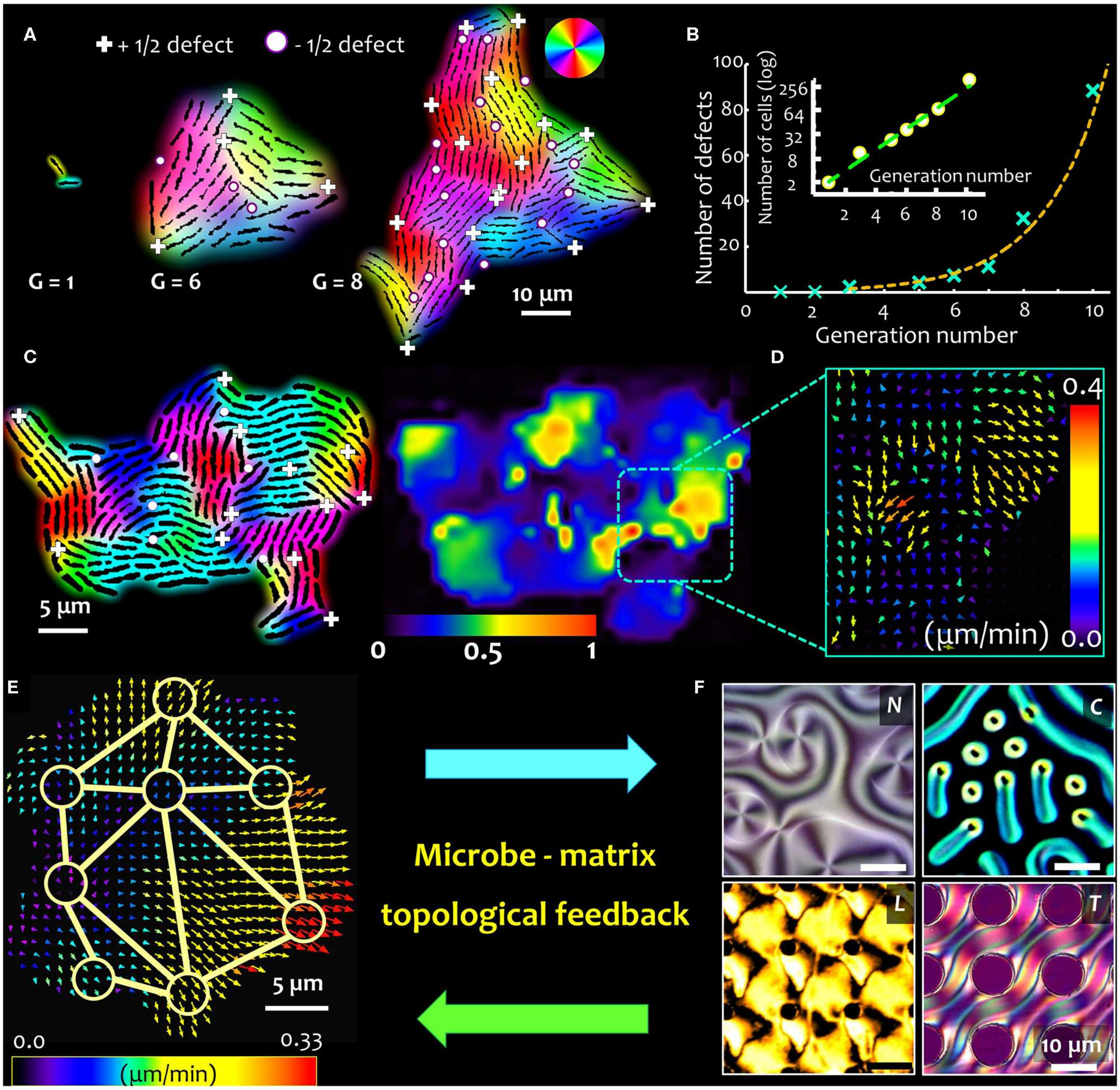

FIGURE 2 | Topological feedback in microbe-matrix ensemble. Close packing of microbes with anisotropic shape trigger spontaneous formation of topological defects. **(A)** Time lapse snapshots of a growing bacterial colony of non-motile *E. coli* strain (NCM 3722 delta-motA), where G refers to the generation time (i.e., the number of cell doubling events). Here the cells divide every ∼45 min. As the colony expands, topological defects emerge spontaneously, either at the periphery or within the bulk of the colony. The defects nucleate at the intersection of 3 or more distinctly oriented microdomains, which are indicated here by (+) and (•) signs, for +1/2 integer and −1/2 integer topological strengths, respectively. **(B)** The total number of topological defects (sum of +1/2 and −1/2 integer defects) increases close to exponentially with time (represented here by the generation number, G), and near linearly to the corresponding cell number in the colony. The corresponding bacterial cell numbers are plotted on a log scale, in the inset. **(C)** As the cells keep dividing, the growth-induced mechanical stresses reorganize the topological defects within the colony, triggering active cell flows within the colony, revealing a patchy flow landscape with counter-rotating vortical regions. The relative strength of the active flows is indicated by the heat map scale bar. **(D)** The local active flow field, with the arrow-heads indicating the direction of the emergent flow, color coded according to the flow speed. Stronger flows are observed in regions with higher density of topological defects. **(E)** Topological defects overlaying active flow field couple with and the surrounding matrix **(F)**. The degree of order in the surrounding matrix, shown here for four distinct cases (clockwise)—nematic (N), cholesteric (C), and lyotropic liquid crystal materials (L), and a complex anisotropic substrate with topographical features (liquid crystal elastomers, T)—underpin the strength of the topological coupling. Stronger microbe-matrix coupling leads to higher feedback stability. Topological defect coupling, in combination with the growth induced mechanical stresses, introduce a novel biomechanical framework to analyze microbial physiology and behavior, both of which could be potentially tuned by the topology of the local micro-environment.

over a physical rotation of 2π around the same point (step 2). **Figures 2A,B**, respectively, track the nucleation and the number of topological defects emerging in an expanding bacterial colony over multiple generations (indicated by *G*). Using time lapse imaging technique (imaging the colony at regular time intervals), the growth rate and dynamics of the defects can be studied over multiple generations. The total number of topological defects (sum of +1/2 and −1/2 integer defects) increases non-linearly over time, with a rate proportionate to the exponential growth of the colony (shown in the inset of **Figure 2B**).

The constellation of topological defects and their dynamics within colonies of different bacterial morphologies have been described as two and three dimensional active nematic systems [51, 53–55]. Theoretically, the shape of growing bacterial colonies was explained using continuum approach wherein cells were treated as active gel growing in an isotropic liquid [53]. Friction, between cells and with the underlying substrate, was found to be a key determinant of the defect dynamics, which ultimately regulated the colony morphology. Growth of bacterial monolayers under soft agarose surfaces demonstrated that topological defects were created at a constant rate, with the motility of +1/2 defects biased toward the colony periphery [54]. More recently, studies on bacterial monolayers were extended to analyze multilayer morphologies, capturing the early developmental stages of bacterial biofilms [51, 55, 56]. Analytical modeling and numerical simulations have revealed that the transition from mono to multilayered morphology (in bacterial colonies of rod-shaped cells) is triggered by a competition between the growth-induced in-plane active stresses and vertical restoring forces due to the cell-substrate interactions [51]. Although the transition is localized and mechanically deterministic for small colony sizes, asynchronous cell division renders the process stochastic in larger colonies. In the limit of high cell numbers, the occurrence of the first division in the colony can be approximated as a Poisson process, the rate of which gives the order parameter of the transition, revealing the mixed deterministic-stochastic nature of the process. For bacterial colonies of chain-shaped cells, the multilayered structure emerged due to an interplay of mechanical stress accumulation and friction, resulting in buckling and edge instabilities [55]. The buckling sites were characterized by nucleation of topological defects that initiated the formation of three-dimensional sporulation points.

ACTIVE MICROBIAL FLOWS: DYNAMICS OF TOPOLOGICAL DEFECTS

The spontaneous formation of nematic microdomains in an expanding bacterial colony nucleates topological defects in the local orientational field. In passive liquid crystals, the coupling between the hydrodynamic and nematic fields determines the dynamics of the topological defects and their influence on the viscoelastic properties of the fluid [57]. This often leads to exotic hydrodynamic ramifications: charge-dependent defect speeds, low Reynolds number cavitation phenomenon and coupling between singularities across disparate fields [58–60]. Topological defects in active nematic systems differ fundamentally from their passive counterparts, on the following two fronts [61]: (i) defects in active nematic systems act as motile self-propelled particles with their motility (speed) proportional to the activity; and (ii) defects in active nematic systems can nucleate continuously due to the local energy input. Consequently, the total number of topological defects (or defect pairs) keeps increasing with time. As defect tracking experiments have revealed [54, 62, 63], −1/2 and +1/2 topological defects possess different intrinsic motilities: while −1/2 defects are observed to be advected with the expansion of the colony, the +1/2 defects have a sustained biased motility, the direction of which is determined by the extensile nature of the active stresses.

As the cells divide, the growth-induced active stresses reorganize the topological defects within the colony, triggering active vortical flows within the colony. In experiments, the local nematic director and the position of the topological defects can be captured using time lapse imaging. The image data are analyzed using particle image velocimetry technique, and the emergent flows are visualized using a heat map that captures the flow magnitudes as shown in **Figure 2C**. The relative strength of the active flow domains is indicated by the accompanying color scale. The patchy flow landscape spatially correlates with the position of the topological defects, following the numerical predictions [2, 64], with the average patch size correlated with the mean separation of the topological defects. A closer look at the flow domains reveals the presence of counter-rotating vortical regions (**Figure 2D**), that emerge due to spontaneous disruption of the local orientational order. The regeneration and transformation of the topological defects allows sustained elastic and hydrodynamic interactions. In general, such flow fields can be broken down into radial and tangential components, through continuum modeling of the experimental data. Along the radial direction, the flow is predominantly expansive owing to the cell growth, whereas no net circulation is captured along the tangential direction [2].

Recent experimental and theoretical studies in a range of living systems have shown that local order and topology can underpin biological functions at cellular and sub-cellular scales [35–37, 50, 65, 66]. The dynamics of phenotypic plasticity can be analyzed in the framework of liquid crystallinity, where local anisotropy, order, and topology underpins emergent mechanics at population, individual and sub-cellular scales. Despite the lasting evidence that liquid crystals are ubiquitous in, and intrinsic to, almost all biological structures [67], their potential role in mediating phenotypic plasticity is largely unexplored, thus, leaving open a major gap in our efforts to understand the physics of life. Material topology, a salient attribute of liquid crystalline systems, goes beyond geometric shape, and can fundamentally impact the biophysics in microbial systems including mechanical pliability of colonies, transmission of mechanical stresses, and transport of molecules and particles (e.g., bacteriophages), all of which are crucial determinants of a cell's physiological state and fitness. A majority of current models of biologically active systems are based on particles possessing single, time-independent phenotypic traits: accounting for time-dependent phenotypes, observed frequently in natural and synthetic microbial systems, should allow development of new models that are not only richer in physics, but also a step closer to *real* microbial systems.

TOPOLOGICAL FEEDBACK: CROSS-TALK BETWEEN MICROBE AND ITS MICRO-ENVIRONMENT

Microbes inhabit highly diverse ecosystems where periodic and stochastic variations in the environmental parameters determine cellular fitness, survival, and succession. Light availability, ambient temperature, fluid flow, and material compliance are typical abiotic factors that define the conditions of microbial environments (or the matrix). Unlike laboratory settings, where environmental factors are well-defined, controllable and tractable over time, natural parameters seldom represent steady state conditions. To bring out the functional role of active matter physics in microbial ecology, microorganisms need to be studied in relation to their environments, accounting for the spatial and temporal dynamics of the matrix attributes. From a biophysical standpoint, a vast majority of microbial matrices is composed of biopolymers, amphiphilic lipids, cytoskeletal and muscle proteins, collagens and proteoglycans, and liquid crystal phases (primarily, lyotropic, or cholesteric phases) [68]. These building blocks for microbial matrices are inherently anisotropic, possessing long-range order with concomitant fluidity. The structured, out-of-equilibrium settings, combined with the inherent fluidity, render them akin to liquid crystal materials. More generally, variations in the environmental parameters can trigger topological transformations in the microbial matrix itself, thus initiating a *topological feedback*—an active cross-talk of underlying topological features of the microbial matter and the micro-environment. Conceptually, the framework for topological feedback was proposed recently in nematic micro-flows, where singularities across different fields interacted in a coexisting setting [59]. Similar dynamics is expected to be at play in microbial ecosystems, wherein topological singularities are coupled across the microbial system and its surrounding matrix, leading to feedbacks that could regulate microbial behavior and physiology.

Recent experiments along this line have been conducted with motile bacteria dispersed in liquid crystalline medium [69, 70]. The results have demonstrated that microbial activity (motility in this case) couples with the topology of the local environment, ultimately biasing microbial migration. Depending upon the local topological characteristics, the cells were found to accumulate in the vicinity of $+1/2$ topological defects, and escape regions of topological $-1/2$ defect. The ability to regulate bacterial motion by imposing topological constraints in the surrounding environment offers a novel route to trap or transport natural and synthetic swimmers in anisotropic liquids. Consequently, patterns of topological defects could be further designed to tune the emergent order of surface-associated bacterial colonies or of dense populations of motile swimmers, to give rise to a novel class of active matter system.

Beyond the exciting premise of engineering model active matter systems that can be tuned by matrix topology, or hydrodynamics or both, the coupling between microbial activity and matrix properties can have more fundamental implications. The dynamic feedback between the material and microbes can regulate the behavior and physiology of microbes in a population or community, offering fitness benefits based on microbial phenotypes. As depicted in **Figures 2E,F** preliminary results by the author [71] indicate that the organization of topological defects in the surrounding matrix influences the spatial and temporal dynamics of the topological defects in the microbial colony. Since a growing colony of non-motile bacteria spontaneously forms a network of topological defects, the dynamics and organization of the defects is modified by the constraints posed by the surrounding matrix. Dynamic landscapes of topological defects in a microbial colony can cross-talk with the network of topological defects—imposed or spontaneously formed—in the surrounding matrix, influencing the active cell flow properties and molecular transport regimes. A number of liquid crystalline materials can be used as potential testbeds for microbe-matrix interaction studies, which when combined with micro-fabricated templating, could provide a rich diversity of topological and topographical landscapes on which microbial dynamics can be studied (**Figure 2F**).

CONCLUSIONS AND PROSPECTS

The advent of cross-disciplinary multi-scale experimental approaches has enabled simultaneous characterization of microbial behavior, physiology and their habitats spanning multiple length and time scales. We are able to investigate and analyze living materials undergoing a major makeover—thanks to the physics of liquid crystals—that has propelled a growing exploration of topology-mediated physics in both fundamental studies and potential applications aimed at tailoring material attributes down to the molecular scale. Our ability to zoom into the micro-scale dynamics will help reveal how microbial environment—both structural and topological—shape the non-equilibrium dynamics, and over longer timescales, equilibrium microbial landscapes for single species or microbial consortia. Crucially, in a converse setting, we are on the verge of uncovering if (and how) micro-scale structural attributes in a given matrix—both topological and topographical—mediate microbial phenotypes, physiology, and population fitness. A further boost in this direction could be provided by incorporating machine learning approaches to study microbe-material interfaces, including deep neural networks for feature recognition and tracking; or recurrent nets and random forests for analysis of time series. As highlighted in a recent Review [72], the promise and prospects of machine learning in active matter research is still in its infancy, however there is a growing interest in exploring this avenue, which has proved valuable in a number of other areas of research. By looking at the ensemble of microbes and their surrounding matrix, active topological feedback can be revealed, with potentially far-reaching implication in the fields of medical, food, and environmental biotechnology. Taken together, the topological framework discussed here represents a rich and dynamic parameter space for material-microbe interactions, still awaiting exploration.

DATA AVAILABILITY STATEMENT

All datasets generated for this study are included in the article/supplementary material.

AUTHOR CONTRIBUTIONS

AS conceptualized the research, conducted experiments, analyzed the data, and wrote the paper.

FUNDING

This work was supported by the ATTRACT Investigator Grant (A17/MS/11572821/MBRACE) of the Luxembourg National Research Fund.

ACKNOWLEDGMENTS

AS was grateful for the valuable discussions with L. Giomi, J. M. Yeomans, M. G. Mazza, W. C. K. Poon, M. M. Telo da Gama, F. Cichos, K. Kroy, C. Wagner, N. Araújo, J. Najafi, M. Ackermann, K. Drescher, J. Dunkel, and members of the *Physics of Living Matter Group*, Luxembourg.

REFERENCES

1. Sengupta A, Carrara F, Stocker R. Phytoplankton can actively diversify their migration strategy in response to turbulent cues. *Nature*. (2017) **543**:555–8. doi: 10.1038/nature21415
2. You Z, Pearce DJG, Sengupta A, Giomi L. Geometry and mechanics of microdomains in growing bacterial colonies. *Phys Rev X*. (2018) **8**:031065. doi: 10.1103/PhysRevX.8.031065
3. Jin Q, Scherp P, Heimann K, Hasenstein KH. Auxin and cytoskeletal organization in algae. *Cell Biol Int*. (2008) **32**:542–5. doi: 10.1016/j.cellbi.2007.11.005
4. Shade A, Peter H, Allison SD, Baho DL, Berga M, Bürgmann H, et al. Fundamentals of microbial community resistance and resilience. *Front Microbiol*. (2012) **3**:417. doi: 10.3389/fmicb.2012.00417
5. Bengtsson-Palme J, Kristiansson E, Joakim Larsson DG. Environmental factors influencing the development and spread of antibiotic resistance. *FEMS Microbiol Rev*. (2018) **42**:68–80. doi: 10.1093/femsre/fux053
6. Pasteur L, Seances Nouvelles CR. Experiences pour démontrer que le germe de la levure qui fait le vin provient de 1'extérieur des grains de raisin. *Acad Sci Paris*. (1872) **75**:781.
7. Hungate RE. Evolution of a microbial ecologist. *Ann Rev Microbiol*. (1979) **33**:1–20. doi: 10.1146/annurev.mi.33.100179.000245
8. Adler A, Dücker E. When pasteurian science went to sea: the birth of marine microbiology. *J His Biol*. (2018) **51**:107–33. doi: 10.1007/s10739-017-9477-8
9. De Wit R, Bouvier T. Everything is everywhere, but, the environment selects' what did Baas Becking and Beijerinck really say? *Environ Microbiol*. (2006) **8**:755–8. doi: 10.1111/j.1462-2920.2006.01017.x
10. Peterson J, Garges S, Giovanni M, McInnes P, Wang L, Schloss JA, et al. The NIH human microbiome project: NIH HMP working group. *Genome Res*. (2009) **19**:2317–23. doi: 10.1101/gr.096651.109
11. Turnbaugh PJ, Ley RE, Hamady M, Fraser-Liggett C, Knight R, Gordon JI. The human microbiome project: exploring the microbial part of ourselves in a changing world. *Nature*. (2007) **449**:804–10. doi: 10.1038/nature 06244
12. Mezzenga R, Schurtenberger P, Burbidge A, Michel M. Understanding foods as soft materials. *Nat Mat*. (2005) **4**:729–40. doi: 10.1038/nmat1496
13. Jansson JK. Soil microbiomes and climate change. *Nat Rev Microbiol*. (2019) **18**:35–46. doi: 10.1038/s41579-019-0265-7
14. Kim Y-K, Noh JH, Nayani K, Abbott NL. Soft matter from liquid crystals. *Soft Matter*. (2019) **15**:6913–29. doi: 10.1039/C9SM01424A
15. Ramanana R, Kim B-H, Cho D-H, Kim H-S. Algae-bacteria interactions: evolution, ecology and emerging applications. *Biotech Adv*. (2016) **34**:14–29. doi: 10.1016/j.biotechadv.2015.12.003
16. Sommer T, Danza F, Berg J, Sengupta A, Constantinescu G, Tokyay T, et al. Bacteria induced mixing in natural waters. *Geophys Res Lett*. (2017) **44**:9424–32. doi: 10.1002/2017GL074868
17. Tshikantwa TS. Ullah MW, He F, Yang G. Current trends and potential applications of microbial interactions for human welfare. *Front Microbiol*. (2018) **9**:1156. doi: 10.3389/fmicb.2018.01156
18. Lederberg J. Ome sweet 'omics-a genealogical treasury of words. *Scientist*. (2001) **15**:8.
19. Bechinger C, Di Leonardo R, Löwen H, Reichhardt C, Volpe G, Volpe G. Active particles in complex and crowded environments. *Rev Mod Phys*. (2016) **88**:045006-1–50. doi: 10.1103/RevModPhys.88.045006
20. Fodor E, Marchetti C. The statistical physics of active matter: from self-catalytic colloids to living cells. *Physica A Stat Mech App*. (2018) **504**:106–20. doi: 10.1016/j.physa.2017.12.137
21. Marchetti MC, Joanny JF, Ramaswamy S, Liverpool TB, Prost J, Rao M, et al. Hydrodynamics of soft active matter. *Rev Mod Phys*. (2013) **85**:114320. doi: 10.1103/RevModPhys.85.1143
22. Cates ME, Tailleur J. Motility-induced phase separation. *Ann Rev Cond Matt Phys*. (2015) **6**:219–44. doi: 10.1146/annurev-conmatphys-031214-014710
23. Klamser JU. Kapfer SC, Krauth W. Thermodynamic phases in two-dimensional active matter. *Nat Commun*. (2018) **9**:5045. doi: 10.1038/s41467-018-07491-5
24. Lauga E. Bacterial hydrodynamics. *Ann Rev Fluid Mech*. (2016) **48**:105–30. doi: 10.1146/annurev-fluid-122414-034606
25. Coelho RCV, Araújo NAM, Telo da Gama MM. Propagation of active nematic-isotropic interfaces on substrates. *Soft Matter*. (2020) **16**:4256–66. doi: 10.1039/C9SM02306B
26. Patteson AE, Gopinath A, Arratia PE. The propagation of active-passive interfaces in bacterial swarms. *Nat Commun*. (2018) **9**:5373. doi: 10.1038/s41467-018-07781-y
27. Xu H, Dauparas J, Das D, Lauga E, Wu Y. Self-organization of swimmers drives long-range fluid transport in bacterial colonies. *Nat Commun*. (2019) **10**:1792. doi: 10.1038/s41467-019-09818-2
28. Riley EE, Lauga E. Enhanced active swimming in viscoelastic fluids. *Europhys Lett*. (2014) **108**:34003. doi: 10.1209/0295-5075/108/34003
29. Zöttl A, Yeomans JM. Enhanced bacterial swimming speeds in macromolecular polymer solutions. *Nat Phys*. (2019) **15**:554–8. doi: 10.1038/s41567-019-0454-3
30. Makarchuk S, Braz VC, Araújo NAM, Ciric L, Volpe G. Enhanced propagation of motile bacteria on surfaces due to forward scattering. *Nat Commun*. (2019) **10**:4110. doi: 10.1038/s41467-019-12010-1
31. Kranz WT, Gelimson A, Zhao K, Wong GCL, Golestanian R. Effective dynamics of microorganisms that interact with their own trail. *Phys Rev Lett*. (2016) **117**:038101. doi: 10.1103/PhysRevLett.117.038101
32. Sackmann E. Activities and future challenges of soft matter and biological physics education. *Soft Matter*. (2013) **9**:5512–5. doi: 10.1039/c3sm90026f
33. Scheffer M, Carpenter SR, Lenton TM, Bascompte J, Brock W, Dakos V, et al. Anticipating critical transitions. *Science*. (2012) **338**:344–8. doi: 10.1126/science.1225244
34. Goldford JE, Lu N, Bajić D, Estrela S, Tikhonov M, Sanchez-Gorostiaga A, et al. Emergent simplicity in microbial community assembly. *Science*. (2018) **361**:469–74. doi: 10.1101/205831
35. Hartmann R, Singh PK, Pearce P, Mok R, Song B, Díaz-Pascual F, et al. Emergence of three-dimensional order and structure in growing biofilms. *Nat Phys*. (2019) **15**:251–6. doi: 10.1038/s41567-018-0356-9

36. Kawaguchi K, Kageyama R, Sano M. Topological defects control collective dynamics in neural progenitor cell cultures. *Nature*. (2017) **545**:327–31. doi: 10.1038/nature22321
37. Beng Saw T, Doostmohammadi A, Nier V, Kocgozlu L, Thampi S, Toyama Y, et al. Topological defects in epithelia govern cell death and extrusion. *Nature*. (2017) **544**:212–16. doi: 10.1038/nature21718
38. Miner BG, Sultan SE, Morgan SG, Padilla DK, Relyea RA. Ecological consequences of phenotypic plasticity. *Trends Ecol Evol*. (2005) **20**:685–92. doi: 10.1016/j.tree.2005.08.002
39. Kussell E, Kishony R, Balaban NQ, Leibler S. Bacterial persistence: a model of survival in changing environments. *Genetics*. (2005) **169**:1807–14. doi: 10.1534/genetics.104.035352
40. Maynard DS, Serván CA, Capitán JA, Allesina S. Phenotypic variability promotes diversity and stability in competitive communities. *Ecol Lett*. (2019) **22**:1776–86. doi: 10.1111/ele.13356
41. Haas PA, Oliveira NM, Goldstein RE. Subpopulations and stability in microbial communities. *Phys Rev Res*. (2020) **2**:022036. doi: 10.1103/PhysRevResearch.2.022036
42. Ackermann M. A functional perspective on phenotypic heterogeneity in microorganisms. *Nat Rev Microbiol*. (2015) **13**:497–508. doi: 10.1038/nrmicro3491
43. Forsman A. Rethinking phenotypic plasticity its consequences for individuals, populations species. *Heredity*. (2015) **115**:276–84. doi: 10.1038/hdy.2014.92
44. Fletcher DA, Mullins RD. Cell mechanics and the cytoskeleton. *Nature*. (2010) **463**:485–92. doi: 10.1038/nature08908
45. Liu Y, Visetsouk M, Mynlieff M, Qin H, Lechtreck KF, Yang P, et al. H^+- and Na^+- elicited rapid changes of the microtubule cytoskeleton in the biflagellated green alga *Chlamydomonas*. *eLife*. (2017) **6**:e26002. doi: 10.7554/eLife.26002
46. Durak GM, Brownlee C, Wheeler GL. The role of the cytoskeleton in biomineralisation in haptophyte algae. *Sci Rep*. (2017) **7**:15409. doi: 10.1038/s41598-017-15562-8
47. Tyszka J, Bickmeyer U, Raitzsch M, Bijma J, Kaczmarek K, Mewes A, et al. Form function of F-actin during biomineralization revealed from live experiments on foraminifera. *Proc Natl Acad Sci USA*. (2019) **116**:4111–6. doi: 10.1073/pnas.1810394116
48. Gemmell BJ, Oh G, Buskey EJ, Villareal TA. Dynamic sinking behaviour in marine phytoplankton: rapid changes in buoyancy may aid in nutrient uptake. *Proc R Soc B*. (2016) **283**:20161126. doi: 10.1098/rspb.2016.1126
49. Matt G, Umen J. Volvox: a simple algal model for embryogenesis, morphogenesis and cellular differentiation. *Dev Biol*. (2016) **419**:99–113. doi: 10.1016/j.ydbio.2016.07.014
50. Pawar N, Donth C, Weis M. Anisotropic diffusion of macromolecules in the contiguous nucleocytoplasmic fluid during eukaryotic cell division. *Curr Biol*. (2014) **24**:1905–8. doi: 10.1016/j.cub.2014.06.072
51. You Z, Pearce DJG, Sengupta A, Giomi L. Mono- to multilayer transition in growing bacterial colonies. *Phys Rev Lett*. (2019) **123**:178001. doi: 10.1103/PhysRevLett.123.178001
52. Smith WPJ, Davit Y, Osborne JM, Kim W, Foster KR, Pitt-Francis JM. Cell morphology drives spatial patterning in microbial communities. *Proc Natl Acad Sci USA*. (2017) **114**:E280–6. doi: 10.1073/pnas.1613007114
53. Doostmohammadi A, Thampi SP, Yeomans JM. Defect-mediated morphologies in growing cell colonies. *Phys Rev Lett*. (2016) **117**:048102. doi: 10.1103/PhysRevLett.117.048102
54. Dell'Arciprete D, Blow ML, Brown AT, Farrell FDC, Lintuvuori JS, McVey AF, et al. A growing bacterial colony in two dimensions as an active nematic. *Nat Commun*. (2018) **9**:4190. doi: 10.1038/s41467-018-06370-3
55. Yaman YI, Demir E, Vetter R, Kocabas A. Emergence of active nematics in chaining bacterial biofilms. *Nat Commun*. (2019) **10**:2285. doi: 10.1038/s41467-019-10311-z
56. Beroz F, Yan J, Meir Y, Sabass B, Stone HA, Bassler BL, et al. Verticalization of bacterial biofilms. *Nat Phys*. (2018) **14**:954–60. doi: 10.1038/s41567-018-0170-4
57. Sengupta A, Herminghaus S, Bahr C. Liquid crystal microfluidics - surface, elastic and viscous interactions at micro-scales. *Liq Cryst Rev*. (2014) **2**:73–110. doi: 10.1080/21680396.2014.963716
58. Tóth G, Denniston C, Yeomans JM. Hydrodynamics of topological defects in nematic liquid crystals. *Phys Rev Lett*. (2002) **88**:105504. doi: 10.1103/PhysRevLett.88.105504
59. Giomi L, Kos Ž, Ravnik M, Sengupta A. Cross-talk between topological defects in different fields revealed by nematic microfluidics. *Proc Nat Acad Sci USA*. (2017) **114**:201702777. doi: 10.1073/pnas.1702777114
60. Stieger T, Agha H, Schoen M, Mazza MG, Sengupta A. Hydrodynamic cavitation in Stokes flow of anisotropic fluids. *Nat Commun*. (2017) **8**:15550. doi: 10.1038/ncomms15550
61. Giomi L, Bowick MJ, Mishra P, Sknepnek R, Cristina Marchetti M. Defect dynamics in active nematics. *Phil Trans R Soc A*. (2014) **372**:20130365. doi: 10.1098/rsta.2013.0365
62. Doostmohammadi A, Mullol JI, Yeomans JM, Sagués F. Active nematics. *Nat Commun*. (2018) **9**:3246. doi: 10.1038/s41467-018-05666-8
63. van Holthe tot Echten D, Nordemann G, Wehrens M, Tans S, Idema T. Defect dynamics in growing bacterial colonies. *arXiv*. (2020) *arXiv*:2003.10509.
64. Thampi SP, Golestanian R, Yeomans JM. Vorticity, defects and correlations in active turbulence. *Phil Trans R Soc A*. (2014) **372**:20130366. doi: 10.1098/rsta.2013.0366
65. Mathijssen AJTM, Guzmán-Lastra F, Kaiser A, Löwen H. Nutrient transport driven by microbial active carpets. *Phys Rev Lett*. (2018) **121**:248101. doi: 10.1103/PhysRevLett.121.248101
66. Tan TH, Liu J, Miller PW, Tekant M, Dunkel J, Fakhri N. Topological turbulence in the membrane of a living cell. *Nat Phys*. (2020). doi: 10.1038/s41567-020-0841-9
67. Brown GH. *Liquid Crystals and Biological Structures*. New York, NY: Academic Press (1979).
68. Sengupta A. Topological microfluidics - present prospects. *Liq Cryst Today*. (2015) **24**:70–80. doi: 10.1080/1358314X.2015.1039196
69. Peng C, Turiv T, Guo Y, Wei Q-H, Lavrentovich OD. Command of active matter by topological defects patterns. *Science*. (2016) **354**:882–5. doi: 10.1126/science.aah6936
70. Genkin MM, Sokolov A, Lavrentovich OD, Aranson IS. Topological defects in a living nematic ensnare swimming bacteria. *Phys Rev X*. (2017) **7**:011029. doi: 10.1103/PhysRevX.7.011029
71. Thai ALP, Sengupta A. Topological coupling at microbe-matrix interfaces (in preparation).
72. Cichos F, Gustavsson K, Mehlig B, Volpe G. Machine learning for active matter. *Nat Mach Intell*. (2020) **2**:94–103. doi: 10.1038/s42256-020-0146-9

Conflict of Interest: The author declares that the research was conducted in the absence of any commercial or financial relationships that could be construed as a potential conflict of interest.

Advantages of publishing in Frontiers

OPEN ACCESS
Articles are free to read
for greatest visibility
and readership

FAST PUBLICATION
Around 90 days
from submission
to decision

HIGH QUALITY PEER-REVIEW
Rigorous, collaborative,
and constructive
peer-review

TRANSPARENT PEER-REVIEW
Editors and reviewers
acknowledged by name
on published articles

Frontiers
Avenue du Tribunal-Fédéral 34
1005 Lausanne | Switzerland

Visit us: www.frontiersin.org
Contact us: info@frontiersin.org | +41 21 510 17 00

REPRODUCIBILITY OF RESEARCH
Support open data
and methods to enhance
research reproducibility

DIGITAL PUBLISHING
Articles designed
for optimal readership
across devices

FOLLOW US
@frontiersin

IMPACT METRICS
Advanced article metrics
track visibility across
digital media

EXTENSIVE PROMOTION
Marketing
and promotion
of impactful research

LOOP RESEARCH NETWORK
Our network
increases your
article's readership